



*Università degli Studi
di Cagliari*



*Università degli Studi
di Sassari*

DOTTORATO DI RICERCA

In Scienze e Tecnologie Chimiche

Ciclo XXXIV

The importance of Laccase immobilisation in Biocatalysis: towards biomass pretreatment

Dottorando
Tutor
Coordinatore Dottorato

Davide Tocco
Prof. Andrea Salis
Prof. Stefano Enzo

Esame finale anno accademico 2021 – 2022

Acknowledgements

There are many people that I would like to acknowledge for their support and guidance during the past 3 years of my PhD. I would like to thank all my research, especially

I would like to thank my supervisor Prof. Andrea Salis for his valuable tips, and for the many opportunities he gave me. I thank him especially for pushing me outside of my comfort zone and making me a better researcher. Additionally, thanks for the countless hours put into drafting papers and this thesis.

Special thanks also go to my 'unofficial' supervisor Prof. Maura Monduzzi, who has been a valuable source of advice throughout my PhD.

I would like to extend my sincere thanks to Dr.ssa Cristina Carucci for all precious scientific advice and moment we have shared during this amazing period of my life!

I would like to thank Prof. Enrico Sanjust, Prof. Edmond Magner, Prof. Martin Hartmann, Dr. Sandro Sgrò and Prof. Gianluca Ottolina who have all assisted with this research at various stages of its progression. Thanks for introducing me to new techniques, and for guiding my understanding of this research project.

Special acknowledgments are dedicated to my colleague and officemate: Monica, David, Fausto, Antonella, Giada e Paola for all the good and bad moments we shared and for many coffees and beers we have drunk together.

I Would like to thank all CSGI group, in particular Dr. Chelazzi, Dr. Casini, Dr.ssa Guaragnone and Dr.ssa Mastrangelo for their help and assistance with research regards the study of enzyme location on MOF

A big thanks must also go to Antonio e Roberto for their technical support.

I would like to thank all my friends, especially: Alessandro (Sdrulik), Federico, Luca, Nicola M. for sharing in this journey with me, for being a part of all of the good times, and for your support through the less than good times. The endless singing, coffee, beers and wines have been a highlight.

I also would like to thank all friends that I met during my research period abroad. In particular way Laura, Carmelo, Marina e Silvia for having kept me company and for all moment of ‘panic’ we have done together.

Lastly, my biggest thanks go to my family. Thanks to Alberto, Monica e Valerio for your kind words, support and company, during the highs and lows of the past few years.

I would like to thank MIUR (PON RI 2014-2020, Azione 1.1 "Dottorati Innovativi con Caratterizzazione industriale"- DOT1304455 2) and Deutsche Akademische Austauschdienst (DAAD) for financing my PhD scholarship and my research period abroad at FAU Erlangen-Nürnberg.



We acknowledge the CeSAR (Centro Servizi di Ateneo per la Ricerca) of the University of Cagliari, Italy for the XRD experiments performed with Bruker Venture D8 as described in PAPER III

List of papers

The PhD project is based on the work reported in the following publications:

Published

1. **Tocco, D.**; Carucci, C.; Monduzzi, M.; Salis, A.; Sanjust, E. Recent Developments in the Delignification and Exploitation of Grass Lignocellulosic Biomass. *ACS Sustain. Chem. Eng.* 2021, 9, 2412–2432.
2. Delpiano, G.R.; **Tocco, D.**; Medda, L.; Magner, E.; Salis, A. Adsorption of malachite green and alizarin red s dyes using Fe-BTC metal organic framework as adsorbent. *Int. J. Mol. Sci.* 2021, 22, 1–16.
3. **Tocco, D.**; Carucci, C.; Todde, D.; Shortall, K.; Otero, F.; Sanjust, E.; Magner, E.; Salis, A. Enzyme Immobilisation. on Metal Organic Frameworks: Laccase from *Aspergillus sp* is better adapted to ZIF-zni rather than Fe-BTC. *Colloids Surfaces B Biointerfaces* 2021, 208, 112147.

Submitted

4. **Tocco, D.**; Wisser D.; Fisher.; Schwieger W.; Salis, A.; Hartmann M. Immobilisation. of *Aspergillus sp.* Laccase on hierarchical Zeolite type MFI.

To be submitted:

5. **Tocco, D.**; Chelazzi, D.; Casini, A.; Mastrangelo, R.; Salis, A.; Baglioni, P. A study about the conformational changes and location of BSA upon immobilisation. on zeolitic imidazolate frameworks (ZIF-8 and ZIF-zni).

Table of Contents

Acknowledgements	2
List of papers.....	4

CHAPTER 1: INTRODUCTION AND LITERATURE REVIEW

1. Catalysis and biocatalysis.....	13
1.1 Enzymes.....	14
1.2 Classification of enzymes.....	15
1.3 Laccase.....	16
1.4 Structure and properties of laccases	17
1.5 Laccases in industrial processes.....	19
1.5.1 Biofuels.....	19
1.5.2 Bioprocessing of Food Industry By-Products.....	19
1.5.3 Removal of pollutants.....	20
1.5.3 Organic synthesis.....	20
1.5.5 Enzyme activity.....	21
1.6 Parameters which affect the laccase activity.....	22
1.6.1 Effect of pH on enzyme activity.....	22
1.6.2 Solvent.....	23
1.6.3 Enzymatic kinetics.....	25

CHAPTER 2: LACCASE IMMOBILISATION ON SUPPORTS

2. Overview of enzyme immobilisation.....	27
2.1 Enzyme immobilisation.....	27
2.1.1 Physical adsorption	28
2.1.2 covalent attachment	29
2.1.3 Cross-linked enzyme aggregated (CLEA)	30
2.1.4 Enzyme encapsulation	31
2.1.5 Entrapment	31
2.2 Support for enzyme immobilisation	32
2.2.1 Ordered mesoporous materials.....	34
2.2.2 Metal Organic Frameworks (MOFs).....	36
2.2.3 Zeolitic imidazolate frameworks (ZIFs)	40
2.2.4 Hierarchical Zeolites	47

CHAPTER 3: SCOPE OF THE THESIS

3.1 Support screening.....	55
3.2 Enzyme location.....	55
3.3 Enzyme secondary structure.....	56

CHAPTER 4: CHARACTERISATION TECHNIQUES

4.1 Powder X-rays Diffraction (XRD)	58
4.2 N ₂ physisorption.....	60

4.3 Thermogravimetric Analysis (TGA):	63
4.4 Fourier Transform Infrared Spectroscopy (FTIR)Infrared.....	64
4.5 Electron Microscopy:	66
4.6 Scanning Electron Microscopy and Transmission Electron Microscopy.....	67
4.7 Confocal laser Microscopy:	69

CHAPTER 5: RESULTS

Results.....	70
--------------	----

CHAPTER 6: CONCLUSIONS

Conclusion	85
Bibliography	88

APPENDIX

PAPER I

PAPER II

PAPER III

PAPER IV

PAPER V

Abbreviations

ABTS (2,2'-Azino-bis (3-ethylbenzothiazoline-6-sulfonic acid) diammonium salt

BET Brunauer-Emmet-Teller

BML lignocellulosic biomass

BOD biochemical oxygen demand

CLEA Cross-linked enzyme aggregates

CLSM Confocal Laser Scanning Microscopy

COD chemical oxygen demand

FITC Fluorescein isothiocyanate

FPA Focal Plane Array

IUB International Union of Biochemistry

LC Laccase

LMSs Laccase mediator systems

MOF Metal-organic framework

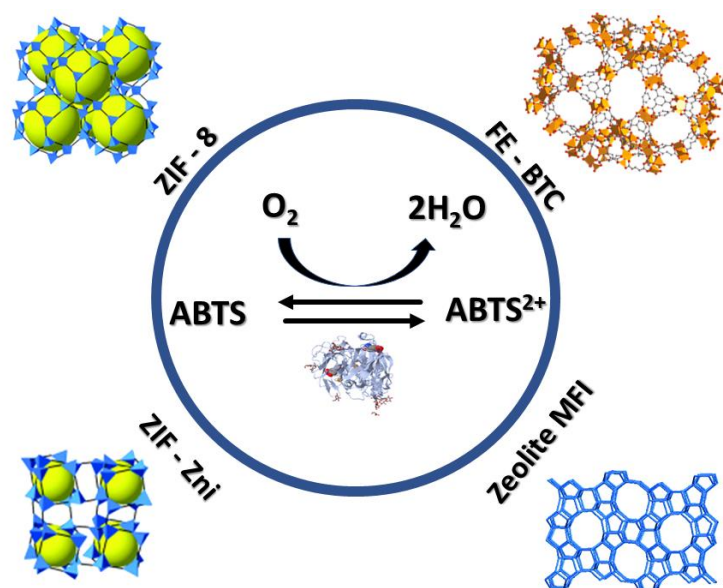
PXRD Powder X-ray diffraction

Sod Sodalite

SEM Scanning electron microscopy

ZIF-8 Zeolitic imidazolate framework-8

ZIF-zni Zeolitic imidazolate framework-zni



Graphical abstract. Immobilisation of *Aspergillus sp.* laccase on MOFs and Zeolite MFI supports.

Abstract

In these last decades, tremendous efforts in using enzymes as catalysts for a wide range of reactions have been made. Although biocatalysis shows many advantages, the use of enzymes to catalyse reactions requires restrictive environmental conditions that are often not compatible with industrial processing. However, these issues could be overcome through enzymatic immobilisation. Immobilisation can improve biocatalytic stability and enable enzyme reuse for several times, resulting in better performance and commercial viability. Since the rate of the catalytic reaction depends on both the enzyme and support chosen, it is worth investigating the best combination between enzyme and support to catalyse a target reaction. Here, three trimesic acid-based MOFs: Fe-BTC, Tb-BTC, Gd-BTC, an imidazolate-based MOF: ZIF-zni and on functionalised pure-silica hierarchical (microporous-macroporous) MFI zeolite (ZMFI) to screen which, among the chosen supports, is more suitable for Laccase (LC) immobilisation. *Aspergillus sp.* Laccase immobilisation within MOFs occurred in situ under mild conditions, e.g. aqueous solution, neutral pH, and at room temperature.

The immobilisation of the laccase on MFI-Type Zeolite particles with embedded macropores was instead carried out post synthesis. All Biocatalysts were characterised through XRD, SEM, FTIR, N₂ adsorption/desorption isotherms and TGA.

The kinetic parameters (K_M and V_{max}) and the specific activity of the immobilised biocatalysts were determined. The effect of enzyme loading was studied for Fe-BTC and ZIF-zni supports. LC@FeBTC had an optimal loading of 45.2 mg g⁻¹, at higher enzyme loadings the specific activity decreased. In contrast, the specific activity of LC@ZIF-zni increased linearly over the loading range investigated. LC@GdBTC showed the highest specific activity compared with other carriers investigated. Nevertheless, a drastic decrease in specific activity was found due to enzyme immobilisation.

Laccase from *Aspergillus sp.* (LC) was immobilised on functionalised pure-silica hierarchical (microporous-macroporous) MFI zeolite (ZMFI). The optimal pH, kinetic parameters (K_M and V_{max}), specific activity, as well as both storage and operational stability of LC@ZMFI were determined. The dependence of specific activity on the pH for free and immobilised LC was investigated in the pH range of 2 to 7. Immobilisation of laccase on hierarchical pure-silica MFI zeolite allows to carry out the reaction under acidic pH values without affecting the support structure.

Although enzymatic immobilisation is gaining an increasing attention, especially regarding of enzyme encapsulated within MOFs, the enzymatic location and its change in conformation after immobilisation within MOFs are still poorly investigated. Commercial enzymes often show a very low grade of purity, and their enzymatic structure is still unknown, these aspects make tricky the investigation of their location and conformation. In this regards Bovine serum albumin (BSA) with high purity (> 98%?) with a known secondary and tertiary structure was used as a model protein.

BSA was immobilised within two different zeolitic imidazolate frameworks (ZIF-zni and ZIF-8) through a one-pot synthesis carried out under mild conditions (room temperature and aqueous solution). The ZIF-zni, ZIF-8 and the BSA@ZIF-zni, BSA@ZIF-8 samples were characterised by X-ray diffraction, scanning electron microscopy, confocal laser scanning microscopy, thermogravimetric

analysis, micro-FTIR and confocal Raman spectroscopy to characterize the MOF structures and evaluate the protein location in the materials. Moreover, the secondary structure and conformation changes of BSA due to its immobilisation. on both ZIF-zni and ZIF-8 were studied. Results showed that BSA seems to concentrate in domains of 5-40 μm , which form an extended network across the MOF. Additional information on changes in the BSA structure upon immobilisation was extracted by the deconvolution of the amide I band in the reflectance spectra. Data showed that the crystalline content of BSA increases significantly when the protein is immobilised on the MOFs in BSA@ZIF-zni and ZIF-8. Before interaction with the MOF, amide I deconvolution indicates that BSA has a strong content in β -turns (~89%), with limited contribution from β -sheets (~4%). Whilst the crystalline content of BSA increases significantly when the protein is immobilised on both ZIF-zni and ZIF -8 resulting in increased up to ~25% (β -sheets + α -helices), and ~40 % (β -sheets + α -helices) respectively with a consequent drastic reduction of β -turns.

CHAPTER 1:

INTRODUCTION AND LITERATURE

REVIEW

1. Catalysis and biocatalysis

The process in which a substance, called “catalyst”, increases the rate of a reaction without modifying the overall standard Gibbs energy change in the reaction; is called catalysis (Figure 1).¹ This phenomenon was observed for the first time by G.S.C. Kirchhoff in 1811-1814, but the name ‘*catalysis*’ was proposed by Berzelius in 1838.² Depending on the reagent and catalyst phases involved in the reaction, catalysis can be classified as homogeneous (reagent and biocatalyst are in the same phase) or heterogeneous (reagent and biocatalyst are in different phases).¹ Catalysts act by lowering the energetic barrier (activation energy) which must be overcome to turn reactants into products without affecting the thermodynamics and hence the equilibrium constant of the reaction.

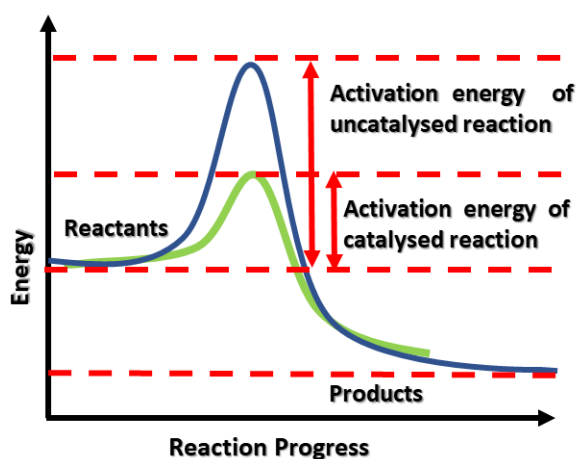


Figure 1: Potential energy plot showing the effect of a catalyst on a reaction.

The catalysts of biological reactions are called enzymes.^{3,4} The chemical process through which enzymes or microorganisms catalyse organic reactions is called biocatalysis.⁵ Since ancient times mankind unwittingly took advantage of microorganisms to perform chemical transformations such as beer fermentation, baking bread, and milk curdling. The alcoholic fermentation process catalysed by cell-free extracts was described for the first time by Buchner in 1897.⁶ Whilst the first enantioselective organic synthesis catalysed by an enzyme was described by Rosenthaler in 1909.⁷ Since then, revolutionary advances have been made in biocatalysis.⁸ Due to their many advantages such as:

- The high efficiency: a low amount of enzyme ($10^{-3} - 10^{-4}$ % w/w) can accelerate chemical reactions with tremendously high efficiency and selectivity. Typically enzymatic reactions are $10^{10} - 10^{15}$ times faster than uncatalyzed chemical reactions.^{9,10}
- High chemo- regio- and stereoselectivity.¹¹ These aspects make the processes more atom and step economic generating less waste and consuming less energy than conventional processes.¹²
- The substrate conversion is performed under mild conditions (aqueous solution, physiological pH, and room temperature) affording high rates and selectivity.¹³

The use of enzymes to catalyse chemical reactions is considered a crucial strategy that perfectly fits most of the 12 principles of ‘*Green chemistry*’. In particular, they allow to eliminate the use or generation of hazardous substances in the design, manufacture, and application of chemical products.¹⁴⁻¹⁶ For these reasons biocatalysis has become a mainstream technology for the synthesis of chemicals production such as polymers, biofuels,¹⁶⁻¹⁸ and for the production of chiral intermediates of drugs such as: antianxiety, antidiabetic, antiviral, HIV protease inhibitor, anti-cancer, anti-cholesterol, anti-Alzheimer, anti-infective, and anti-hypertensive.^{19,20} Recently, Slagman *et al.* published a review about the study of biocatalytic routes to anti-viral agents and their synthetic intermediates of potential antiviral agents including antivirals against SARS-CoV-2.²¹

1.1 Enzymes

The term enzyme was used for the first time by German physiologist Wilhelm Kühne.² Its etymology derives from the Greek words “en” (meaning ‘within’) and “zume” (meaning ‘yeast’). Enzymes are globular proteins constituted by a maximum of four layers of structural complexity. Their primary structure consists in a linear sequence of amino acids: polypeptides with various side chains. Secondary structure is the local structure of the peptide backbone of the protein. There are two common types of secondary structure: the α -helices, which are feature a clockwise spiral structure, and β -sheets, which have a pleated structure. Tertiary structure is the three-dimensional structure of

the entire polypeptide subunit, including side chains. Finally, the quaternary structure is how different subunits fit together to form the entire protein (Figure 2).²²

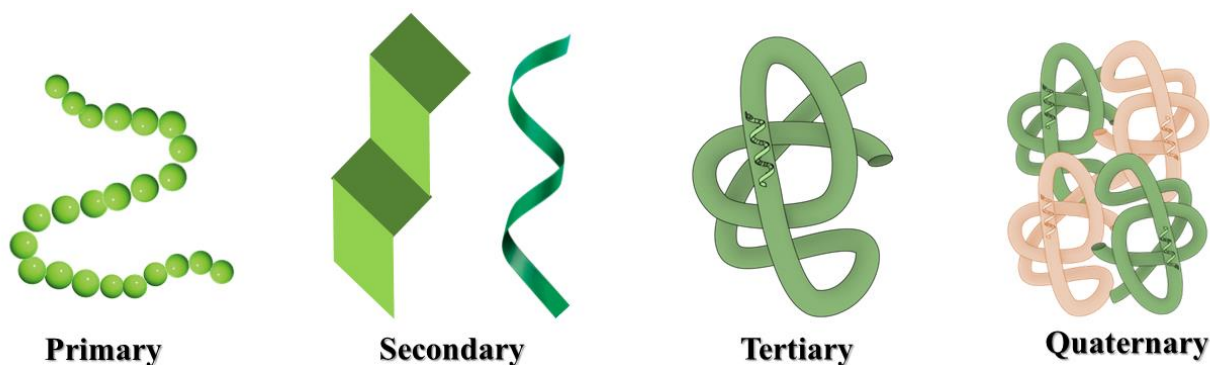


Figure 2: The four protein structural levels in order of increasing complexity

Enzymes are biocatalysts that accelerate the biochemical reactions in living organisms by lowering the activation energy barrier between reactants and products. Compared to conventional catalysts, such as transition metals, enzymes are generally more selective, non-toxic, and biodegradable.^{16,18} Moreover, they are known to catalyse more than 5.000 biochemical reaction types and they can be produced by microorganisms for several industrial applications.^{23–25} Due to the rising demand for sustainable biocatalysts,²⁶ the global market of enzymes has grown fast in the last few years considering that the global enzyme market value reached 8.2 billion USD in 2015 and is expected to reach 18.5 billion USD by 2024.^{27,28}

1.2 Classification of enzymes

In 1961 the need for a unique enzymatic classification has led the International Union of Biochemistry (IUB) to publish the first enzyme classification.²⁹ Enzymes are classified into seven categories according to the type of reaction they catalyse: oxidoreductases, transferases, hydrolases, lyases, ligases, isomerases and translocases (table 1).³⁰ The enzyme names are composed by a four-number code which is prefixed by EC. It defines the type of reaction catalyzed, the subclass, the sub-subclass and the serial number of the enzyme in its sub-subclass.³⁰

Table 1: Main classes of enzymes in EC system.

First EC digit	Enzyme class	Reaction type
1.	<i>Oxidoreductases</i>	Transfer of electrons
2.	<i>Transferases</i>	Atom/group transfer
3.	<i>Hydrolases</i>	Hydrolysis
4.	<i>Lyases</i>	Group removal
5.	<i>Isomerases</i>	Isomerization
6.	<i>Ligases</i>	Joining of molecules linked to the breakage of a pyrophosphate bond
7.	<i>Translocases</i>	Catalysing the movement of ions or molecules across membranes or their separation within membranes

1.3 Laccases

Laccases, LCs (EC 1.10.3.2, benzenediol:oxygen oxidoreductase), are extracellular N-glycosylated multicopper oxidases able to oxidize various phenolic and nonphenolic compounds by one electron transfer with the concomitant reduction of dioxygen to water.³¹ LCs are monomer or homodimers of glycosylated proteins; bacterial laccases contain 10–25% of sugar residues compared to plants laccases that have higher contents of saccharides. They are widespread among higher plants, bacteria, insects and fungi.³² Laccases were first discovered by Yoshida in 1883³³ who extracted them from the exudates of the Japanese lacquer tree *Rhus vernicifera*. Laccases were firstly isolated from fungi in 1896 by Bertrand.³⁴ Their physicochemical proprieties, such as isoelectric point, molecular size, stability, activity, etc. depend on the source.³⁵ Fungal laccases exhibit a higher redox potential compared to bacterial or plant laccases. Indeed, due to their higher redox potential and their low substrate specificity, LCs are widely used in biorefineries and bioremediation such as for biomass delignification, pulp bleaching, removal of phenolics from wines, organic synthesis, biosensors,

synthesis of complex medical compounds to dye transfer blocking functions in detergents and washing powders.¹⁷

1.4 Structure and properties of laccases

LCs are constituted of a polypeptide chain containing about 500 amino acids residues and linked to saccharide molecules. The amino acids residues are arranged in three domains^{31,36} One mononuclear copper site containing a type I Cu is located at the T1 site, where the reducing substrate binds, and it is responsible for the characteristic colour of the enzyme in the oxidized state Cu^{2+} . The trinuclear copper site contains one type II Cu and two type III Cu. Substrate oxidation at the mononuclear site generates electrons that are transferred to the trinuclear site where O_2 is reduced to H_2O .³⁷ Due to the use of O_2 as co-substrate rather than H_2O_2 like oxidoreductases (lignin peroxidase and manganese peroxidase) LCs are considered 'Green Catalysts' for biotechnological applications.³⁸ Copper species can be classified according to their spectroscopic behaviour.

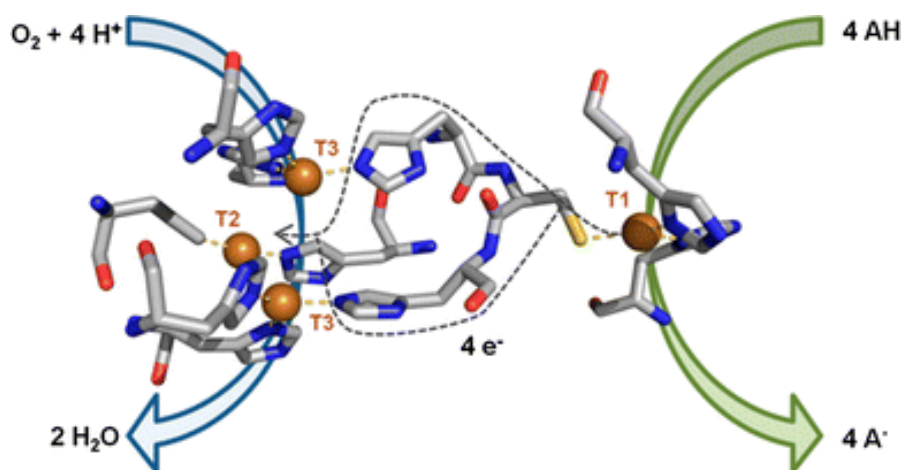


Figure 3: Catalytic site of *Pycnoporus cinnabarinus* laccase (PDB 2XYB) showing the Cu sites for oxidation of the reducing substrate (T1), and for reduction of O_2 (T2/T3) and proposed electron transfer pathway between both sites. Catalytic coppers are shown as spheres and coordinating residues are shown as sticks. Figure adapted from ref.³⁹

The T1 copper has a strong absorption around 600 nm, while the T2 copper shows a weak absorption in the visible region but is EPR-active. The two coppers of the T3 site display an absorption band at

about 330 nm. They are EPR silent due to an antiferromagnetic coupling mediated by a bridging ligand.³⁶ Their molecular mass commonly ranges between 50 and 140 kDa, but it has been reported to be from 34 to 383 kDa for laccases from *Pleurotus eryngii* and *Podospora anserina*.¹⁷ The LC's isoelectric point is usually around 4.0, even if there are some laccases with basic isoelectric points.⁴⁰ According to their T1Cu (E^0 T1) redox potential, LCs are classified as low-, medium- or high-redox potential. Generally, laccases bacterial and plant show a low redox potential (E^0 T1 < +460 mV versus Normal Hydrogen Electrode). Fungal laccases show both medium- and high-redox potential depending on their nature. For example, laccases from *ascomycetes* and *basidiomycetes* have an E^0 T1 ranging from +460 to +710 mV versus hydrogen electrode whilst high-redox potential laccases are produced by basidiomycete white-rot fungi, with an E^0 T1 between +730 mV and +790 mV versus Normal Hydrogen Electrode.⁴¹ Thanks to their low substrate specificity they are able to oxidise a wide range of substrates like aromatic amines, polyphenols, methoxy phenols, and various other inorganic substances.⁴² LCs are widely used as biocatalysts however, due to their relatively low redox potential (500 mV – 800 mV), they cannot oxidise substances with a high redox potential. These issues can be overcome using mediators (small, soluble molecules able to transfer electrons from the to-be-oxidized molecules to the LC active site), laccase mediator systems (LMSs) have a higher redox potential (E^0 T1 > 1100 mV) in comparison to LC in the Cu T1 site.

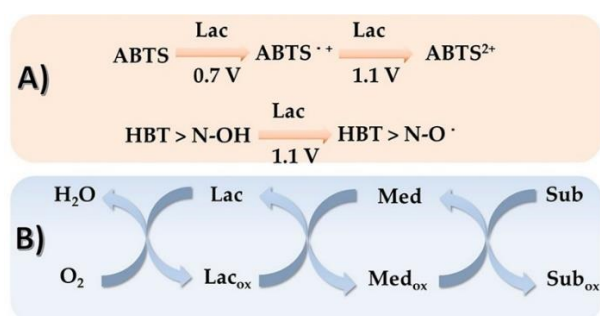


Figure 4: Redox potentials of the oxidation reactions of ABTS and HBT by laccase and (B) LMS mechanism. Figure adapted from ref.¹⁷

1.5 Laccases in industrial processes

1.5.1 Biofuels

Global Energy demand is projected to grow by more than 50% by 2025.⁴³ Clearly the massive use of energy from non-renewable sources involves undergoing their depletion. These drawbacks have led to a growing interest in renewable technologies such as the conversion of biomass into biofuels.²⁴ For this reason the role of LCs in the production of bioethanol through the pre-treatment of ligninolytic residues has been studied. It is known that LMSs degrade almost 80–90% of the lignin structure.¹⁷ Recently, Deng *et al.* investigated the alkali lignin pre-treatment acted by LMS. Data show that the reducing sugar yield during subsequent enzymatic hydrolysis increased by 26% after LMS treatment.⁴⁴ Bilal *et al.* reported the use of a ligninolytic enzyme cocktail from *Ganoderma lucidum* IBL-05 immobilised on alginate–chitosan beds to delignify sorghum stover, obtaining a delignification of 57.3% after 15 h.⁴⁵ Gutiérrez *et al.* investigated the Eucalyptus globulus wood and Pennisetum purpureum nonwood by the use of LC from *Trametes villosa*, with HBT as mediator and alkaline extraction, obtaining a lignin removal of 48% and 32%, respectively.⁴⁶ Nevertheless, the conversion of lignocellulose into biofuels is one of the main goals of biorefineries. The whole lignin removal from lignocellulosic biomass is still a big challenge for researchers.⁴⁷

1.5.2 Bioprocessing of Food Industry By-Products

It has been common knowledge for a long time that the food industry processes generate by-products with high content of phenolic compounds. Due to their complex characteristics, such as long reaction times and the acidic pH, as well the high biochemical oxygen demand (BOD) and chemical oxygen demand (COD) the enzymatic treatment is recommended rather than microorganisms' treatment which generally requires longer reaction time. In this regard several studies have been carried out to remove phenolic compounds by mean of LCs biocatalysis. A good overview about the use of LCs in food industry processes has been recently published by Deloisa *et al.*⁴⁸ In a recent work, Zrinski *et al.* reported the use of a biosensor based on immobilised laccase, for the detection of phenolic

compounds. The biosensor showed excellent electro-catalytic activity towards the oxidation of hydroquinone.⁴⁹

1.5.3 Removal of pollutants

LCs are widely used to synthesize various functional organic compounds such as polymers with specific mechanical/electrical/optical properties, textile dyes, cosmetic pigments, flavour agents, and pesticides. Lima *et al.* described the use of laccase to degraded malachite green (50 mg mL⁻¹) in only 2 h. moreover the enzyme was tested to degrade other dyes belonging to different classes. Their results showed a 85% and 83% decolorization of methylene blue and trypan blue using ABTS as the mediator.⁵⁰ Motamedi *et al.* used a novel thermostable/halotolerant metagenome-derived laccase to remove textile dyes. LC was tested on eight different textile dyes from azo, anthraquinone, and triphenylmethane families. It decolorized 500 mg L⁻¹ of Alizarin yellow, Carmine, Congo red and Bromothymol blue with 99.74–55.85% efficiency after 15 min, at 50 °C, without using mediators.⁵¹

1.5.4 Organic synthesis

LCs are considered a potential tool in organic synthesis. Cannatelli *et al.* reported the use of laccase from *Trametes villosa* for the synthesis of 2,3-ethylenedithio-1,4-quinones carried out in one step avoiding multi steps of reactions, harsh conditions and a chemical oxidant (cerium ammonium nitrate).⁵² Granda *et al.* reported the oxidation of fourteen propargylic alcohols carried out by laccase from *Trametes versicolor* using TEMPO as the mediator. The catalysed reaction lead to the formation of propargylic ketones with high yield (87→99%), data showed the efficiency of the chemoenzymatic methodology in comparison with traditional chemical oxidants ,which usually lead to the formation of by-products.⁵³

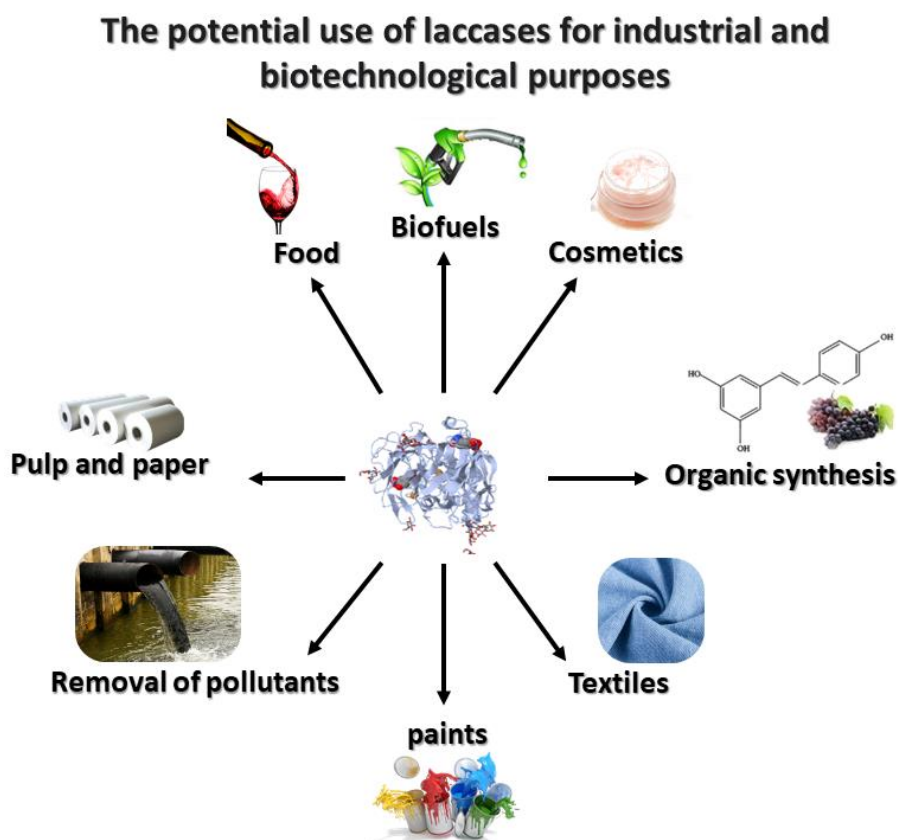


Figure 5: Breakdown of the biotechnological applications of laccases.

In this thesis the laccase from *Aspergillus sp.* was immobilised on different materials as described in chapter 4.

1.5.5 Enzyme activity

Enzyme activity is the initial rate of reaction catalysed by an enzyme under specified conditions of pH and temperature,⁵⁴ and is measured in activity units (U). 1 U is the amount of enzyme that catalyse the conversion/formation of 1 micromole (μmol) of substrate/product per minute. According to the International System of Units (SI), catalytic activity is measured in katal (kat). 1 kat is the amount of enzyme which converts 1 mol of substrate per second (1 kat = 60.000.000 U). Some parameters related to enzyme kinetics are summarized in Table 2.

Table 2: Enzyme catalysis parameters.

Name	Definition	Notation	Dimension
Activity Units	Amount of enzyme for converting 1 μmol substrate per min	Unit (U)	$\mu\text{mol min}^{-1}$
Volumetric Activity	Enzyme Units per volume unit	U/volume	U mL^{-1}
Specific Activity	Enzyme Units per mg protein	U/mg (protein)	U mg^{-1}
Maximum Velocity	Turnover number per time unit at the saturated substrate concentration under standard conditions	V_{max}	$\mu\text{mol min}^{-1}$
Turnover Number	Maximum velocity divided by the enzyme concentration	k_{cat}	s^{-1}
Michaelis Constant	Substrate concentration at half of the maximum velocity	K_{M}	M

The enzyme kinetic parameters can be affected by reaction conditions such as pH, solvent, substrate concentration, ionic strength, nature of salts present in the buffer, and temperature.

1.6 Parameters which affect the laccase activity

1.6.1 Effect of pH on enzyme activity

The amino acids that constitute the enzymes generally carry a positive or negative charge which contributes to the enzyme molecule folding, its shape, and the active site shape. In addition, the changes in pH in the reaction mixture can lead to a change in the charge resulting in enzymatic deactivation. Extreme values of pH can also result in enzyme denaturation. Since the enzymes are active only within a limited range of pH it is necessary to keep the pH value under control during the enzyme assay. The activity versus pH curve is typically bell-shaped, with its maximum representing the optimal pH work for the enzyme.^{54,55} According to the substrate involved in the reaction mixture,

the LCs show different optimal pH values. For example, in the case of phenolic and arylamine substrates involved in the reaction, which entail the release of a proton and an electron, laccases exhibit a bell-shaped pH activity profile with an optimal pH dependent on the laccase and the substrate. This is due to two opposing effects, i) The redox potential difference between the reducing substrate and the T1 Cu (correlating to the electron transfer rate, promoted by higher pH), and ii) The binds of a hydroxide anion to the T2/T3 Cu (which inhibits the activity at a higher pH).

It is important to point out that also that the optimal pH work is related to the nature of LCs. Indeed, fungal laccases such as the LC from *Trametes versicolor* show maximal rates at acidic pH, whilst bacterial laccases show a clear preference for the basic pH values.⁴¹ The laccase from *aspergillus sp.* investigated in this PhD thesis, showed an optimal activity at acidic pH values.

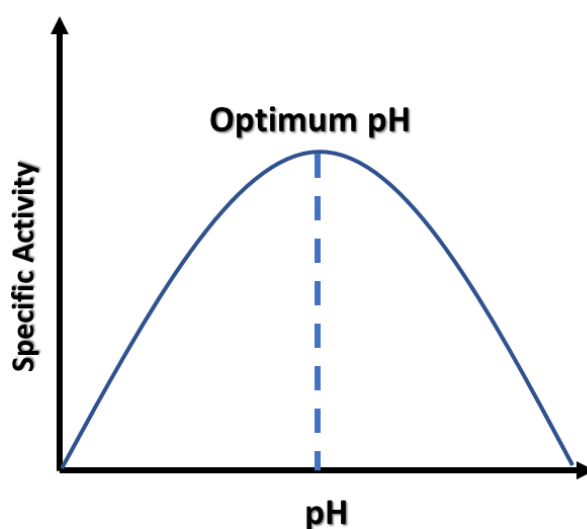


Figure 6: optimal pH work for laccase from *aspergillus sp.* using ABTS (2,2'-Azino-bis (3-ethylbenzothiazoline-6-sulfonic acid) diammonium salt) as the substrate.

1.6.2 Solvent

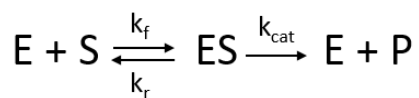
Generally, the reactions catalysed by enzymes are carried out in water media except for some enzymes connected with the membrane, or lipases which are active at the water/oil interface. Lipases are also active in apolar organic solvents or even under solvent-free conditions.⁵⁶ In some cases, the substrate used for the enzymatic assay is sparingly soluble in water. Since the use of organic solvents might

denature the enzymes resulting in their loss of enzymatic activity, it is suggested to solubilize the substrate in a higher concentration in an organic, water-miscible solvent, like ethanol, DMSO, or acetone. A small aliquot of solution can be added to the reaction mixture to keep the organic solvent concentration in the reaction mixture as small as possible.⁵⁵ Most of the reported fungal laccases from *Trametes hirsuta*, *Trametes versicolor*, *Myceliophthora thermophila*, *Pycnoporus cinnabarinus*, *Coriolopsis gallica* and *Pleurotus ostreatus* retained low activity if incubated in organic solvents.⁵⁷ To overcome this issue several works have been carried out on LCs able to work under non-conventional media. Wu *et al.* investigated the effect of acetone, methanol, DMF and acetonitrile on a high efficiency fungal laccase. Data showed that the LC can work under high organic solvent concentration maintaining its 3D structure intact.⁵⁸ Nevertheless the use of organic solvents in the mix reactions often results in LCs denaturation. A new class of green solvents composed of a hydrogen bond acceptor (HBA, usually a quaternary ammonium salt) and a hydrogen bond donor (HBD) such as glycerol, succinic acid etc, known as Deep eutectic solvents (DESs) due to their promising compatibility with enzymes and sustainable derivation is becoming an attractive tool for enhancing LCs activity. Toledo *et al.* screened laccase activity in 16 different DES/water mixtures. Data showed that most of DESs did not change the enzyme activity, whereas in some cases, such as with ChDHC/Xyl (Choline dihydrogen citrate in xylitol) (2:1) at 25 wt %, an increase of relative activity up to 200% was observed.⁵⁹ Recently, Aybike *et al.* investigated several DESs as templates in the laccase-catalyzed polymerization of aniline. Although the laccase enzyme was significantly inhibited by DES and aniline. However, by decreasing their concentrations in the medium, a high yield of polyaniline was achieved.⁶⁰ Delorme *et al.* studied the thermostability of laccase in presence of DESs. Data showed that LC from *Trametes versicolor* is thermally inactivated when it is incubated at 60°C in the reference solution. On the other hand, when laccase is incubated in aqueous 25 wt% 1Bet:3Xyl at 60 °C the thermal inactivation of laccase is significantly slower than laccase in the reference

solution, demonstrating a remarkable enhancement of the thermostability of laccase compared to the reference solution.⁶¹

1.6.3 Enzyme kinetics

The Michaelis-Menten model is the simplest and best-known model to describe enzyme kinetics. It assumes that an enzyme (E) is bound to a substrate (S) to form a complex enzyme-substrate (ES) by the interaction of substrate with the active site of the enzyme which in turn releases a product, P, regenerating the original enzyme. This may be represented schematically as:



Where k_f , k_r and k_{cat} are forward, reverse, and catalytic rate constants, respectively.

This system can be described by the so called Michaelis-Menten equation:

$$velocity (v) = \frac{d[P]}{dt} = \frac{V_{max} [S]}{K_M + [S]}$$

Through the Michaelis-Menten equation it is possible to predict the reaction rate as a function of substrate concentration. The kinetic parameters K_M and V_{max} indicate the substrate concentration at the half of the maximum velocity and the maximum velocity respectively (Figure 7).

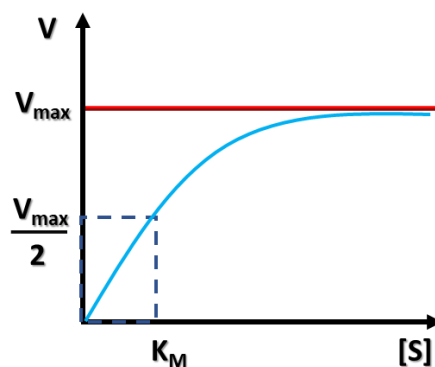


Figure 7: Michaelis-Menten plot.

CHAPTER 2:
LACCASE IMMOBILISATION ON
SUPPORTS

2. Overview of enzyme immobilisation

The excellent properties of enzymes as catalysts in sustainable chemistry are widely reported in literature.^{13,18,62} Nevertheless, the use of native enzymes on large scale still entails several practical problems such as the high cost regarding their isolation and purification. Moreover, enzymes act generally as homogeneous catalysts in water media. This makes their recovery and reuse very difficult. In addition, their application is often prevented both by extreme conditions (temperature and pH) and by their low long-term operational stability owing to loss of the tertiary structure (denaturation). Furthermore, free enzyme molecules may aggregate close their isoelectric point, resulting in a decreased enzyme activity.¹² Enzyme engineering together with enzyme immobilisation are considered promising tools to overcome these issues enabling their use in industry. Therefore, immobilising enzymes into an inert, insoluble material can lead to an increase of their operational stability and allow an easier biocatalyst recycling. In 1916, Nelson and Griffin immobilised the invertase by physical adsorption on charcoal demonstrating that the immobilised enzyme was able to hydrolyse sucrose.⁶³ This is considered as the first enzymatic immobilisation reported in literature. However, the first industrial application of an immobilised enzyme dates back to 1953.⁶⁴ Since then, the interest toward enzymatic immobilisation started to gain more attention.

2.1 Enzyme immobilisation.

In these last decades, the industry is making a tremendous effort to increase the stability and reusability of new biocatalysts able to satisfy current market demands. The main goal of immobilisation is to increase enzyme performance. Indeed, immobilisation allows the easy recovery of the enzyme and its reusability reducing the operational cost. Nevertheless, in order to choose the enzymatic support it must be taken into account some important parameters such as the particle size, pore diameter, morphology, and functional groups present on the carrier surface.⁶⁵ There are various approaches in classifying immobilisation techniques. They are widely classified as reversible and irreversible e

depending upon the reaction between the enzyme and the support.⁶⁶ Further, they are classified depending on the physical or chemical method used for the immobilisation (Figure 8).

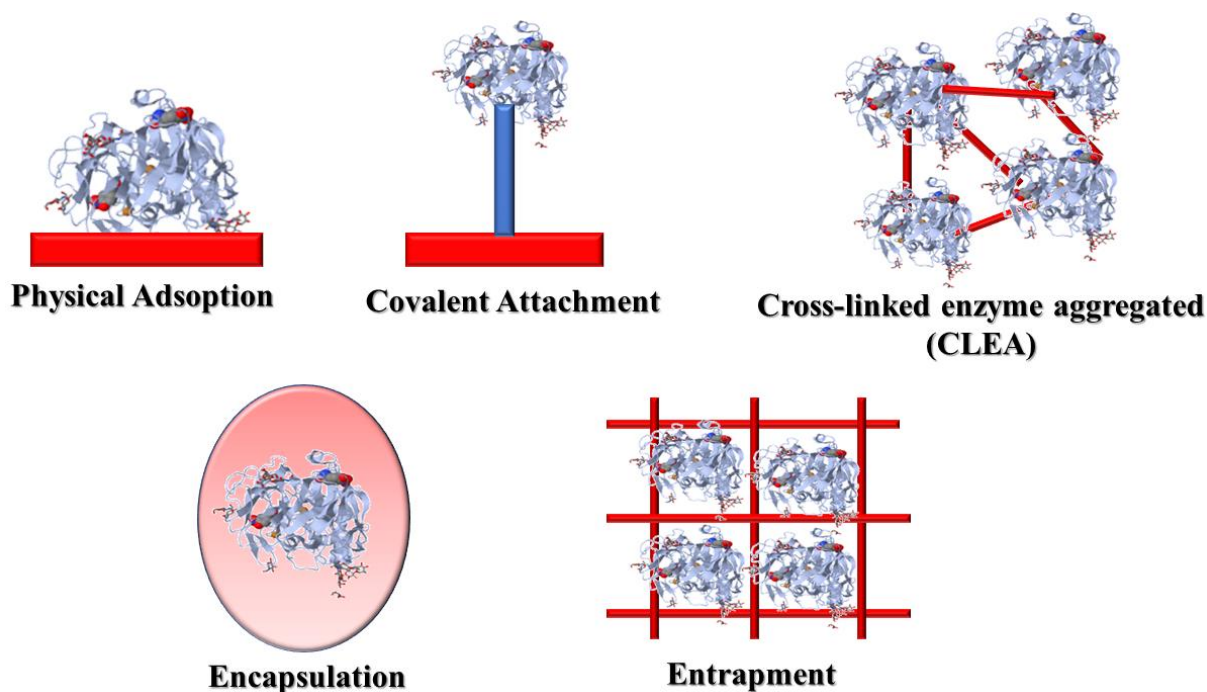


Figure 8: Enzymatic immobilisation techniques.

The most common immobilisation methods can be listed as:

2.1.1 *Physical adsorption*

It is a simple technique for enzymatic immobilisation. This method is usually carried out by suspending the support particles in the protein solution under suitable conditions of pH and temperature until equilibrium of the adsorption process is reached. Although in some cases the functionalisation of the carrier surface is recommended to maximise the protein adsorbed, according to the nature the immobilisation can be carried out directly on the unmodified support. The forces involved during the adsorption process are hydrogen bonding, van der Waals forces, hydrophobic, and electrostatic interactions.⁶⁷ Since the interaction energy is usually weak. (around 20 -50 kJ mol⁻¹),^{68,69} immobilisation by physical adsorption usually preserves the catalytic activity of the enzyme, on the

other hand, if the interaction between the enzyme and the carrier is too weak thus may result in enzyme leakage. Among forces involved in the physical adsorption, electrostatic interactions are the strongest physical forces, and they are promoted when the enzyme is oppositely charged respect to the material. This can occur at pH above or below the isoelectric point (pI) of the enzyme. Noncovalent immobilisation or adsorption could be reversed by changing the conditions that influence the strength of the interaction such as the pH, ionic strength, temperature, or polarities of the solvent. Every carrier could theoretically be used on any enzyme for adsorption, but not every enzyme can be immobilised on all carriers. A carrier material can be successfully used on an enzyme molecule when the affinity between the carrier and the enzyme molecule is high. It depends on the presence of active groups on the carrier, surface area, particle size, and pore structure. Due to their several advantages such as the fast reaction immobilisation time, mild condition of reaction (room temperature and atmospheric pressure) immobilisation by physical adsorption is considered one of the easiest immobilisation methods. Nevertheless, this technique can lead to the leaching of the enzyme. Even if it could be prevented by a proper carrier design and the chosen reaction condition.

2.1.2 Covalent *attachment*

Covalent binding is another common technique used for enzyme immobilisation. In comparison to the physical adsorption, the covalent attachment of the enzyme onto the support has the advantage that the enzyme is tightly fixed.⁷⁰ The coupling reaction between enzyme and the support can be divided into two types: activation of the matrix by the addition of a reactive function to a polymer, and modification of the polymer backbone to produce an activated group. Although the covalent binding occurs usually by means of the side chains of amino acid residues such as lysine (amino group), cysteine (thiol group), aspartic and glutamic acids (carboxylic group, imidazole, and phenolic groups) which are not essential for catalysis, the enzymatic activity can be influenced due to the distortion of the secondary and tertiary structure.

2.1.3 Cross-linked enzyme aggregated (CLEA)

Cross-linked enzymes (CLEs) were first reported in 1960s.⁷¹ Since they had several issues such as low activity, poor reproducibility and low stability CLEs did not receive attention. In 1990s Altus Biologics introduced the use of cross-linked enzyme crystals (CLECs) as industrial biocatalysts. Cross-linking is an irreversible enzyme immobilisation. technique.⁷² Although CLECs exhibit excellent properties, their synthesis requires enzyme of high purity making the process laborious and expensive. Due to the possibility to replace the crystallisation step by precipitation of the enzyme from an aqueous buffer, the synthesis of cross-linked enzyme aggregates (CLEAs) results to be cheaper compared to that of CLECs. Indeed, CLEAs can be obtained directly from a crude enzyme solution by addition of a precipitant such as $(\text{NH}_4)_2\text{SO}_4$ or t-butanol, and then of a cross-linking agent (i.e. glutaraldehyde, glutaraldehyde-ethylene diamine polymers, or dextran aldehyde) resulting in a stable aggregate. Cross-linking occurs between lysine residues on the surfaces of neighbouring enzyme molecules and organic linkers through the formation of Schiff's bases.⁷³ A typical procedure for the preparation of CLEAs is shown in Figure 9.

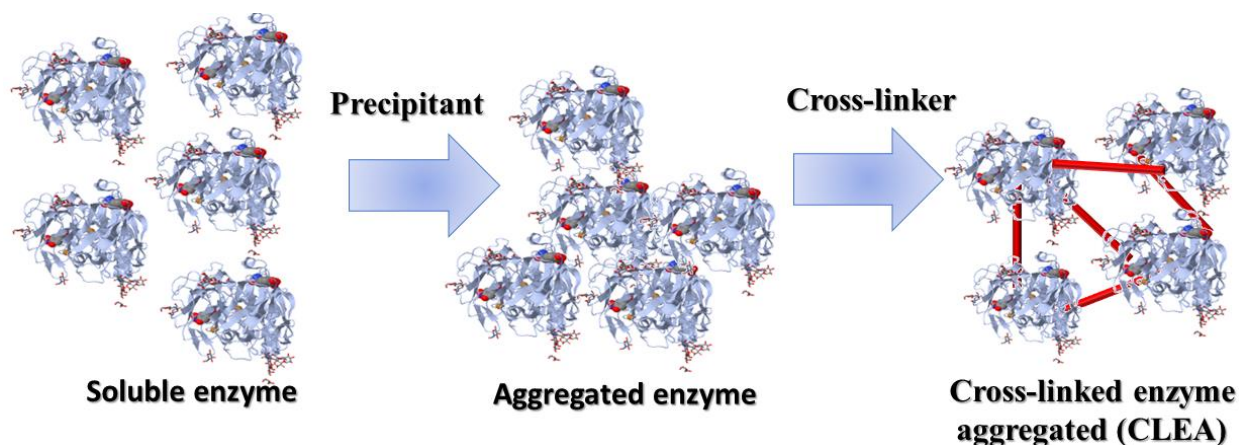


Figure 9: Preparation of CLEA.

CLEAs show many advantages such a possible increase of the space time yields (STY $\frac{\text{Desired product quantity}}{\text{Catalyst volume} \cdot \text{time}} = \text{mol L}^{-1} \text{ h}^{-1}$),^{74,75} improved storage and operational stability to denaturation by heat, organic solvents and drastic pH condition. Moreover, the three-dimensional

structure of the enzyme in CLEAs is preserved resulting in an enzymatic activity retention. However, disadvantages as high cost of the biocatalyst and low number of available active sites have to be taken into consideration when approaching this immobilisation method.⁷⁶

2.1.4 Enzyme encapsulation

The encapsulation method allows the enzyme to be entirely embedded in the support without letting it interact with the outer environment resulting in its protection against direct contact with drastic reaction conditions.⁷⁷ In this immobilisation method, unlike the entrapment, the enzyme is enclosed in a membrane and not in a matrix of a specific material. To avoid the enzyme leaching it is important to take into consideration the size of the enzyme.¹⁸ Also, the choice of the support is important, indeed porous materials may result in mass transfer limitations for both substrate and product.

2.1.5 Entrapment

Entrapment immobilisation refers to the physical limitation of the enzyme within matrix made by sol-gel processes.⁷⁸ The most common entrapment method consists in trapping the enzyme through the gelation of polyanionic or polycationic polymers by the addition of multivalent counter-ions. A gel is constituted by a solid crosslinked matrix and a confined liquid. The liquid within provides an environment for the protein which can be engineered to optimize performance. Ideally, this process creates a negligible impact on the catalytic properties without significantly affecting their structures and functions. Moreover, it is carried out in mild reaction conditions of temperature without carrying out harsh chemical reactions.

2.2 Supports for enzyme immobilisation

Immobilised enzymes usually display higher resistance to harsh environmental conditions, allow reusability and may result in improved thermal stability if compared to free enzymes.⁷⁰ The enzymatic activity and stability depend on the choice of the support as well as the type (e.g. physical or covalent) of enzyme immobilisation.^{18,79–81} However, the choice of the most appropriate immobilisation method and support material depends mainly on the type and conditions of the catalytic process. A wide range of materials can be used as supports for enzyme immobilisation.⁸² According to their chemical composition they are classified in organic, inorganic, and hybrid or composite. The support should protect the enzyme structure against harsh reaction conditions and thus help the immobilised enzyme to retain high catalytic activity. The main required features of support materials for effective enzyme immobilisation. are: chemical and thermal stability under reaction conditions, high affinity to enzymes, biocompatibility, presence of reactive functional groups, availability and price, regeneration and reusability (Figure 10).⁸³



Figure 10: Main features of support materials used for enzyme immobilisation. Figure adapted from Zdarta *et. al.*⁸³

However, it should be considered that the choice of material is related to both the type of enzyme and the process in which the biocatalytic system will be used. Scientific research regards laccase immobilisation has been reported in the literature since the '80s, as shown in Fig.11. The number of articles related to the immobilisation of laccases is greatly increasing year by years. This trend shows the increasing interest in the development of new supports for laccases.

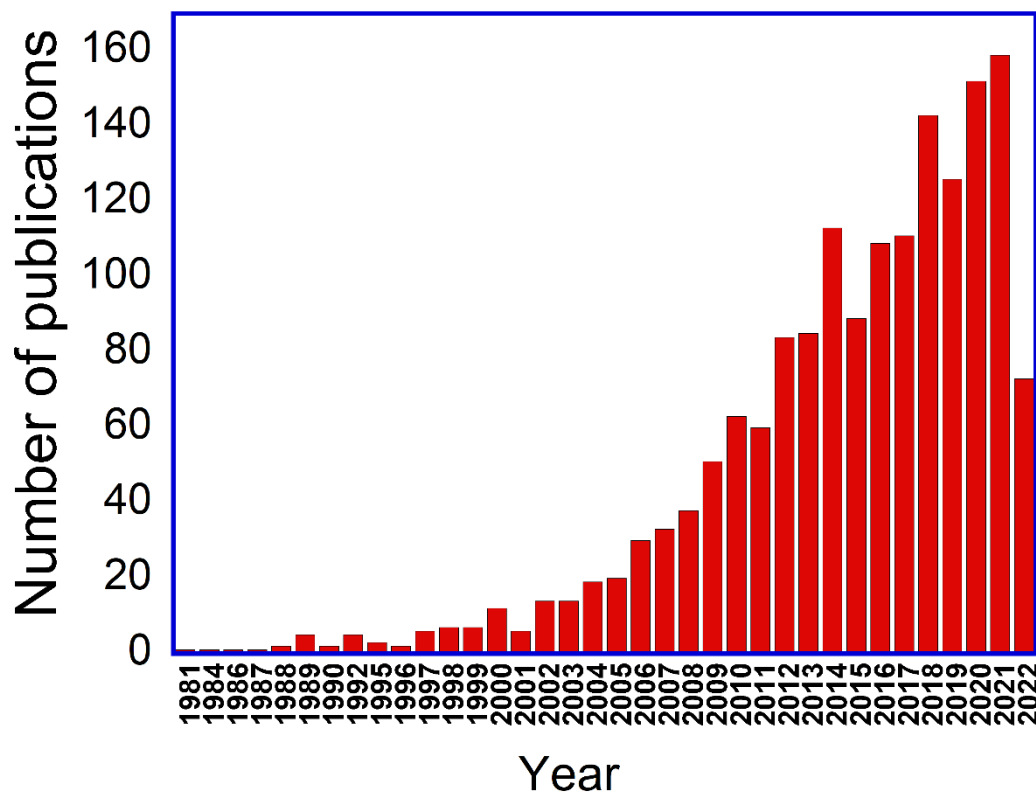


Figure 11: Publications data for “laccase” and “immobilisation.” in articles by Scopus, 15th May 2022.

Among the several materials investigated for the enzyme immobilisation until now, porous materials offer high surface area, tuning of pore dimensions and high enzyme immobilisation efficiency. For these reasons, their use as enzyme carriers is promising and widely investigated. Particularly, meso- and macro-porous materials are more suitable compared to microporous. Indeed, several studies demonstrate that enzyme loading, and activity can be affected by the pore size of the support.

Therefore, not all porous materials are suitable for enzyme immobilisation. For example, even if zeolites have a large surface area, due to their small pore size, ($d_p < 1.3$ nm) they are not used as carriers for adsorption of the large enzyme molecules (molecular size > 3 – 30 nm). On the other hand, if the pore size is much wider than the enzyme molecules size, the latter cannot be retained resulting in leaching of enzyme molecules from the pores in case of physical adsorption immobilisation.⁷⁰

2.2.1 Ordered mesoporous materials

According to the IUPAC (International Union of Pure and Applied Chemistry) definition,⁸⁴ the porous materials are classified as:

- Micropores: pore size < 2 nm are called,
- Mesopores: 2 nm $<$ pore size < 50 nm ,
- Macropores: pore size > 50 nm .

In nature both microporous and microporous materials can be found. In 1992 the researchers of Mobil Oil. company firstly developed a class of ordered mesoporous materials (OMM) prepared using surfactants as templates known with the acronym of MCM (Mobile Composite of Matter) with a pore diameter in the mesopores' range.⁸⁵ A typical MCM material synthesis is generally carried out in a basic aqueous solution of a cationic surfactant (i.e. cetyl trimethylammonium bromide, CTAB) to which a silica precursor (i.e. tetraethyl orthosilicate, TEOS) is added. In 1998 a new class of OMMs called "Santa Barbara Amorphous" (SBA) family was discovered. SBA materials are synthesized using non-ionic surfactants, like pluronic triblock copolymers, PEO–PPO–PEO, are one of the families of polymeric surfactants, where PEO stands for poly(ethylene oxide) and PPO stands for poly(propylene oxide).⁸⁶ Generally, MCM materials show average pore diameters of less than 4 nm making them not suitable for enzyme immobilisation. On the other hand, SBAs with pore diameters

of 7–10 nm are much more suitable for enzyme immobilisation.⁸⁰ Kresge *et al.* first proposed a mechanism for OMM synthesis called liquid crystal templating (LCT) mechanism, consisting of two main steps (Figure 12):⁸⁷

- The formation of the ordered structure due to the self-assembly of surfactant molecules.
- Hydrolysis of the silica precursor (TEOS) followed by the silica condensation around the previously formed ordered structure

Afterwards, Monnier *et al.* proposed a more complex mechanism for the formation of mesoporous materials called cooperative templating mechanism (CTM) consisting of three main steps:

- Formation of surfactant micelles.
- Hydrolysis of the silica precursor (TEOS) followed by silica polymerization.
- Adsorption of the silica polymers on the micelles surface and formation of the ordered structure.

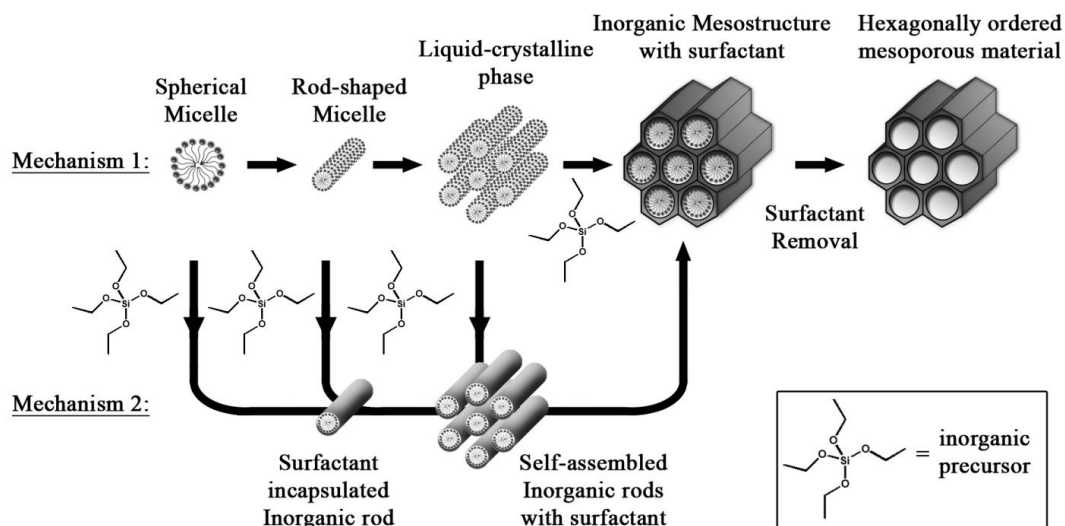


Figure 12: Possible mechanisms involved in mesostructure formation. Path 1 is denoted as the true liquid-crystal templating mechanism and path 2 is designated as the cooperative templating mechanism. Figure adapted from ref.⁸⁸

According to the reaction conditions such as pH, temperature, surfactant nature and concentration, ionic strength, counterion charge the OMM synthesis can be modified resulting in modulation of pore size, particles size and physico-chemical material properties.⁸⁹ In 1996 Diaz and Balkus immobilised globular enzymes in MCM-41 material. Since then silica materials were widely used for enzyme immobilisation.⁹⁰

2.2.2 Metal Organic Frameworks (MOFs)

Metal-Organic Frameworks (MOFs), defined by IUPAC as a coordination network with organic ligands containing potential voids,⁹¹ are a new emergent class of porous coordination polymers (PCPs) constituted by a metal node/cluster and an organic ligand linked through coordination bonds (Figure 13).

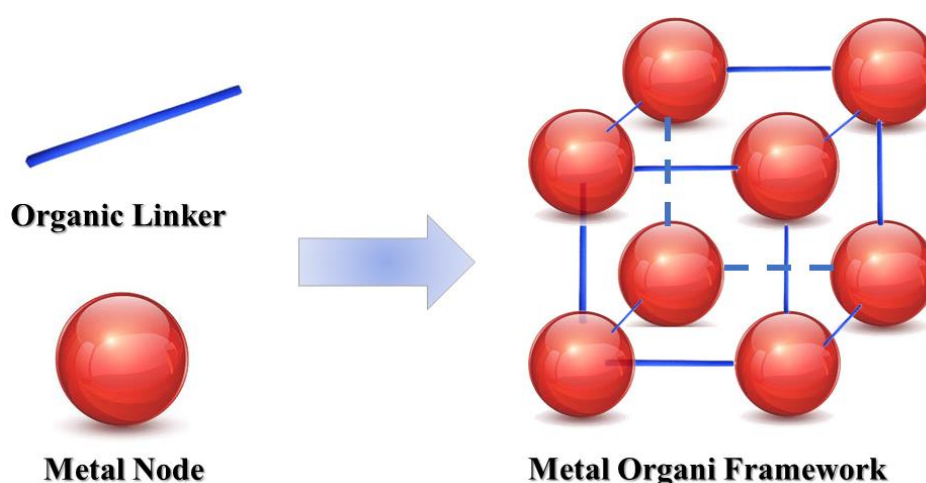


Figure 13: Schematic MOF composition.

The first MOFs publication dates to 1989, but the term MOF was first used by Yaghi in 1995 for a material constituted by a copper 4,4'-bipyridyl complex.⁹² Since that time the interest in these materials is steadily increased and numerous MOFs have been synthesised.⁹³ In general, the term MOF is used to indicate the group of compounds, when it is followed by a number it regards an individual MOF such as MOF 74, MOF 177 etc.⁹⁴ In other cases, MOFs are named by the institutes in which they have been discovered such as UiO (Universitetet I Oslo) MOFs for example UiO-66 or the MIL (Materials of istitut Lavoisier) MOFs for example MIL-100-Fe.^{95,96} (Figure 14)

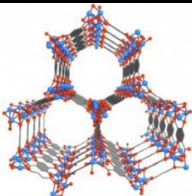
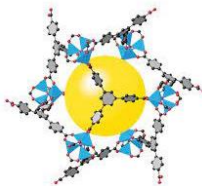
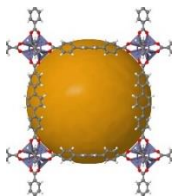
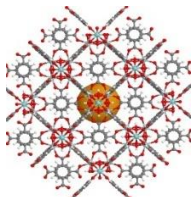
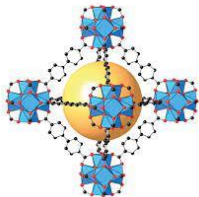
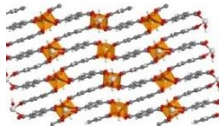
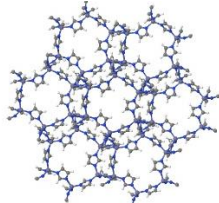
Name	Formula	Notation	
MOF-74	Zn ₂ DOT	Metal organic Frameworks	
MOF-177	Zn ₄ O(BTB) ₂	Metal organic Frameworks	
IRMOF-16	Zn ₄ O(TPDC) ₃ ·17DEF·H ₂ O	Isorecticular Metal organic Frameworks	
UiO-66	Zr ₆ O ₆ (BDC) ₆	Universitetet i Oslo	
UiO-67	Zr ₆ O ₆ (BPDC) ₆	Universitetet i Oslo	
MIL-53	Al(OH)(BDC)	Material of institute Lavoisier	
ZIF-8	Zn(MIM) ₂	Zeolite Imidazolate Framework	

Figure 14: Example of MOF structures

MOFs are generally porous (up to 90% free volume) with high surface area (extending beyond 6000 m² g⁻¹).⁹⁷ Due to their properties MOFs are suitable for several applications such as the removal of water pollutants,⁹⁸ gas adsorption,⁹⁹ catalysis,¹⁰⁰ sensing, drug delivery system¹⁰¹ and other industrial applications.^{17,98} Among them, MOFs have shown great potential for enzymatic immobilisation.¹⁰²^{103,104} Synthetic strategies of enzyme-MOF are divided in chemical (covalent attachment and cross linking) and physical methods (entrapment/encapsulation and adsorption).⁶⁵

Since MOFs are generally microporous/mesoporous materials post-synthesis enzymatic immobilisation is limited owing to the large size of enzyme molecules. In this regard, synthesis of MOFs with macropores would therefore solve this problem. Zhou *et al.* immobilised *Aspergillus niger* lipase in macroporous ZIF-8. The biocatalyst showed higher enzymatic activity (6.5-fold) and was used to catalyse a biodiesel production reaction.¹⁰⁵ Sun *et al.* synthesized a hierarchically porous ZIF-8 by polyphenol treatment method to immobilise glucose oxidase. The resultant enzyme@ZIF-8 composites exhibited significantly increased stability.¹⁰⁶ Nevertheless, typical solvothermal/hydrothermal methods for MOFs synthesis require long reaction times (1-3 days)¹⁰⁷ and up to 1 – 2 weeks for diffusion methods.¹⁰⁸⁻¹¹⁰ In addition, the MOF synthesis is often carried out under harsh conditions (high temperatures, use of organic solvents) resulting in unsuitable for enzymatic immobilisation. Therefore, the most promising alternative is the enzymatic entrapment method. This strategy, also known as the de novo approach,¹¹¹ occurs in situ under mild conditions and aqueous solution. According to the presence or absence of co-precipitating de novo approach is classified in:

- Co-precipitation: Auxiliary stabilizers are required to keep the enzyme in active form during the preparation such as polyvinyl pyrrolidone (PVP which helps to maintain dispersion and protect enzyme in solution during the encapsulation on MOFs.
- Biomimetic mineralization: The enzyme is directly added during the MOF synthesis in the form enzyme@MOF biocomposite.

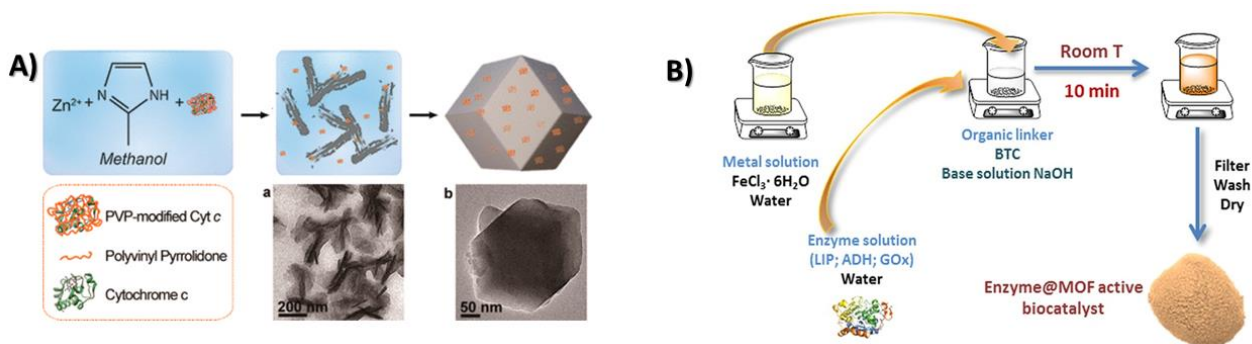


Figure 15: Schematic **A)** co-precipitation and **B)** biomimetic mineralization. Figure adapted from ref.^{104,112}

The encapsulation involves the MOF formation around the enzyme in situ, via a ‘one pot’ approach, and thus requires biocompatible synthetic conditions.¹¹³ Employing this strategy, enzymes larger than the average pore size of the MOF material can be embedded within a three-dimensional network framework that prevents leaching of the enzyme, while retaining free substrate diffusion. The encapsulation strategy must be carried out in an environment ‘enzymatically friendly’ so that the enzyme retains its higher activity.¹¹⁴ Recently, Molina *et al.* reported the immobilisation. of laccase from the fungus *Myceliophthora thermophila* carried out by in situ and post-synthesis procedure on NH₂-MIL-53(Al) MOF in order to obtain Lac@NH₂-MIL-53(Al) and Lac#NH₂-MIL-53(Al) respectively. The Lac@NH₂-MIL-53(Al) showed an immobilisation. efficiency of 100% in contrast only 9.2 % of the enzyme was immobilised in the case of Lac#NH₂-MIL-53(Al). Lac@NH₂-MIL-53(Al) was used to remove bisphenol A (BPA) from water. Data shows a complete removal of BPA (more than 98%) in only 3 min, that is, it is even able to beat the performance of the free enzyme. Due to the low enzyme immobilisation. by the post-synthesis approach on NH₂-MIL-53(Al) the Lac#NH₂-MIL-53(Al) was not tested.¹¹⁵ A similar study regards in situ and post-synthesis immobilisation. of enzymes on nanocrystalline MOF platforms to yield active biocatalysts was performed by Gascon *et al.* Data showed that the enzyme loadings for biocatalysts prepared in situ became richer in (> 85% of the enzyme added to the synthesis media), more catalytically active, and leaked less of the immobilised enzymes, whereas the intrinsic catalytic activity per enzyme molecule was higher in the

post-synthesis biocatalysts. The in situ approach even led to active biocatalysts in a non-aqueous adverse media for enzymes, N,N-dimethylformamide.¹¹⁶ Carucci *et al.* reported the immobilisation of a hyperhalophilic alcohol dehydrogenase in a Fe-BTC MOF material. Their results showed an increase of optimal work temperature (from 50 to 60 °C), a broader range of working pH, a decrease in the requirement for high concentrations of salt, good storage stability, and retention of activity in organic media (DMSO).¹¹⁷ These works emphasize the in situ immobilisation potential for enzymes on MOFs.

In recent years, MOFs have shown great advantages in enzyme encapsulation. In situ encapsulation has been reported for both microporous MOFs such as ZIF-8,¹¹⁸ ZIF-90,¹¹⁹ HKUST-1@Fe₃O₄,¹²⁰ and mesoporous MOFs such as mesoporous ZIF-8, Zn-MOF, PCN- 222(Fe), MIL-88B, H-MOF(Zr), MIL-101(Cr), Cu-BTC-based MOF. According to the biomimetic mineralization method, the enzyme is directly mixed with an organic linker and a metal node in the absence of co-precipitating agents leading the enzyme embedding in the MOF. The main method reported in the literature to investigate the enzyme location are confocal laser and TGA coupled with SEM.¹²¹ All these procedures require long time and do not give the exact enzyme location.

2.2.3 Zeolitic imidazolate frameworks (ZIFs)

A subgroup of MOFs, called zeolitic imidazolate frameworks (ZIFs) have revealed remarkable potential applications for enzyme encapsulation. ZIFs are formed by the coordination of Zn²⁺ or Co²⁺ with imidazole-type links.¹²² Due to the metal-imidazole-metal angle being similar to the 145° Si-O-Si angle in zeolites, ZIFs are topologically isomorphic with zeolites (Fig.16).¹²³

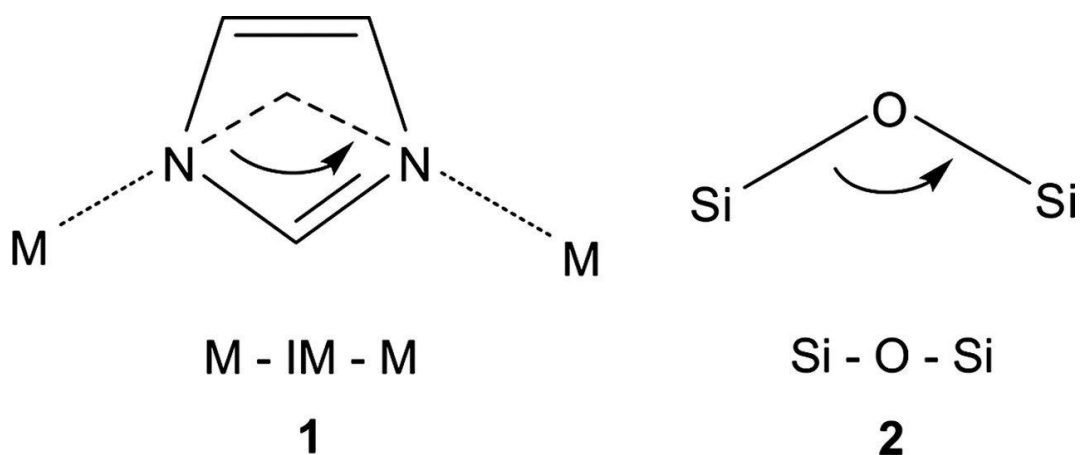


Figure 16: The bridging angles in metal IMs (1) and zeolites (2). Adapted to ref. ¹²³

The strong interaction between the charged imidazolate linkers and the metal ions, together with the formation of rigid cages, make ZIFs highly robust porous materials, thus setting them apart from classic coordination networks. Both the ratio of imidazole derivatives/metal nodes and the reaction time and temperature can significantly influence the formation of the final crystalline product (Fig.17).¹²⁴

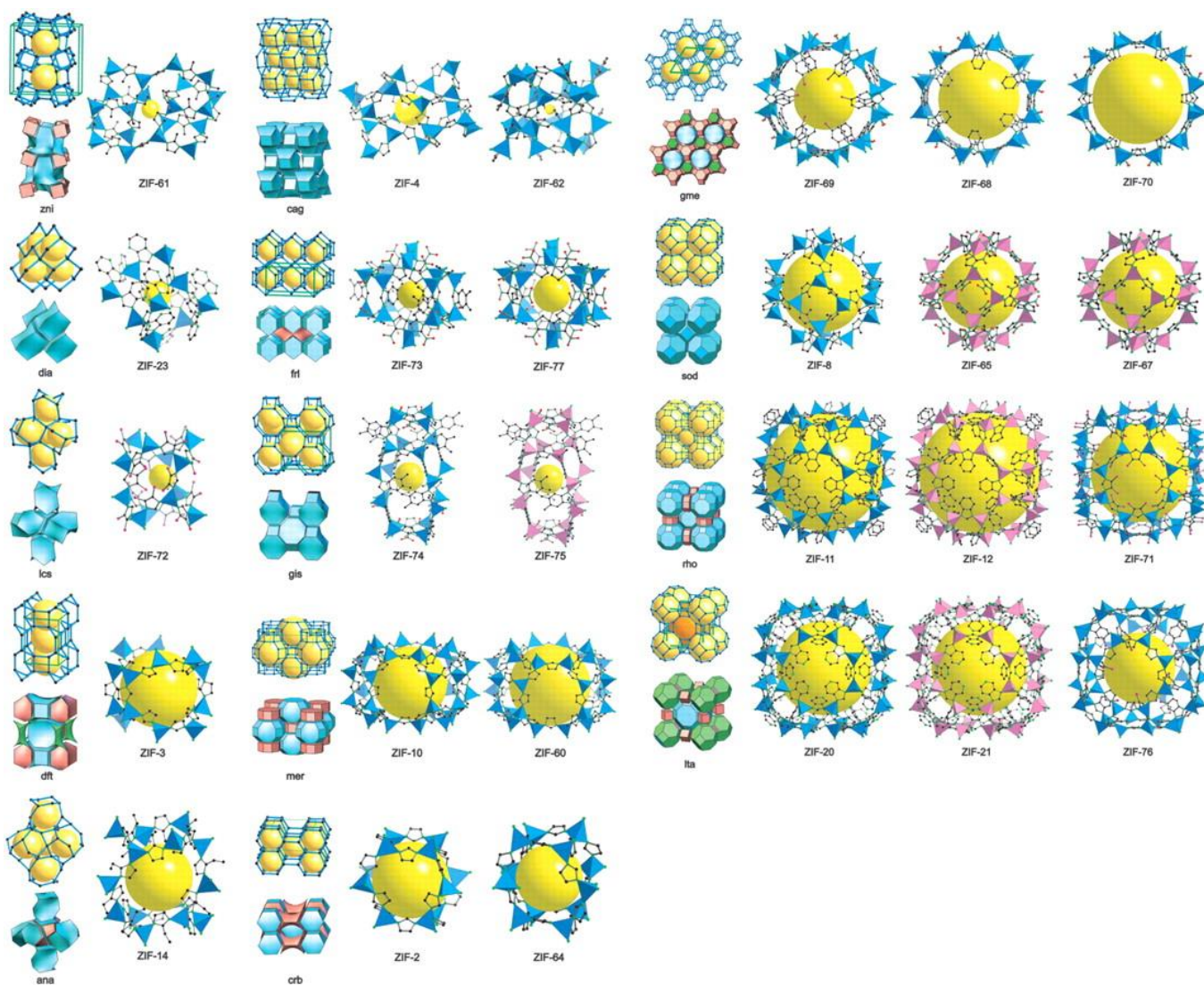


Figure 17: Examples of ZIFs and their topology. Adapted to ref.¹²⁵

Among the ZIFs, ZIF-8 is one of the most studied materials attributed to its exceptional thermal stability (up to 350°C), and the tenable porosity.¹²⁶ These aspects make it a suitable carrier for enzyme immobilisation. ZIF-8 forms crystals with rhombic dodecahedral morphology and sodalite (sod) topology. The pore shape is similar to that of a truncated octahedron with a diameter of 11.6 Å and a window size of about 3.4 Å (Fig.18).¹²⁷

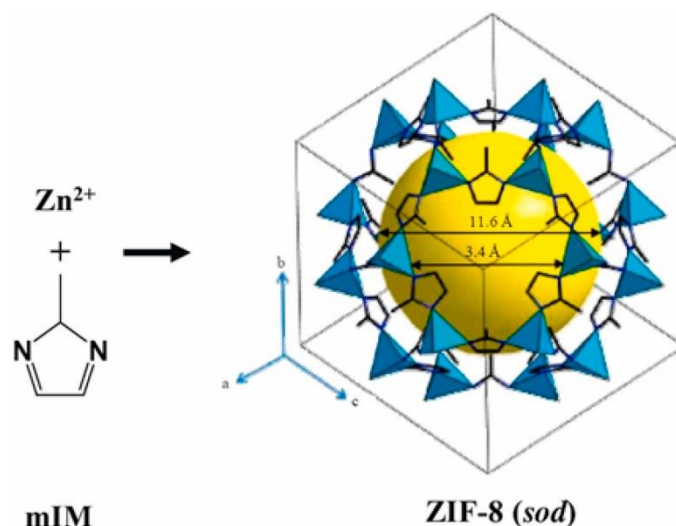


Figure 18: Three-dimensional structure of ZIF-8 in cubic unit cell at 111 plane, Zn (polyhedral), N (sphere), and C (line)). Figure adapted from ref. ¹²⁸

The first in situ immobilisation of enzyme, cytochrome c (Cyt c), on ZIF-8 was reported by Lyu *et al.*¹¹² Cyt c was incubated in a methanolic solution for 24 hours. Surprisingly, the authors claimed that the presence of methanol increased the Cyt c activity (up to 311 %).¹¹² However, the presence of polar organic solvents in the reaction mixture usually leads to enzyme denaturation resulting in a loss of activity. Therefore, an immobilisation procedure carried out under aqueous media is preferred. In 2015, Shieh *et al.* reported the first protein encapsulation within ZIF-90 carried out under aqueous media.¹¹⁹ Since that moment different enzymatic immobilisation approaches were investigated to evaluate the best immobilisation conditions to retain high enzymatic activity. For example, Wei *et al.* immobilised β -glucosidase, invertase, β -galactosidase, and catalase, enzymes in ZIF-8, UiO-66-NH₂, or Zn-MOF-74 via a ball milling process.¹²⁹ This green approach allows to minimize the use of organic solvents and strong acids during synthesis, while retaining enzyme activity. Pitzalis *et al.* described the “one-pot” immobilisation of *Pseudomonas fluorescens* lipase into a ZIF-8 at different zinc / 2-methylimidazole molar ratio in aqueous medium.¹³⁰ Lipases encapsulated in ZIFs have been used for biodiesel production refs. For example, Rafiei *et al.* reported the encapsulation of *Candida rugosa*

lipase into the microporous zeolite imidazolate framework, ZIF-67¹³¹ as well as Adnan *et al.* encapsulated a lipase from *Rhizomucor miehei* within X-Shaped ZIF-8 for biodiesel production.¹³²

Table 3: Examples of enzyme encapsulation on ZIF-8.

Enzymes	Comment	Refs
Lipase B from <i>Candida antarctica</i>	Synthesis of different biocomposite particle size to investigate the changing in rate of CALB@ZIF-8 catalysis	133
CgL1 laccase from <i>Corynebacterium glutamicum</i>	Laccase@ZIF-8 composite showed enhanced thermal (up to 70°C) and chemical (N,N-dimethylformamide) stability, resulting in a stable heterogenous catalyst	134
Laccase from <i>Trametes hirsuta</i> MTCC-1171	Thermostability of Lac@ZIF-8 was enhanced 3.6-folds at given temperature (50-70 8C) compared to its native form	135
Carbonic anhydrase from bovine erythrocytes	The Carbonic anhydrase maintained 93 % of its original activity after being immobilised in ZIF-8. The enzymatic stability and reusability were improved after its immobilisation	136
Lipase B from <i>Candida antarctica</i>	Biocatalyst was successfully applied in size-selective transesterification reaction in organic solvent	137
Lipase from <i>Aspergillus niger</i>	The immobilised enzymes showed excellent thermo-stability in the temperature range of 50–70 °C due to shielding effect. Also, storage stability (20 days) and reusability (upto six cycles)	138

Another broadly utilised framework for protein encapsulation in iron-based metal-organic frameworks is the Fe-BTC (commercialized as Basolite F300). Fe-BTC is comprised of Fe^{3+} linked with 1,3,5-benzenetricarboxylic acid.^{139,140}

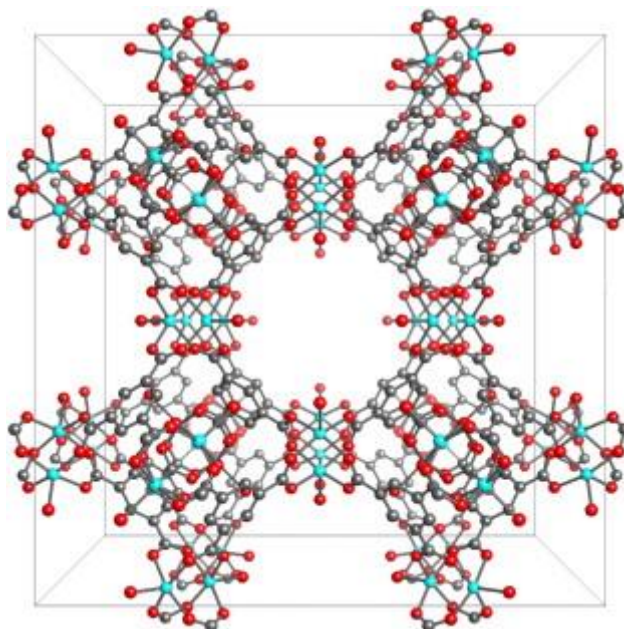


Figure 19: Fe-BTC structure.

Due to its poor crystallinity, Fe-BTC has been described in the literature as being disordered as it is not crystalline nor amorphous material.¹⁴¹ Typically, the Fe-BTC synthesis requires solvothermal treatment resulting in time-consuming and energy-intensive. In addition, post treatments such as the calcinations are required to a large surface area.^{142,143} Sanchez *et al.* reported a method to obtain a Basolite F300-like MOF (Fe-BTC) in only 10 mins.¹⁴⁴ Subsequently, Gascòn *et al.* used the same procedure to synthesise and encapsulate enzymes such as alcohol dehydrogenase (ADH), glucose oxidase (GOx), and lipase through a one-pot procedure.^{96,103,104} The simultaneous synthesis and immobilisation of the enzyme within the MOF based on Fe^{3+} and the tridentate linker trimesic acid, occurred in situ in an aqueous medium and mild conditions (room temperature and almost neutral pH).¹⁰⁴ The ADH@Fe-BTC shows an increase in optimal work temperature (from 50 to 60 °C), a broader range of working pH, a good storage stability, and retention of activity in organic media such as DMSO and ACN compared to its native form in water media.¹¹⁷ Other works on enzyme

encapsulated on MOFs by one pot synthesis carried out under mild temperatures and pressures were recently reported.^{102,104,135,145,146}

Compared to the other immobilisation techniques the encapsulation method is faster and cheaper leading to a more suitable biocatalysts for industrial processes. But till now, it is not well understood where the enzyme is located on the MOFs during its encapsulation.^{104,129,147,148} Another crucial point to take into account is the MOFs stability in the reaction mixture. Recent studies about MOFs have highlighted their poor stability under certain pH or salts concentration conditions.^{149–151} For example ZIFs are not stable to $\text{pH} < 6$ and certain buffer or salt concentration.^{152,153} Pu *et al* investigated the effects of different concentration of NaCl on (R)-1-phenylethanol dehydrogenase encapsulated by ZIF-8. The results show that the (R)-PEDH@ZIF-8 morphology changes with the increasing of NaCl concentration (Figure 11). The maximum activity for (R)-PEDH@ZIF-8 was reached at 0.1 M NaCl (2.5 folds higher compared to the NaCl free).¹⁵⁴ In another work, Gassensmith *et al.* demonstrated that ZIF-8 is more stable in some buffers and cell media.¹⁵⁵ Also the Fe-BTC MOF is affected by acidic pH condition resulting in the iron release,¹⁰² thus limiting their potential application.

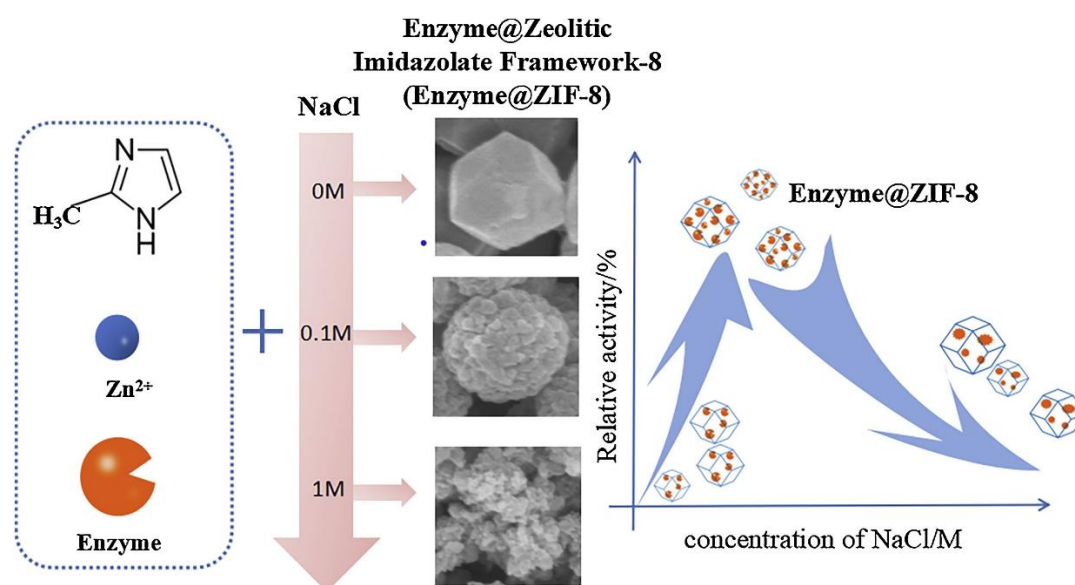


Figure 20: Schematic illustration of the effects of NaCl on the shape and enzyme activity of Enzyme@ZIF-8. Figure adapted from ref.¹⁵⁴

2.2.4 Hierarchical Zeolites

Zeolites are generally microporous, crystalline silicate and aluminosilicate widely used as catalysts and sorbents. Their general formula is $M_xAl_xSi_{1-x}O_2 \cdot yH_2O$ where M is either a metal ion or H^+ . The value of x is between 0 and 1 and y is the number of water molecules in the formula unit. Due to their high surface area and well-defined pore systems, zeolites could be suitable carriers for enzyme immobilisation. There are several studies regarding enzymes immobilised onto zeolites.¹⁵⁶ Recently, Miller *et al.* immobilised laccase from *P. ostreatus*, from *Aspergillus sp.* and from *A. bisporus* onto nano-zeolite for TEMPO-mediated glycerol oxidation.¹⁵⁷ Their results showed that the biocatalyst lead to low yields of conversion (5%), nonetheless, significant selectivity to glyceraldehyde was observed (up to 100%). Lim *et al.* reported the immobilisation of recombinant monooxygenase, dioxygenase and flavin reductase on zeolite type X for the 4-chlorophenol degradation.¹⁵⁸ Khojaewa *et al.* found that the binase-zeolite complexes can have a potential application in treating colorectal cancer or malignant skin neoplasms.¹⁵⁹ The distribution of sizes, shapes and volumes of the void spaces in porous materials directly relates to their ability to perform the desired function in a particular application. Mass transfer and pore size are important key factors need to be considered when selecting materials. Although the utilization of zeolites as enzyme carriers is limited by their narrow micropores (pore diameter < 20 Å), in the last 15 years a new class of materials called hierarchically ordered zeolites, constituted by a hierarchical pore system has received an increasing attention for enzyme immobilisation.¹⁶⁰ (Table 4)

Table 4: Examples of enzymes immobilised on Zeolite

Enzymes	Zeolite	Application	Refs
Lysozyme	NaY (FAU)	Micrococcus lysodeikticus cells disruption	161
Lysozyme	Pure-silica (MFI)	Coatings for implantable devices	162
Laccase	NaY, DSY, DAY (FAU)	Bisphenol A biodegradation	163
Glucose oxidase, HRP	TS-1 (MFI)	Glucose oxidation + olefin epoxidation	164
Laccase	X (FAU)	Dyes decolorization	165
Lipase	TS-1, GIS, LTA, BEA, X (MFI, GIS, LTA, *BEA, FAU)	Microalgae oil ethanolysis transesterification to FAEEs	166

According to the material porosity it is possible to classify hierarchical zeolites into two main categories (modular and bimodular).

I) Bimodular systems: Micro/meso porous systems

- Micro/macro porous systems

II) Multimodular (multiple) pore systems: Micro/meso/macro porous systems

- Micro/multiple meso
- Micro/multiple macro
- Multiple micro (at least two zeolites) and an additional porous system

Hierarchical zeolites can be obtained by bottom–up or top–down approaches. In the bottom–up approach, the zeolite formation starts from precursors. The hierarchy of the system will be induced by multiple self-organization processes forming both the microporous zeolite and the additional pore system in one preparation. Three main cases can be differentiated: i) hard templating, ii) soft templating, and iii) “non-templating” methods.¹⁶⁰

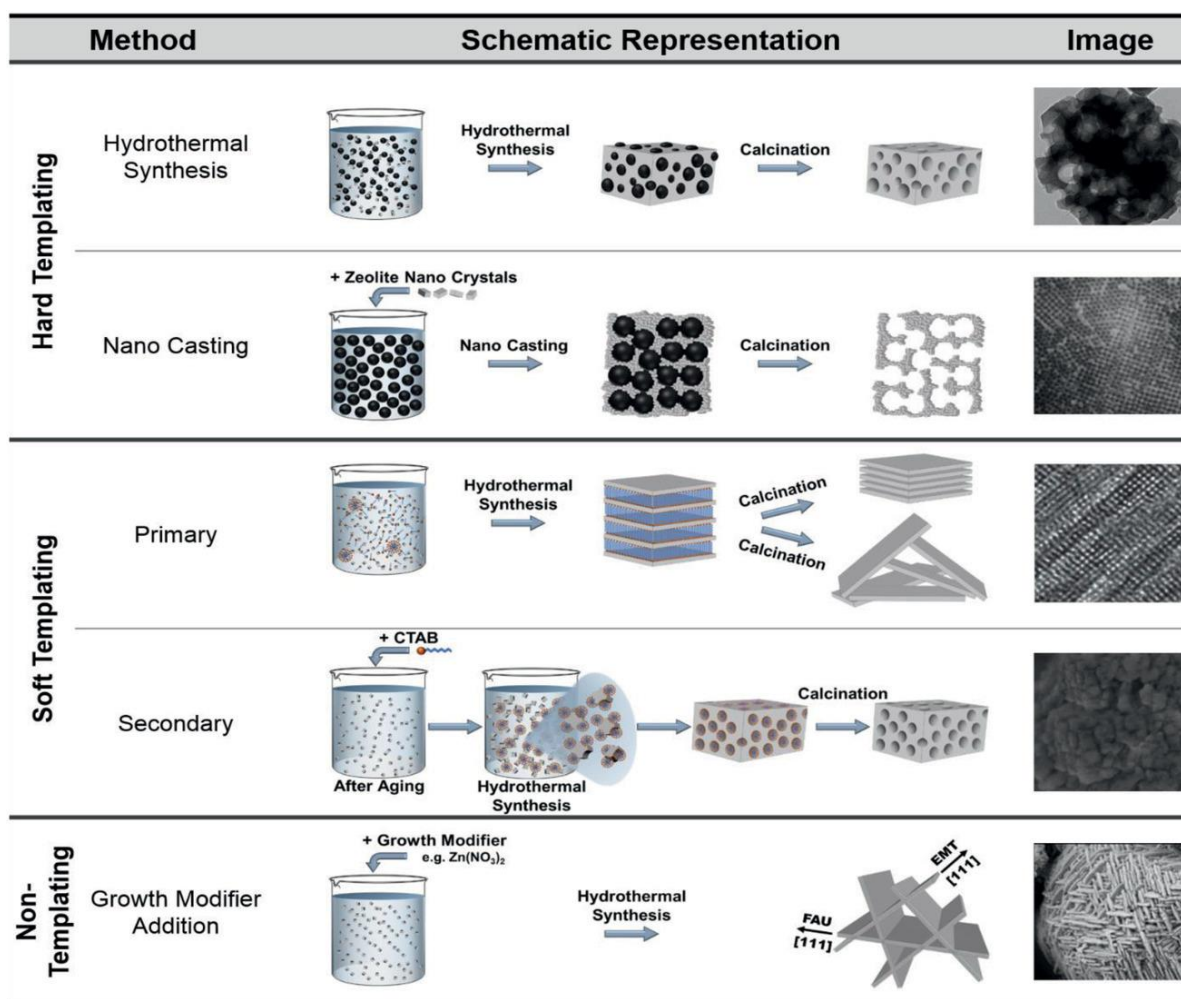


Figure 21: Schematic illustration of the three main methods, hard templating, soft templating, and non-templating, which are classified as “Bottom–Up” approaches. Figure adapted from ref.¹⁶⁰

On the contrary, top-down approaches consist of introducing an additional pore system into already preformed zeolite crystals using strong acids or bases to remove aluminium or silicon atoms, hence digging new cavities, into the preformed material. Three main cases can be differentiated: i) “extractive” methods ii) delamination/re-arrangement and/or modification treatments of sheets of layered zeolites, and iii) dissolution/ recrystallization.

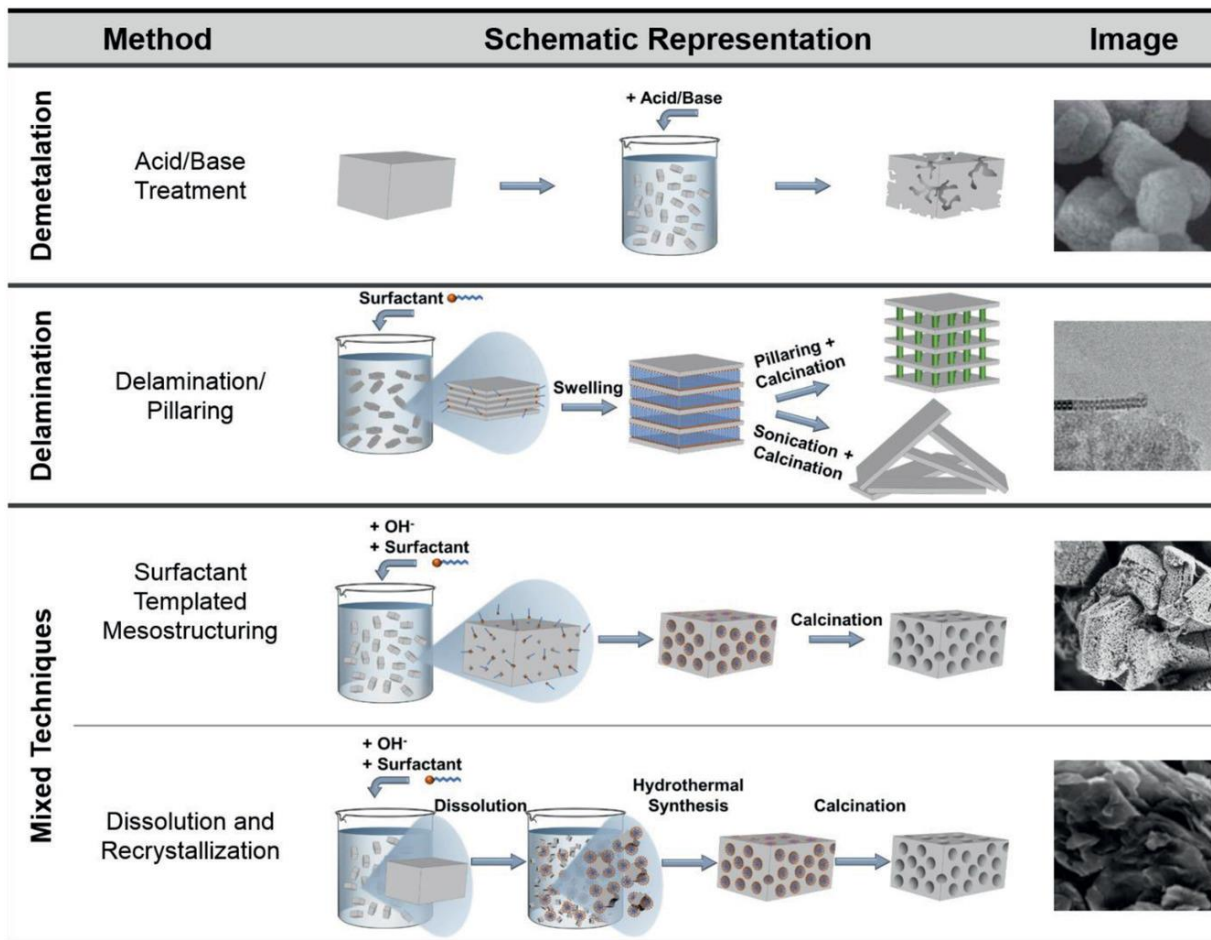


Figure 22: Schematic illustration of the three main methods, demetalation, delamination, and so-called mixed techniques which are classified as “Top-Down” approaches. Figure adapted from ref.¹⁶⁰

The synthesis of hierarchical zeolitic systems with intracrystalline meso- or macropores can overcome the pore size issue making zeolites a suitable material to host enzymes or other biomacromolecules.^{160,167–170} In addition, due to the presence of different pores, the mass transfer issue could be overcome as well. Recently, Ameri *et al.* reported the synthesis of both NaY and ZSM-5

zeolites and their hierarchical forms (HR-Y and HR-Z) through dealumination and soft templating procedure, and the immobilisation of laccase from *Trametes versicolor* by physical adsorption onto HR-Y and HR-Z. The result showed significant increase in the average pore diameter size for HR-Y (2.43 nm) and HR-Z (5.07 nm) compared to those of the parent types (NaY and ZSM-5: 1.85 and 2.01 nm, respectively). Laccase was subsequently immobilised on NaY and ZSM-5 zeolites, and their hierarchical forms by immobilisation efficiency of $74.4 \pm 1.4\%$, $71.6 \pm 1.0\%$, $98 \pm 2.9\%$, and $94 \pm 1.8\%$ for Lac@NaY, Lac@ZSM-5, Lac@HR-Y, and Lac@HR-Z, respectively. Thermal and pH stability of the immobilised laccases were enhanced compared with the free enzyme.¹⁷¹ In another work, Taghizadeh *et al.* immobilised by physical adsorption a laccase from *Trametes versicolor* on NaY (laccase@NaY) and its modified desilicated and dealuminated forms in order to obtain hierarchical zeolites, laccase@DSY and laccase@DAY respectively. The enzyme immobilised on hierarchical zeolites showed higher bisphenol A biodegradation compared to that in its native form. In addition, the hierarchical carrier also improved the pH stability, catalytic stability and reusability of the laccase.¹⁶³ Mitchell and Pérez-Ramírez synthesized by top-down approach a mesoporous ZSM-5. Subsequently, a lipase was immobilised on zeolite after surface treatment by organosilanes and glutaraldehyde. The results show a higher lipase immobilisation yield for meso/micro porous ZSM-5 than microporous ZSM-5. The surface modification of mesoporous ZSM-5 resulted in improved enzyme immobilisation efficiency, catalytic activity and reusability of enzyme compared with unmodified counterparts.¹⁷⁰ Many enzymes with medicinal value can be immobilised on zeolites to improve their stability and performances.¹⁷² Hu *et al.* immobilised a catalase onto hierarchically mesoporous zeolite A (a carrier with LTA topology obtained via a one-pot wet chemical method) to enhance real-time ultrasound contrast and improving photodynamic therapy of pancreatic cancer in a mice model.¹⁷²

Among several materials such as polymer nanofibers, mesoporous silica, graphene and graphene oxide, carbon nanotubes, natural biopolymers, metal nanoparticles, biochar etc., both hierarchical

zeolites and metal organic framework materials have become ideal supports for enzyme immobilisation. owing to their diverse pore structures, adjustable surface properties, relatively low cost, and good environmental compatibility. Here it was investigated the enzyme immobilisation by encapsulation into MOFs and via covalent attachment into a hierarchical zeolite.

CHAPTER 3:
SCOPE OF THE THESIS

In this Ph.D. thesis is the immobilisation of *Aspergillus sp.* Laccase on different supports was studied. This enzyme was chosen because of its importance in biomass pre-treatment.

The main aim of the thesis was trying to answer to the following general questions about enzyme immobilisation:

i) What is the best support for enzyme immobilisation?

Unfortunately, there is no general answer to this question *a priori*. For this reason, a screening of a number of supports for Laccase immobilisation was carried out. Among different possible supports for enzyme immobilisation three trimesic acid-based MOFs (Fe-BTC, Tb-BTC, Gd-BTC), an imidazolate-based MOF (ZIF-zni) and a functionalised pure-silica hierarchical (microporous-macroporous) MFI zeolite (ZMFI) were chosen. As reported in paragraph 2.2.2 the enzymatic encapsulation on trimesic acid-based MOFs and imidazolate-based MOF is facile, rapid, and results in high enzyme loadings. Nevertheless, MOFs are generally poorly stable under acidic conditions. On the contrary, the use of the pure silica hierarchical zeolite allows to carry out the reaction under the optimal pH of laccase avoiding the dissolution of the support. The purpose of the screening was to find the support which allowed the best performance in terms of activity and stability to the immobilised laccase.

ii) Where is the enzyme located after immobilisation?

This is an important issue, because the enzymatic performance could be different depending on the fact it is either on the external or on the internal surface of the support.

iii) Does the immobilisation procedure affect the secondary structure of the enzyme?

After the immobilisation, the enzyme is active only if the secondary structure has not been too modified compared with that of the free enzyme.

In order to try to answer the questions above, a multi-technique approach has been followed as better explained in the following paragraphs.

3.1 Support screening

Different supports, namely metal organic frameworks and silica zeolite for the immobilisation of the laccase from *Aspergillus sp.* were compared. The investigated materials were three trimesic acid-based (Fe-BTC, Tb-BTC, and Gd-BTC) MOFs and a pure silica macroporous (MFI) zeolite. The texture and the structure of the synthesized materials were characterised through N₂ adsorption/desorption isotherms and X-ray diffraction analysis (XRD). SEM and Confocal laser scanning microscopy (CLSM) analysis were employed to evaluate the morphological properties of the material. Chemical composition and the effective immobilisation of the enzymes were determined through thermogravimetric analysis (TGA), whilst the spectroscopic characterisation was performed by attenuated total reflection Fourier transform infrared (ATR-FTIR), micro-FTIR and confocal Raman spectroscopy.

3.2 Enzyme location

The enzymatic immobilisation within Metal-Organic Frameworks has gained great attention in these last years. Nevertheless, the enzymatic location during its encapsulation within MOFs is a topic poorly investigated in literature which worth further investigation. Indeed, the precise distribution of enzymes during their encapsulation in the MOFs is still unknown. Currently, the main procedures used to study the enzyme position on MOFs are the calcination of Enzyme@MOFs in the temperature range of protein decomposition to collect SEM images pre- and post-enzymatic immobilisation. This technique could give useful information about protein location in the support. However, it does not give information about the precise protein location. Another widely used technique is the CLSM. However, it requires the labelling of protein by

fluorescent molecules i.e. Fluorescein isothiocyanate (FITC) resulting in an expensive and time consuming approach. It is very complicated to determinate the protein location on MOFs during the encapsulation process using only one technique. Here, besides both the above-mentioned techniques a novel approach based on micro-FTIR 2D imaging using a Focal Plane Array (FPA) detector was used to evaluate the protein distribution.

3.3 Enzyme secondary structure

Commercial enzymes often show a very low degree of purity, and their enzymatic structure are likely still unknown. These aspects make tricky the investigation of their location and the determination of the structure conformation. In this regards a highly pure sample of bovine serum albumin (BSA) with a known structure was used as a model protein. BSA was immobilised within two different zeolitic imidazolate frameworks (ZIF-zni and ZIF-8) through a one-pot synthesis carried out under mild conditions (room temperature and aqueous solution).

The same technique was also used to investigate the secondary structure and conformation changes of free bovine serum albumin (BSA) due to its immobilisation on both ZIF-zni (BSA@ZIF) and ZIF-8 (BSA@ZIF-8). Protein conformation plays a crucial role in determining the catalytic efficiency of enzymes.

CHAPTER 4:
CHARACTERISATION
TECHNIQUES

4.1 Powder X-rays Diffraction (XRD)

XRD is a non-destructive technique employed to determine the crystal structure of a material. Some important information such as the calculation of the material lattice parameters, the orientation of a crystal, the stress in crystalline regions, and secondary phases in the sample can be obtained by fitting of the XRD patterns. Crystals and polycrystalline materials consist of crystal planes from which diffraction can occur. When a crystalline powder undergoes to X-ray beam ($10 \text{ nm} < \lambda < 1 \text{ pm}$) a portion of the radiation is reflected at the upper surface whilst rays also penetrate the crystal and reflect from the plane below. This phenomenon leads to constructive or destructive interference.¹⁷³ The condition to have constructive interferences is described by Bragg's law:

$$2d_{hkl} \sin \theta = n\lambda$$

Where d is the spacing between diffracting planes, θ is the incident angle, n is an integer, and λ is the beam wavelength

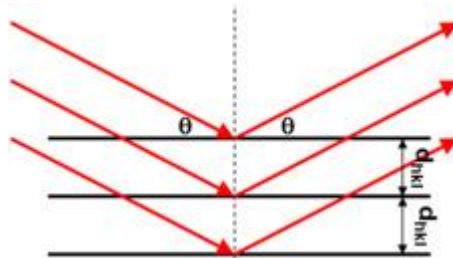


Figure 23: Representation of the X-rays scattering by the atomic planes of a material.

Interference maxima occur when the path difference between the recombining rays is an integer multiple of the incident wavelength.

X-ray diffraction (XRD) occurs when X-ray wavelength λ and the distance between atom layers in the sample have comparable sizes. According to the Bragg's law, the explored angular region ranges from 5° to 50° . The sum of diffraction patterns of each of the constituent phases gives the diffraction

pattern of the sample. Due to the absence of interference maxima, the amorphous phases show broad and featureless peaks. In contrast, powdered or polycrystalline samples show peaks in the diffraction pattern at each of the orientations. Through the patterns comparison is possible to know peak positions and intensities for a given material (qualitative analysis). whilst the Fitting pattern can provide additional information (quantitative analysis) such as the lattice parameters.¹⁷⁴ In addition, the Full Width at Half Maximum (FWHM) of peaks gives information on crystallinity, nonuniform lattice strain, crystallite size, and defects. Indeed, it depends in an inversely proportional way on the size of the particles (D), in accordance with the Debye-Scherrer law:

$$FWHM = \frac{K\lambda}{D \cos\theta}$$

where K is a dimensionless shape factor (~1) that varies with the actual shape of the crystallite, λ is the X-ray wavelength (nm) and θ is the Bragg angle. The intensity of the peaks depends on the atomic weight of the atoms of the unit cell and on their position inside the cell.

The zeolite and Laccase immobilised on zeolite synthesised for this work were characterised by at University of Nuremberg. All MOFs materials and enzyme immobilised on MOFs were characterised by X'Pert Pro PANanalytical at University of Cagliari. Figure 24

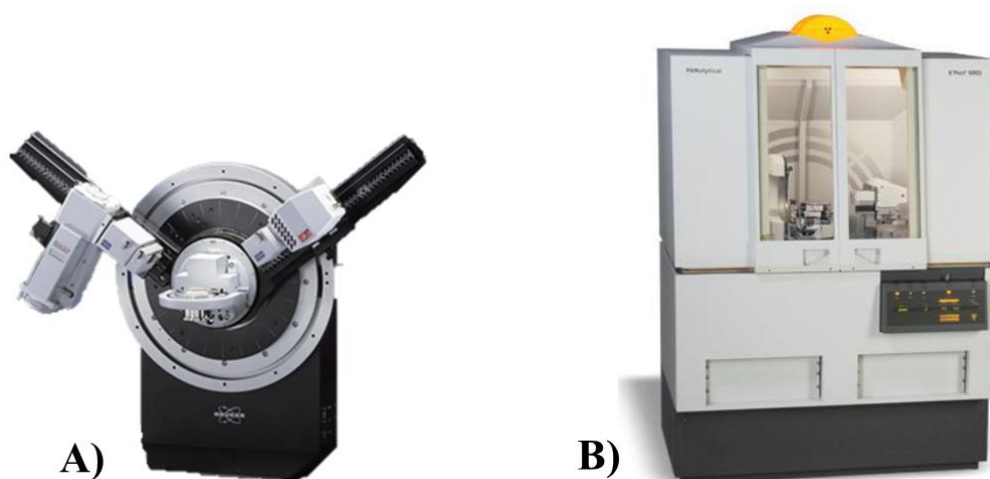


Figure 24: Picture of **A)** Bruker D8 Advance **B)** X'Pert Pro PANanalytical.

4.2 N₂ physisorption

Gas adsorption is an important tool for the textural characterisation of porous solids and fine powders. The adsorption isotherm is usually constructed by the admission of successive charges of gas to the adsorbent with the aid of a dosing technique and application of the appropriate gas laws. The quantity of gas adsorbed is measured in any convenient units, but for the presentation of the data, it is recommended that the amount adsorbed should be expressed in moles per gram of outgassed adsorbent. The adsorption isotherms are usually plotted as the amount adsorbed (generally expressed in mol·g⁻¹) against the equilibrium relative pressure (p/p_0), where p_0 is the saturation pressure of the pure adsorptive at the operational temperature, or against p , when the temperature is above the critical temperature of the adsorptive. Physisorption isotherms and hysteresis loops are classified in six and five types respectively as reported in figure 25.

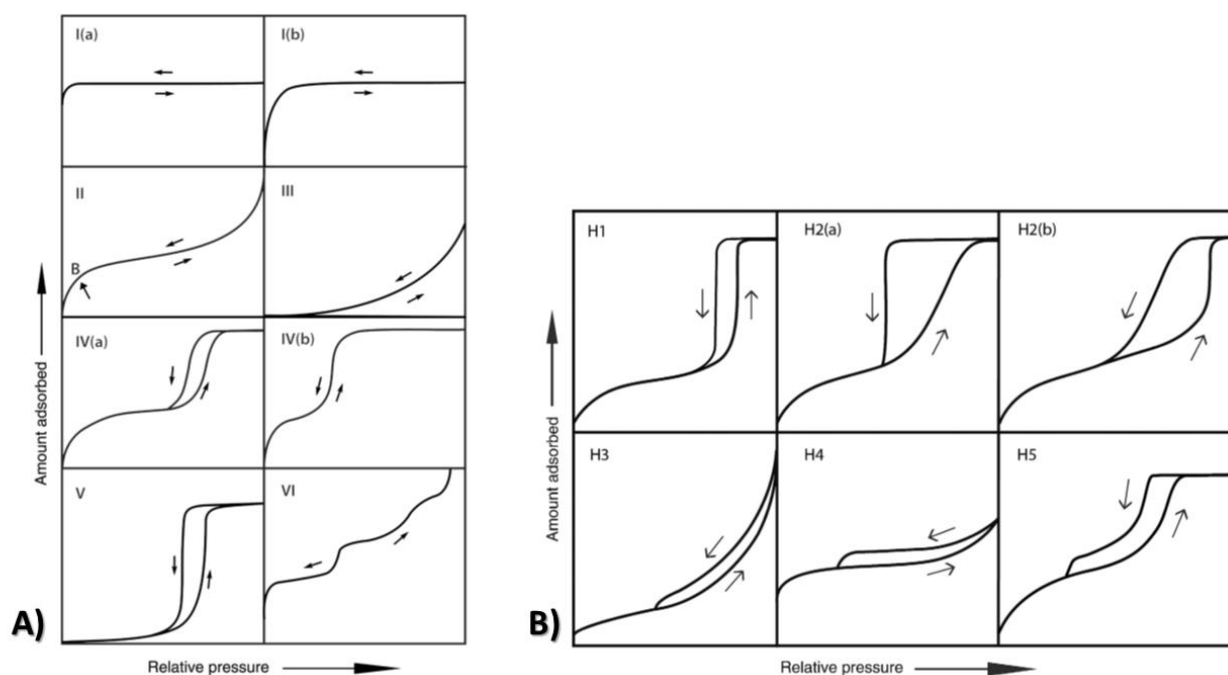


Figure 25: A) physisorption isotherms; B) hysteresis loops according to the IUPAC classification.

Reproduced from ref.⁸⁴

Reversible Type I isotherms show a steep rise at low pressures, then plateau. It refers to microporous solids having relatively small external surfaces such as some activated carbons, molecular sieve zeolites and certain porous oxides. According to the material pore dimension the Type I isotherms are divided in

- Type I(a) isotherms are characteristic for microporous materials having mainly narrow micropores (of width < 1 nm);
- Type I(b) isotherms are found with materials having pore size distributions over a broader range including wider micropores and possibly narrow mesopores (< 2.5 nm).

Reversible Type II isotherms are first concave, then almost linear, and finally convex to the p axis. less steep rise at low pressures, then further increase with change in concavity. They are given by the physisorption of most gases on nonporous or macroporous adsorbents.

Reversible Type III isotherms are always convex to the p axis. They refer to non-porous or macroporous adsorbents weakly interacting with the adsorbate.

Type IV isotherms are given by mesoporous adsorbents such as oxide gels, industrial adsorbents, and mesoporous molecular sieves). The adsorption behavior in mesopores is determined by both adsorbent adsorptive/interactions and by the interactions between the molecules in the condensed state.

According to the hysteresis type the isotherms IV are classified by Type IVa and IVb isotherms

- Type IVa isotherm, capillary condensation is accompanied by hysteresis. This occurs when the pore width exceeds a certain critical width, which is dependent on the adsorption system and temperature (e.g., for nitrogen and argon adsorption in cylindrical pores at 77 K and 87 K, respectively, hysteresis starts to occur for pores wider than ~ 4 nm) With adsorbents having mesopores of smaller width, completely reversible. the hysteresis loop

is associated with the filling and emptying of the mesopores by capillary condensation (the exact shape of the hysteresis loop varies from one system to another); quite common

- Type IVb isotherms are observed. In principle, Type IVb isotherms are also given by conical and cylindrical mesopores that are closed at the tapered end. Type IVb isotherm: the rise is almost vertical (at a characteristic p/p_0) and the isotherm is completely reversible; given only by a few ordered mesoporous structures (notably MCM-41, characterised by uniform near-cylindrical pores of critical size, when N_2 is adsorbed at 77 K)

Type V isotherms are observed for water adsorption on hydrophobic microporous and mesoporous adsorbents. The initial region of the adsorption branch is like a Type III isotherm (convex to the (p/p_0) axis). levels off at high relative pressures with a saturation plateau (which may be short and reduced to an inflexion point).

The reversible stepwise Type VI isotherm is representative of layer-by-layer adsorption on a highly uniform nonporous surface. Type VI isotherms are obtained with argon or krypton at low temperature on graphitized carbon blacks.

In 1938, Stephen Brunauer, Paul Hugh Emmett, and Edward Teller developed a theory, called B.E.T, to determine the specific surface of a porous material. B.E.T theory is an extension of the Langmuir model, which consider the multilayer physical adsorption assuming that gas molecules can interact with adjacent layers without influencing the interaction with the deeper layers. The equation is:

$$\frac{p/p^\circ}{n(1-p/p^\circ)} = \frac{1}{n_m C} + \frac{C-1}{n_m C} (p/p^\circ)$$

Figure 26: BET equation in the linear form.

where n is the specific amount adsorbed at the relative pressure p/p° and n_m is the specific monolayer capacity. The parameter C is exponentially related to the energy of monolayer adsorption. Fitting the equation in figure X it is possible to obtain the specific surface area

$$a_s(\text{BET}) = n_m \cdot L \cdot \sigma_m / m$$

where the σ_m (molecular cross-sectional area), occupied by the adsorbate molecule in the complete monolayer, $a_s(\text{BET})$ is the BET specific area of the adsorbent (of mass m).



Figure 27: Image of the ASAP 2020.

4.3 Thermogravimetric Analysis (TGA)

Thermogravimetric analysis (TGA) is a technique used to measure the material's thermal stability through the sample mass variation as a function of temperature. The apparatus consists of a sensitive

scale that measures the weight changes and a programmable furnace act to control the heat-up rate of the sample. The balance is located above the furnace and is thermally isolated from the heat. A high-precision wire is suspended from the balance down into the furnace. The sample pan is located at the end of the wire. The specimen is usually positioned in a pan made of ceramic or platinum. The resulting plot (thermogravigram) is reported as a mass loss % against temperature. Since the obtained curves are characteristics for each type of material. It is possible to extract information from the thermogravigram such as the thermal stability and composition of a specimen.

A STA6000 Perkin Elmer TGA (Fig. 28) was used for the thermogravimetric analysis of all samples investigated during this Ph.D. work.



Figure 28: STA6000 Perkin Elmer.

4.4 Fourier Transform Infrared Spectroscopy (FTIR) Infrared

During analysis by infrared spectroscopy (IR), a sample interacts with electromagnetic radiation in the infrared region of the spectrum. The radiation absorption depends on the nature of the chemical groups present in the sample. Absorption over the infrared spectrum is a fingerprint characteristic of organic material. Infrared spectra can also be obtained by reflecting the IR beam on the surface of a sample. Attenuated total reflectance (ATR), also known as ATIR (attenuated total internal reflectance), allows the non-destructive direct analysis of a liquid or solid sample without the necessity of the KBr pellet. is based on multiple internal reflectances of the IR beam on the sample surface using

a high refractive index crystal (e.g., thallium Bromo-iodide). Therefore, using the property of total internal reflection of the crystal results in an evanescent wave that hits the sample in contact with the crystal.

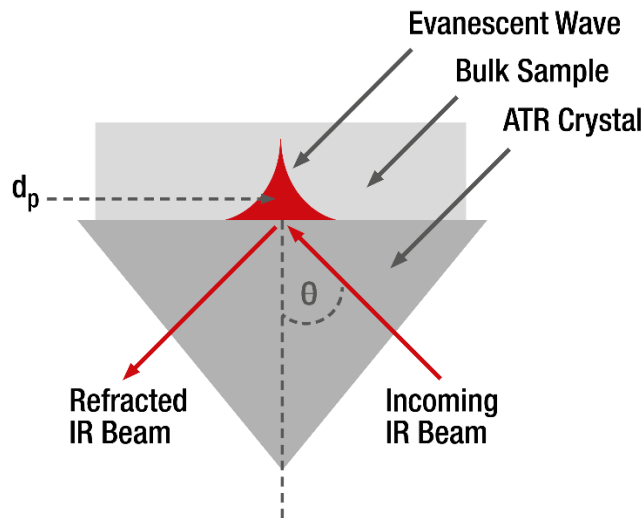


Figure 29: Evanescent wave resulting from total internal reflection. From <https://wiki.anton-paar.com/be-fr/reflexion-totale-attenuuee-atr/>

The evanescent wave goes through the crystal surface and penetrates the sample only for some microns ($0.5 \mu\text{m} - 2 \mu\text{m}$), with the exact value determined by the wavelength of light, the angle of incidence, and the indices of refraction for the ATR crystal and the medium being probed.

$$d_p = \frac{\lambda}{2\pi n_1 \sqrt{\sin^2 \theta - \left(\frac{n_1}{n_2}\right)^2}}$$

Figure 30: Calculation of penetration depth: λ : wavelength of incident light in vacuum; n_1 : refractive index of ATR crystal (dense medium); n_2 : refractive index of sample (rare medium); θ : angle of incidence.

4.5 Electron Microscopy

Tab. 5 vibration modes of typical bonds that can be identified by means of IR spectroscopy.

Typical vibration modes	Wavenumbers (cm ⁻¹)
C-H stretching	2850-2960
C-H bending	1340-1465
C-C stretching	700-1250
C=C stretching	2100-2260
stretching C HCH	2100-2260
O-H stretching	3590-3650
Hydrogen bonds	3200-3570
C=O stretching	1654-1780
N-H stretching	3200-3500
N-H bending	1546
Amide I and amide II	1650 and 1550
Si-O-Si symmetric stretching	800
Si-O-Si asymmetric stretching	1067-1070
C=N stretching	1584
Aromatic rings bending	900-1350
Zn-N stretching	421

Electron microscopy is used to obtain high-resolution images of biological and non-biological specimens. Every electron microscope works by accelerating a focused stream of electrons in a vacuum towards a sample. The Interaction between the electron beam and the sample leads to an image of a sample's surface or internal composition, depending on the type of electron microscope that is used. In comparison to light microscopy, electron microscopes can capture higher-resolution

images. Indeed, the lateral resolution $d=0,6098 \lambda AN$ is inversely proportional to the resolving power, however, the lateral resolution is directly proportional to the wavelength of the radiation. Thus, using a very small λ , it is possible to observe small objects. Electron microscopes using a beam of electrons rather than photons as a radiation source, possess a resolving power that greatly exceeds that of optical microscopes, since the wavelength of electrons is significantly smaller than that of light.

4.6 Scanning Electron Microscopy (SEM) and Transmission Electron Microscopy (TEM)

Scanning Electron Microscopy (SEM) and Transmission Electron Microscopy (TEM) are the main types of electron microscopy. TEM and SEM differ in how they work and what types of images they can capture.

Tab. 6: Summary of the differences between SEM and TEM.

	Scanning Electron Microscopes (SEM)	Transmission Electron Microscopes (TEM)
Electron stream	Fine, focused beam	Broad beam
Image taken	Topographical/surface	Internal structure
Resolution	Lower resolution	Higher resolution
Magnification	Up to 2,000,000 times	Up to 50,000,000 times
Image dimension	3-D	2-D
Sample thickness	Thin and thick samples okay	Ultrathin samples only
Penetrates sample	No	Yes
Sample preparation	Less preparation required	More preparation required
Cost	Less expensive	More expensive
Speed	Faster	Slower

In scanning electron microscopy (SEM), electrons are emitted from a cathode made of W or LaB₆. The primary beam of electrons is focused on a fine spot, and collides with the sample passing through scanning coils, determining the scan of a rectangular area. The sample emits a secondary beam that can be revealed resulting in a 3D image of the sample that shows the surface structure.

Transmission electron microscopy (TEM) is a high-resolution imaging technique in which a beam of electrons, generated from a cathode filament of an electron gun, passes through a thin sample (< 150 nm), creating an image that details a sample's morphology, composition, and crystal structure. The beam is collected to condenser lens and hits the sample determining a scattered diffraction pattern. The beam interacts with the sample resulting in an image that can be impressed into a photographic layer or revealed by a charge-coupled device camera. If the direct beam is chosen to form the TEM image, this produces a bright-field image, while the scattered electrons from the sample produce a dark-field image.

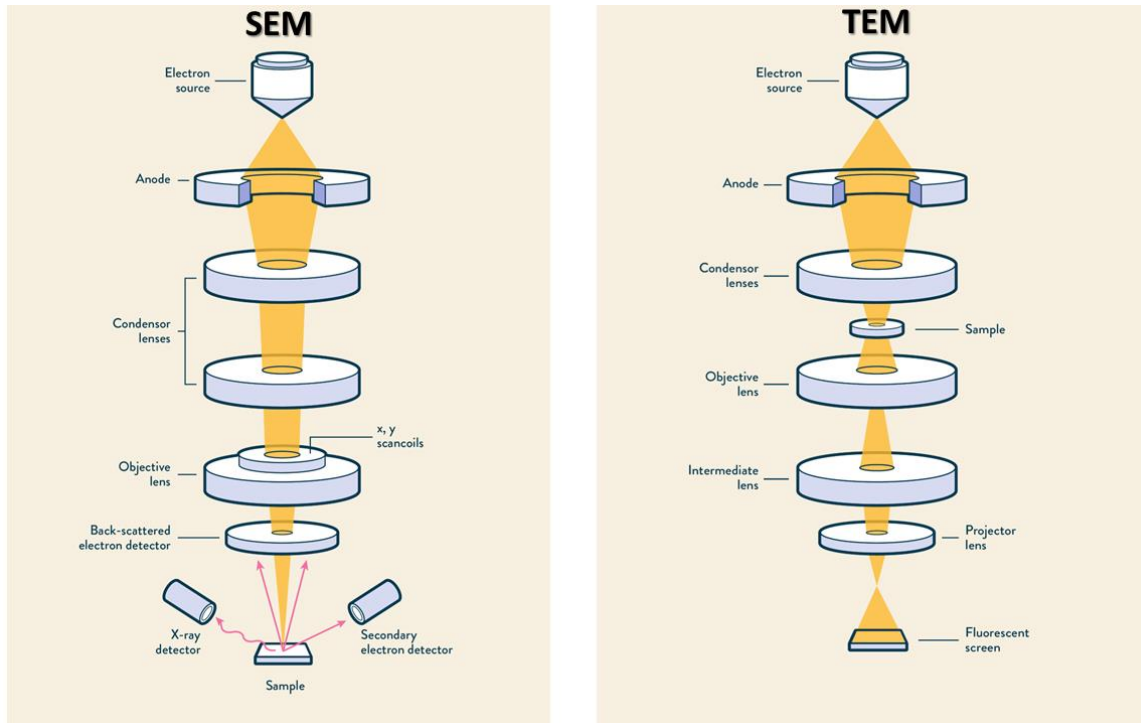


Figure 31: Schematic representation of SEM and TEM microscopy

4.7 Confocal laser microscopy

Fluorescence microscopy is a type of light microscope that works on the principle of fluorescence widely used in diagnostic microbiology and in microbial ecology. In a conventional widefield optical epifluorescence microscope. In an epi-fluorescence laser scanning microscope, the coherent light emitted by the laser system crosses a pinhole aperture which is located in a conjugate plane with a scanning point on the specimen and a second pinhole aperture positioned in front of the detector. The specimen is crossed in a defined focal plane, and secondary fluorescence emitted from points on the specimen (in the same focal plane) passes back through the dichromatic mirror and is focused as a confocal point at the detector pinhole aperture

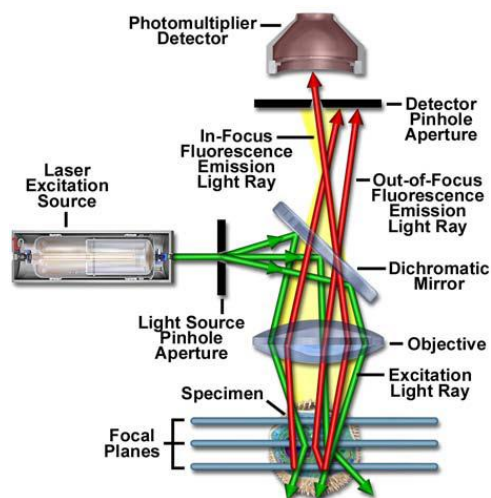


Figure 32: Schematic diagram of the optical pathway and principal components in a laser scanning confocal microscope. Reproduced from ref.¹⁷⁵

A Leica TCS SP8 (Fig. 28) was used for the analysis of all samples investigated during this Ph.D. work.

CHAPTER 5:

RESULTS

In this chapter a short overview of published and unpublished results is given. The detailed motivation, the experimental details and the full set of result, suitably discussed, are given in Appendix. where both published and submitted papers, along with the respective Supporting Information Files, are reported.

As reported in chapter 2 laccases oxidise various phenolic compounds by one electron transfer with the concomitant reduction of dioxygen to water. It has been demonstrated that these enzymes are involved in the delignification mechanism, and for that reason they are of potential technological interest for green chemistry applications, such as bioethanol production.

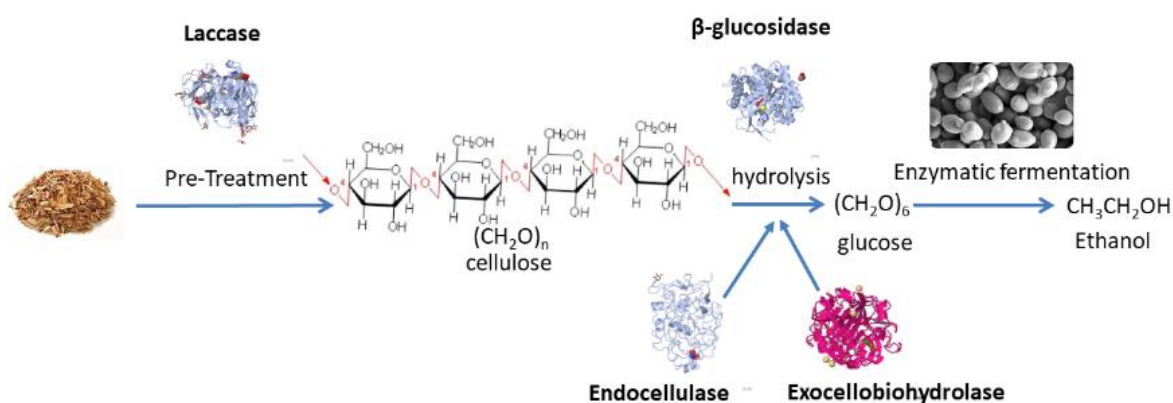


Figure 33: schematic process of bioethanol production from BML carried out by enzymes.

The most critical step in the process is the pre-treatment of biomass. Many papers have been published about laccase involved in pre-treatment. Due to COVID-19 pandemic and restricted access to research laboratories, with a consequential slowdown of experimental activity, I used this time to go through the literature and write a review about laccases involved in biomass pre-treatment. The work was aimed to give an overview of the importance of laccases, mediators, and the best reaction conditions for biomass treatment. **(PAPER I).**

As reported/explained in chapter 2 the use of free enzymes is often hampered by several limitations such as high costs, low operational stability (extreme conditions of T and pH), and difficulty recovery and reuse. This makes enzyme immobilisation. on solid supports a possible solution of those issues.

The experimental work of this thesis involved the use of hierarchical zeolites and metal organic frameworks (MOFs) as possible supports for enzyme immobilisation. In this regard, three trimesic acid-based frameworks such as Fe-BTC (commercially known as Basolite F-300), Tb-BTC and Gd-BTC were investigated for the immobilisation of the LC from *Aspergillus sp.* The Fe-BTC material was initially used for a different application, namely, the removal of Malachite Green (MG) and Alizarin Red S (ARS) organic dyes from water (**PAPER II**). Fe-BTC was characterised by means of Powder X-rays Scattering (XRD), Scanning Electron Microscopy (SEM), N₂ physisorption, Thermogravimetric Analysis (TGA) and Fourier-Transform Infrared spectroscopy (FT-IR). The thermodynamic and kinetic parameters regarding both adsorption processes were determined by UV-Vis spectrophotometric analysis. Experimental data were compared with theoretical models. The Langmuir model provided the best fit to the adsorption process, with maximum adsorption capacities of 80 and 177 mg g⁻¹ for ARS and MG on Fe-BTC MOF, respectively.

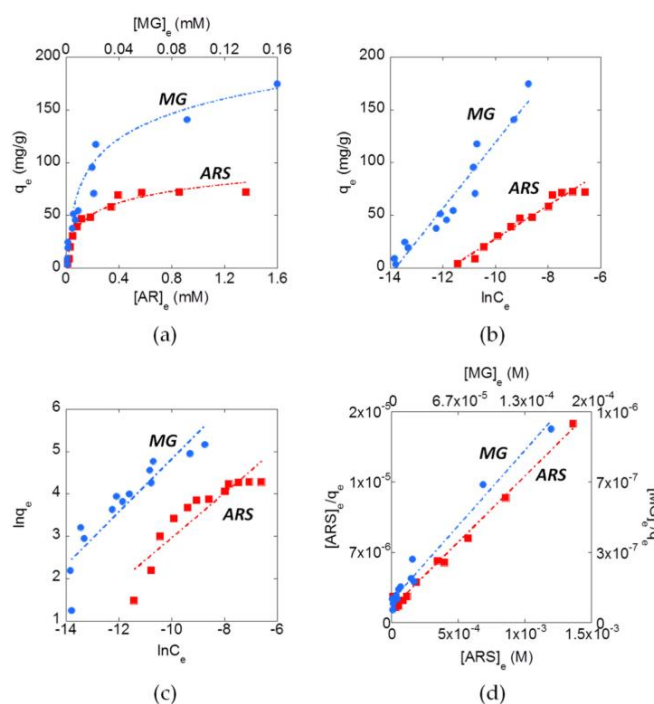


Figure 34: A) Adsorption isotherms of MG and ARS with MOF where q_e is a function of the equilibrium concentration. Adsorption data were fitted using linearized isotherms; (b) Temkin; (c) Freundlich; (d) Langmuir. The experiments were carried out in distilled water for 24 h, at $T = 298$ K.

In **PAPER III** two different MOFs were compared as supports for laccase immobilisation. First, Fe-BTC MOF was prepared through the method proposed by Sanchez⁹⁶ then a zeolite imidazolate framework (ZIF-zni) MOFs. LC immobilisation. occurred *in situ* under mild conditions, e.g. aqueous solution, neutral pH, and at room temperature for both MOFs. Immobilisation. efficiency was 100% for LC@Fe-BTC while was 99%, 70% and 52% and for LC@ZIF-zni, LC@TbBTC and LC@GdBTC samples respectively. Immobilised LCs resulted in a lower specific activity compared with that of the free LC ($7.7 \mu\text{mol min}^{-1} \text{mg}^{-1}$). LC@Fe-BTC showed the lower specific activity ($0.17 \mu\text{mol min}^{-1} \text{mg}^{-1}$) compared with LC@GdBTC ($3.3 \mu\text{mol min}^{-1} \text{mg}^{-1}$), LC@ZIF-zni ($1.3 \mu\text{mol min}^{-1} \text{mg}^{-1}$) and LC@TbBTC ($1.2 \mu\text{mol min}^{-1} \text{mg}^{-1}$). The K_M value of LC@ZIF-zni is lower ($21.6 \mu\text{M}$) than those of LC@Fe-BTC ($35.5 \mu\text{M}$), LC@GdBTC ($60 \mu\text{M}$) and LC@TbBTC ($116.5 \mu\text{M}$) suggesting more efficient substrate binding by laccase in ZIF-zni.

Table 7: Kinetic parameters obtained with free laccase, LCMOFs samples.

Samples	K_M (μM)	V_{max} ($\mu\text{mol} \cdot \text{mg}^{-1} \text{min}^{-1}$)
Free LC	13.3	7.7
LC@TbBTC	116.5	1.16
LC@GdBTC	59.8	3.28
LC@FeBTC	35.5	0.17
LC@ZIF-zni	21.6	1.32

The effect of enzyme loading was evaluated in case of Fe-BTC and ZIF-zni MOFs. LC@Fe-BTC had an optimal loading of 45.2 mg g^{-1} , at higher enzyme loadings the specific activity decreased. In

contrast, the specific activity of LC@ZIF-zni increased linearly over the loading range investigated indicating that a higher amount of laccase can be immobilised without observed limitations.

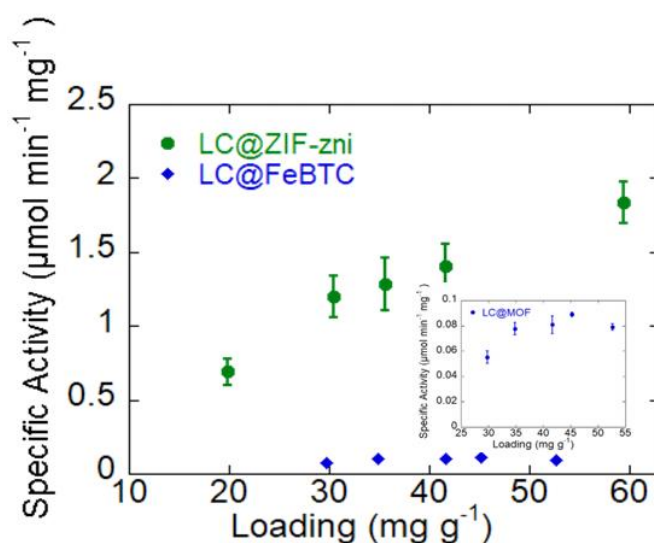


Figure 35: Effect of loading on specific activity of LC@Fe-BTC and LC@ZIF-zni. Inset: enlargement of data for LC@Fe-BTC.

The storage stability of LC@Fe-BTC was low with a significant decrease in activity after 5 days, while LC@ZIF-zni retained up to 50% of its original activity after 30 days storage whilst LC@TbBTC and LC@GdBTC retained up to 30% of its original activity after 21 days storage. The difference in activity and stability between LC@Fe-BTC and other supports is likely due to release of Fe³⁺ and the low stability of Fe-BTC MOF. Together, these results indicate that ZIF-zni and GdBTC are promising supports for the immobilisation of *Aspergillus sp.* laccase. However, it is necessary to consider that all trimesic based MOFs investigated in this work do not have a crystalline structure. On the contrary ZIF shows a crystalline structure allowing a good synthesis reproducibility.

The work related to Tb-BTC, Gd-BTC, Lc@Tb-BTC, and Lc@Gd-BTC is reported here in detail since they have not been published yet. The XRD patterns of both free and immobilised laccase (LC@GdBTC and LC@Tb-BTC) showed amorphous structure. Scanning electron microscopy (SEM) images of GdBTC and TbBTC show a regular morphology with a needle shape. The LC

immobilised into the support led to a change of particles morphology turning the material from needle shape to spherical one

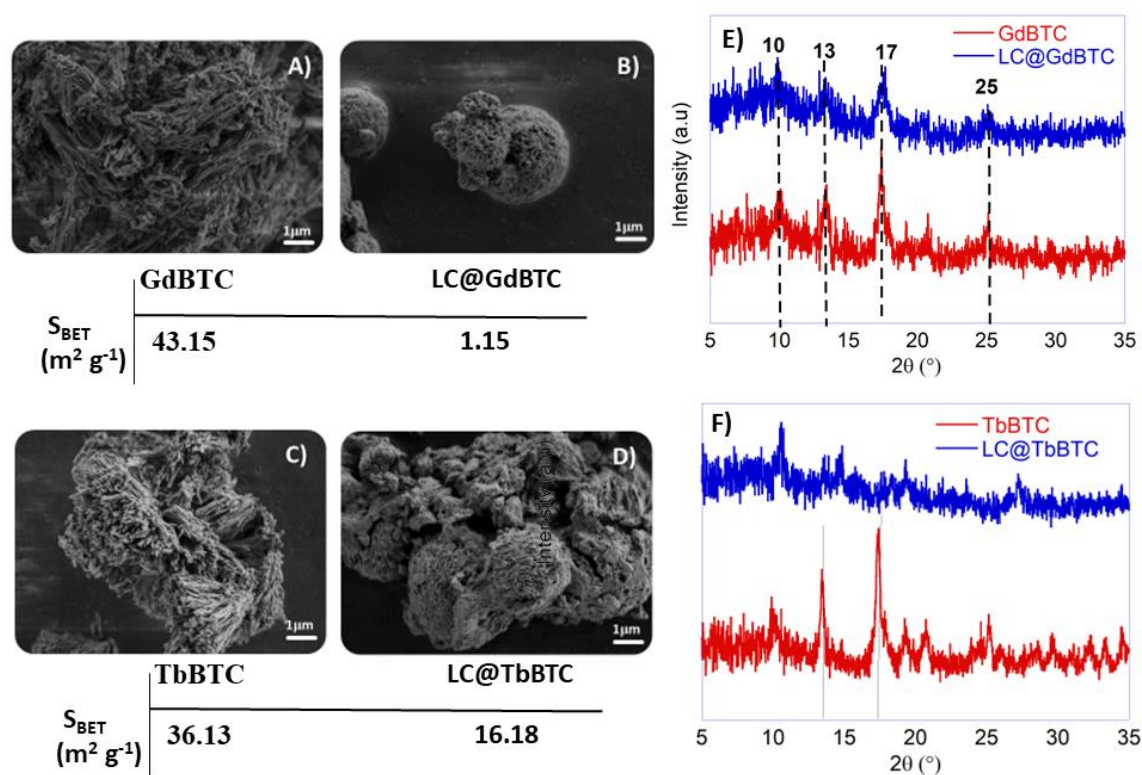


Figure 36: SEM image of A) GdBTC B) LC@GdBTC C) TbBTC D) LC@TbBTC; XRD patterns of E) GdBTC, LC@GdBTC F) TbBTC, LC@TbBTC.

Figure 35 shows FTIR spectra of the synthesised samples. For the Fe-BTC MOF sample, the peak at 1610 cm^{-1} can be attributed to the C=O bond of carboxylate groups, while the bands at 1445 and 1362 cm^{-1} are due to asymmetric and symmetric stretching of the O-C-O group, respectively. The other two sharp peaks at 750 and 703 cm^{-1} correspond to the bending of aromatic C-H bonds. The two peaks at 1625 cm^{-1} and 1362 cm^{-1} arising from the carboxylate groups of the linker of the MOF likely mask the C=O amide stretching bands of the protein. TGA and FTIR characterisations, together with the Encapsulation efficiency values (70.2% and 52.3% for LC@TbBTC and LC@GdBTC respectively) confirm the successful immobilisation of the LC within the two trimesic based MOF.

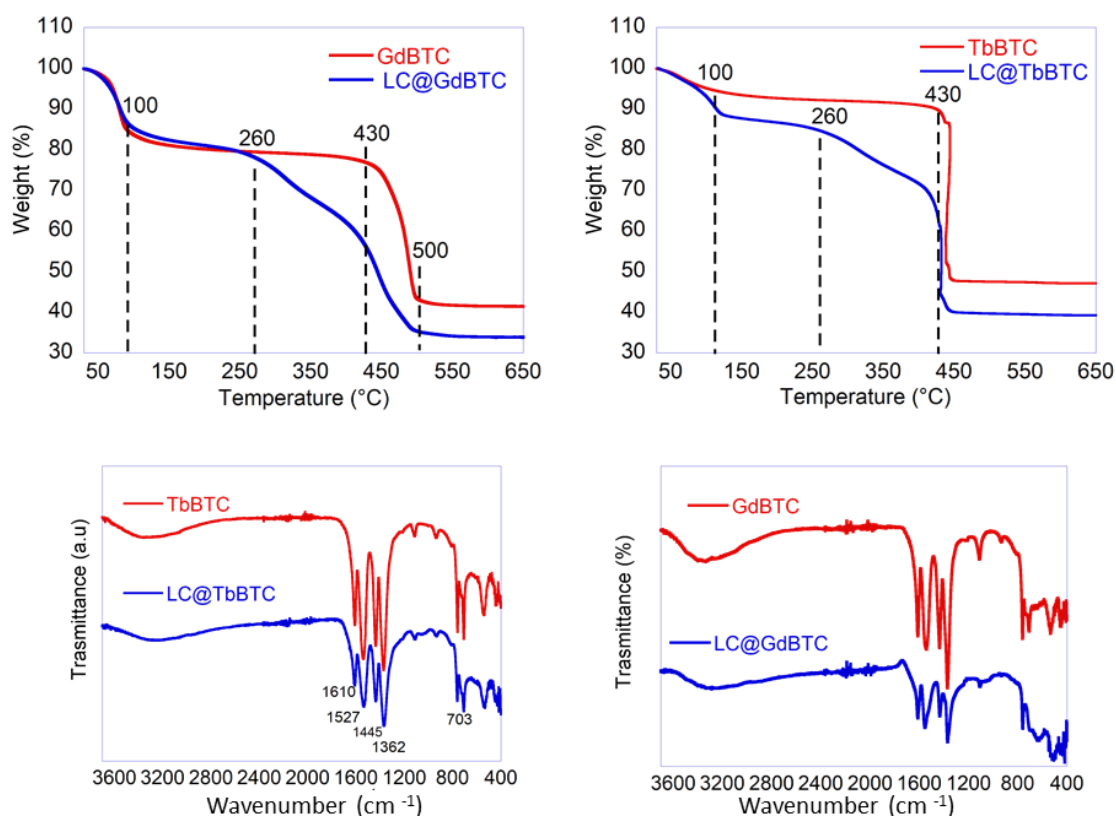


Figure 37: Thermogravimetric analysis (TGA) and FT-IR spectrum of MOF material the biocatalysts LC@MOF.

The operational and storage stability of LC@TbBTC and LC@GdBTC were then studied. The operational stability LC@GdBTC (Fig. 36A) decreased in specific activity up to 30 % after 3 days. From the 3rd day it decreased up to ~75% of its initial specific activity and retained a constant activity up to 20th day. The storage stability of LC@GdBTC retained ~60 % of its initial activity at the 6th day and about ~20% of its initial activity at the 32th day. LC@TbBTC operational stability (Fig. 36B) decreased up to ~50 % and retained a constant activity up to 3 weeks. The same trend was also observed for the LC@TbBTC storage stability (Fig36D).

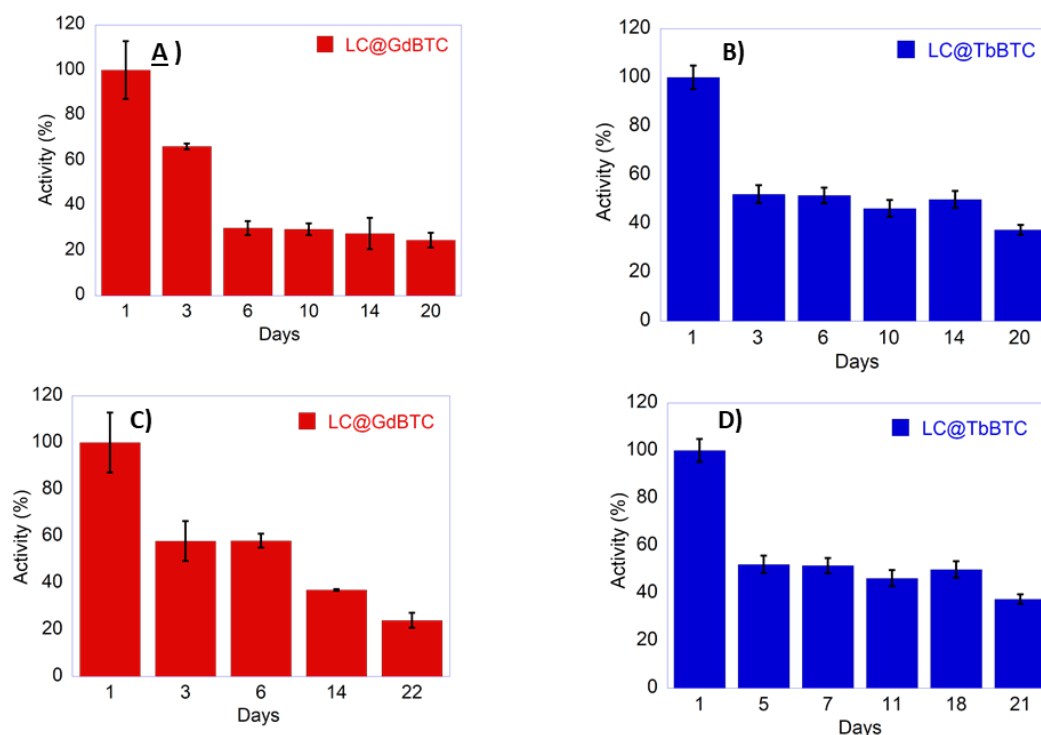


Figure 38: Operational stability of **A) LC@GdBTC B) LC@TbBTC**; Storage stability of **C) LC@GdBTC D) LC@TbBTC**.

In **PAPER IV** the same laccase was immobilised via post-synthetic treatment on a pure silica macroporous (MFI) zeolite with embedded micropores. The biocatalyst was characterised by SEM, FTIR, N₂ adsorption and TGA. In addition, the support functionalisation was investigated through Fourier transform infrared spectroscopy (ATR-FTIR), N₂ adsorption/desorption isotherms, solid-state NMR spectroscopy and EPR spectroscopy (Fig.34). The FT-IR spectrum of the ZMFI shows a broad band at about 1060 cm⁻¹ due to Si-O-Si asymmetric stretching, a band at 960 cm⁻¹ due to Si-OH stretching and one at 795 cm⁻¹ due to Si-O-Si symmetric stretching. After surface modification with 3-aminopropyl-triethoxysilane (APTES), the band at 960 cm⁻¹ disappears and a new band appears at 690 cm⁻¹ that is ascribed to N-H bending vibrations. Additional evidence for the zeolite modification are the stretching vibration of C-H bonds at 2870 cm⁻¹, 2900 cm⁻¹ and bending vibration of H-C-H bond at 1380 cm⁻¹ appear confirming the reaction of free silanols with APTES.¹⁷⁶⁻¹⁷⁸ As a result of laccase immobilisation, a band at 1647 cm⁻¹ (-C=N- bonds), due to the reaction between the -ZMFI-

CHO and laccase appears. ^{13}C Cross Polarization (CP) solid-state NMR spectra clearly show the grafting of APTES onto the zeolite, by appearance of resonances at 10, 21, 42 and 58 ppm, characteristic for $\text{C}_1\text{-C}_3$ and the amine carbon atom of APTES (Figure 3 a).¹⁷⁹ After modification with glutaraldehyde, additional resonances appear at around 30 ppm, indicative for additional aliphatic groups, and at 62 ppm, assigned to the $\text{C}=\text{N}$ functionality, but possibly overlapping with unreacted C-NH_2 amine groups from APTES. At 200 ppm, a particularly characteristic resonance for the aldehyde functionality appears. The successful immobilisation of LC is furthermore confirmed by ESR spectroscopy (Fig. 34A), showing that the solid biocatalyst contains LC with no major effect on the close environment of the ESR-active Cu centers of the enzyme.

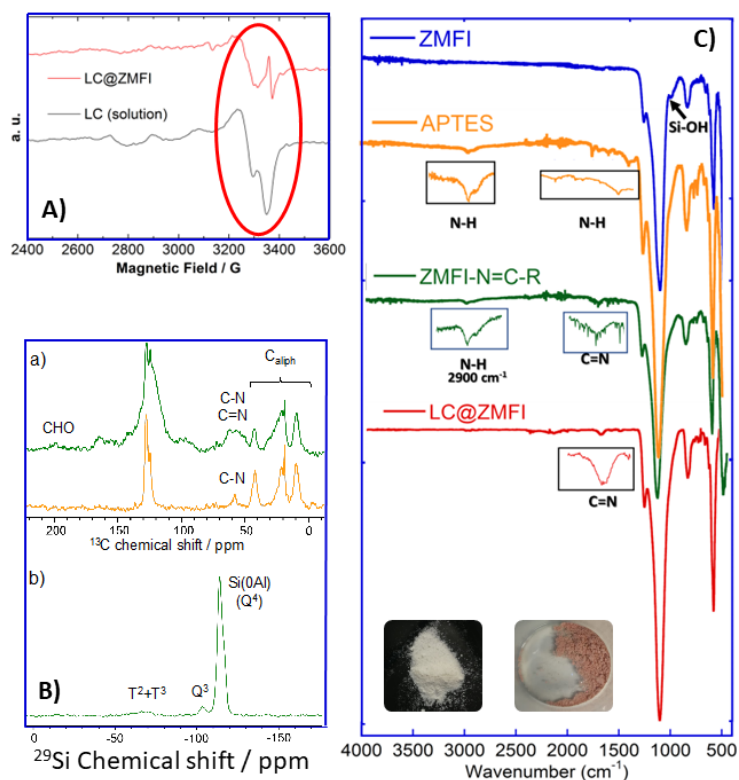


Figure 39: A) ESR spectra of laccase in solution as supplied and immobilised on ZMFI recorded at 100 K. B) ^{13}C CP MAS NMR spectra of ZMFI-NH₂ (yellow) and ZMFI-N=C-R (green). Line broadening: 100 Hz. Signals between 110-130 ppm correspond to toluene from synthesis. b) ^{29}Si HPDEC MAS NMR spectrum of ZMFI-N=C-R. Line broadening: 50 Hz. C) ATR-FT-IR spectrum of parent ZMFI zeolite, the with APTES modified sample and the LC@ZMFI biocatalyst.

Zeolite MFI type had a SBET of $534 \text{ m}^2 \text{ g}^{-1}$ that decreased by 45 % in the presence of laccase. The optimal pH, kinetic parameters (K_M and V_{max}), specific activity, as well as both storage and operational stability of LC@ZMF1 were determined. The LC@ZMF1 K_M and V_{max} values amount to $10.3 \text{ }\mu\text{M}$ and $0.74 \text{ }\mu\text{mol} \cdot \text{mg}^{-1} \text{ min}^{-1}$, respectively. The dependence of specific activity on the pH for free and immobilised LC, was investigated in the pH range of 2 to 7, The highest specific activity was obtained at $\text{pH} = 3$ for both free LC and LC@ZMF1. LC@ZMF1 retained up to 50% and 30% of its original activity after storage of 21 and 30 days, respectively. Immobilisation. of laccase on hierarchical pure-silica MFI zeolite allows to carry out the reaction under acidic pH values without affecting the support structure.

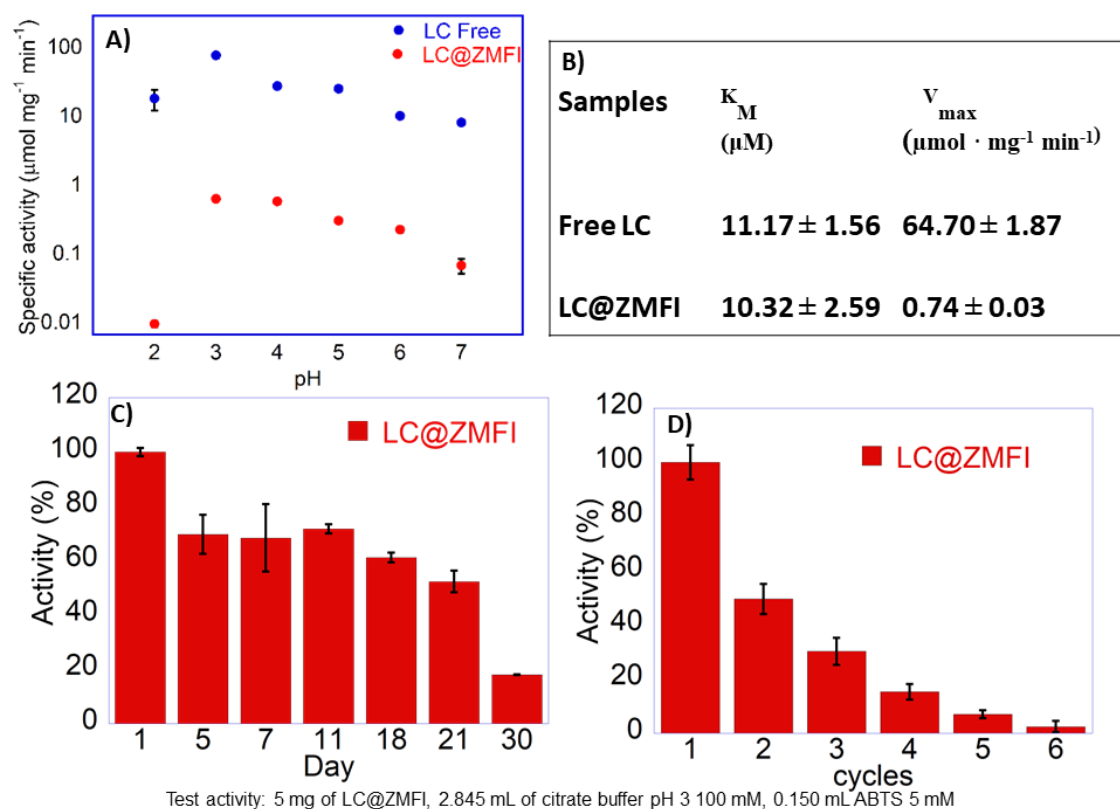


Figure 40: A) Specific activity as a function of pH for free laccase and @ZMF1 B) Michaelis-Menten of Free laccase and LC@ZMF1 C) Storage stability of LC@ZMF1, activity normalized at $1.12 \text{ }\mu\text{mol min}^{-1} \text{ mg}^{-1}$ D) Reuse of LC@ZMF1, activity normalized at $0.9 \text{ }\mu\text{mol min}^{-1} \text{ mg}^{-1}$.

For each LC support screened a decrease of specific activity and an increase of K_M (Except for Zeolite MFI) were observed. This aspect could be ascribable to the possible enzymatic structure distortion due to enzyme immobilisation.

In **PAPER V** the location and the secondary structure and conformation changes of the model protein serum albumin (BSA) due to its in-situ immobilisation within two different zeolitic imidazolate frameworks (ZIF-8 and ZIF-zni) were investigated. TG analyses were performed to evaluate the BSA mass loss in the supports. Data showed that BSA mass loss is in the temperature range comprised from 200 °C and 430 °C. Therefore BSA@ZIF-8 and BSA@ZIF.zni were calcinated at 380 °C for 2 hours. SEM images were collected pre and post support calcination to investigate the morphology change due to protein combustion. Due to the calcination, a change of the morphology from spherical to pitted and uneven was observed for both carriers.

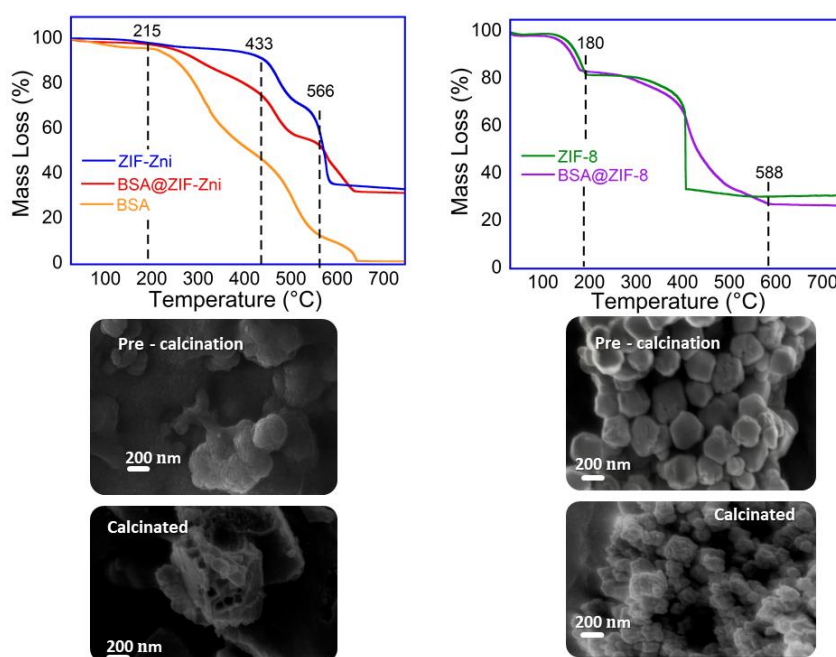


Figure 41: A) Thermogravimetric analysis (TGA) curve from 25 °C to 800 °C of ZIF-zni, BSA@ZIF-zni and BSA B) SEM images of BSA@ZIF-zni pre and post calcination at 380 °C.

This result is most likely due to protein decomposition. Moreover, the BSA was labeled by FITC to evaluate its position after immobilisation. by Confocal laser Confocal laser scanning microscopy.

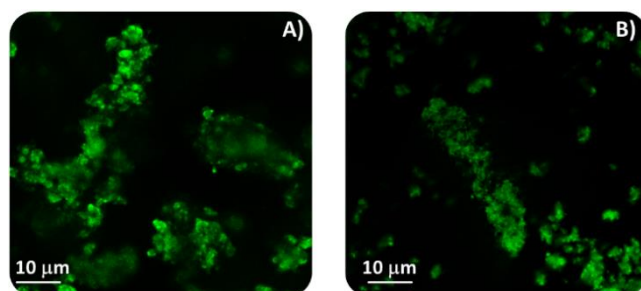


Figure 42: Confocal laser A) BSA-FITC@ZIF-zni and B) BSA-FITC@ZIF-8 samples.

The results showed that protein was evenly distributed in domains of 5-40 μm . FTIR 2D Imaging provided further information on the location of protein in the BSA@ZIF sample. Mapping the absorbance intensity (peak area) of the 3450-3200 cm^{-1} and 1565-1525 cm^{-1} regions, which correspond respectively to the central portion of amide A and to the amide II band of BSA, showed that the protein is found all over the MOF in BSA@ZIF. In addition, details of the imaging maps at higher magnification highlighted that the protein seems to concentrate in domains of 5-40 μm , which form an extended network across the MOF surface, while such domains are not observed in the pure BSA sample. Additional information on changes in the BSA structure upon immobilisation was extracted by the deconvolution of the amide I band in the reflectance spectra. Data showed that the crystalline content of BSA increases significantly when the protein is immobilised on the MOFs in BSA@ZIF-zni resulting in increased up to $\sim 25\%$ (β -sheets + α -helices), and a drastic reduction of β -turns. A marked red shift of amide I, indicating protein-MOF interactions, and protein structuration, was also observed on BSA@ZIF-8.

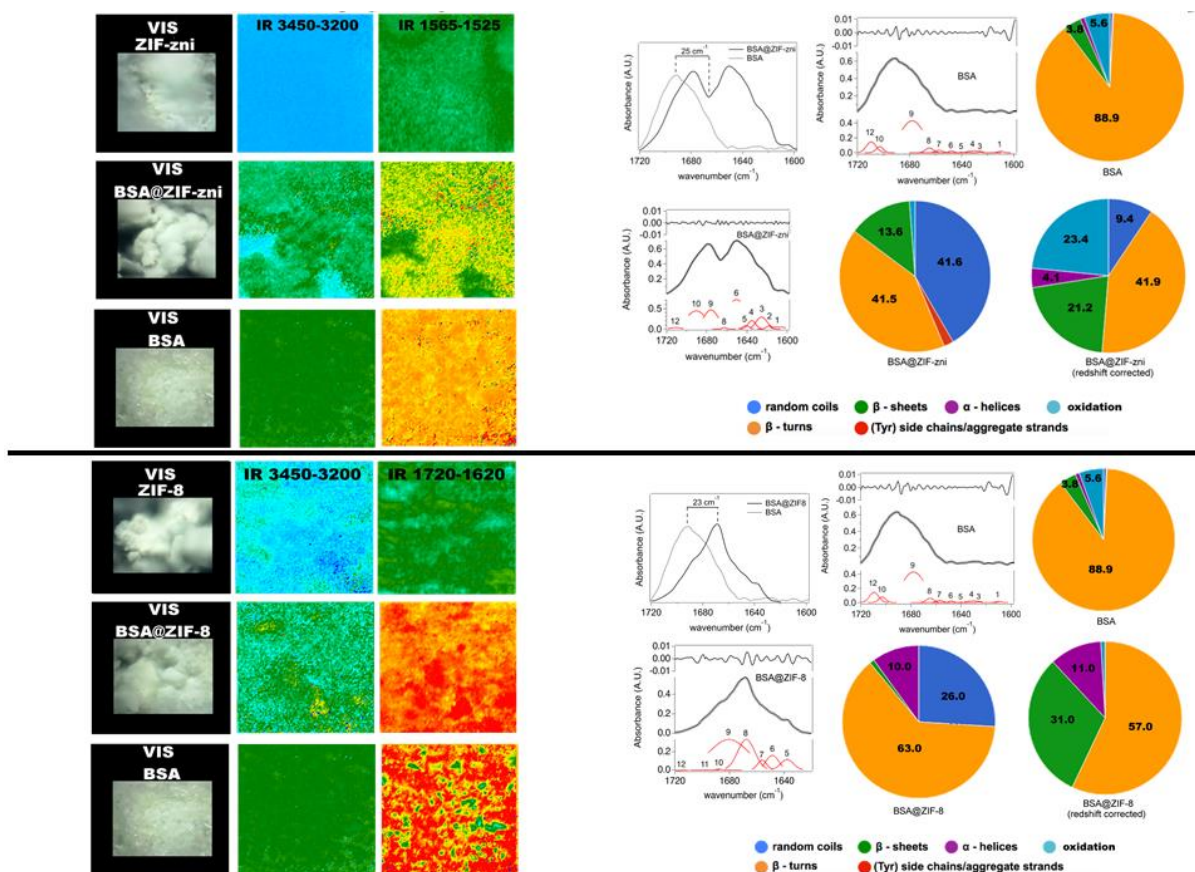


Figure 43 LOCATION MAPS. (Top and down panel, upper row) Visible (VIS) and FTIR 2D Imaging maps of the BSA@ZIF samples. DECONVOLUTION (Top and down right) FTIR Reflectance spectra of BSA and BSA@ZIF (after subtraction of a representative ZIF spectrum).

Work in progress

The final goal of the biocatalysts obtained during this Ph.D. would have been to test them against lignin polymer. Unfortunately, there has not been enough time. Therefore, I tested only the free laccase against lignin.

Aspergillus sp. and *Trametes versicolor* Laccases were used to oxidize lignin. Results showed an increase of band at 280 nm (at 25 °C) most likely due to the formation of new carbohydrates because of the LCs action. *Aspergillus sp.* seems to be better than *Trametes Versicolor*. The experiment was also carried out at 40 °C. Surprisingly the peak at 280 nm increased in absorbance

Cuvette: 150 uL alkali lignin, 10uL enzyme (tram 12mg/mL; asp 22.04 mg/mL), 2840 uL acetate buffere pH 5 0.1M

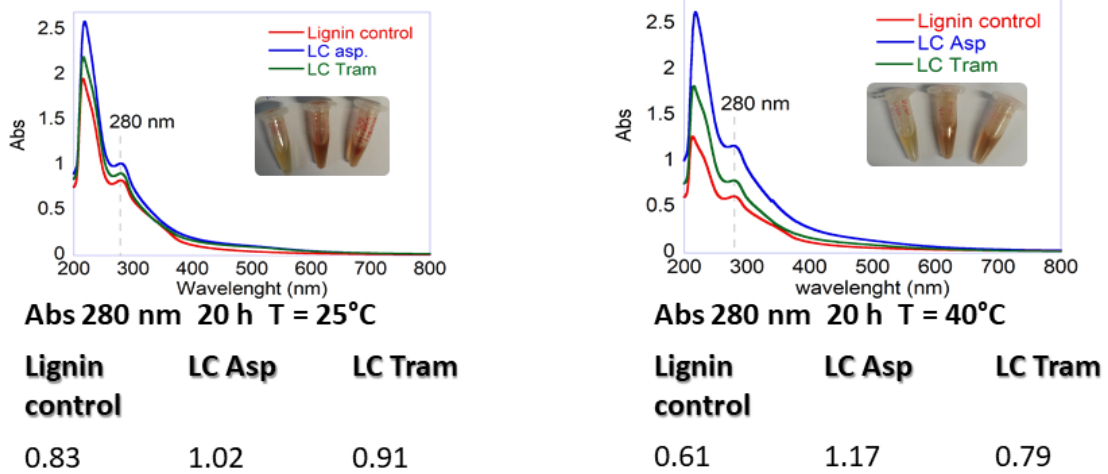


Figure 44: Alkali lignin degradation carried out by Laccase from *Trametes Versicolor* and *Aspergillus sp.*

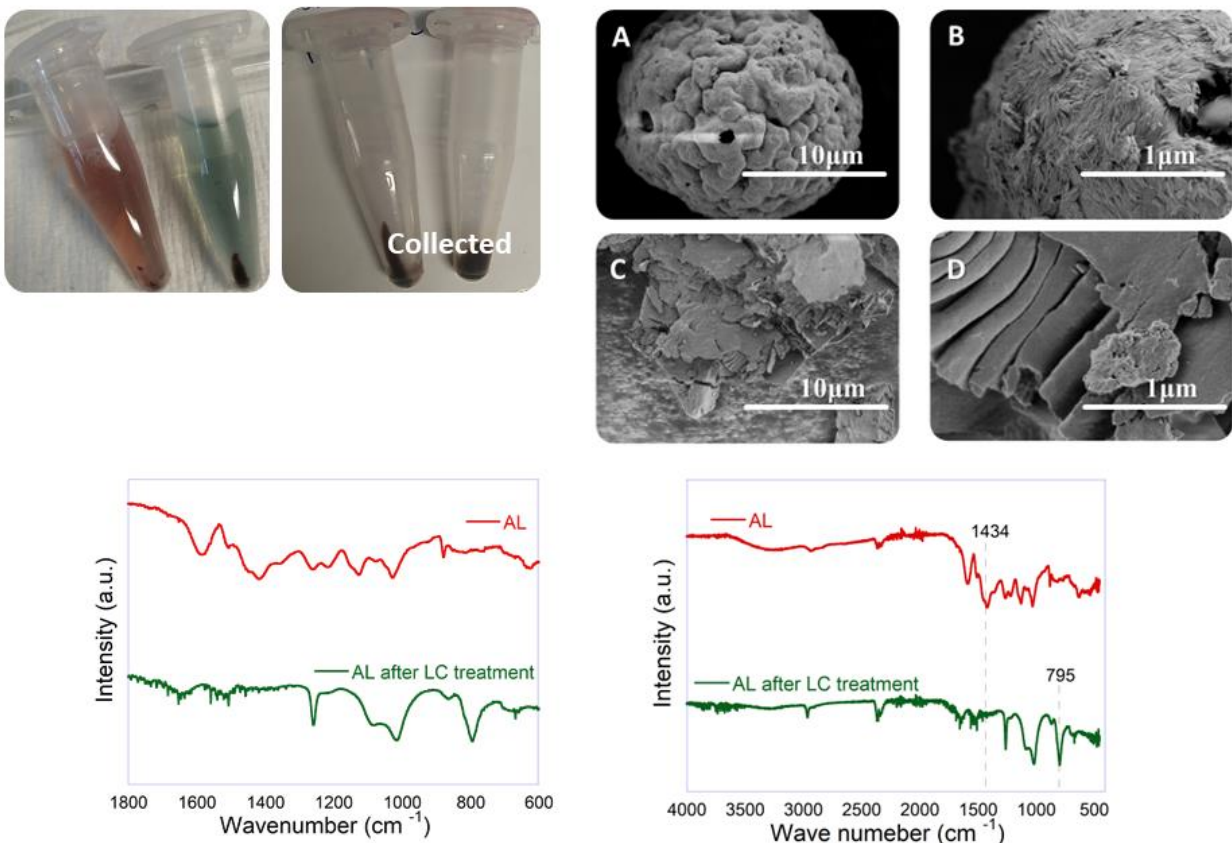


Figure 45: SEM images of Lignin A) B) pre and C) D) post LC treatment. FTIR spectra regarding of lignin pre and post treatment were reported at the bottom of the image

The lignin was collected by a centrifuge from the reaction mixture. The lignin powder was analysed by SEM and FT-IR pre- and post-reaction. SEM images showed a change in morphology due to the reaction acted by the enzyme. IR Spectra showed a new peak at 795 cm^{-1} whilst the peak at 1434 cm^{-1} disappeared after the reaction. These data are part of a preliminary study. Further investigation must be carried out.

CHAPTER 6:
CONCLUSIONS

This thesis was aimed to give an answer to three questions concerning enzyme immobilisation (see Chapter 3). The conclusions of this work can be summarised in the following points:

1. *Aspergillus sp.* Laccase immobilisation was successfully carried out within MOFs in situ under mild conditions, e.g. aqueous solution, neutral pH, and at room temperature. The immobilisation of the laccase on MFI-Type Zeolite crystals with embedded macropores was instead carried out post synthesis. The immobilised biocatalysts were fully characterised by mean of several techniques, e.g. XRD, SEM, FTIR and TGA for LC@MOF and also N₂ adsorption/desorption isotherms, solid-state MAS NMR spectroscopy for LC@ZMFI. LC@GdBTC showed higher catalytic activity (3.28 $\mu\text{mol} \cdot \text{mg}^{-1} \cdot \text{min}^{-1}$) compared with other materials. Whilst the LC@ZIF-zni showed the lower value of K_M and the better storage stability (it retains ~ 50 % of its initial activity up to 30 days) among MOFs materials. The LC@ZMFI showed the lower value of K_M compared with other materials. However, LC@ZMFI test activity were carried out under pH 3 and therefore not comparable with kinetics parameters obtained for LC@MOFs.

2. The location of the protein into the material was investigated through confocal laser scanning microscope (CLSM) and TGA coupled with SEM. The LC immobilised samples reveal a XRD patterns like the free enzyme materials demonstrating that laccase immobilisation did not affect their structure. Chemical composition was determined through thermogravimetric analysis (TGA). Thermogravigrams confirmed the enzymatic presence in the materials. This was confirmed by Bradford assay too. SEM and CLSM analysis were employed to evaluate the morphological properties of the material. SEM images of material pre and post calcination at 380 °C showed a noticeable change in morphology. This agrees with literature confirming the presence of enzyme inside the materials.¹²¹ Confocal microscope images of FITC-BSA@ZIF-zni and FITC-BSA@ZIF-8 samples show a homogeneous distribution of BSA molecules within the MOFs. All these results suggests that BSA

could be both encapsulated within ZIFs structure and on the external surface of the material. XRD (X-ray Diffraction) was used to analyse the crystalline phases of the materials.

- 3 Finally, the quantification of enzyme structure distortion due to its interaction with MOF support. whilst the spectroscopic characterisation of BSA, ZIF-zni, ZIF-8, BSA@ZIF-zni and BSA@ZIF-8 was performed by attenuated total reflection Fourier transform infrared (ATR-FTIR), micro-FTIR and confocal Raman spectroscopy. In particular, micro-FTIR 2D imaging using a Focal Plane Array (FPA) detector was used to investigate the secondary structure and conformation changes of free bovine serum albumin (BSA) due to its immobilisation. on both ZIF-zni (BSA@ZIF) and ZIF-8. Before interaction with the MOF, amide I deconvolution indicates that BSA has a strong content in β -turns (~89%), with limited contribution from β -sheets (~4%). Whilst the crystalline content of BSA increases significantly when the protein is immobilised on both ZIF-zni and ZIF-8 resulting in increased up to ~25% (β -sheets + α -helices), and ~40% (β -sheets + α -helices) respectively with a consequent drastic reduction of β -turns.

Bibliography

- (1) Laidler, K. J. A Glossary of Terms Used in Chemical Kinetics, Including Reaction Dynamics (IUPAC Recommendations 1996). *Pure Appl. Chem.* **1996**, *68* (1), 149–192.
<https://doi.org/10.1351/pac199668010149>.
- (2) SUMNER, J. B.; SOMERS, G. F. General Properties of Enzymes. In *Chemistry and Methods of Enzymes*; SUMNER, J. B., SOMERS, G. F., Eds.; Elsevier, 1953; pp 1–67.
<https://doi.org/10.1016/B978-1-4832-3150-1.50008-1>.
- (3) Ong, Y. C.; Gasser, G. Organometallic Compounds in Drug Discovery: Past, Present and Future. *Drug Discov. Today Technol.* **2020**, *37* (Ii), 117–124.
<https://doi.org/10.1016/j.ddtec.2019.06.001>.
- (4) Hanefeld, U.; Hollmann, F.; Paul, C. E. Biocatalysis Making Waves in Organic Chemistry. *Chem. Soc. Rev.* **2022**, *51* (2), 594–627. <https://doi.org/10.1039/D1CS00100K>.
- (5) Hughes, G.; Lewis, J. C. Introduction: Biocatalysis in Industry. *Chem. Rev.* **2018**, *118* (1), 1–3. <https://doi.org/10.1021/acs.chemrev.7b00741>.
- (6) Barnett, J. A.; Lichtenthaler, F. W. A History of Research on Yeasts 3: Emil Fischer, Eduard Buchner and Their Contemporaries, 1880-1900. *Yeast* **2001**, *18* (4), 363–388.
[https://doi.org/10.1002/1097-0061\(20010315\)18:4<363::AID-YEA677>3.0.CO;2-R](https://doi.org/10.1002/1097-0061(20010315)18:4<363::AID-YEA677>3.0.CO;2-R).
- (7) Rosenthaler, L. Durch Enzyme Bewirkte Asymmetrische Synthesen. 2. Mitteilung. *Biochem. Z.* **1909**, *17*, 257.
- (8) Alcántara, A. R.; Domínguez de María, P.; Littlechild, J. A.; Schürmann, M.; Sheldon, R. A.; Wohlgemuth, R. Biocatalysis as Key to Sustainable Industrial Chemistry. *ChemSusChem* **2022**, *202102709*. <https://doi.org/10.1002/cssc.202102709>.
- (9) Kirby, A. J. Enzyme Mechanisms, Models, and Mimics. *Angew. Chemie Int. Ed. English*

- 1996, 35 (7), 706–724. <https://doi.org/10.1002/anie.199607061>.
- (10) Hammes-Schiffer, S. Catalytic Efficiency of Enzymes: A Theoretical Analysis. *Biochemistry* **2013**, 52 (12), 2012–2020. <https://doi.org/10.1021/bi301515j>.
- (11) Bering, L.; Craven, E. J.; Sowerby Thomas, S. A.; Shepherd, S. A.; Micklefield, J. Merging Enzymes with Chemocatalysis for Amide Bond Synthesis. *Nat. Commun.* **2022**, 13 (1), 380. <https://doi.org/10.1038/s41467-022-28005-4>.
- (12) Sun, H.; Zhang, H.; Ang, E. L.; Zhao, H. Biocatalysis for the Synthesis of Pharmaceuticals and Pharmaceutical Intermediates. *Bioorg. Med. Chem.* **2018**, 26 (7), 1275–1284. <https://doi.org/10.1016/j.bmc.2017.06.043>.
- (13) Basso, A.; Serban, S. Industrial Applications of Immobilized Enzymes—A Review. *Mol. Catal.* **2019**, 479 (March), 110607. <https://doi.org/10.1016/j.mcat.2019.110607>.
- (14) Anastas, P.; Eghbali, N. Green Chemistry: Principles and Practice. *Chem. Soc. Rev.* **2010**, 39 (1), 301–312. <https://doi.org/10.1039/B918763B>.
- (15) Li, C.; Anastas, P. T. Green Chemistry Themed Issue Green Chemistry : Present and Future W. **2012**, No. 4. <https://doi.org/10.1039/and>.
- (16) Sheldon, R. A. Metrics of Green Chemistry and Sustainability: Past, Present, and Future. *ACS Sustain. Chem. Eng.* **2018**, 6 (1), 32–48. <https://doi.org/10.1021/acssuschemeng.7b03505>.
- (17) Tocco, D.; Carucci, C.; Monduzzi, M.; Salis, A.; Sanjust, E. Recent Developments in the Delignification and Exploitation of Grass Lignocellulosic Biomass. *ACS Sustain. Chem. Eng.* **2021**, 9 (6), 2412–2432. <https://doi.org/10.1021/acssuschemeng.0c07266>.
- (18) Sheldon, R. A.; van Pelt, S. Enzyme Immobilisation in Biocatalysis: Why, What and How. *Chem. Soc. Rev.* **2013**, 42 (15), 6223–6235. <https://doi.org/10.1039/c3cs60075k>.
- (19) Wang, Y.; Cao, Y.; Li, Y.; Jin, J.; Li, J.; Song, H. Asymmetric Biosynthesis of Intermediates of Anti-HIV Drugs. *Tetrahedron: Asymmetry* **2017**, 28 (6), 745–757. <https://doi.org/10.1016/j.tetasy.2017.04.008>.

- (20) Zhang, G. Q.; Chen, Q. J.; Wang, H. X.; Ng, T. B. A Laccase with Inhibitory Activity against HIV-1 Reverse Transcriptase from the Mycorrhizal Fungus *Lepiota Ventriospora*. *J. Mol. Catal. B Enzym.* **2013**, *85–86*, 31–36. <https://doi.org/10.1016/j.molcatb.2012.08.001>.
- (21) Slagman, S.; Fessner, W.-D. Biocatalytic Routes to Anti-Viral Agents and Their Synthetic Intermediates. *Chem. Soc. Rev.* **2021**, *50* (3), 1968–2009. <https://doi.org/10.1039/D0CS00763C>.
- (22) Robinson, P. K. Enzymes: Principles and Biotechnological Applications. *Essays Biochem.* **2015**, *59*, 1–41. <https://doi.org/10.1042/bse0590001>.
- (23) Li, G.; Wang, J.; Reetz, M. T. Biocatalysts for the Pharmaceutical Industry Created by Structure-Guided Directed Evolution of Stereoselective Enzymes. *Bioorg. Med. Chem.* **2018**, *26* (7), 1241–1251. <https://doi.org/https://doi.org/10.1016/j.bmc.2017.05.021>.
- (24) Salis, A.; Pinna, M.; Monduzzi, M.; Solinas, V. Biodiesel Production from Triolein and Short Chain Alcohols through Biocatalysis. *J. Biotechnol.* **2005**, *119* (3), 291–299. <https://doi.org/10.1016/j.jbiotec.2005.04.009>.
- (25) de Souza Vandenberghe, L. P.; Karp, S. G.; Pagnoncelli, M. G. B.; Rodrigues, C.; Medeiros, A. B. P.; Soccol, C. R. Digestive Enzymes: Industrial Applications in Food Products. In *Green Bio-processes: Enzymes in Industrial Food Processing*; Parameswaran, B., Varjani, S., Raveendran, S., Eds.; Springer Singapore: Singapore, 2019; pp 267–291. https://doi.org/10.1007/978-981-13-3263-0_14.
- (26) Woodley, J. M. New Frontiers in Biocatalysis for Sustainable Synthesis. *Curr. Opin. Green Sustain. Chem.* **2020**, *21*, 22–26. <https://doi.org/10.1016/j.cogsc.2019.08.006>.
- (27) Sutay Kocabaş, D.; Grumet, R. Evolving Regulatory Policies Regarding Food Enzymes Produced by Recombinant Microorganisms. *GM Crops Food* **2019**, *10* (4), 191–207. <https://doi.org/10.1080/21645698.2019.1649531>.
- (28) Pellis, A.; Cantone, S.; Ebert, C.; Gardossi, L. Evolving Biocatalysis to Meet Bioeconomy

Challenges and Opportunities. *N. Biotechnol.* **2018**, *40*, 154–169.

<https://doi.org/10.1016/j.nbt.2017.07.005>.

- (29) McDonald, A. G.; Tipton, K. F. Fifty-Five Years of Enzyme Classification: Advances and Difficulties. *FEBS J.* **2014**, *281* (2), 583–592. <https://doi.org/10.1111/febs.12530>.
- (30) McDonald, A. G.; Tipton, K. F. Enzyme Nomenclature and Classification: The State of the Art. *FEBS J.* **2022**. <https://doi.org/10.1111/febs.16274>.
- (31) Riva, S. Laccases: Blue Enzymes for Green Chemistry. *Trends Biotechnol.* **2006**, *24* (5), 219–226. <https://doi.org/10.1016/j.tibtech.2006.03.006>.
- (32) Viswanath, B.; Rajesh, B.; Janardhan, A.; Kumar, A. P.; Narasimha, G. Fungal Laccases and Their Applications in Bioremediation. *Enzyme Res.* **2014**, *2014*, 1–21. <https://doi.org/10.1155/2014/163242>.
- (33) YOSHIDA; H. Chemistry of Laquer (Urushi). *J. Chem. Soc.* **1883**, *43*, 472–486.
- (34) Wong, D. W. S. Structure and Action Mechanism of Ligninolytic Enzymes. *Appl. Biochem. Biotechnol.* **2009**, *157* (2), 174–209. <https://doi.org/10.1007/s12010-008-8279-z>.
- (35) Baldrian, P. Fungal Laccases-Occurrence and Properties. *FEMS Microbiol. Rev.* **2006**, *30* (2), 215–242. <https://doi.org/10.1111/j.1574-4976.2005.00010.x>.
- (36) Piontek, K.; Antorini, M.; Choinowski, T. Crystal Structure of a Laccase from the Fungus *Trametes Versicolor* at 1.90-Å Resolution Containing a Full Complement of Coppers. *J. Biol. Chem.* **2002**, *277* (40), 37663–37669. <https://doi.org/10.1074/jbc.M204571200>.
- (37) Wong, D. W. S. Structure and Action Mechanism of Ligninolytic Enzymes. *Appl. Biochem. Biotechnol.* **2009**, *157* (2), 174.
- (38) Agrawal, K.; Chaturvedi, V.; Verma, P. Fungal Laccase Discovered but yet Undiscovered. *Bioresour. Bioprocess.* **2018**, *5* (1). <https://doi.org/10.1186/s40643-018-0190-z>.
- (39) Pardo, I.; Camarero, S. Laccase Engineering by Rational and Evolutionary Design. **2015**, 897–910. <https://doi.org/10.1007/s00018-014-1824-8>.

- (40) Mukhopadhyay, M.; Banerjee, R. Purification and Biochemical Characterization of a Newly Produced Yellow Laccase from *Lentinus Squarrosulus* MR13. *3 Biotech* **2015**, *5* (3), 227–236. <https://doi.org/10.1007/s13205-014-0219-8>.
- (41) Mate, D. M.; Alcalde, M. Laccase: A Multi-purpose Biocatalyst at the Forefront of Biotechnology. *Microb. Biotechnol.* **2017**, *10* (6), 1457–1467. <https://doi.org/10.1111/1751-7915.12422>.
- (42) Mehra, R.; Muschiol, J.; Meyer, A. S.; Kepp, K. P. A Structural-Chemical Explanation of Fungal Laccase Activity. *Sci. Rep.* **2018**, *8* (1), 1–16. <https://doi.org/10.1038/s41598-018-35633-8>.
- (43) Hoffert, M. I.; Caldeira, K.; Benford, G.; Criswell, D. R.; Green, C.; Herzog, H.; Jain, A. K.; Kheshgi, H. S.; Lackner, K. S.; Lewis, J. S.; Lightfoot, H. D.; Manheimer, W.; Mankins, J. C.; Mauel, M. E.; Perkins, L. J.; Schlesinger, M. E.; Volk, T.; Wigley, T. M. L. Advanced Technology Paths to Global Climate Stability: Energy for a Greenhouse Planet. *Science* (80-). **2002**, *298* (5595), 981–987. <https://doi.org/10.1126/science.1072357>.
- (44) Deng, Z.; Xia, A.; Liao, Q.; Zhu, X.; Huang, Y.; Fu, Q. Laccase Pretreatment of Wheat Straw: Effects of the Physicochemical Characteristics and the Kinetics of Enzymatic Hydrolysis. *Biotechnol. Biofuels* **2019**, *12* (1), 1–12. <https://doi.org/10.1186/s13068-019-1499-3>.
- (45) Bilal, M.; Asgher, M.; Iqbal, H. M. N.; Hu, H.; Zhang, X. Delignification and Fruit Juice Clarification Properties of Alginate-Chitosan-Immobilized Ligninolytic Cocktail. *LWT - Food Sci. Technol.* **2017**, *80*, 348–354. <https://doi.org/10.1016/j.lwt.2017.02.040>.
- (46) Gutiérrez, A.; Rencoret, J.; Cadena, E. M.; Rico, A.; Barth, D.; del Río, J. C.; Martínez, Á. T. Demonstration of Laccase-Based Removal of Lignin from Wood and Non-Wood Plant Feedstocks. *Bioresour. Technol.* **2012**, *119*, 114.
- (47) Ponnusamy, V. K.; Nguyen, D. D.; Dharmaraja, J.; Shobana, S.; Banu, J. R.; Saratale, R. G.;

- Chang, S. W.; Kumar, G. A Review on Lignin Structure, Pretreatments, Fermentation Reactions and Biorefinery Potential. *Bioresour. Technol.* **2019**, *271* (August 2018), 462–472. <https://doi.org/10.1016/j.biortech.2018.09.070>.
- (48) Mayolo-Deloya, K.; González-González, M.; Rito-Palomares, M. Laccases in Food Industry: Bioprocessing, Potential Industrial and Biotechnological Applications. *Front. Bioeng. Biotechnol.* **2020**, *8*. <https://doi.org/10.3389/fbioe.2020.00222>.
- (49) Zrinski, I.; Pungjunun, K.; Martinez, S.; Zavašnik, J.; Stanković, D.; Kalcher, K.; Mehmeti, E. Evaluation of Phenolic Antioxidant Capacity in Beverages Based on Laccase Immobilized on Screen-Printed Carbon Electrode Modified with Graphene Nanoplatelets and Gold Nanoparticles. *Microchem. J.* **2020**, *152* (September 2019), 104282. <https://doi.org/10.1016/j.microc.2019.104282>.
- (50) Lima, N. S. M.; Gomes-Pepe, E. S.; Campanharo, J. C.; de Macedo Lemos, E. G. Broad Thermal Spectrum Metagenomic Laccase with Action for Dye Decolorization and Fentin Hydroxide Treatment. *AMB Express* **2022**, *12* (1). <https://doi.org/10.1186/s13568-022-01375-0>.
- (51) Motamedi, E.; Kavousi, K.; Sadeghian Motahar, S. F.; Reza Ghaffari, M.; Sheykh Abdollahzadeh Mamaghani, A.; Hosseini Salekdeh, G.; Ariaeenejad, S. Efficient Removal of Various Textile Dyes from Wastewater by Novel Thermo-Halotolerant Laccase. *Bioresour. Technol.* **2021**, *337* (May), 125468. <https://doi.org/10.1016/j.biortech.2021.125468>.
- (52) Cannatelli, M. D.; Ragauskas, A. J. Laccase-Catalyzed Synthesis of 2,3-Ethylenedithio-1,4-Quinones. *J. Mol. Catal. B Enzym.* **2015**, *119*, 85–89. <https://doi.org/10.1016/j.molcatb.2015.05.016>.
- (53) González-Granda, S.; Méndez-Sánchez, D.; Lavandera, I.; Gotor-Fernández, V. Laccase-Mediated Oxidations of Propargylic Alcohols. Application in the Deracemization of 1-Arylprop-2-Yn-1-Ols in Combination with Alcohol Dehydrogenases. *ChemCatChem* **2020**,

- 12 (2), 520–527. <https://doi.org/10.1002/cctc.201901543>.
- (54) Scopes, R. K. Enzyme Activity and Assays. In *eLS*; Wiley, 2002; pp 1–6.
<https://doi.org/10.1038/npg.els.0000712>.
- (55) Bisswanger, H. Enzyme Assays. *Perspect. Sci.* **2014**, *1* (1–6), 41–55.
<https://doi.org/10.1016/j.pisc.2014.02.005>.
- (56) Salis, A.; Monduzzi, M.; Solinas, V. Use of Lipases for the Production of Biodiesel. In *Industrial Enzymes*; Springer Netherlands: Dordrecht, 2007; pp 317–339.
https://doi.org/10.1007/1-4020-5377-0_19.
- (57) Zumárraga, M.; Bulter, T.; Shleev, S.; Polaina, J.; Martínez-Arias, A.; Plou, F. J.; Ballesteros, A.; Alcalde, M. In Vitro Evolution of a Fungal Laccase in High Concentrations of Organic Cosolvents. *Chem. Biol.* **2007**, *14* (9), 1052–1064.
<https://doi.org/10.1016/j.chembiol.2007.08.010>.
- (58) Wu, M. H.; Lin, M. C.; Lee, C. C.; Yu, S. M.; Wang, A. H. J.; Ho, T. H. D. Enhancement of Laccase Activity by Pre-Incubation with Organic Solvents. *Sci. Rep.* **2019**, *9* (1), 1–11.
<https://doi.org/10.1038/s41598-019-45118-x>.
- (59) Toledo, M. L.; Pereira, M. M.; Freire, M. G.; Silva, J. P. A.; Coutinho, J. A. P.; Tavares, A. P. M. Laccase Activation in Deep Eutectic Solvents. *ACS Sustain. Chem. Eng.* **2019**, *7* (13), 11806–11814. <https://doi.org/10.1021/acssuschemeng.9b02179>.
- (60) Altundağ, A.; Ünlü, A. E.; Takaç, S. Deep Eutectic Solvent-assisted Synthesis of Polyaniline by Laccase Enzyme. *J. Chem. Technol. Biotechnol.* **2021**, *96* (4), 1107–1115.
<https://doi.org/10.1002/jctb.6626>.
- (61) Delorme, A. E.; Andanson, J. M.; Verney, V. Improving Laccase Thermostability with Aqueous Natural Deep Eutectic Solvents. *Int. J. Biol. Macromol.* **2020**, *163*, 919–926.
<https://doi.org/10.1016/j.ijbiomac.2020.07.022>.
- (62) Fernandes, P.; Carvalho, F. Enzymes in Food Processing. In *Agro-Industrial Wastes as*

- Feedstock for Enzyme Production*; Dhillon, G. S., Kaur, S. B. T.-A.-I. W. as F. for E. P., Eds.; Elsevier: San Diego, 2016; pp 173–199. <https://doi.org/10.1016/B978-0-12-802392-1.00008-3>.
- (63) Nelson, J. M.; Griffin, E. G. ADSORPTION OF INVERTASE. *J. Am. Chem. Soc.* **1916**, *38* (5), 1109–1115. <https://doi.org/10.1021/ja02262a018>.
- (64) Sato, T.; Tosa, T. <sc>L</Sc> -Amino Acids Production by Aminoacylase. In *Encyclopedia of Industrial Biotechnology*; John Wiley & Sons, Inc.: Hoboken, NJ, USA, 2010; pp 3–6. <https://doi.org/10.1002/9780470054581.eib497>.
- (65) Boudrant, J.; Woodley, J. M.; Fernandez-Lafuente, R. Parameters Necessary to Define an Immobilized Enzyme Preparation. *Process Biochem.* **2020**, *90* (November 2019), 66–80. <https://doi.org/10.1016/j.procbio.2019.11.026>.
- (66) Kadam, A. A.; Saratale, G. D.; Ghodake, G. S.; Saratale, R. G.; Shahzad, A.; Magotra, V. K.; Kumar, M.; Palem, R. R.; Sung, J. S. Recent Advances in the Development of Laccase-Based Biosensors via Nano-Immobilization Techniques. *Chemosensors* **2022**, *10* (2), 1–27. <https://doi.org/10.3390/chemosensors10020058>.
- (67) Sneha, H. P.; Beulah, K. C.; Murthy, P. S. Enzyme Immobilization Methods and Applications in the Food Industry. In *Enzymes in Food Biotechnology*; Elsevier, 2019; pp 645–658. <https://doi.org/10.1016/B978-0-12-813280-7.00037-2>.
- (68) Da Silva, A. C. S. L.; Valetti, N. W.; Brassesco, M. E.; Teixeira, J. A.; Picó, G. Adsorption of Peroxidase from *Raphanus Sativus* L onto Alginate-Guar Gum Matrix: Kinetic, Equilibrium and Thermodynamic Analysis. *Adsorpt. Sci. Technol.* **2016**, *34* (6), 388–402. <https://doi.org/10.1177/0263617416659287>.
- (69) Thangaraj, B.; Solomon, P. R. Immobilization of Lipases – A Review. Part I: Enzyme Immobilization. *ChemBioEng Rev.* **2019**, *6* (5), 157–166. <https://doi.org/10.1002/cben.201900016>.

- (70) Hartmann, M.; Kostrov, X. Immobilization of Enzymes on Porous Silicas – Benefits and Challenges. *Chem. Soc. Rev.* **2013**, *42* (15), 6277. <https://doi.org/10.1039/c3cs60021a>.
- (71) Cuatrecasas, P. Biochemical Tools: Immobilized Enzymes . Oskar Zaborsky. CRC Press (Chemical Rubber Co.), Cleveland, Ohio, 1973. Xiv, 176 Pp., Illus. \$26.50. *Science* (80-.). **1974**, *184* (4132), 56–56. <https://doi.org/10.1126/science.184.4132.56.a>.
- (72) St. Clair, N. L.; Navia, M. A. Cross-Linked Enzyme Crystals as Robust Biocatalysts. *J. Am. Chem. Soc.* **1992**, *114* (18), 7314–7316. <https://doi.org/10.1021/ja00044a064>.
- (73) Yamaguchi, H.; Kiyota, Y.; Miyazaki, M. Techniques for Preparation of Cross-Linked Enzyme Aggregates and Their Applications in Bioconversions. *Catalysts* **2018**, *8* (5), 174. <https://doi.org/10.3390/catal8050174>.
- (74) Hagen, J. Industrial Catalysis: A Practical Approach. *Ind. Catal. A Pract. approach* **2015**, 1–16.
- (75) Fernandes, P.; de Carvalho, C. C. C. R. Multi-Enzyme Systems in Flow Chemistry. *Processes* **2021**, *9* (2), 225. <https://doi.org/10.3390/pr9020225>.
- (76) Sheldon, R. A. Cleas, Combi-Cleas and ‘Smart’ Magnetic Cleas: Biocatalysis in a Bio-Based Economy. *Catalysts* **2019**, *9* (3), 1–31. <https://doi.org/10.3390/catal9030261>.
- (77) Patil, P. D.; Yadav, G. D. Rapid In Situ Encapsulation of Laccase into Metal-Organic Framework Support (ZIF-8) under Biocompatible Conditions. *ChemistrySelect* **2018**, *3* (17), 4669–4675. <https://doi.org/10.1002/slct.201702852>.
- (78) Imam, H. T.; Marr, P. C.; Marr, A. C. Enzyme Entrapment, Biocatalyst Immobilization without Covalent Attachment. *Green Chem.* **2021**, *23* (14), 4980–5005. <https://doi.org/10.1039/d1gc01852c>.
- (79) showed how the CLEA(s) can be used as stable and recyclable biocatalysts. By precipitating with salt (i.e. ammonium sulphate) and an organic linker (i.e. glutaraldehyde) the enzyme molecule condensate and they can be aggregated together creating the CLEAs, U.; Gardossi,

- L.; Magner, E. Understanding Enzyme Immobilisation. *Chem. Soc. Rev.* **2009**, *38* (2), 453–468. <https://doi.org/10.1039/B711564B>.
- (80) Magner, E. Immobilisation of Enzymes on Mesoporous Silicate Materials. *Chem. Soc. Rev.* **2013**, *42* (15), 6213. <https://doi.org/10.1039/c2cs35450k>.
- (81) Valdeperas, M.; Salis, A.; Barauskas, J.; Tiberg, F.; Arnebrant, T.; Razumas, V.; Monduzzi, M.; Nylander, T. Enzyme Encapsulation in Nanostructured Self-Assembled Structures: Toward Biofunctional Supramolecular Assemblies. *Curr. Opin. Colloid Interface Sci.* **2019**, *44*, 130–142. <https://doi.org/10.1016/j.cocis.2019.09.007>.
- (82) Sirisha, V. L.; Jain, A.; Jain, A. Enzyme Immobilization: An Overview on Methods, Support Material, and Applications of Immobilized Enzymes. *Adv. Food Nutr. Res.* **2016**, *79*, 179–211. <https://doi.org/10.1016/bs.afnr.2016.07.004>.
- (83) Zdarta, J.; Meyer, A. S.; Jesionowski, T.; Pinelo, M. A General Overview of Support Materials for Enzyme Immobilization: Characteristics, Properties, Practical Utility. *Catalysts* **2018**, *8* (2). <https://doi.org/10.3390/catal8020092>.
- (84) Thommes, M.; Kaneko, K.; Neimark, A. V.; Olivier, J. P.; Rodriguez-Reinoso, F.; Rouquerol, J.; Sing, K. S. W. Physisorption of Gases, with Special Reference to the Evaluation of Surface Area and Pore Size Distribution (IUPAC Technical Report). *Pure Appl. Chem.* **2015**, *87* (9–10), 1051–1069. <https://doi.org/10.1515/pac-2014-1117>.
- (85) Beck, J. S.; Vartuli, J. C.; Roth, W. J.; Leonowicz, M. E.; Kresge, C. T.; Schmitt, K. D.; Chu, C. T. W.; Olson, D. H.; Sheppard, E. W.; McCullen, S. B.; Higgins, J. B.; Schlenker, J. L. A New Family of Mesoporous Molecular Sieves Prepared with Liquid Crystal Templates. *J. Am. Chem. Soc.* **1992**, *114* (27), 10834–10843. <https://doi.org/10.1021/ja00053a020>.
- (86) Zhao, D.; Huo, Q.; Feng, J.; Chmelka, B. F.; Stucky, G. D. Nonionic Triblock and Star Diblock Copolymer and Oligomeric Surfactant Syntheses of Highly Ordered, Hydrothermally Stable, Mesoporous Silica Structures. *J. Am. Chem. Soc.* **1998**, *120* (24), 6024–6036.

<https://doi.org/10.1021/ja974025i>.

- (87) Kresge, C. T.; Leonowicz, M. E.; Roth, W. J.; Vartuli, J. C.; Beck, J. S. Ordered Mesoporous Molecular Sieves Synthesized by a Liquid-Crystal Template Mechanism. *Nature* **1992**, *359* (6397), 710–712. <https://doi.org/10.1038/359710a0>.
- (88) Vercaemst, C. Isomeric Olefinic Periodic Mesoporous Organosilicas : An Emerging Class of Versatile Nanomaterials. **2009**, 1–278.
- (89) Salis, A.; Fanti, M.; Medda, L.; Nairi, V.; Cugia, F.; Piludu, M.; Sogos, V.; Monduzzi, M. Mesoporous Silica Nanoparticles Functionalized with Hyaluronic Acid and Chitosan Biopolymers. Effect of Functionalization on Cell Internalization. *ACS Biomater. Sci. Eng.* **2016**, *2* (5), 741–751. <https://doi.org/10.1021/acsbiomaterials.5b00502>.
- (90) Díaz, J. F.; Balkus, K. J. Enzyme Immobilization in MCM-41 Molecular Sieve. *J. Mol. Catal. B Enzym.* **1996**, *2* (2–3), 115–126. [https://doi.org/10.1016/S1381-1177\(96\)00017-3](https://doi.org/10.1016/S1381-1177(96)00017-3).
- (91) Batten, S. R.; Champness, N. R.; Chen, X.-M.; Garcia-Martinez, J.; Kitagawa, S.; Öhrström, L.; O’Keeffe, M.; Paik Suh, M.; Reedijk, J. Terminology of Metal–Organic Frameworks and Coordination Polymers (IUPAC Recommendations 2013). *Pure Appl. Chem.* **2013**, *85* (8), 1715–1724. <https://doi.org/10.1351/PAC-REC-12-11-20>.
- (92) Yaghi, O. M.; Li, H. Hydrothermal Synthesis of a Metal-Organic Framework Containing Large Rectangular Channels. *J. Am. Chem. Soc.* **1995**, *117* (41), 10401–10402. <https://doi.org/10.1021/ja00146a033>.
- (93) Hoskins, B. F.; Robson, R. Infinite Polymeric Frameworks Consisting of Three Dimensionally Linked Rod-like Segments. *J. Am. Chem. Soc.* **1989**, *111* (15), 5962–5964. <https://doi.org/10.1021/ja00197a079>.
- (94) Millward, A. R.; Yaghi, O. M. Metal–Organic Frameworks with Exceptionally High Capacity for Storage of Carbon Dioxide at Room Temperature. *J. Am. Chem. Soc.* **2005**, *127* (51), 17998–17999. <https://doi.org/10.1021/ja0570032>.

- (95) Yang, Y.; Arqué, X.; Patiño, T.; Guillerm, V.; Blersch, P.-R.; Pérez-Carvajal, J.; Imaz, I.; Maspoch, D.; Sánchez, S. Enzyme-Powered Porous Micromotors Built from a Hierarchical Micro- and Mesoporous UiO-Type Metal–Organic Framework. *J. Am. Chem. Soc.* **2020**, *142* (50), 20962–20967. <https://doi.org/10.1021/jacs.0c11061>.
- (96) Sanchez-Sanchez, M.; de Asua, I.; Ruano, D.; Diaz, K. Direct Synthesis, Structural Features, and Enhanced Catalytic Activity of the Basolite F300-like Semiamorphous Fe-BTC Framework. *Cryst. Growth Des.* **2015**, *15* (9), 4498–4506. <https://doi.org/10.1021/acs.cgd.5b00755>.
- (97) Furukawa, H.; Ko, N.; Go, Y. B.; Aratani, N.; Choi, S. B.; Choi, E.; Yazaydin, A. Ö.; Snurr, R. Q.; O’Keeffe, M.; Kim, J.; Yaghi, O. M. Ultrahigh Porosity in Metal-Organic Frameworks. *Science* (80-.). **2010**, *329* (5990), 424–428. <https://doi.org/10.1126/science.1192160>.
- (98) Delpiano, G. R.; Tocco, D.; Medda, L.; Magner, E.; Salis, A. Adsorption of Malachite Green and Alizarin Red S Dyes Using Fe-BTC Metal Organic Framework as Adsorbent. *Int. J. Mol. Sci.* **2021**, *22* (2), 788. <https://doi.org/10.3390/ijms22020788>.
- (99) Autie-Castro, G.; Autie, M. A.; Rodríguez-Castellón, E.; Aguirre, C.; Reguera, E. Cu-BTC and Fe-BTC Metal-Organic Frameworks: Role of the Materials Structural Features on Their Performance for Volatile Hydrocarbons Separation. *Colloids Surfaces A Physicochem. Eng. Asp.* **2015**, *481*, 351–357. <https://doi.org/10.1016/j.colsurfa.2015.05.044>.
- (100) Hemmer, K.; Cokoja, M.; Fischer, R. A. Exploitation of Intrinsic Confinement Effects of MOFs in Catalysis. *ChemCatChem* **2021**, *13* (7), 1683–1691. <https://doi.org/10.1002/cctc.202001606>.
- (101) Wu, M.-X.; Yang, Y.-W. Metal-Organic Framework (MOF)-Based Drug/Cargo Delivery and Cancer Therapy. *Adv. Mater.* **2017**, *29* (23), 1606134. <https://doi.org/10.1002/adma.201606134>.
- (102) Tocco, D.; Carucci, C.; Todde, D.; Shortall, K.; Otero, F.; Sanjust, E.; Magner, E.; Salis, A.

- Enzyme Immobilization on Metal Organic Frameworks: Laccase from *Aspergillus* Sp. Is Better Adapted to ZIF-Zni Rather than Fe-BTC. *Colloids Surfaces B Biointerfaces* **2021**, *208* (September), 112147. <https://doi.org/10.1016/j.colsurfb.2021.112147>.
- (103) Gascón, V.; Jiménez, M. B.; Blanco, R. M.; Sanchez-Sanchez, M. Semi-Crystalline Fe-BTC MOF Material as an Efficient Support for Enzyme Immobilization. *Catal. Today* **2018**, *304* (October 2017), 119–126. <https://doi.org/10.1016/j.cattod.2017.10.022>.
- (104) Gascón, V.; Carucci, C.; Jiménez, M. B.; Blanco, R. M.; Sánchez-Sánchez, M.; Magner, E. Rapid In Situ Immobilization of Enzymes in Metal-Organic Framework Supports under Mild Conditions. *ChemCatChem* **2017**, *9* (7), 1182–1186. <https://doi.org/10.1002/cctc.201601342>.
- (105) Hu, Y.; Zhou, H.; Dai, L.; Liu, D.; Al-Zuhair, S.; Du, W. Lipase Immobilization on Macroporous ZIF-8 for Enhanced Enzymatic Biodiesel Production. *ACS Omega* **2021**, *6* (3), 2143–2148. <https://doi.org/10.1021/acsomega.0c05225>.
- (106) Sun, Y.; Shi, J.; Zhang, S.; Wu, Y.; Mei, S.; Qian, W.; Jiang, Z. Hierarchically Porous and Water-Tolerant Metal-Organic Frameworks for Enzyme Encapsulation. *Ind. Eng. Chem. Res.* **2019**, *58* (28), 12835–12844. <https://doi.org/10.1021/acs.iecr.9b02164>.
- (107) Lee, Y.-R.; Kim, J.; Ahn, W.-S. Synthesis of Metal-Organic Frameworks: A Mini Review. *Korean J. Chem. Eng.* **2013**, *30* (9), 1667–1680. <https://doi.org/10.1007/s11814-013-0140-6>.
- (108) Tranchemontagne, D. J.; Hunt, J. R.; Yaghi, O. M. Room Temperature Synthesis of Metal-Organic Frameworks: MOF-5, MOF-74, MOF-177, MOF-199, and IRMOF-0. *Tetrahedron* **2008**, *64* (36), 8553–8557. <https://doi.org/10.1016/j.tet.2008.06.036>.
- (109) Shi, X.; Zhu, G.; Qiu, S.; Huang, K.; Yu, J.; Xu, R. Zn₂[(S)-O₃PCH₂NHC₄H₇CO₂]₂: A Homochiral 3D Zinc Phosphonate with Helical Channels. *Angew. Chemie Int. Ed.* **2004**, *43* (47), 6482–6485. <https://doi.org/10.1002/anie.200460724>.
- (110) Xia, Q.; Wang, H.; Huang, B.; Yuan, X.; Zhang, J.; Zhang, J.; Jiang, L.; Xiong, T.; Zeng, G. State-of-the-Art Advances and Challenges of Iron-Based Metal Organic Frameworks from

Attractive Features, Synthesis to Multifunctional Applications. *Small* **2019**, *15* (2), 1–25.

<https://doi.org/10.1002/sml.201803088>.

- (111) Nadar, S. S.; Vaidya, L.; Rathod, V. K. International Journal of Biological Macromolecules Enzyme Embedded Metal Organic Framework (Enzyme – MOF): De Novo Approaches for Immobilization. *Int. J. Biol. Macromol.* **2020**, *149*, 861–876.
<https://doi.org/10.1016/j.ijbiomac.2020.01.240>.
- (112) Lyu, F.; Zhang, Y.; Zare, R. N.; Ge, J.; Liu, Z. One-Pot Synthesis of Protein-Embedded Metal–Organic Frameworks with Enhanced Biological Activities. *Nano Lett.* **2014**, *14* (10), 5761–5765. <https://doi.org/10.1021/nl5026419>.
- (113) Drout, R. J.; Robison, L.; Farha, O. K. Catalytic Applications of Enzymes Encapsulated in Metal – Organic Frameworks. *Coord. Chem. Rev.* **2019**, *381*, 151–160.
<https://doi.org/10.1016/j.ccr.2018.11.009>.
- (114) Nadar, S. S.; Rathod, V. K. Encapsulation of Lipase within Metal-Organic Framework (MOF) with Enhanced Activity Intensified under Ultrasound. *Enzyme Microb. Technol.* **2018**, *108* (August 2017), 11–20. <https://doi.org/10.1016/j.enzmictec.2017.08.008>.
- (115) Molina, M. A.; Díez-Jaén, J.; Sánchez-Sánchez, M.; Blanco, R. M. One-Pot Laccase@MOF Biocatalysts Efficiently Remove Bisphenol A from Water. *Catal. Today* **2022**, *390–391* (July 2021), 265–271. <https://doi.org/10.1016/j.cattod.2021.10.005>.
- (116) Gascón, V.; Castro-Miguel, E.; Díaz-García, M.; Blanco, R. M.; Sanchez-Sanchez, M. In Situ and Post-Synthesis Immobilization of Enzymes on Nanocrystalline MOF Platforms to Yield Active Biocatalysts. *J. Chem. Technol. Biotechnol.* **2017**, *92* (10), 2583–2593.
<https://doi.org/10.1002/jctb.5274>.
- (117) Carucci, C.; Bruen, L.; Gascón, V.; Paradisi, F.; Magner, E. Significant Enhancement of Structural Stability of the Hyperhalophilic ADH from *Haloferax Volcanii* via Entrapment on Metal Organic Framework Support. *Langmuir* **2018**, *34* (28), 8274–8280.

<https://doi.org/10.1021/acs.langmuir.8b01037>.

- (118) Naseri, M.; Pitzalis, F.; Carucci, C.; Medda, L.; Fotouhi, L.; Magner, E.; Salis, A. Lipase and Laccase Encapsulated on Zeolite Imidazolate Framework: Enzyme Activity and Stability from Voltammetric Measurements. *ChemCatChem* **2018**, *10* (23), 5425.
- (119) Shieh, F.-K.; Wang, S.-C.; Yen, C.-I.; Wu, C.-C.; Dutta, S.; Chou, L.-Y.; Morabito, J. V.; Hu, P.; Hsu, M.-H.; Wu, K. C. W.; Tsung, C.-K. Imparting Functionality to Biocatalysts via Embedding Enzymes into Nanoporous Materials by a de Novo Approach: Size-Selective Sheltering of Catalase in Metal–Organic Framework Microcrystals. *J. Am. Chem. Soc.* **2015**, *137* (13), 4276–4279. <https://doi.org/10.1021/ja513058h>.
- (120) Chen, S.; Wen, L.; Svec, F.; Tan, T.; Lv, Y. Magnetic Metal-Organic Frameworks as Scaffolds for Spatial Co-Location and Positional Assembly of Multi-Enzyme Systems Enabling Enhanced Cascade Biocatalysis. *RSC Adv.* **2017**, *7* (34), 21205–21213. <https://doi.org/10.1039/c7ra02291c>.
- (121) Wang, C.; Liao, K. Recent Advances in Emerging Metal– and Covalent–Organic Frameworks for Enzyme Encapsulation. *ACS Appl. Mater. Interfaces* **2021**, *13* (48), 56752–56776. <https://doi.org/10.1021/acsami.1c13408>.
- (122) Liu, Y.; Pang, H.; Wang, X.; Yu, S.; Chen, Z.; Zhang, P.; Chen, L.; Song, G.; Saleh Alharbi, N.; Omar Rabah, S.; Wang, X. Zeolitic Imidazolate Framework-Based Nanomaterials for the Capture of Heavy Metal Ions and Radionuclides: A Review. *Chem. Eng. J.* **2021**, *406* (September 2020), 127139. <https://doi.org/10.1016/j.cej.2020.127139>.
- (123) Park, K. S.; Ni, Z.; Côté, A. P.; Choi, J. Y.; Huang, R.; Uribe-Romo, F. J.; Chae, H. K.; O’Keeffe, M.; Yaghi, O. M. Exceptional Chemical and Thermal Stability of Zeolitic Imidazolate Frameworks. *Proc. Natl. Acad. Sci. U. S. A.* **2006**, *103* (27), 10186–10191. <https://doi.org/10.1073/pnas.0602439103>.
- (124) Yaghi, O. M.; Kalmutzki, M. J.; Diercks, C. S. Zeolitic Imidazolate Frameworks. *Introd. to*

Reticular Chem. **2019**, 463–479. <https://doi.org/10.1002/9783527821099.ch20>.

- (125) Banerjee, R.; Phan, A.; Wang, B.; Knobler, C.; Furukawa, H.; O’Keeffe, M.; Yaghi, O. M. High-Throughput Synthesis of Zeolitic Imidazolate Frameworks and Application to CO₂ Capture. *Science (80-.)*. **2008**, *319* (5865), 939–943. <https://doi.org/10.1126/science.1152516>.
- (126) Polyukhov, D. M.; Poryvaev, A. S.; Gromilov, S. A.; Fedin, M. V. Precise Measurement and Controlled Tuning of Effective Window Sizes in ZIF-8 Framework for Efficient Separation of Xylenes. *Nano Lett.* **2019**, *19* (9), 6506–6510. <https://doi.org/10.1021/acs.nanolett.9b02730>.
- (127) Glante, S.; Bette, S.; Gallo, G.; Dinnebier, R. E.; Hartmann, M. Crystal Structure and De- and Rehydration Behavior of Two New Chloride-Containing Zeolitic Imidazolate Frameworks. *Cryst. Growth Des.* **2019**, *19* (8), 4844–4853. <https://doi.org/10.1021/acs.cgd.9b00838>.
- (128) Bergaoui, M.; Khalfaoui, M.; Awadallah-F, A.; Al-Muhtaseb, S. A Review of the Features and Applications of ZIF-8 and Its Derivatives for Separating CO₂ and Isomers of C₃- and C₄- Hydrocarbons. *J. Nat. Gas Sci. Eng.* **2021**, *96* (September), 104289. <https://doi.org/10.1016/j.jngse.2021.104289>.
- (129) Wei, T. H.; Wu, S. H.; Huang, Y. Da; Lo, W. S.; Williams, B. P.; Chen, S. Y.; Yang, H. C.; Hsu, Y. S.; Lin, Z. Y.; Chen, X. H.; Kuo, P. E.; Chou, L. Y.; Tsung, C. K.; Shieh, F. K. Rapid Mechanochemical Encapsulation of Biocatalysts into Robust Metal–Organic Frameworks. *Nat. Commun.* **2019**, *10* (1), 1–8. <https://doi.org/10.1038/s41467-019-12966-0>.
- (130) Pitzalis, F.; Carucci, C.; Naseri, M.; Fotouhi, L.; Magner, E.; Salis, A. Lipase Encapsulation onto ZIF-8: A Comparison between Biocatalysts Obtained at Low and High Zinc/2-Methylimidazole Molar Ratio in Aqueous Medium. *ChemCatChem* **2018**, *10* (7), 1578–1585. <https://doi.org/10.1002/cctc.201701984>.
- (131) Rafiei, S.; Tangestaninejad, S.; Horcajada, P.; Moghadam, M.; Mirkhani, V.; Mohammadpoor-Baltork, I.; Kardanpour, R.; Zadehahmadi, F. Efficient Biodiesel Production

- Using a Lipase@ZIF-67 Nanobioreactor. *Chem. Eng. J.* **2018**, *334* (October 2017), 1233–1241. <https://doi.org/10.1016/j.cej.2017.10.094>.
- (132) Adnan, M.; Li, K.; Xu, L.; Yan, Y. X-Shaped ZIF-8 for Immobilization Rhizomucor Miehei Lipase via Encapsulation and Its Application toward Biodiesel Production. *Catalysts* **2018**, *8* (3), 96. <https://doi.org/10.3390/catal8030096>.
- (133) Maddigan, N. K.; Linder-Patton, O. M.; Falcaro, P.; Sumby, C. J.; Bell, S. G.; Doonan, C. J. Influence of the Synthesis and Storage Conditions on the Activity of Candida Antarctica Lipase B ZIF-8 Biocomposites. *ACS Appl. Mater. Interfaces* **2021**. <https://doi.org/10.1021/acsami.1c04785>.
- (134) Knedel, T. O.; Ricklefs, E.; Schlüsener, C.; Urlacher, V. B.; Janiak, C. Laccase Encapsulation in ZIF-8 Metal-Organic Framework Shows Stability Enhancement and Substrate Selectivity. *ChemistryOpen* **2019**, *8* (11), 1337–1344. <https://doi.org/10.1002/open.201900146>.
- (135) Patil, P. D.; Yadav, G. D. Rapid In Situ Encapsulation of Laccase into Metal-Organic Framework Support (ZIF-8) under Biocompatible Conditions. *ChemistrySelect* **2018**, *3* (17), 4669–4675. <https://doi.org/10.1002/slct.201702852>.
- (136) Du, M.; Chen, H.; Ye, J.; Zhang, S.; Chen, J.; Wang, L. One-Pot Synthesis of Efficient Carbonic Anhydrase-Zeolitic Imidazolate Framework-8 Composite for Enhancing CO₂ Absorption. *J. CO₂ Util.* **2020**, *40* (June), 101211. <https://doi.org/10.1016/j.jcou.2020.101211>.
- (137) Wang, Y.; Zhang, N.; Tan, D.; Qi, Z.; Wu, C. Facile Synthesis of Enzyme-Embedded Metal–Organic Frameworks for Size-Selective Biocatalysis in Organic Solvent. *Front. Bioeng. Biotechnol.* **2020**, *8* (July), 1–9. <https://doi.org/10.3389/fbioe.2020.00714>.
- (138) Vaidya, L. B.; Nadar, S. S.; Rathod, V. K. Entrapment of Surfactant Modified Lipase within Zeolitic Imidazolate Framework (ZIF)-8. *Int. J. Biol. Macromol.* **2020**, *146*, 678–686. <https://doi.org/10.1016/j.ijbiomac.2019.12.164>.

- (139) Dhakshinamoorthy, A.; Alvaro, M.; Horcajada, P.; Gibson, E.; Vishnuvarthan, M.; Vimont, A.; Grenèche, J.-M.; Serre, C.; Daturi, M.; Garcia, H. Comparison of Porous Iron Trimesates Basolite F300 and MIL-100(Fe) As Heterogeneous Catalysts for Lewis Acid and Oxidation Reactions: Roles of Structural Defects and Stability. *ACS Catal.* **2012**, *2* (10), 2060–2065. <https://doi.org/10.1021/cs300345b>.
- (140) Dhakshinamoorthy, A.; Alvaro, M.; Garcia, H. Alkanes Catalysed by Metal – Organic Frameworks. **2011**, 6256–6262. <https://doi.org/10.1002/chem.201002664>.
- (141) Sciortino, L.; Alessi, A.; Messina, F.; Buscarino, G.; Gelardi, F. M. Structure of the FeBTC Metal-Organic Framework: A Model Based on the Local Environment Study. *J. Phys. Chem. C* **2015**, *119* (14), 7826–7830. <https://doi.org/10.1021/acs.jpcc.5b01336>.
- (142) Majano, G.; Ingold, O.; Yulikov, M.; Jeschke, G.; Pérez-Ramírez, J. Room-Temperature Synthesis of Fe–BTC from Layered Iron Hydroxides: The Influence of Precursor Organisation. *CrystEngComm* **2013**, *15* (46), 9885. <https://doi.org/10.1039/c3ce41366g>.
- (143) Han, Q.; Wang, Z.; Chen, X.; Jiao, C.; Li, H.; Yu, R. Facile Synthesis of Fe-Based MOFs(Fe-BTC) as Efficient Adsorbent for Water Purifications. *Chem. Res. Chinese Univ.* **2019**, *35* (4), 564–569. <https://doi.org/10.1007/s40242-019-8415-z>.
- (144) Sanchez-Sanchez, M.; de Asua, I.; Ruano, D.; Diaz, K. Direct Synthesis, Structural Features, and Enhanced Catalytic Activity of the Basolite F300-like Semiamorphous Fe-BTC Framework. *Cryst. Growth Des.* **2015**, *15* (9), 4498–4506. <https://doi.org/10.1021/acs.cgd.5b00755>.
- (145) Drout, R. J.; Robison, L.; Farha, O. K. Catalytic Applications of Enzymes Encapsulated in Metal–Organic Frameworks. *Coord. Chem. Rev.* **2019**, *381*, 151–160. <https://doi.org/10.1016/j.ccr.2018.11.009>.
- (146) Naseri, M.; Pitzalis, F.; Carucci, C.; Medda, L.; Fotouhi, L.; Magner, E.; Salis, A. Lipase and Laccase Encapsulated on Zeolite Imidazolate Framework: Enzyme Activity and Stability

from Voltammetric Measurements. *ChemCatChem* **2018**, *10* (23), 5425–5433.

<https://doi.org/10.1002/cctc.201801293>.

- (147) Chen, W.-H.; Vázquez-González, M.; Zoabi, A.; Abu-Reziq, R.; Willner, I. Biocatalytic Cascades Driven by Enzymes Encapsulated in Metal–Organic Framework Nanoparticles. *Nat. Catal.* **2018**, *1* (9), 689–695. <https://doi.org/10.1038/s41929-018-0117-2>.
- (148) Li, X.; Li, D.; Zhang, Y.; Lv, P.; Feng, Q.; Wei, Q. Encapsulation of Enzyme by Metal–Organic Framework for Single-Enzymatic Biofuel Cell-Based Self-Powered Biosensor. *Nano Energy* **2020**, *68* (November 2019), 104308. <https://doi.org/10.1016/j.nanoen.2019.104308>.
- (149) Velásquez-Hernández, M. D. J.; Ricco, R.; Carraro, F.; Limpoco, F. T.; Linares-Moreau, M.; Leitner, E.; Wiltsche, H.; Rattenberger, J.; Schröttner, H.; Frühwirt, P.; Stadler, E. M.; Gescheidt, G.; Amenitsch, H.; Doonan, C. J.; Falcaro, P. Degradation of ZIF-8 in Phosphate Buffered Saline Media. *CrystEngComm* **2019**, *21* (31), 4538–4544. <https://doi.org/10.1039/c9ce00757a>.
- (150) Bůžek, D.; Adamec, S.; Lang, K.; Demel, J. Metal–Organic Frameworks: Vs. Buffers: Case Study of UiO-66 Stability. *Inorg. Chem. Front.* **2021**, *8* (3), 720–734. <https://doi.org/10.1039/d0qi00973c>.
- (151) Hashem, T.; Valadez Sanchez, E. P.; Bogdanova, E.; Ugodchikova, A.; Mohamed, A.; Schwotzer, M.; Alkordi, M. H.; Wöll, C. Stability of Monolithic Mof Thin Films in Acidic and Alkaline Aqueous Media. *Membranes (Basel)*. **2021**, *11* (3), 1–12. <https://doi.org/10.3390/membranes11030207>.
- (152) Velásquez-Hernández, M. D. J.; Ricco, R.; Carraro, F.; Limpoco, F. T.; Linares-Moreau, M.; Leitner, E.; Wiltsche, H.; Rattenberger, J.; Schröttner, H.; Frühwirt, P.; Stadler, E. M.; Gescheidt, G.; Amenitsch, H.; Doonan, C. J.; Falcaro, P. Degradation of ZIF-8 in Phosphate Buffered Saline Media. *CrystEngComm* **2019**, *21* (31), 4538–4544. <https://doi.org/10.1039/C9CE00757A>.

- (153) Sun, C. Y.; Qin, C.; Wang, X. L.; Yang, G. S.; Shao, K. Z.; Lan, Y. Q.; Su, Z. M.; Huang, P.; Wang, C. G.; Wang, E. B. Zeolitic Imidazolate Framework-8 as Efficient PH-Sensitive Drug Delivery Vehicle. *Dalt. Trans.* **2012**, *41* (23), 6906–6909.
<https://doi.org/10.1039/c2dt30357d>.
- (154) Pu, S.; Zhang, X.; Yang, C.; Naseer, S.; Zhang, X.; Ouyang, J.; Li, D.; Yang, J. The Effects of NaCl on Enzyme Encapsulation by Zeolitic Imidazolate Frameworks-8. *Enzyme Microb. Technol.* **2019**, *122* (November 2018), 1–6. <https://doi.org/10.1016/j.enzmictec.2018.12.003>.
- (155) Luzuriaga, M. A.; Benjamin, C. E.; Gaertner, M. W.; Lee, H.; Herbert, F. C.; Mallick, S.; Gassensmith, J. J. ZIF-8 Degrades in Cell Media, Serum, and Some—but Not All—Common Laboratory Buffers. *Supramol. Chem.* **2019**, *31* (8), 485–490.
<https://doi.org/10.1080/10610278.2019.1616089>.
- (156) Zhang, H.; Jiang, Z.; Xia, Q.; Zhou, D. Progress and Perspective of Enzyme Immobilization on Zeolite Crystal Materials. *Biochem. Eng. J.* **2021**, *172*, 108033.
<https://doi.org/10.1016/j.bej.2021.108033>.
- (157) Miller, A. H.; de Vasconcellos, A.; Fielding, A. J.; Nery, J. G. Nanozeolites as Support for Laccase Immobilization: Application to Mediated Glycerol Oxidation. *Appl. Catal. A Gen.* **2021**, *626* (July), 118361. <https://doi.org/10.1016/j.apcata.2021.118361>.
- (158) Lim, Y.; Yu, J.; Park, S.; Kim, M.; Chen, S.; Bakri, N. A. B.; Sabri, N. I. A. B. M.; Bae, S.; Kim, H. S. Development of Biocatalysts Immobilized on Coal Ash-Derived Ni-Zeolite for Facilitating 4-Chlorophenol Degradation. *Bioresour. Technol.* **2020**, *307* (March), 123201.
<https://doi.org/10.1016/j.biortech.2020.123201>.
- (159) Khojaewa, V.; Lopatin, O.; Zelenikhin, P.; Ilinskaya, O. Zeolites as Carriers of Antitumor Ribonuclease Binas. *Front. Pharmacol.* **2019**, *10* (MAY), 1–7.
<https://doi.org/10.3389/fphar.2019.00442>.
- (160) Hartmann, M.; Thommes, M.; Schwieger, W. Hierarchically-Ordered Zeolites: A Critical

Assessment. *Adv. Mater. Interfaces* **2021**, *8* (4), 2001841.

<https://doi.org/10.1002/admi.202001841>.

- (161) Lee, S. Y.; Show, P. L.; Ko, C. M.; Chang, Y. K. A Simple Method for Cell Disruption by Immobilization of Lysozyme on the Extrudate-Shaped Na-Y Zeolite: Recirculating Packed Bed Disruption Process. *Biochem. Eng. J.* **2019**, *141* (September 2018), 210–216.
<https://doi.org/10.1016/j.bej.2018.10.016>.
- (162) Avery, K. L.; Peixoto, C.; Barcellona, M.; Bernards, M. T.; Hunt, H. K. Lysozyme Sorption by Pure-Silica Zeolite MFI Films. *Mater. Today Commun.* **2019**, *19* (July 2018), 352–359.
<https://doi.org/10.1016/j.mtcomm.2019.03.004>.
- (163) Taghizadeh, T.; Talebian-Kiakalaieh, A.; Jahandar, H.; Amin, M.; Tarighi, S.; Faramarzi, M. A. Biodegradation of Bisphenol A by the Immobilized Laccase on Some Synthesized and Modified Forms of Zeolite Y. *J. Hazard. Mater.* **2020**, *386* (October 2019), 121950.
<https://doi.org/10.1016/j.jhazmat.2019.121950>.
- (164) Smeets, V.; Baaziz, W.; Ersen, O.; Gaigneaux, E. M.; Boissière, C.; Sanchez, C.; Debecker, D. P. Hollow Zeolite Microspheres as a Nest for Enzymes: A New Route to Hybrid Heterogeneous Catalysts. *Chem. Sci.* **2020**, *11* (4), 954–961.
<https://doi.org/10.1039/C9SC04615A>.
- (165) Wehaidy, H. R.; Abdel-Naby, M. A.; El-Hennawi, H. M.; Youssef, H. F. Nanoporous Zeolite-X as a New Carrier for Laccase Immobilization and Its Application in Dyes Decolorization. *Biocatal. Agric. Biotechnol.* **2019**, *19* (February), 101135.
<https://doi.org/10.1016/j.bcab.2019.101135>.
- (166) de Vasconcellos, A.; Miller, A. H.; Aranda, D. A. G.; Nery, J. G. Biocatalysts Based on Nanozeolite-Enzyme Complexes: Effects of Alkoxysilane Surface Functionalization and Biofuel Production Using Microalgae Lipids Feedstock. *Colloids Surfaces B Biointerfaces* **2018**, *165*, 150–157. <https://doi.org/10.1016/j.colsurfb.2018.02.029>.

- (167) Machoke, A. G.; Beltrán, A. M.; Inayat, A.; Winter, B.; Weissenberger, T.; Kruse, N.; Güttel, R.; Spiecker, E.; Schwieger, W. Micro/Macroporous System: MFI-Type Zeolite Crystals with Embedded Macropores. *Adv. Mater.* **2015**, *27* (6), 1066–1070.
<https://doi.org/10.1002/adma.201404493>.
- (168) Weissenberger, T.; Machoke, A. G. F.; Reiprich, B.; Schwieger, W. Preparation and Potential Catalytic Applications of Hierarchically Structured Zeolites with Macropores. *Adv. Mater. Interfaces* **2021**, *8* (4), 2001653. <https://doi.org/10.1002/admi.202001653>.
- (169) Marthala, V. R. R.; Urmoneit, L.; Zhou, Z.; Machoke, A. G. F.; Schmiele, M.; Unruh, T.; Schwieger, W.; Hartmann, M. Boron-Containing MFI-Type Zeolites with a Hierarchical Nanosheet Assembly for Lipase Immobilization. *Dalt. Trans.* **2017**, *46* (13), 4165–4169.
<https://doi.org/10.1039/C7DT00092H>.
- (170) Mitchell, S.; Pérez-Ramírez, J. Mesoporous Zeolites as Enzyme Carriers: Synthesis, Characterization, and Application in Biocatalysis. *Catal. Today* **2011**, *168* (1), 28–37.
<https://doi.org/10.1016/j.cattod.2010.10.058>.
- (171) Fernández-Fernández, M.; Sanromán, M. Á.; Moldes, D. Recent Developments and Applications of Immobilized Laccase. *Biotechnol. Adv.* **2013**, *31* (8), 1808–1825.
<https://doi.org/10.1016/j.biotechadv.2012.02.013>.
- (172) Hu, D.; Chen, Z.; Sheng, Z.; Gao, D.; Yan, F.; Ma, T.; Zheng, H.; Hong, M. A Catalase-Loaded Hierarchical Zeolite as an Implantable Nanocapsule for Ultrasound-Guided Oxygen Self-Sufficient Photodynamic Therapy against Pancreatic Cancer. *Nanoscale* **2018**, *10* (36), 17283–17292. <https://doi.org/10.1039/c8nr05548c>.
- (173) Outline, C. Methods for Assessing Surface Cleanliness. In *Developments in Surface Contamination and Cleaning, Volume 12*; Elsevier, 2019; Vol. 12, pp 23–105.
<https://doi.org/10.1016/B978-0-12-816081-7.00003-6>.
- (174) Fleck, N.; Amlı, H.; Dhanak, V.; Ahmed, W. Characterization Techniques in Energy

- Generation and Storage. In *Emerging Nanotechnologies for Renewable Energy*; Elsevier, 2021; pp 259–285. <https://doi.org/10.1016/B978-0-12-821346-9.00003-1>.
- (175) Claxton, N. S.; Fellers, T. J.; Davidson, M. W. Laser Scanning Confocal Microscopy (LSCM). In *SpringerReference*; Springer-Verlag: Berlin/Heidelberg, 2011; Vol. 1979. https://doi.org/10.1007/SpringerReference_67032.
- (176) Weigler, M.; Brodrecht, M.; Breitzke, H.; Dietrich, F.; Sattig, M.; Buntkowsky, G.; Vogel, M. ²H NMR Studies on Water Dynamics in Functionalized Mesoporous Silica. *Zeitschrift für Phys. Chemie* **2018**, 232 (7–8), 1041–1058. <https://doi.org/10.1515/zpch-2017-1034>.
- (177) Salis, A.; Pisano, M.; Monduzzi, M.; Solinas, V.; Sanjust, E. Laccase from *Pleurotus Sajor-Caju* on Functionalised SBA-15 Mesoporous Silica: Immobilisation and Use for the Oxidation of Phenolic Compounds. *J. Mol. Catal. B Enzym.* **2009**, 58 (1–4), 175.
- (178) Larkin, P. J. Introduction. In *Infrared and Raman Spectroscopy*; Larkin, P. J. B. T.-I. and R. S. (Second E., Ed.; Elsevier, 2018; pp 1–5. <https://doi.org/10.1016/B978-0-12-804162-8.00001-X>.
- (179) Boyd, R.; Smith, G. NMR Spectroscopy. In *Polymer Dynamics and Relaxation*; Cambridge University Press: Cambridge, 2001; Vol. 14, pp 44–56. <https://doi.org/10.1017/CBO9780511600319.005>.

La borsa di dottorato è stata cofinanziata con risorse del
Programma Operativo Nazionale Ricerca e Innovazione 2014-2020 (CCI 2014IT16M2OP005),
Fondo Sociale Europeo, Azione I.1 “Dottorati Innovativi con caratterizzazione Industriale”



UNIONE EUROPEA
Fondo Sociale Europeo



*Ministero dell'Università
e della Ricerca*



APPENDIX

PAPER I

Recent Developments in the Delignification and Exploitation of Grass Lignocellulosic Biomass

Davide Tocco, Cristina Carucci, Maura Monduzzi, Andrea Salis,* and Enrico Sanjust*

Cite This: *ACS Sustainable Chem. Eng.* 2021, 9, 2412–2432

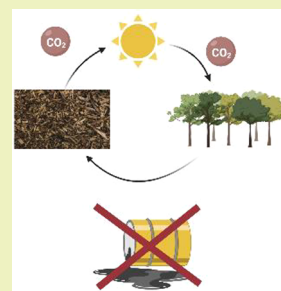
Read Online

ACCESS |

Metrics & More

Article Recommendations

ABSTRACT: Biofuels could be defined as the fuels of the future, although much work is still required before they will replace fossil fuels. In this review, lignocellulosic biomass based on straw and related crops and wastes is described concerning its lignin contents, structure, and properties, and an overview on the means of current and predictable delignification protocols is presented. The discussion is focused on herbaceous monocot materials and their available pretreatments (physical, chemical, and enzymatic), with special emphasis on fungal ligninolytic enzymes and the most recent findings and developments in their current application, issues, and perspectives.



KEYWORDS: Biofuels, Lignocellulosic biomass, Grass lignin, Delignification, Pretreatments, Ligninolytic enzymes

INTRODUCTION

Extensive use of fossil fuels is considered the main source of greenhouse gases and other polluting emissions. These phenomena have deep consequences on climate change and public health.¹ Conceivably, global energy demand will strongly rise in the next decade and beyond.^{2,3} These issues have led to a growing interest in renewable energies such as biofuels.⁴ Among these, bioethanol is used as a renewable substitute for gasoline. Bioethanol is obtained by fermentation of sugars (sugar cane, beet) or starch (maize). As it can be mixed in almost any ratio with gasoline, bioethanol is often used as an additive. It has been estimated that its use could potentially bring a reduction of 30% in our current oil consumption.⁵ “First generation” bioethanol has been produced from food sources and is not sustainable because it competes with food crops. Instead, “second generation” bioethanol is obtained from nonedible materials, such as cellulose obtained from lignocellulosic biomass (LBM).^{6–8} The economic assessment of lignocellulosic ethanol production has also been extensively studied.^{9,10} LBM, earth’s most abundant biopolymer-based material, is mainly composed of cellulose (40–50 wt %), hemicellulose (25–35 wt %), and lignin (15–30 wt %) biopolymers and a small percentage of minerals and extractives.¹¹ Cellulose, the main biopolymer present in lignocellulosic biomass, is a linear, regular, microcrystalline homopolymer $H(C_6H_{10}O_5)_nOH$, where n (degree of polymerization) is some thousands. Cellulose consists exclusively of glucose units linked by β -1,4 glycosidic bonds. Hemicelluloses are irregular, branched, amorphous heteropolymers consisting of different C_5 and C_6 monosaccharide units, such as xylose, mannose, galactose, arabinose, rhamnose,

glucuronic acid, and galacturonic acid in various amounts and chemical linkage types, depending on biomass source.

Cellulose, hemicelluloses, and lignin are connected among themselves to form LBM (Figure 1). Cellulose is encapsulated in a cross-linked hemicellulose/pectin matrix through hydrogen bond linkages and van der Waals forces. Hemicellulose is presumably linked with lignin mainly via ester covalent bonds due to hydroxycinnamic acids present in lignin–carbohydrate complexes in the case of grasses.^{12–14}

Bioethanol is only one among many products obtainable from cellulose processing. Indeed, according to the type of pretreatment, cellulose hydrolysis leads to a mixture of sugars (glucose, cellobiose, cellotriose, cellodextrins) and lower amounts of other compounds, such as 5-hydroxymethylfurfural (HMF), lactic acid, levulinic acid (LA), 1,2-ethylene glycol, sorbitol, 2,5-bis(hydroxymethyl)furan, formic acid, gluconic acid, and glycolic acid. Hemicellulose hydrolysis results in a mixture of xylose and other monosaccharides, such as arabinose, glucose, mannose, and uronic acids, depending on the particular source of the LBM. Lower amounts of furfural, LA, and γ -valerolactone (GVL) are also formed. Very recently, the topic of cellulose and hemicellulose enzymatic hydrolysis has been extensively reviewed.¹⁵ Except for glucose and xylose, the other “platform compounds” can be valorized by synthesizing other value-added

Received: October 2, 2020

Revised: January 7, 2021

Published: February 4, 2021



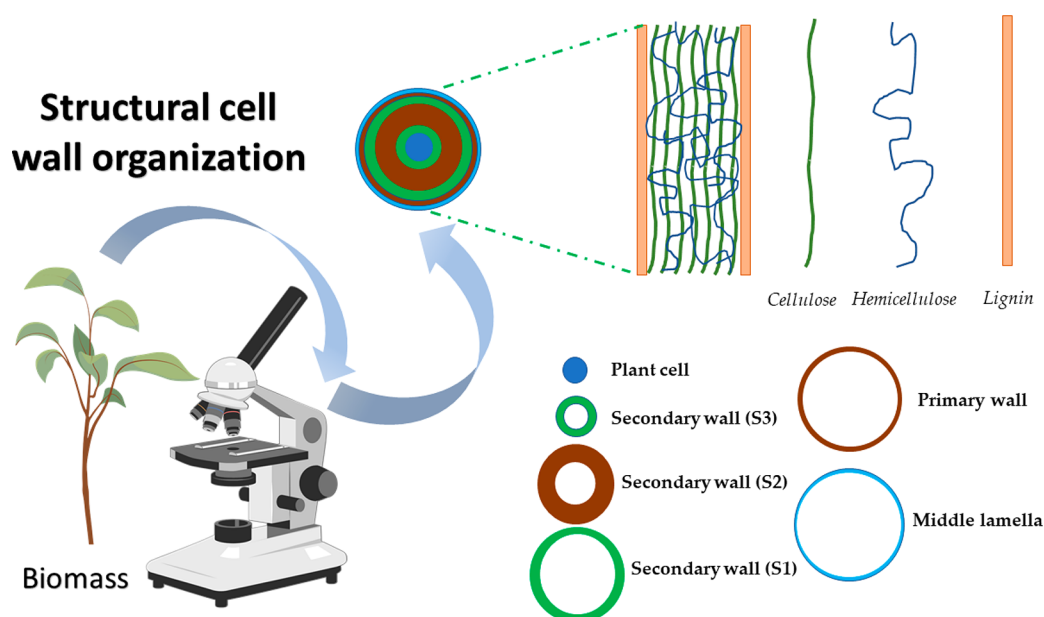


Figure 1. Lignocellulose biomass composition: cell wall composition and structure.

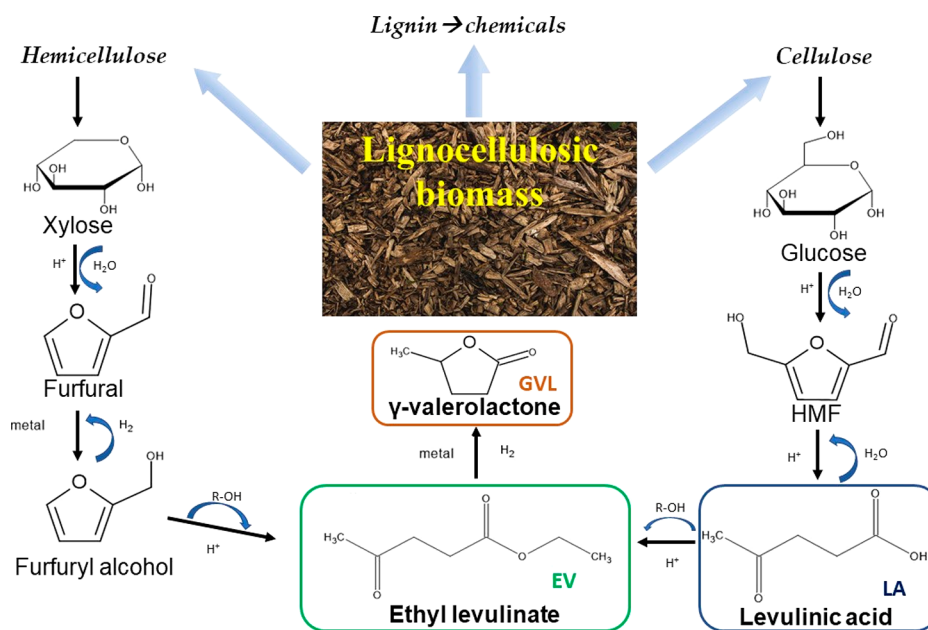


Figure 2. LA, EV, and GVL production from LBM.

chemicals or fuels. For example, LA is one of the most promising platform compounds obtainable from lignocellulose (Figure 2). LA can be used to produce fuel additives as GVL^{16,17} or ethyl valerate (EV)^{18,19} (Figure 2).

Among the various sources of LBM, grasses (in a general sense, but with particular emphasis on monocots, that is, essentially Poaceae, formerly Gramineae) occupy a special position for various reasons: (i) their lignin content is generally lower in comparison with woody LBM, and conversely their hydrolyzable and fermentable polysaccharide content is higher; (ii) herbaceous LBM usually derives as wastes from other crops or also can be purposely cultivated in marginal areas without hampering food production for humans and animals such as sheep or cattle; (iii) the lifecycle of these vegetables is often annual, and therefore they represent typical renewable

resources. As a consequence, they have been and are nowadays the subject of many studies^{20,21} to shed light on the particular structural and chemical properties of their lignin fraction and to find the best ways to exploit their high potential to obtain fermentable sugars, fine chemicals, and renewable biofuels.

The aim of the present review is to encompass the state of the art in the knowledge of these LBM materials and to critically examine the main issues and perspectives in their utilization.

■ AN OVERVIEW ON LIGNIN GENERAL FEATURES AND STRUCTURE

Lignin is completely different from the other biopolymers forming LBM, being a cross-linked molecular network based on phenylpropanoid units (monolignols) such as *p*-coumaryl, coniferyl, and syringyl alcohols (Figure 3) and minor amounts

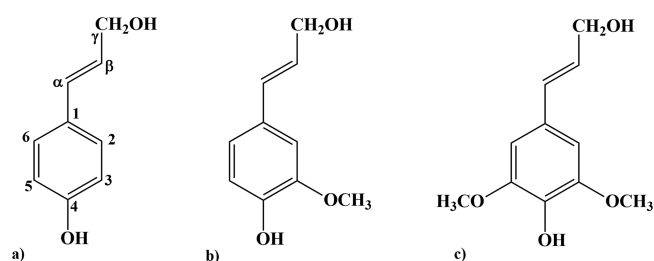


Figure 3. Three monolignols acting as the main comonomers in lignin biosynthesis: (a) *p*-coumaryl alcohol, becoming the *p*-hydroxyphenyl unit H in the polymer; (b) coniferyl alcohol, becoming the guaiacyl unit G in the polymer; (c) sinapyl alcohol, becoming the syringyl unit S in the polymer.

of other monomers.²² To a certain extent, lignins show a different composition depending on the particular class of vegetables where they are found. Generally speaking, lignin structure forms a dense 3-D texture, based on *p*-hydroxyphenyl (H), guaiacyl (G), and syringyl (S) units, linked by a variety of C–O and C–C (most commonly, β -O-4, β -5, β - β , 5-5, 4-O-5, β -1 and α -O-4) bonds (Figure 4).^{14,22} As noted above, the lignin content in LBM depends on the source: softwoods show the highest lignin content (28–32%), followed by hardwoods (20–25%) and grasses (17–24%).^{24,25} Also, the relative amounts of the three main monomers differ significantly²³ among hardwood lignin (H/G/S = trace:50:50, GS-lignin), softwood lignin (H/G/S = 4:96:trace, G-lignin), and grass (monocot) lignin (H/G/S = 5:70:25, HGS-lignin). Important variations in the relative amounts of the three monolignols are often found within the same lignin group.^{26,27} Moreover, the large uncertainty in the quantitative determinations of such percentages and ratios should be taken into due account, as the obtained values deeply depend both on the lignin isolation procedures and on the chosen analytical methods.²⁸

As noted above, lignins of different botanical origin differ considerably in the proportions among the three main monolignols. This has important consequences in the 3-D structure of the resulting heteropolymers, because S units cannot participate in interunit linkages involving their 5-positions, which are occupied by methoxy substituents and indeed unavailable for participation in other bonds.²⁹ Consequently, S units cannot participate in 5-5, 4-O-5, and β -5 linkages. As a result, decidedly more cross-links are present in softwood lignin (nearly no S units) in comparison with hardwood lignin and, to a certain extent, in grass lignin (about 25% S units, although with high variations among different botanical species). Therefore, although present in substantially lower amounts, grass lignin forms a denser network with respect to the much more abundant hardwood lignin and is conceivably harder to remove.²⁹

■ GRASS LIGNIN: RECALCITRANT THOUGH SCARCE

For the reasons underlined above, grasses (both crops and wastes coming from herbaceous crop processing) are of high interest as inexpensive and rich sources of polysaccharides and therefore fermentable sugars, as well as other sugar-derived chemicals. However, such potential is hindered by the recalcitrance of their lignin fraction,³⁰ which must be removed in whole or at least in part to fully exploit the polysaccharides. Accordingly, grass lignin structure has been and is nowadays the subject of much research to understand its peculiar structural motifs and to find suitable delignification treatments.

Grasses *stricto sensu* belong to the Poales,³¹ and in particular to the family Poaceae, although also Cyperaceae include a vast variety of herbaceous species. On the other hand, many Bambusoideae have woody stems, though their “wood” shows the anatomical features, and the general chemical composition, typical of monocots,³² and this is why they are considered in this description.

Since the pioneering studies, some points have been established about grass lignin general structure and properties, although with sometimes contradictory conclusions referring to, for example, the presence (if any) and abundance of α -O-4 ether linkages connecting the monolignol units.^{33,34} Another special feature emphasized by early studies is the high relative abundance of H units in wheat straw lignin and therefore presumably also in taxonomically related straws. In the same study, the highly complex structure of Poaceae lignin in comparison to both hardwood and softwood lignin was confirmed.³⁵ This outstanding feature was also underlined in a general review²⁰ focused on the peculiarity of grass cell wall in comparison with dicots: in particular, a significant percentage of H units (\sim 4–15%) was claimed to be usually present in grass lignins, together with etherified or esterified ferulic and *p*-coumaric acids (Figure 5). However, the use of combined, different analytical techniques has shown that the relative abundance of H units is usually overestimated, because *p*-coumaryl residues are often and incorrectly ascribed to H units.³⁶ Also protein residues in cell walls contribute to such an overestimation.³⁷ Neither H units nor hydroxycinnamic acids are present in noticeable amounts in the large majority of dicot lignins. That of lignin acylation by hydroxycinnamic acid is a crucial feature in lignin of monocot grasses,³⁸ not only for their differentiation from nongrass lignins but because these hydroxycinnamoyl residues are the chemical bridges between lignin and cell wall polysaccharides. In particular, the γ position, predominantly or also exclusively of S units, is the acylation site, by acetyl, *p*-hydroxybenzoyl, and *p*-coumaroyl moieties. Also ferulic acid is present, though usually in smaller amounts than *p*-coumaric acid, as a constituent of grass lignins. Ferulic acid should be considered among the monomeric units of grass lignins, where it most probably acts as a polymerization initiator.³⁸ However, rather than forming esters at the γ positions of S units, ferulic acid tends to be linked preferentially to G units³⁹ as an α -alkyl-aryl ether (by means of its phenolic hydroxyl at the 4 (or *para*) position), whereas its carboxy function is esterified to hemicelluloses, mainly at the 5 positions of arabinose residues of arabinoxylans. Such ester bonds are alkali-labile, whereas the α -alkyl-aryl ether bonds are acid-labile. This observation has important practical consequences and should be taken into due account when planning delignification protocols for herbaceous crops (*vide infra*). Another peculiar feature of feruloyl residues in grass lignins is the definite tendency of these moieties to exist in part as various isomeric C–C and C–O dimers, arising from peroxidase action. Such dimers contribute to a close covalent bonding between lignin and cell wall polysaccharides. The very complicated topic of lignin–carbohydrate complexes (LCCs) has been recently reviewed⁴⁰ and has been and is still the objective of several studies, owing to its implications in delignification procedures (*vide infra*). In addition to the “indirect” mode of interaction (feruloyl moieties acting as bridges between lignin and carbohydrates), direct α ether linkages have been found, binding together lignin and arabinoxylans. In particular, the ether linkages involve usually the 5 position of the arabinose units. Moreover, a minor fraction

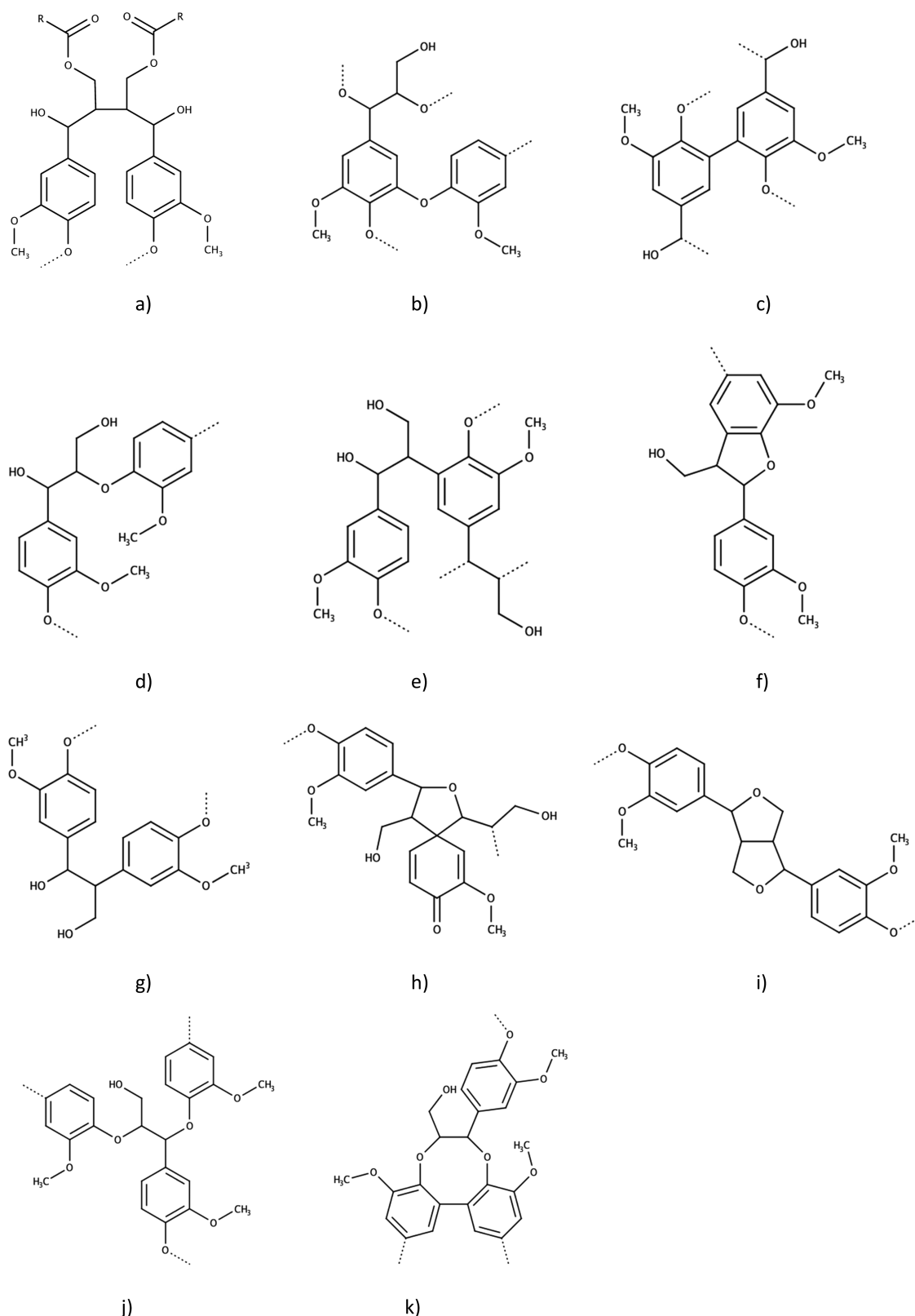


Figure 4. Most common chemical linkages interconnecting the monomeric units within the lignin 3-D polymer: (a) β - β ; (b) 4-O-5; (c) 5-5; (d) β -O-4; (e) β -5; (f) phenylcoumaran, (α -O-4 and β -5); (g) β -1; (h) spirodienone (α -O- α and β -1); (i) resinol (α -O- γ , β - β , and γ -O- α); (j) α,β -diarylether (α -O-4 and β -O-4); (k) dibenzodioxocin (α -O-4, β -O-4, and 5-5).

of polysaccharides can form ester linkages involving glucuronic acid or 4-O-methyl-glucuronic acid moieties of the glucurono-arabinoxylans. The preferentially involved esterification sites are the γ positions of G units.^{38,40}

The widely accepted structural models for cell walls in monocot grasses^{20,41} suggest that the prevailing interbiopolymer covalent bonds mainly involve hemicelluloses. However, some indications of direct bonding between lignin and cellulose exist

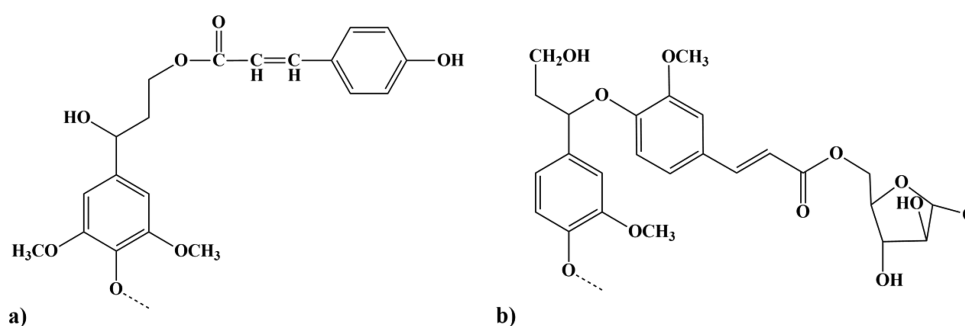


Figure 5. *p*-Coumaric (a) and ferulic (b) acids and their mode of bonding to grass lignin.

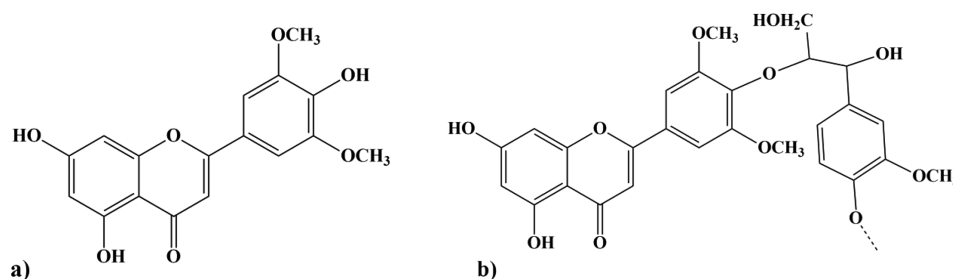


Figure 6. Flavone tricetin (a) and its mode of bonding to the lignin (b).

from a long time ago and were recently confirmed with new analyses.⁴² In particular, systematic NMR analysis of 80 species of the Poaceae has confirmed the wide presence of such bonds, involving essentially the 6-OH along the cellulose chains and the phenolic 4-OH of the monolignol units. In spite of the greater steric hindrance, also the 2- and 3-OH groups along the cellulose chains could be involved in such linkages, as well as the α - and β -hydroxyls of the phenylpropanoid moieties.

Another peculiar feature of the grass lignins is the significant presence of monomers, different from the “classical” monolignols,²² that are sometimes found also in wood lignins, but as quite marginal components. Among those, the flavone tricetin (Figure 6) occupies an outstanding position as a minor comonomer in grass lignins, where it participates in the formation of polymeric chains exclusively through 4'-*O*- β linkages. Therefore, it can occupy only the terminal positions in the lignin chains. A role for this flavonoid as a possible initiation molecule for lignification in monocots has been suggested.⁴³

The large variety of monomers, additional compounds, and possible interunit linkages, together with the variety of grass LCCs, gives rise to a grass lignin family, where the main common features are counterbalanced by particular compositional and structural motifs, such as are briefly encompassed here below.

A comparative study⁴⁴ among wheat, barley, maize, alfa (*Stipa tenacissima*), *Miscanthus* straws, and oat husks has shown that the respective lignins are quite similar, with an almost identical S/G ratio (0.78 and 0.79, respectively) for barley and wheat straw lignins. Other Poaceae would be slightly different, with S/G ratios of 0.76 for maize and 0.81 for *Miscanthus* straws, respectively. These values have been determined by FT-IR analysis. In the same study, the condensation indices (CI, meaning the fraction of monolignol subunits, participating in additional C-C linkages or diphenyl ether linkages, besides those usually binding the monolignols) were measured. However, the claimed strict resemblance among cereal lignins has been questioned by other studies.^{38,41} The H/G/S ratio is

4:35:61, 5:49:46, and 15:45:40 for maize stover, wheat straw, and rice straw, respectively. In particular, rice (*Oryza sativa*) straw contains less lignin in comparison with maize and wheat; wheat straw shows the almost unique property of containing a significant fraction ($\approx 20\%$) of its total lignin content that is readily soluble in alkaline solutions. However, as a general observation, such data as well as other analytical measurements have to be considered with the greatest caution, owing to the significant structural alterations lignins can undergo as a consequence of even mild extraction and separation procedures.^{45,46}

Bamboo⁴⁷ and giant bamboo⁴⁸ lignins have been investigated in detail with concern to their structural features, owing to the great importance of many Bambusoideae as potential pulp and paper sources as well as with reference to their application as starting raw materials in biorefineries. In brief, *Bambusa* lignin shows an unusual abundance of S units that sharply prevail over both G and H units (S/G ratio > 1.5). The monolignol units are bound by means of the usual linkages such as β -O-4 and so on, with the significant presence of α,β -diaryl ether motifs. The *Bambusa* lignin is noticeably heterogeneous, as a fraction with a lower S/G ratio could be separated by means of a milder extraction, whereas an alkaline extractant allows the dissolution of the high S/G ratio component. Also, significant amounts of *p*-coumaric and ferulic acids have been detected, covalently bound to the polymer. For *Dendrocalamus sinicus* (giant bamboo), the most interesting result is perhaps the high incidence of α -O-sugar linkages, maintaining covalently bound to both other lignins and hemicelluloses. The involved C atoms can be either terminal carbons (C₆ or C₅ depending on the hexose or pentose nature of the involved sugar) or secondary (C₂ or C₃) carbons. A detailed study on *Arundo donax* (common reed) lignins⁴⁹ revealed that, as found for other monocot grasses, some differences exist between stem and foliage lignins. On the whole, in spite of the apparent resemblance between reed and bamboo, the S/G ratio is decidedly lower in the former (<1), although with significant differences between stem and foliage

lignins: the latter contains more H units and its S/G ratio is even lower. The β -O-4 linkages largely prevail in both lignins, although with higher frequency in stem; conversely, acylation at the γ positions is more present in the foliage lignin.

Alfa (*St. tenacissima*) is not to be confused with alfalfa (*Medicago sativa*), which belongs to Fabaceae and is therefore a dicot. Alfa lignin analyzed after a mild organosolv process,²⁶ revealed a “normal” composition of an HGS type polymer, where the main interunit linkage is, as usual, β -O-4 alkyl-aryl ether. Moreover, it contains a high amount of acetate, hydroxybenzoate, and hydroxycinnamate esters, with the acetyl residues mainly linked to the γ positions of the S units.

Sugar cane (*Saccharum* spp.) bagasse and straw are produced in large amounts in tropical countries as byproducts of the sugar industry. Therefore, they have been deeply studied as a potential source of fermentable sugars after saccharification. Consequently, their lignins have been the subject of a number of investigations to determine their structure and chemical properties.⁵⁰ In particular, bagasse lignin is a HGS-type polymer with a high S/G ratio, whereas the opposite is found in the straw, where G units sharply prevail. This finding is in full agreement with the consideration that bagasse arise mainly from mature stems, whereas straw contains also young leaves in addition to mature foliage. Moreover, the two types of lignin differ also in the proportions among the interunit linkages. In fact, bagasse lignin units are largely linked by β -O-4 bridges, whereas straw lignin contains comparatively higher proportions of other linking modes, such as phenylcoumaran (benzoxolane) moieties.

Pennisetum purpureum (elephant grass) is in top position for LBM productivity and is easily cultivated in tropical areas, and therefore its lignin is worth investigating in detail.³⁶ This lignin contains a low content of H units (~3%) and exhibits a high degree of γ -acylation by *p*-coumaric acid.

Switchgrass (*Panicum virgatum* L.), Poaceae, is a perennial monocot grass native of North America, forming vast prairies along the plains, in particular in marginal, arid, and poorly productive areas, although it has been introduced in Europe, owing to its high potential as an energy crop for ethanol production.⁵¹ The switchgrass lignin, arising from the use of polysaccharide hydrolases, is characterized by a high prevalence of β -O-4 interunit linkage, followed by β -5- α -O-4 (phenylcoumaran) and β - β (resinol) linkages.⁵² Inspection of lignin content and composition among different varieties of switchgrass showed very little variations, whereas lignin content and S/G ratio varied greatly when comparing internodes, nodes, and leaves: the content increases from internodes to nodes to leaves, whereas the S/G ratio decreases from about 0.7 for internodes to 0.6 for nodes to 0.46 for leaves.⁵³ A detailed comparative experimental study about the techno-economic feasibility of different delignification pretreatment procedures for switchgrass has been published.⁵⁴

In conclusion, grass lignins are generally present in lesser amounts in straw in comparison to wood lignins, but their particular structure, typical for noticeable presence of etherified and esterified hydroxycinnamic acids, making close linkages with cell wall polysaccharides, requires careful (pre)treatments to fully exploit the fermentable sugar potential of the LBM.

■ DELIGNIFICATION MAIN STRATEGIES AND PROTOCOLS

As already noted, due to its highly cross-linked, three-dimensional structure, grass LBM is recalcitrant to degradation,

making the overall lignocellulose conversion a challenge.¹⁴ In order to separate cellulose and hemicelluloses from lignin, delignification pretreatments are needed.^{55–57} During pretreatment, lignin is modified or partially separated and also dissolved and removed from cellulose and hemicelluloses making them more accessible to hydrolytic enzymes. With respect to the processes needed to obtain ethanol or the platform compounds from cellulose and hemicellulose, the delignification step is undoubtedly the most challenging and critical of the overall process. Different delignification strategies can be used:

- mechanical (microwave, ultrasound, mechanical extrusion),⁵⁸
- physico-chemical (steam explosion, hot water, CO₂ explosion, NH₃ fiber explosion),^{59,60}
- chemical (acid or alkali hydrolysis, organosolv, ionic liquids, reductive catalytic fractionation, selective oxidation),^{61–67}
- biological (microorganisms, redox enzymes).⁶⁸

Most of the listed pretreatments involve harsh conditions (high temperature and pressure, use of solvents, or extreme pH values) causing partial biomass degradation. As a consequence, wastes as well as enzyme inhibitors are produced, making such processes unsuitable from economic and environmental points of view.^{6,69} Among pretreatments, the use of redox enzymes is very attractive for overcoming these drawbacks.⁷⁰ Moreover, they prevent the formation of furfural and phenolics, inhibitors of hydrolytic enzymes needed to obtain monosaccharides from cellulose and hemicelluloses, which are typically generated during mechanical, physicochemical, and chemical pretreatments.⁷¹ For these reasons, the use of redox enzymes is becoming of increasing importance in the biorefinery field. In the last years, the role of enzymes for the production of biofuels has been widely investigated.⁷²

The aim of the present section is to give an overview of the most recent developments in the field of industrial delignification, with particular focus on the use of redox enzymes.

A Brief Survey on the Nonenzymatic Delignification Methods for Straw. It is common knowledge that hemicelluloses, owing to their branched and irregular structure, are comparatively easier to remove than the other biopolymers forming LBM, and therefore relatively mild treatment such as extraction with hot water allows their removal. Conversely, lignin stubbornly resists such treatments, as does cellulose. As underlined in the previous section, grass lignins are engaged in a wide variety of covalent bonds with hemicelluloses and cellulose, and therefore any attempt at separation among the three main biopolymers usually produces raw fractions containing significant amounts of the other biopolymers, unless very harsh operative conditions (such as Kraft protocols) are adopted.⁷³ However, although the Kraft method is very suitable for preparing cellulose fibers (pulp and paper industries), it shows the drawback of completely dissolving the hemicelluloses, essentially (glucurono)arabinoxylans, which constitute a substantial source of fermentable sugars in straw.^{74,75} Also for this reason, the Kraft process is not usually applied to straw delignification. The same could be said for the other widespread wood delignification process, which is based on soluble sulfites.⁷⁶ Therefore, some other protocols, not so destructive and above all more ecofriendly, have been developed, and some are currently used at industrial or semi-industrial scale. In particular, mild alkaline pretreatments could be resolute for preliminary hemicellulose separation from lignin, owing to the

labile ester bonds joining the two polymers by means of ferulic acid bridges (*vide supra*). It is also worth noting that the fractionation protocols useful for research at laboratory scale are usually not suitable at all for the purpose of polysaccharide recovery. In fact, hemicelluloses are readily dissolved by comparatively smooth treatments, contrary to cellulose and lignin. Consequently, biorefinery-oriented procedures must include operative methods devoted to hemicellulose recovery and exploitation. Finally, the whole biorefinery process must be inexpensive enough to ensure a substantial profit when selling the obtained chemicals such as ethanol, xylose or xylitol, and so on.^{77,78}

Physicochemical Treatments. These include the use of solvent systems that ideally do not alter significantly the covalent structures of the main LBM constituents. In practice, the dense 3-D lignin structure requires a partial molecular simplification to be brought into solution, unless hydrotropic solvents are used.⁷⁹ Generally speaking, there is growing interest in the field of lignin removal by organic aqueous solvents.⁵⁵ These should be inexpensive, easily recoverable and recyclable, and environmental friendly. Progress in this field has been recently reviewed.⁸⁰ Particularly promising appears a recent method based on lignin solubilization (“organosolv” process) with an ethanol–water mixture (60:40) under pressure at 160 °C. The dissolved lignin was then precipitated by proper dilution with moderately acidified water.⁸¹ Ethanol (80% aqueous solution) was used similarly for solubilization of lignin from *Miscanthus*.⁸² Another organosolv procedure on straw and other byproducts from cereals has been described, affording a highly efficient lignin extraction and recovery.⁸³ However, the whole fractionation process for the studied LBM was somewhat laborious. Other studies^{84,85} have shown the efficient solubilizing action of hot imidazole over lignin, which could be isolated by simple dilution of the imidazole solution; this latter could be later recovered.

Ionic liquids (ILs) are organic salts that are nonvolatile liquids at room temperature (Figure 7). ILs have high solvating power and excellent chemical and thermal stabilities, and their solubilizing power toward lignin has been assessed by some studies.^{86,87}

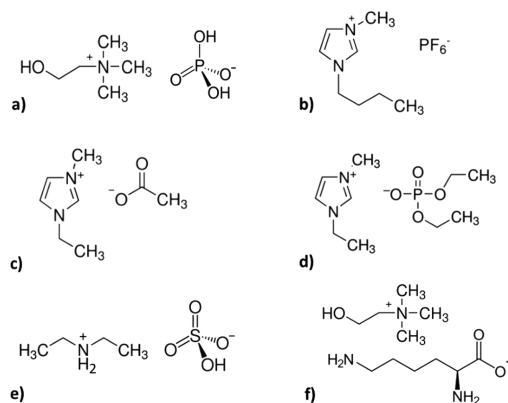


Figure 7. Common ILs used in delignification process: (a) Cholinium dihydrogen phosphate [Ch][H₂PO₄]; (b) 1-butyl-3-methylimidazolium hexafluorophosphate [Bmim][PF₆]; (c) 1-ethyl-3-methylimidazolium acetate [EMIM][OAc]; (d) 1-ethyl-3-methylimidazolium-diethyl phosphate [EMIM][DEP]; (e) diethylammonium hydrogensulfate ([DEA][HSO₄]); (f) cholinium L-lysinate [Ch][Lys].

Steam and Ammonia Explosion and Extrusion.

Although known from about a century, steam explosion is still current and its use in LBM pretreatments is widespread. Several studies, even at the pilot or industrial scales, have been described related to various LBM materials from different plant sources and have been recently reviewed.^{88,7} The main advantage of the technique is the absence of added chemicals, whereas the main limitation is the partial hydrolysis of the hemicelluloses and the formation of free acids such as acetic and hydroxycinnamic. These cause dehydration and cyclization of xylose leading to the undesired 2-furaldehyde.

Ammonia explosion⁸⁹ is a related technique that among other effects prevents furaldehyde formation caused by free acidity. The technique, commonly referred to as AFEX (ammonia fiber expansion/explosion), requires the use of anhydrous ammonia,⁹⁰ that can be recovered at the end of the treatment owing to its high volatility. Excess ammonia could also be recovered by stripping with hot steam, resulting in a concentrated ammonia solution. On the whole such a pretreatment does not alter the LBM chemical composition too deeply, whereas it acts on ultrastructure,⁹¹ making the material more accessible to further treatments such as those involving polysaccharide hydrolytic enzymes. This pretreatment has been recently reviewed together with the use of ammonia aqueous solutions.⁹⁰

Extrusion⁹² is to a certain extent similar to steam explosion. In this case, steam is substituted by a strong shear pressure, obtained by forcing LBM through a screw system, which also causes the LBM to heat at the same time.

Chemical Pretreatments. These could be subclassified into two main groups: (i) hydrolytic methods and (ii) oxidative methods.

In principle, hydrolysis could take place under either acidic or alkaline catalysis. Mild acidic hydrolysis is effective toward hemicelluloses, while lignin and cellulose remain untouched; as expected, the stronger the acidic conditions, the more efficient is the hydrolysis. However, excessive acidity could promote, besides other unwanted side reactions, partial hydrolysis of both cellulose and lignin. In particular, strong acids promote the formation of the undesired 2-furaldehyde and 5-hydroxymethyl-2-furaldehyde, so milder conditions are generally adopted. On the other hand, alkaline hydrolysis removes a fraction of hemicellulose without forming 2-furaldehyde, but also a significant lignin fraction is removed and contaminates the obtained solubilized hemicellulose. A mild acidic pretreatment to remove and partly hydrolyze hemicellulose, followed by an alkaline one to remove a substantial lignin fraction, could be the optimal solution, although more costly and requiring more complex biorefineries. All these considerations have been extensively and recently reviewed.⁹³

Some other pretreatments, in particular oxidative ones, find application in pulp and paper industry, as they leave a solid residue mainly formed of cellulose. In other words, hemicelluloses are removed (and substantially wasted) together with lignin. To prevent such waste, the above-mentioned mild acidic pretreatment⁹⁴ could allow for hemicellulose hydrolysate recovery prior to the delignification process.⁹³

Lignin interunit linkages mainly arise from radical-based addition reactions, and consequently their hydrolysis requires harsh conditions (in the case of C–O–C diphenyl ethers or alkyl-aryl ethers) or is quite impossible (C–C bonds). Therefore, lignin solubilization, apart from the harsh pulping treatments such as Kraft, sulfite, or soda processes, is achieved by means of oxidative cleavage. Ozone treatment under suitable

operative conditions could be effective,^{95,96} but its use is limited by high production costs, impossible storage, and the explosive and toxic nature of the reagent.

Chlorite pretreatment of LBM is a well-known process, affording substantial lignin removal without significant formation of highly recalcitrant chlorolignins. A deep study on the sodium chlorite/acetic acid pretreatment of hybrid *Pennisetum* straw, citing also recent developments with reference to biofuel production, has been recently published.⁹⁴ It is worth noting that such a pretreatment is rather selective toward lignin and increases substantially polysaccharide digestibility. A treatment of rice straw with chlorine dioxide has shown promising results⁶⁶ with respect to delignification of such a LBM. Alas, chlorine dioxide is an expensive, toxic, unstable, and explosive reagent, so these substantial limitations should be taken into due account.

A huge number of studies have been published concerning the use of hydrogen peroxide as a delignifying agent for LBM, usually under moderate alkaline conditions. Effectiveness of the process ranges from moderate to good, and its main advantages are economical (hydrogen peroxide is a comparatively inexpensive reagent and is manageable and safe enough for industrial applications) and environmental (the only stable end-products of its action are molecular oxygen and water). Generally speaking, although hydrogen peroxide is a stronger oxidant at low pH values, it is often more effective under moderately alkaline (pH 10–12) conditions, where its mode of action is at least in part based on the formation of superoxide and hydroxyl radicals and also the extremely reactive singlet oxygen. Important changes toward a more substantial, if not exclusively, radical character of H₂O₂ action are observed in the presence of certain redox-active transition metals such as Cu, Mn, and especially Fe (Fenton or Fenton-like reactions).

These general features of lignin oxidation by hydrogen peroxide have been recently reviewed.^{97,98} Some outstanding examples are cited here, relative to straw LBM pretreatments involving H₂O₂. *Panicum virgatum* and *Zea mays* derived LBM were subjected to alkaline hydrogen peroxide pretreatment; in both materials, a substantial cleavage of alkyl aryl ether linkages was found, in particular of β -O-4 ones, leading to lignin solubilization and increase of polysaccharide hydrolysis.⁹⁹ Barley straw was investigated with relation to its response to optimized alkaline hydrogen peroxide pretreatment, and a substantial improvement of glucose yields through enzymatic hydrolysis of the solid residue was assessed.¹⁰⁰ Another promising study deals with hydrogen peroxide pretreatment prior to ammonia fiber expansion of corn stover; in detail, demethylation of G units took place, concomitant with cleavage of a significant fraction of β -O-4 linkages; conversely, resinol and phenylcoumaran moieties remained substantially unchanged. Some γ carbons were oxidized, and the primary alcohol functions were changed into carbamides. As a result, a substantial decrease in lignin MW was observed. Indeed, a sharp improvement in saccharification was obtained.¹⁰¹

Addition of hydrogen peroxide to acidic pretreating solutions affords the production of hydrolyzed hemicelluloses, where undesired furane aldehydes have been oxidized to carboxylic acids, thus preventing any inhibition phenomena of the microorganisms used to produce bioethanol. Various studies have been recently published^{102–104} employing hydrogen peroxide in acetic or phosphoric acids; satisfactory extent of ligninolysis was observed besides a substantial hemicellulose hydrolytic removal. Performic acid (arising from the direct reaction between formic acid and H₂O₂) has a noticeable

tendency toward heterolytic scission affording the virtual hydroxylum ion, which is a very effective electrophile and could efficiently break lignin down through a Baeyer–Villiger-like oxidation reaction cutting the α -C β linkages within the phenylpropanoid units.^{105,106}

As noted above, H₂O₂ could also act as a source of hydroxyl radicals, under the conditions of the Fenton (and also Haber–Weiss) reaction, causing a noticeable improvement in straw LBM digestibility.^{107–109}

Fungal Redox Enzymes for the Delignification of Straw LBM. In Nature some fungi, like white rot fungi (WRF), brown rot fungi (BRF), and soft rot fungi (SRF), live and grow on wood or on LBM, both natural or artificial. WRF and BRF belong to the group of basidiomycetes, while the SRF group consists mostly of ascomycetes.¹¹⁰ It has been shown that basidiomycetous WRF are able to delignify lignocellulosic feedstock efficiently, unlike the BRF, which delignify biomass slowly and incompletely; SRF mainly attack polysaccharides, so their delignification efficiency is irrelevant.^{111,112}

The use of fungi to pretreat biomass is called biological pretreatment. Due to its many advantages in the delignification process such as low energy supply, low environmental impact, and high substrate specificity, biological pretreatment is considered a cleaner and greener approach compared to physical and chemical pretreatments.^{111,113,114} Nevertheless, this approach shows several drawbacks such as the loss of polysaccharides, which leads to low sugar and ethanol yields, and long reaction times (from 13 up to 50 days) to obtain high yields of delignification. Moreover, the process depends on many factors such as cultivation time, fungal strains, and culture conditions.¹¹⁵ Therefore, biological pretreatments on industrial scale are still limited.¹¹⁶ Fungal degradation of lignin is the result of the cooperative actions of several enzymes. The use of ligninolytic enzymes secreted by WRF involved in natural delignification processes could overcome these drawbacks.¹¹⁷ Enzymatic delignification is attractive because it is faster than biological pretreatment and can operate in a wide range of pH (3–8) and temperature (25–80 °C). Moreover, it does not require supplementation of nutrients.

The most important ligninolytic enzymes (Figure 8) from WRF extracts²⁵ are laccases (phenol oxidases) and hemeperoxidases (lignin peroxidase, manganese peroxidase, versatile peroxidase). The delignification process could be enhanced by the cooperative action of several accessory enzymes, such as glyoxal oxidase, aryl alcohol oxidase, and veratryl alcohol oxidase able to generate hydrogen peroxide essential for peroxidase mechanism.^{23,118} Initially somewhat surprisingly, early studies showed that purified ligninolytic enzymes are often most active toward oligomeric model compounds, whereas their activity tends to decrease when facing real lignin preparations. Moreover, it has been well-known for decades that sometimes the main effect of ligninolytic enzymes is further polymerization rather than depolymerization.^{119,120} This depends mainly on the radical character of the reactions catalyzed by the ligninolytic enzymes: the arising radicals could spontaneously undergo cleavage, reaction with molecular oxygen, or disproportionation to quinones or can polymerize. *In vivo*, polymerization is usually prevented by the intervention of other enzymes, reducing reactive quinones to catechols,¹²¹ which in turn undergo irreversible cleavage by dioxygenases. Obviously, the use of such complex mixtures of enzymes along industrial applications is only seldom feasible, and therefore other shrewdness must be adopted to overcome the problem.

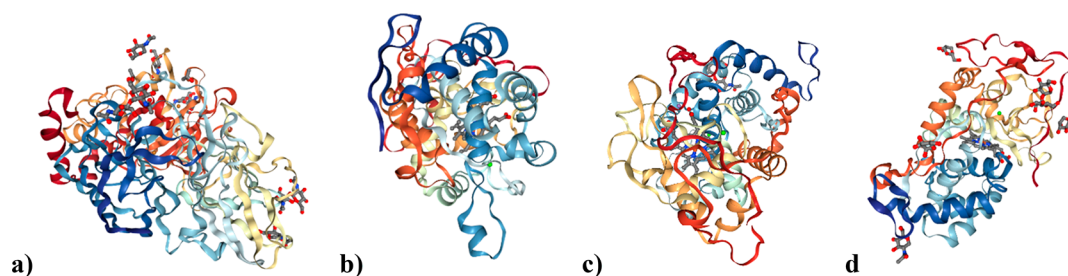


Figure 8. Structures of some ligninolytic enzymes: (a) laccase from *Trametes versicolor*, 1GYC; (b) lignin peroxidase from *Phanerochaete chrysosporium*, 1B85; (c) manganese peroxidase from *P. chrysosporium*, 1MNP, (d) Versatile peroxidase from *Pleurotus eryngii*, 3FJW.

Ligninolytic redox enzymes are described in the following paragraphs. The ligninolytic enzymes will be initially listed and briefly described, then the most promising strategies to improve their performance in terms of activity and stability will be described.¹¹⁰

Laccases. Laccases, LCs (EC 1.10.3.2, benzenediol:oxygen oxidoreductase), are extracellular N-glycosylated multicopper oxidases able to oxidize various phenolic and nonphenolic compounds by one electron transfer with the concomitant reduction of dioxygen to water.¹²² They are widespread among higher plants, bacteria, insects and WRF.¹²³ Their physicochemical properties, such as isoelectric point, molecular size, stability, activity, etc. depend on the source. Indeed, due to their higher redox potential,¹²⁴ fungal laccases rather than bacterial laccases are widely used in biorefineries and bioremediation processes.²³ LCs typically comprise three domains and contain four copper ions arranged in mononuclear and trinuclear clusters. Substrate oxidation at the mononuclear site generates electrons that are transferred one by one to the trinuclear site where O₂ is reduced to water.¹²⁵ Their molecular mass commonly ranges between 50 and 140 kDa, but it has been reported to be from 34 to 383 kDa for laccases from *Pleurotus eryngii* and *Podospora anserina*.^{116,122,126,127} Due to their low substrate specificity, LCs can degrade several compounds with a phenolic structure, including lignins.¹²⁸ For example, Sondhi et al. obtained a 28% reduction in kappa number (a measurement of total amount of material oxidizable by KMnO₄) by means of thermophilic LC from *Bacillus tequilensis*.¹²⁹

To date, the number of microorganisms involved in the delignification process is still unknown;²⁵ however it is certain that the features of their secreted ligninolytic enzymes depend on their nature and ecology.¹³⁰ Due to their ability to produce ligninolytic enzymes showing different properties compared to terrestrial enzymes (such as high salt tolerance, pH extremes, and thermostability), interest in marine-derived fungal species is growing. Rodriguez-Couto investigated the ability of the marine fungus *Phlebia* sp. MG-60 to degrade sugar cane bagasse for 30 days. The treatment leads to about 52% decrease of lignin in the raw material.¹³¹ D'Souza-Ticlo et al. extracted from fungus MTCC 5159 (*Cerrena unicolor*) a LC stable at pH 9 and able to retain >60% of its activity up to 180 min at 50 and 60 °C. The same enzyme was tested in the presence of Pb, Fe, Ni, Li, Co, and Cd ions at 1 mmol. The results showed no inhibition by salts.¹³² Brenelli et al. obtained oxidative enzymes under saline and nonsaline conditions from the white-rot basidiomycete *Peniophora* sp. CBMAI 1063.¹³³ A LC form with thermal stability ranging from 30 to 50 °C (120 min) was extracted and characterized from the same fungus.¹³⁴

The use of enzymes in their native form employed directly on industrial scales is often hampered by the industrial harsh

reaction conditions (such as extreme values of pH and temperature), which could lead to a loss of activity.¹³⁵ Due to the need for obtaining enzymes able to work under extreme operative conditions, enzyme engineering is considered an attractive technology for making them suitable for industrial and biotechnological applications.¹³⁶ This technique implies the modification of the amino acid sequence, the main approaches reported in literature being rational design and directed evolution.¹³⁷ The engineering of ligninolytic enzymes could play a crucial role in the field of biomass delignification. Several works about this topic have been reported. The LC from *Pycnoporus cinnabarinus* is considered one of the most promising high-redox-potential enzymes for environmental biocatalysis; Camarero et al. expressed it in *Saccharomyces cerevisiae* obtaining a laccase total activity enhanced 8000-fold.¹³⁸ Kwiatos et al. described the engineering of *Fusarium oxysporum* LC expressed in *Saccharomyces cerevisiae* and engineered toward higher expression levels and higher reactivity toward 2,6-dimethoxyphenol, which could be used as a mediator for lignin modification.¹³⁹ It is known that laccases typically show their optimum activity below neutral pH values. It is supposed that the excess of OH⁻ ions inhibits electron transfer from T1 Cu to the trinuclear copper cluster. However, some important industrial applications require LCs active at pH ≥ 7, such as paper pulp bleaching and decolorization of industrial dyes.¹⁴⁰ LC engineering is considered a promising tool to overcome this bottleneck. Fang et al. expressed Lac15D, a bacterial LC screened from a marine metagenomic library, in *E. coli*, obtaining an enzyme with a high tolerance to halogen ions able to work under alkaline conditions.^{141,142} Yin et al. engineered the LC from the basidiomycete *Coprinopsis cinerea*, which showed an optimum pH of 8.5 toward guaiacol and retained more than 70% of its activity at pH range of 7–9.¹⁴³

However, due to their relatively low redox potential (0.5–0.8 V), LCs are not able to oxidize nonphenolic subunits with a high redox potential, which comprise more than 80% of lignin.^{23,144} Moreover, because of their size, LCs are unable to penetrate the small pores of plant cell walls.¹¹⁷ To overcome these issues, the use of mediators has been proposed.^{145,146}

Laccase Mediators. Mediators are small, soluble molecules able to transfer electrons from the to-be-oxidized molecules to the LC active site.¹¹⁷ In the case of LBM, they can shuttle between the surface of the solid substrate and the enzyme. Laccase mediator systems (LMSs) have a higher redox potential ($E^{\circ} > 1.1$ V) in comparison to LC in the Cu T1 site ($E^{\circ} = 0.5$ – 0.8 V) and are able to oxidize lignin to a good extent (Figure 9).^{72,147,148}

Among them (Figure 10), 2,2'-azino-bis(3-ethylbenzothiazoline-6-sulfonic acid diammonium salt (ABTS), 1-hydroxybenzotriazole (HBT), and 2,2,6,6-tetramethylpiperidine-1-oxyl

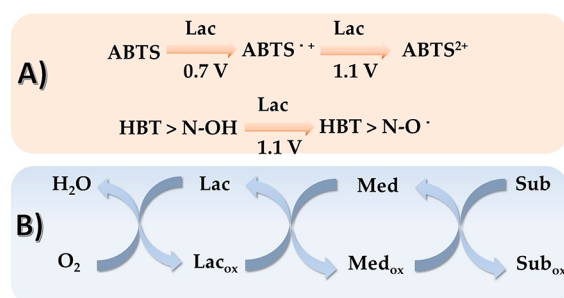


Figure 9. (A) Redox potentials of the oxidation reactions of ABTS and HBT by laccase and (B) LMS mechanism.

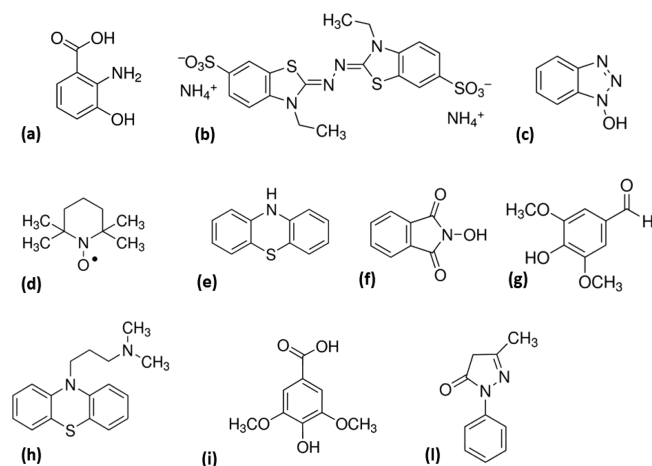


Figure 10. Most common laccase mediators: (a) 3-hydroxyanthranilic acid; (b) ABTS; (c) HBT; (d) TEMPO; (e) phenothiazine; (f) *N*-hydroxyphthalimide (HPI); (g) 3,5-dimethoxy-4-hydroxybenzaldehyde, 4-hydroxy-3,5-dimethoxybenzaldehyde (Syringaldehyde); (h) 10-(3-(dimethylamino)propyl)phenothiazine (Promazine); (i) methyl ester of 4-hydroxy-3,5-dimethoxy-benzoic acid (syringic acid); (l) 1-phenyl-3-methyl-5-pyrazolone.

(TEMPO) are likely the most used mediators.¹¹⁷ However, a substantial substitution of 4-hydroxy-TEMPO for TEMPO in the near future could be reasonably forecast, as the former is substantially less expensive than the latter and shows comparable catalytic efficiency.¹⁴⁹

It has been common knowledge for a long time that LC is deeply involved in delignification of LBM by WRF. However, fungal LCs alone are generally unable to efficiently promote delignification *in vitro*, most probably because of the

concomitant presence of other necessary enzymes or natural redox mediators *in vivo*. The delignification degree in the presence of such mediators depends on reaction conditions, as well as on LBM type and enzyme source. For these reasons, the attainment of the highest delignification yield requires the systematic screening of enzymes from different sources, as well as of mediators and of operating conditions. Gutiérrez et al. reported the use of LC from *Trametes villosa*, with HBT as mediator and alkaline extraction, to delignify *Eucalyptus globulus* wood and *Pennisetum purpureum* nonwood with lignin removal of 48% and 32%, respectively.¹⁵⁰ Xie et al. achieved 35% solubilization of the insoluble Kraft lignin through the use of LC from *Trametes versicolor* in the presence of HBT.¹⁵¹ The use of thermophilic enzymatic sources could allow overcoming of low thermal stabilities of conventional LCs. Navas et al. used a thermophilic LC from *Thermus* sp. 2.9 incubated with steam-exploded biomass (*Eucalyptus globulus*) at 60 °C for 24 h in the presence of HBT as mediator obtaining a decrease in the intensity of the IR bands associated with lignin aromatic backbone and lignin–hemicellulose linkages.¹⁵² A very recent study sheds light on the intimate mechanism of straw delignification by a LC/HBT mediator system:¹⁵³ subtle analytical methods revealed C α oxidation and C α –C β and β -O–4 oxidative cleavage. In the same study, a significant reduction in phenylcoumaran and resinol linkages was found, showing that also the poorly reactive β – β and β –5 C–C links could be targets of the laccase/mediator system. The final result is a substantial delignification. Another study¹⁵⁴ on corn cob lignin and two fungal LCs (from *Cerrena unicolor* and *Trametes versicolor*) in the presence of some redox mediators has shown the importance of mediators in the delignification process. In another study¹⁵⁵ on sugar cane bagasse and straw, the LC from *Pycnoporus cinnabarinus* in the presence of HBT caused a noticeable delignification, which correlates with a substantial improvement of saccharification yields. Recombinant LC from *Pleurotus ostreatus* was shown to be able to degrade corn stover lignin in the presence of suitable mediators.¹⁵⁶ Also a bacterial LC from *Bacillus ligniniphilus*, alone or in the presence of mediators such as ABTS, has proven effective¹⁵⁷ in lignin (alkaline lignin and milled wood lignin) oxidative degradation, as it has been recently shown. In particular, a selective removal of S units, within the frame of general demethoxylation, was observed. Different from other fungal and bacterial LCs, this enzyme promoted only limited repolymerization of the hydroxyaromatics it obtained from lignin. Overall, whereas being *per se* capable of degrading lignin, the enzyme worked better in the

Table 1. A Synopsis of Various LCs, Their Mediators (if Any), and Their Substrates

laccase source	mediator	solvent	lignocellulosic feedstock	lignin loss %	refs
<i>Trametes versicolor</i>	HBT	35 mM phosphate buffer (pH 7)		35%	151
Ascomycete <i>Myceliophthora thermophila</i>	Methyl syringate	50 mM sodium dihydrogen phosphate (pH 6.5)	<i>Eucalyptus globulus</i>	up to 50% (after alkaline peroxide extraction)	72
<i>Trametes villosa</i>	HBT	50 mM sodium tartrate buffer (pH 4)	<i>Eucalyptus globulus</i>	up to 48% (after alkaline peroxide extraction)	150
<i>Thermus</i> sp. 2.9			<i>Eucalyptus globulus</i>		152
<i>Trametes versicolor</i>	HBT	[C ₂ mim][OAc]	seaweed biomass (a mix of <i>Chaetomorpha</i> and <i>Cladophora</i>)	up to 27%	162
<i>Aquisalibacillus elongatus</i>		[Bmim][PF ₆]	sugar beet pulp	78.4%	163
<i>Trametes</i> sp.	HBT	[EMIM][DEP]	oil palm biomass	35.4%	158
<i>Trametes versicolor</i> IBL-04		50 mM sodium malonate buffer pH 4.5	sugar cane bagasse	78.3%	165
<i>Trametes versicolor</i>		[Bmim][PF ₆]	lignocellulosic biomass	kappa number 77.3%	166

presence of ABTS mediator. Table 1 presents some examples of laccases, alone or in the presence of suitable mediators, acting on the specified substrates.

Laccases in Ionic Liquids. Recent works have reported the possibility to obtain a quick conversion of lignocellulosic biomass to cellulose through the combined use of ionic liquids (ILs) and redox enzymes.^{138,159}

These features allow such solvents to increase the enzyme accessible surface area of LBM, leading to a more efficient enzymatic delignification. Depending on the cation–anion pair, ILs can either activate or inhibit ligninolytic enzymes.^{14,160} Galai et al. screened *Trametes versicolor* LC (TvL) activity in 56 different ILs and found that 13 of them improved laccase activity in comparison to buffer solutions. The most notable improvement was seen in 10 mM [Ch][H₂PO₄] (cholinium dihydrogen phosphate) in sodium acetate buffer (50 mM; pH 7.0), which increased TvL activity by 451% compared to the IL-free control acetate buffer.¹⁶¹ Stevens et al. measured the enzyme activity of the LC from *Trametes versicolor* in different ILs. They found that [DEA][HSO₄] (diethylammonium hydrogen sulfate) allowed TvL to oxidize ABTS, while [EMIM][OAc] (1-ethyl-3-methylimidazolium acetate) and [Ch][Lys] (cholinium lysinate) inactivated the laccase even at very low concentrations.¹⁶⁰

Financie et al. obtained a significantly enhanced rate of enzymatic delignification of palm oil biomass (OPFB) by LC from *Trametes* sp. in [EMIM][DEP] (1-ethyl-3-methylimidazolium-diethyl phosphate). They obtained a final lignin content of about 8.5 wt %, compared to the initial 24.0 wt % of untreated OPFB.¹⁵⁸ Al-Zuhair et al. investigated the enzymatic delignification of seaweed biomass (a mix of *Chaetomorpha* and *Cladophora* species), carried out using TvL, HBT, and [EMIM][OAc] obtaining a delignification degree up to 27%.¹⁶² Rezaei et al. reported the use of LC from the halophilic bacterium *Aquisalibacillus elongatus* in the presence of [BMIM][PF₆] (1-butyl-3-methylimidazolium hexafluorophosphate) to delignify sugar beet pulp, obtaining a delignification yield of 78.4% after 24 h.¹⁶³ The same enzyme was also tested in the same conditions in [BMIM][PF₆] to remove lignin from peanut shell, obtaining a lignin removal of 87% after 24 h.¹⁶⁴

Deep Eutectic Solvents. Deep eutectic solvents (DESs) are a new class of green solvents composed of a hydrogen bond acceptor (HBA, usually a quaternary ammonium salt) and a hydrogen bond donor (HBD) such as glycerol, succinic acid, etc. (Figure 11). DESs are becoming an attractive alternative to ILs.¹⁶⁷

Indeed, DESs show similar physical properties compared to traditional ILs, with the advantage of being less toxic, cheaper, and easier to prepare.¹⁶⁸ Some applications have been described where DESs are able to dissolve and remove lignin.^{169,170} Moreover, DESs could avoid the loss of catalytic activity or enzyme denaturation that can occur in several organic solvents.^{168,171} Toledo et al. screened laccase activity in 16 different DES/water mixtures.¹⁷² The activity did not change in the presence of most DESs, whereas in some cases, such as with ChDHC/Xyl (Choline dihydrogen citrate in xylitol) (2:1) at 25 wt %, an increase of relative activity up to 200% was observed.¹⁷² Khodaverdian et al.¹⁷⁴ studied the activity and stability of laccase from *Bacillus* HR03 in betaine-based natural DESs. These DESs are obtained from two or more compounds that are generally plant based primary metabolites, that is, organic acids, sugars, alcohols, amines, and amino acids.¹⁷³ The highest activity was obtained in 20% (v/v) glycerol/betaine (2:1).¹⁷⁴ Interest in DESs used in combination with mechanical^{175,176} and chemical

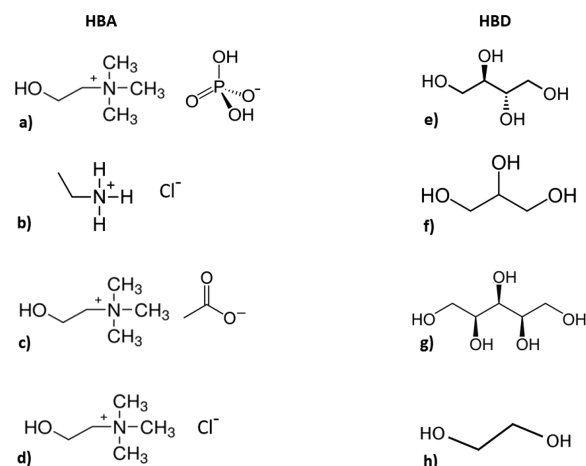


Figure 11. Some examples of acceptors (HBAs): (a) cholinium dihydrogen phosphate (ChH₂PO₄); (b) ethylammonium chloride (EACl); (c) cholinium acetate (ChAc); (d) Cholinium chloride (ChCl). Some examples of hydrogen bond donors (HBDs): (e) erythritol (Ery); (f) glycerol (Gly); (g) xylitol (Xyl); (h) ethylene glycol (EtG).

pretreatment^{177,178} is growing. However, the use of DESs for enzymatic LBM delignification has still not been extensively studied. To date, very few works regarding laccases and DESs have been reported.^{171,172,174} Hence, this topic is worthy of further investigation.

Peroxidases. Heme peroxidases are hemoproteins catalyzing the oxidation of various organic and inorganic substrates in the presence of hydrogen peroxide as the electron acceptor. They are widely distributed in nature: plants, animals, and microbes. Extracellular fungal peroxidases (lignin modifying peroxidases), such as lignin peroxidase (LiP), manganese peroxidase (MnP), and versatile peroxidase (VP), are involved in lignin degradation.^{179–181} In spite of looking like the best candidates for biodelignification, until now the ligninolytic peroxidases have been rather disappointing, owing to some important reasons: low productivity, unsuccessful attempts of heterologous expression and mutagenesis, and facile irreversible inactivation,¹⁸² especially in the presence of even a slight excess of H₂O₂.¹⁸³ Therefore, the use of ligninolytic peroxidases could be considered as a blind alley. On the other hand, they are quite worth being studied, as at least some of the cited drawbacks could be conceivably removed in the near future. In fact, some promising studies have been carried out in the field of ligninolytic peroxidase engineering. For example, Pham et al. engineered the LiPH8 from *Phanerochaete chrysosporium*, which is generally unstable under acidic pH conditions, to make it able to work under acidic conditions.¹⁸⁴ One of the main issues that occur frequently during biomass pretreatment is the formation of inhibitory compounds such as 5-hydroxymethyl-2-furaldehyde (HMF) and 2-furaldehyde (furfural). Yee et al. reported that a recombinant manganese peroxidase (rMnP) produced from the yeast *Pichia pastoris* was able to degrade furfural and HMF.¹⁸⁵ Peroxidases are generally sensitive to H₂O₂ concentration. In the literature, several reports concern the engineering of peroxidases to avoid this issue and make them more suitable for delignification process.^{186–188} Gonzalez-Perez et al. improved versatile peroxidase (VP) resistance to H₂O₂; an evolved version of this enzyme was subjected to a range of directed evolution and hybrid strategies in *Saccharomyces cerevisiae*. The result showed an increase of the half-life of the

protein from 3 (parental type) to 35 min in the presence of 3000 equiv of H_2O_2 and with a 6 °C upward shift in thermostability.¹⁸⁸

Lignin Peroxidase. Lignin peroxidase (EC 1.11.1.14) with its various isoforms, was first discovered in the extracellular medium of white rot fungus *Phanerochaete chrysosporium* by Tien and Kirk.¹⁸⁹ The crystal structure of *P. chrysosporium* LiP is constituted by 343 amino acids. Two glycosylation sites, two Ca^{2+} binding sites, and four disulfide bridges stabilize the three-dimensional structure of the enzyme.¹⁹⁰ The molecular mass of LiPs ranges from 35 to 48 kDa, and *pI* values range from 3.1 to 4.7 depending on the enzymatic source. Due to their high redox potential (around 1.2 V at pH 3), LiPs are able to oxidize the aromatic rings of lignin (irrespective of their methoxylation degree, but with preference for nonphenolic units), dyes, and a variety of recalcitrant pollutants.^{127,191,118} The LiP reaction cycle is comparable to other peroxidase cycle mechanisms (Figure 12).²⁵ First, the enzyme is oxidized by H_2O_2 , leading to

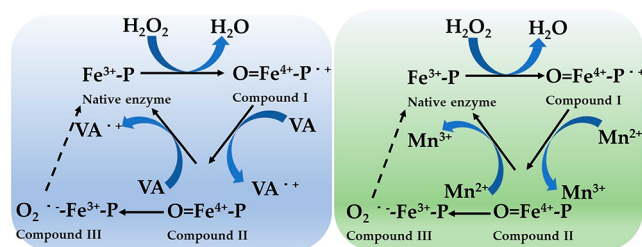


Figure 12. Catalytic cycle of LiP (left) and MnP (right).

the generation of the compound I that exists as a ferryl (iron(IV)-oxo complex) cation radical intermediate [$\text{O}=\text{Fe}^{\text{IV}}-\text{P}^{\bullet+}$]. Then, this undergoes two one-electron reduction steps by the electron donor substrate, such as lignin, lignin oligomers, or veratryl alcohol (VA), which acts as a mediator, leading to a transient formation of compound II [$\text{O}=\text{Fe}^{\text{IV}}-\text{P}$] and a very reactive radical cation ($\text{VA}^{\bullet+}$).¹⁹² Compound II further oxidizes the second VA molecule, returning it to its native state before starting a new catalytic cycle of LiP.²³ The eventual excess of H_2O_2 at pH 3 in the absence of a substrate converts compound II to compound III [$\text{Fe}^{\text{III}}\text{O}_2^{\bullet-}$], which is rapidly and irreversibly bleached or returns to its native form by spontaneous autoxidation or oxidation through $\text{VA}^{\bullet+}$.^{23,110,190}

Manganese Peroxidase. Manganese peroxidase (EC 1.11.1.13) and its isoforms were first detected in *P. chrysosporium* (the teleomorph of *Sporotrichum pruinosum*) by Glenn, Gold, et al.¹⁷⁹ It is an oxidoreductase with its heme group included between two α -helix domains, 350 amino acids, and a 43% sequence similarity with LiP.¹⁹⁰ It contains five disulfide bridges and two Ca^{2+} ions, which maintain the structure of the active enzyme. The Mn^{II} -binding site consists of two glutamate and one aspartate γ -carboxylic groups and is located close to the porphyrin macrocycle. Their molecular mass ranges from 38 to 62.5 kDa, and their *pI* values range from 2.9 to 7.1. The catalytic cycles of MnPs and LiPs are very similar, with the exception for the use of Mn^{II} as their reducing substrate, generating Mn^{III} , which diffuses from enzymes into the lignocellulose structure (Figure 8). To date, MnP has not been used for biomass delignification. Nevertheless, it is widely used for dye decolorization. For example, Zhang et al. reported the dye decolorization by a manganese peroxidase from *Cerrena unicolor* BBP6.¹⁹³ Siddeeq et al. immobilized MnP enzyme extracted

from *Anthracoophyllum discolor* on iron oxide/chitosan magnetic nanocomposite for decolorization of textile wastewater.¹⁹⁴

Versatile Peroxidase. Versatile peroxidase (EC 1.11.1.16) was found for the first time in *Pleurotus eryngii* and *Bjerkandera adusta*.¹⁹⁵ It shows functional characteristics of both LiP (oxidation of substrates like VA and aromatic compounds) and MnP (oxidation of Mn^{II} to Mn^{III}) that make it able to oxidize high and medium redox potential compounds in the absence of mediators. VP shows a structure constituted by 11–12 helices, four disulfide bridges, two structural Ca^{2+} sites, a heme pocket, and a Mn^{2+} -binding site.¹²⁷ Its molecular mass ranges from 40 to 45 kDa with a *pI* range from 3.4 and 3.9. The basic catalytic cycle of VPs is similar to those of other peroxidases with the two intermediary compounds I and II.²⁵ One could expect that VP should be a very effective ligninolytic catalyst, combining the features of LiP and MnP. On the contrary, *Pleurotus eryngii*, a good VP producer, is slow and poorly efficient in ligninolysis.

Crude Enzyme Mixtures. The use of a single peroxidase for biomass pretreatment is ineffective to obtain a high delignification degree. Nevertheless, the use of crude enzyme mixtures (enzymatic cocktails composed mainly of LCs, LiP, MnP, and VP) constitutes a more effective strategy,¹⁹⁶ also when taking into account that LiP acts preferentially on nonphenolic units, whereas MnP shows sharp preference for the phenolic ones. There are several advantages in using crude enzyme mixtures. As reported by Asgher et al., they could contain accessory enzymes that enhance the degradation of lignin compounds. Moreover, some studies show that the extract could contain cellulases able to hydrolyze the delignified lignocellulosic biomass simultaneously. The delignification by means of crude enzyme mixtures is generally carried out under mild conditions.¹¹⁵ Nonetheless, the efficiency of the process depends on several aspects, such as biomass features and operating conditions (pH, temperature, mediator(s), oxygen, and use of surfactants).¹⁹⁶ Asgher et al. reported the use of a crude enzyme mixture containing LiP, MnP, and LC extract from *Pleurotus ostreatus* IBL-02 to pretreat sugar cane bagasse, obtaining a 33.6% lignin loss.¹⁹⁷ Kong et al. reported the use of crude enzyme extract (MnP and LC) from white-rot fungus *Echinodontium taxodii* 2538 to delignify bamboo biomass. Their results showed a higher lignin degradation when enzymes were used simultaneously rather than singularly.¹⁹⁸

Immobilized Enzymes. The use of free ligninolytic enzymes can often result in several limitations such as low operational stability (under extreme conditions of temperature and pH) and difficult recovery and reuse.¹⁹⁹ Most of these problems can be overcome through enzyme immobilization on solid supports such as xerogels, sand, clay, nanofibrous polymers, or nanoparticles.¹⁴⁷ Although immobilization usually worsens the kinetic parameters of the enzyme and therefore its overall catalytic efficiency, the facile recovery, in particular when using magnetic particles, and the improved stability largely counterbalance the drawback. In the case of LBM, the problem of the insolubility of lignin could be overcome in two ways: (a) the use of ILs or DESs at least in part solubilizes the lignin and therefore it can be efficiently oxidized by the enzyme; (b) the use of suitable mediators as molecular shuttles allows the effective flux of the electrons from lignin to LC. The two ways could well operate together for optimal performance of immobilized LCs. The choice of the support and the method involved in enzyme immobilization are important factors that affect the enzyme activity and stability. To the best of our knowledge, very few

Table 2. Immobilized Ligninolytic Enzymes at Work

enzyme	enzyme source	carrier	solvent	lignocellulosic feedstock	lignin loss %	refs
LC	<i>Trametes versicolor</i> IBL-04	alginate–chitosan	50 mM sodium malonate buffer (pH 4.5)	sugar cane bagasse	78.3%	165
LC	<i>Trametes versicolor</i>	Fe ₃ O ₄ @SiO ₂ @Kit-6 magnetite nanoparticles	[Bmim][PF ₆]	olive pomace biowaste	kappa number 77.3%	166
LC	<i>Trametes versicolor</i>	ferrite (MNPs)	50 mM sodium citrate buffer (pH 4.8)	<i>Ipomoea carnea</i>	38.16	204
LC	<i>Trametes versicolor</i>	copper ferrite magnetic nanoparticles (CuMNPs)	50 mM sodium citrate buffer (pH 4.8)	<i>Ipomoea carnea</i>	43.3%	204
LiP, MnP, LC	<i>Ganoderma lucidum</i> IBL-05	alginate–chitosan beads	50 mM sodium malonate buffer (pH 4.5)		57.3%	200
LC	<i>Lentinus tigrinus</i>	SBA-15 mesoporous silica	50 mM citrate buffer (pH 4.5)	pistachio shell	91%	205
LC, cellulase, and β -glucosidase		co-immobilization in sodium alginate beds	100 mM citrate buffer (pH 4.8)	<i>Ipomoea carnea</i>	35.7	206
LC, cellulase, and β -glucosidase		co-immobilization in sodium alginate beds	100 mm citrate buffer (pH 4.8)	<i>Saccharum arundinaceum</i>	24.1%	206

works about the immobilization of crude enzyme mixtures have been reported. In contrast, LC immobilization has widely been investigated.^{200–202} Bilal et al. reported the use of a ligninolytic enzyme cocktail from *Ganoderma lucidum* IBL-05 immobilized on alginate–chitosan beds to delignify sorghum stover, obtaining a delignification of 57.3% after 15 h. The reaction was carried out in 50 mM sodium malonate buffer (pH 4.5) and is relevant as delignification proceeds without the use of mediators.²⁰⁰ Chang et al. studied the entrapment of laccase from the lacquer tree *Rhus vernicifera* in a cellulose ester membrane, finding that the immobilized LC had much higher levels of retained activity (20.34% after 2 days) compared with the free LC.²⁰³ Amin et al. immobilized LC from *Trametes versicolor* by covalent attachment on modified Fe₃O₄@SiO₂@Kit-6 magnetite nanoparticles in the presence of IL for enhanced delignification of olive pomace biowaste.¹⁶⁶ They obtained up to 77.3% decrease in kappa number (after 6 h of incubation of the biomass with immobilized LC and [Bmim][PF₆]) as ionic liquid without any mediator. Muthuvelu et al. immobilized LC from *Trametes versicolor* on ferrite (MNPs) and copper ferrite magnetic nanoparticles (CuMNPs).²⁰⁴ They obtained higher activity recovery for the LC immobilized on CuMNPs (13.2 U/mL) than for that on MNPs (10.93 U/mL). Moreover, they investigated the delignification of *Ipomoea carnea* using both free and immobilized LC without mediator. After 20 h of incubation, they obtained lignin removal of 43% for the enzyme immobilized on CuMNPs, 40% for LC immobilized on MNPs, and 38% for the free enzyme.²⁰⁴ Asgher et al. reported the use of LC from *Trametes versicolor* IBL-04 immobilized on alginate–chitosan beads.¹⁶⁵ A marked reduction in lignin content of all the studied LBM was obtained after 15 h, with the highest delignification (78%) for sugar cane bagasse, followed by wheat bran and maize stover. The experiments were carried out in 50 mM sodium malonate buffer (pH 4.5) without any mediator. Sadeghian-Abadi et al.²⁰⁵ immobilized LC from *Lentinus tigrinus* by covalent attachment on SBA-15 mesoporous silica. The immobilized enzyme was active toward the delignification of pistachio shell, achieving an efficiency of 91% after 12 h of incubation without mediator in 50 mM citrate buffer (pH 4.5). Moreover, they screened a range of mediators (2,6-dimethoxyphenol, GA, HBT, TEMPO, and vanillin) at different concentration (1, 5, 10 mM) to test their effect on enzymatic delignification. Their results show that TEMPO was the most effective mediator at all concentrations with a maximum delignification degree of 68.77% after 8 h of reaction.

This work showed that it is possible to obtain a good delignification degree with purified laccases without using mediators.²⁰⁵ Muthuvelu et al. developed the coimmobilization of three enzymes (laccase, cellulase, and β -glucosidase) in sodium alginate beds for delignification of different biomasses such as *Typha angustifolia*, *Arundo donax*, *Saccharum arundinaceum*, and *Ipomoea carnea*.²⁰⁶

Table 2 encompasses some outstanding examples of ligninolytic enzymes (mainly LCs) working on the specified LBM.

CONCLUSIONS

Turning herbaceous LBM into platform chemicals and fuels is an important opportunity to produce sustainable economies. Nevertheless, their exploitation is affected by the need for pretreatments, enzymatic hydrolysis, and fermentation stages. One of the most critical steps is the pretreatment one. Among those reported in literature, enzymatic pretreatments are considered the most ecosustainable. However, due to high prices, possible low stability, and catalytic activity of the involved enzymes, this technology is still a challenge. Moreover, the delignification degree depends on the chosen enzymes, suitable supports for immobilization, use of redox mediators, reaction conditions, and solvents. Some of these issues have been analyzed in this review. In these last years, the interest to overcome these problems in order to increase the cost-effectiveness of biofuel production and to make the transition from the laboratory to the industrial/commercial scale is widely growing. The future goals to overcome these drawbacks could enhance the enzymatic stability and activity using new supports for enzyme immobilization, solvents as DESs, and redox mediators. To the best of our knowledge, there are not studies where white-rot fungi (WRF) ligninolytic peroxidases have been used on their own to delignify LBM, for the reasons depicted above. So the use of such promising but disappointing enzymes has not found any significant utilization in delignification processes, although these peroxidases are useful, for example, in decolorizing wastewaters from paint and textile factories. In contrast, fungal LCs fully keep what they promise, and therefore their use, under the operative conditions and tricks above-described, is actually booming. And a further expansion of their use could be easily and reasonably anticipated.

AUTHOR INFORMATION

Corresponding Authors

Andrea Salis – Department of Chemical and Geological Sciences and Centro NanoBiotecnologie Sardegna (CNBS), University of Cagliari Cittadella Universitaria, 09042 Monserrato, CA, Italy; Consorzio Interuniversitario per lo Sviluppo dei Sistemi a Grande Interfase (CSGI), 50019 Sesto Fiorentino, FI, Italy; Unità Operativa, University of Cagliari, 09042 Monserrato, CA, Italy; orcid.org/0000-0001-5746-2693; Email: asalis@unica.it

Enrico Sanjust – Consorzio Interuniversitario per lo Sviluppo dei Sistemi a Grande Interfase (CSGI), 50019 Sesto Fiorentino, FI, Italy; Unità Operativa, University of Cagliari, 09042 Monserrato, CA, Italy; Department of Biomedical Sciences, University of Cagliari Cittadella Universitaria, 09042 Monserrato, CA, Italy; orcid.org/0000-0003-3365-912X; Email: sanjust@unica.it

Authors

Davide Tocco – Department of Chemical and Geological Sciences and Centro NanoBiotecnologie Sardegna (CNBS), University of Cagliari Cittadella Universitaria, 09042 Monserrato, CA, Italy

Cristina Carucci – Department of Chemical and Geological Sciences and Centro NanoBiotecnologie Sardegna (CNBS), University of Cagliari Cittadella Universitaria, 09042 Monserrato, CA, Italy; Consorzio Interuniversitario per lo Sviluppo dei Sistemi a Grande Interfase (CSGI), 50019 Sesto Fiorentino, FI, Italy; Unità Operativa, University of Cagliari, 09042 Monserrato, CA, Italy; orcid.org/0000-0001-8660-788X

Maura Monduzzi – Department of Chemical and Geological Sciences and Centro NanoBiotecnologie Sardegna (CNBS), University of Cagliari Cittadella Universitaria, 09042 Monserrato, CA, Italy; Consorzio Interuniversitario per lo Sviluppo dei Sistemi a Grande Interfase (CSGI), 50019 Sesto Fiorentino, FI, Italy; Unità Operativa, University of Cagliari, 09042 Monserrato, CA, Italy; orcid.org/0000-0003-0200-7700

Complete contact information is available at:
<https://pubs.acs.org/10.1021/acssuschemeng.0c07266>

Notes

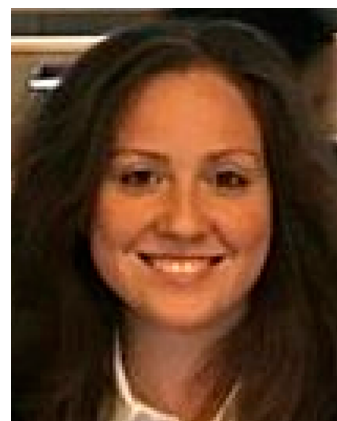
The authors declare no competing financial interest.

Biographies



Davide Tocco graduated from University of Cagliari-Italy (M.Sc.) in 2018. He has been Erasmus student at University of Limerick (Ireland). In 2019, He won a Ph.D. Scholarship PON-Cycle XXXIV (2019–

2021) with a project entitled “Biofuels from biocatalysis: the importance of enzyme immobilization”. His research focuses on the immobilization of enzymes within metal–organic frameworks (MOFs), in particular fungal laccases for delignification of lignocellulosic biomass and lipases to produce biodiesel from exhaust oils. Currently, he was awarded a DAAD Scholarship, and he is spending a research period at Universität Erlangen-Nürnberg to develop a biocatalytic process to obtain cellulose from lignocellulosic biomass, to be used to produce bioethanol.



Dr. Cristina Carucci graduated in Chemistry (M.Sc. in Chemical Sciences) from University of Cagliari (Italy) in 2014. From 2014 to 2018, she studied at the University of Limerick (Ireland), and in 2018, she was awarded a Ph.D. with a thesis entitled “Screening of supports for immobilization of enzymes”. In the same year, she was recruited as a Postdoctoral researcher at the Université de Bordeaux (France) working between the “NanoSystèmes Analytiques” and the “Centre de Recherche Paul Pascal”. Currently, she is a researcher in Physical Chemistry at the Department of Chemical and Geological Sciences in Cagliari (Italy). Her research interests focus on materials design as supports and for biocatalysis, enzyme immobilization, and biophysical chemistry.



Maura Monduzzi is Full Professor of Physical Chemistry, Faculty of Sciences, University of Cagliari. Prof. Monduzzi’s main expertise includes colloid science, surfactant systems, liquid crystals, soft and hard matter nanostructured functional materials, modeling of NMR self-diffusion and relaxation data in complex fluids, specific ion effects in biological systems, charged interfaces, and biotechnology.



Andrea Salis (<http://people.unica.it/andreasalis/>) is Associate Professor of Physical Chemistry at the University of Cagliari. He received his Ph.D. in chemistry (2002). He has been a visiting student at Lund University (Sweden) and a Research Fellow at the Australian National University (Australia). His research interests include bio–nano-interfaces, ion specific effects, nanomedicine, and biocatalysis, particularly, enzyme immobilization on nanostructures and their use to remove pollutants and to treat biomass for the obtainment of biofuels.



Enrico Sanjust is Full Professor of Biochemistry at the University of Cagliari where he graduated in Chemistry in 1980 and gained his Ph.D. in Biotechnology in 1995 at the Cranfield Institute of Technology (U.K.). His research interests range from fungal ligninolytic enzymes to redox enzyme immobilization and emulsion by means of synthetic metalloporphyrin based systems.

ACKNOWLEDGMENTS

D.T. thanks MIUR (PON RI 2014-2020, Azione I.1 “Dottorati Innovativi con Caratterizzazione industriale”; DOT1304455 2) for financing his Ph.D. scholarship. CC acknowledges MIUR (PON-AIM Azione I.2; DD no. 407-27.02.2018, AIM1890410-2). TOC image has been created at Biorender.com.

REFERENCES

- (1) Stocker, T. F.; Clarke, G. K. C.; Le Treut, H.; Lindzen, R. S.; Meleshko, V. P.; Mugara, R. K.; Palmer, T. N.; Pierrehumbert, R. T.; Sellers, P. J.; Trenberth, K. E.; Willebrand, J. Physical Climate Processes and Feedbacks. *Clim. Chang. 2001 Sci. Bases. Contrib. Work. Gr. I to Third Assess. Rep. Intergov. Panel Clim. Chang.* **2001**, 881.
- (2) Hoffert, M. I.; Caldeira, K.; Benford, G.; Criswell, D. R.; Green, C.; Herzog, H.; Jain, A. K.; Keshgi, H. S.; Lackner, K. S.; Lewis, J. S.; Lightfoot, H. D.; Manheimer, W.; Mankins, J. C.; Mauel, M. E.; Perkins, L. J.; Schlesinger, M. E.; Volk, T.; Wigley, T. M. L. Advanced

Technology Paths to Global Climate Stability: Energy for a Greenhouse Planet. *Science (Washington, DC, U. S.)* **2002**, 298 (5595), 981–987.

(3) Lane, J.-E. Global Warming Is an Energy Conundrum. *Earth Sci. Res.* **2018**, 7 (2), 1.

(4) Salis, A.; Pinna, M.; Monduzzi, M.; Solinas, V. Biodiesel Production from Triolein and Short Chain Alcohols through Biocatalysis. *J. Biotechnol.* **2005**, 119 (3), 291–299.

(5) Schmer, M. R.; Vogel, K. P.; Mitchell, R. B.; Perrin, R. K. Net Energy of Cellulosic Ethanol from Switchgrass. *Proc. Natl. Acad. Sci. U. S. A.* **2008**, 105 (2), 464–469.

(6) Robak, K.; Balcerak, M. Review of Second-Generation Bioethanol Production from Residual Biomass. *Food Technol. Biotechnol.* **2018**, 56 (2), 174–187.

(7) Saini, J. K.; Saini, R.; Tewari, L. Lignocellulosic Agriculture Wastes as Biomass Feedstocks for Second-Generation Bioethanol Production: Concepts and Recent Developments. *3 Biotech* **2015**, 5 (4), 337–353.

(8) Galbe, M.; Wallberg, O.; Zacchi, G. Cellulosic Bioethanol Production. In *Separation and Purification Technologies in Biorefineries*; Ramaswamy, S., Huang, H.-J., Ramarao, B. V., Eds.; John Wiley & Sons Ltd, 2013; pp 487–501.

(9) Macrelli, S.; Galbe, M.; Wallberg, O. Effects of Production and Market Factors on Ethanol Profitability for an Integrated First and Second Generation Ethanol Plant Using the Whole Sugarcane as Feedstock. *Biotechnol. Biofuels* **2014**, 7 (1), 26.

(10) Olofsson, J.; Barta, Z.; Börjesson, P.; Wallberg, O. Integrating Enzyme Fermentation in Lignocellulosic Ethanol Production: Life-Cycle Assessment and Techno-Economic Analysis. *Biotechnol. Biofuels* **2017**, 10 (1), 1–14.

(11) Kumar, A.; Anushree; Kumar, J.; Bhaskar, T. Utilization of Lignin: A Sustainable and Eco-Friendly Approach. *J. Energy Inst.* **2020**, 93 (1), 235–271.

(12) Chen, H. Lignocellulose Biorefinery Feedstock Engineering. In *Lignocellulose Biorefinery Engineering*; Chen, H., Ed.; Elsevier, 2015; pp 37–86.

(13) Wen, J.-L.; Xiao, L.-P.; Sun, Y.-C.; Sun, S.-N.; Xu, F.; Sun, R.-C.; Zhang, X.-L. Comparative Study of Alkali-Soluble Hemicelluloses Isolated from Bamboo (*Bambusa Rigida*). *Carbohydr. Res.* **2011**, 346 (1), 111–120.

(14) Brandt, A.; Gräsvik, J.; Hallett, J. P.; Welton, T. Deconstruction of Lignocellulosic Biomass with Ionic Liquids. *Green Chem.* **2013**, 15 (3), 550–583.

(15) Houfani, A. A.; Anders, N.; Spiess, A. C.; Baldrian, P.; Benallaoua, S. Insights from Enzymatic Degradation of Cellulose and Hemicellulose to Fermentable Sugars— a Review. *Biomass Bioenergy* **2020**, 134, 105481.

(16) Ye, L.; Han, Y.; Feng, J.; Lu, X. A Review about GVL Production from Lignocellulose: Focusing on the Full Components Utilization. *Ind. Crops Prod.* **2020**, 144, 112031.

(17) Chen, H.; Xu, Q.; Zhang, D.; Liu, W.; Liu, X.; Yin, D. Highly Efficient Synthesis of γ -Valerolactone by Catalytic Conversion of Biomass-Derived Levulinic Esters over Support-Free Mesoporous Ni. *Renewable Energy* **2021**, 163, 1023–1032.

(18) Yan, L.; Yao, Q.; Fu, Y. Conversion of Levulinic Acid and Alkyl Levulinates into Biofuels and High-Value Chemicals. *Green Chem.* **2017**, 19 (23), 5527–5547.

(19) Ghosh, M. K.; Howard, M. S.; Zhang, Y.; Djebbi, K.; Capriolo, G.; Farooq, A.; Curran, H. J.; Dooley, S. The Combustion Kinetics of the Lignocellulosic Biofuel, Ethyl Levulinate. *Combust. Flame* **2018**, 193, 157–169.

(20) Vogel, J. Unique Aspects of the Grass Cell Wall. *Curr. Opin. Plant Biol.* **2008**, 11 (3), 301–307.

(21) Smith, B. G.; Harris, P. J. The Polysaccharide Composition of Poales Cell Walls: Poaceae Cell Walls Are Not Unique. *Biochem. Syst. Ecol.* **1999**, 27 (1), 33–53.

(22) del Río, J. C.; Rencoret, J.; Gutiérrez, A.; Elder, T.; Kim, H.; Ralph, J. Lignin Monomers from beyond the Canonical Monolignol Biosynthetic Pathway: Another Brick in the Wall. *ACS Sustainable Chem. Eng.* **2020**, 8, 4997.

- (23) Wong, D. W. S. Structure and Action Mechanism of Ligninolytic Enzymes. *Appl. Biochem. Biotechnol.* **2009**, *157* (2), 174–209.
- (24) Geng, W.; Narron, R.; Jiang, X.; Pawlak, J. J.; Chang, H.; Park, S.; Jameel, H.; Venditti, R. A. The Influence of Lignin Content and Structure on Hemicellulose Alkaline Extraction for Non-Wood and Hardwood Lignocellulosic Biomass. *Cellulose* **2019**, *26* (5), 3219–3230.
- (25) Janusz, G.; Pawlik, A.; Sulej, J.; Świdarska-Burek, U.; Jarosz-Wilkolazka, A.; Paszczyński, A. Lignin Degradation: Microorganisms, Enzymes Involved, Genomes Analysis and Evolution. *FEMS Microbiol. Rev.* **2017**, *41* (6), 941–962.
- (26) Abdelkafi, F.; Ammar, H.; Rousseau, B.; Tessier, M.; El Gharbi, R.; Fradet, A. Structural Analysis of Alfa Grass (*Stipa Tenacissima* L.) Lignin Obtained by Acetic Acid/Formic Acid Delignification. *Biomacromolecules* **2011**, *12* (11), 3895–3902.
- (27) Alves, A.; Simoes, R.; Stackpole, D. J.; Vaillancourt, R. E.; Potts, B. M.; Schwanninger, M.; Rodrigues, J. Determination of the Syringyl/Guaiacyl Ratio of Eucalyptus Globulus Wood Lignin by near Infrared-Based Partial Least Squares Regression Models Using Analytical Pyrolysis as the Reference Method. *J. Near Infrared Spectrosc.* **2011**, *19* (5), 343–348.
- (28) Lu, Y.; Lu, Y. C.; Hu, H. Q.; Xie, F. J.; Wei, X. Y.; Fan, X. Structural Characterization of Lignin and Its Degradation Products with Spectroscopic Methods. *J. Spectrosc.* **2017**, *2017*, 1.
- (29) Akpan, E. I. Chemistry and Structure of Lignin. In *Sustainable Lignin for carbon Fibers*; Akpan, E. I., Adeosun, S. O., Eds.; 2019; pp 1–50.
- (30) Oliveira, D. M.; Mota, T. R.; Grandis, A.; de Morais, G. R.; de Lucas, R. C.; Polizeli, M. L. T. M.; Marchiosi, R.; Buckeridge, M. S.; Ferrarese-Filho, O.; dos Santos, W. D. Lignin Plays a Key Role in Determining Biomass Recalcitrance in Forage Grasses. *Renewable Energy* **2020**, *147*, 2206–2217.
- (31) Chase, M. W.; Christenhusz, M. J. M.; Fay, M. F.; Byng, J. W.; Judd, W. S.; Soltis, D. E.; Mabberley, D. J.; Sennikov, A. N.; Soltis, P. S.; Stevens, P. F.; Briggs, B.; Brockington, S.; Chautems, A.; Clark, J. C.; Conran, J.; Haston, E.; Möller, M.; Moore, M.; Olmstead, R.; Perret, M.; Skog, L.; Smith, J.; Tank, D.; Vorontsova, M.; Weber, A. An Update of the Angiosperm Phylogeny Group Classification for the Orders and Families of Flowering Plants: APG IV. *Bot. J. Linn. Soc.* **2016**, *181* (1), 1–20.
- (32) Luo, J.; Liu, R.; Zhang, S.; Lian, C.; Yang, F.; Fei, B. Comparative Culm Anatomy of Metaxylem Vessel Pits in Three Different Types of Bamboo Rhizome. *IAWA J.* **2020**, *41* (2), 141–158.
- (33) Crestini, C.; Argyropoulos, D. S. Structural Analysis of Wheat Straw Lignin by Quantitative 31P and 2D NMR Spectroscopy. The Occurrence of Ester Bonds and α -O-4 Substructures. *J. Agric. Food Chem.* **1997**, *45* (4), 1212–1219.
- (34) Sun, R.; Lawther, J. M.; Banks, W. B. A Tentative Chemical Structure of Wheat Straw Lignin. *Ind. Crops Prod.* **1997**, *6* (1), 1–8.
- (35) Billa, E.; Toller, M. T.; Monties, B. Characterisation of the Monomeric Composition of in Situ Wheat Straw Lignins by Alkaline Nitrobenzene Oxidation: Effect of Temperature and Reaction Time. *J. Sci. Food Agric.* **1996**, *72* (2), 250–256.
- (36) Del Río, J. C.; Prinsen, P.; Rencoret, J.; Nieto, L.; Jiménez-Barbero, J.; Ralph, J.; Martínez, Á. T.; Gutiérrez, A. Structural Characterization of the Lignin in the Cortex and Pith of Elephant Grass (*Pennisetum Purpureum*) Stems. *J. Agric. Food Chem.* **2012**, *60* (14), 3619–3634.
- (37) Kim, H.; Padmakshan, D.; Li, Y.; Rencoret, J.; Hatfield, R. D.; Ralph, J. Characterization and Elimination of Undesirable Protein Residues in Plant Cell Wall Materials for Enhancing Lignin Analysis by Solution-State Nuclear Magnetic Resonance Spectroscopy. *Biomacromolecules* **2017**, *18* (12), 4184–4195.
- (38) Buranov, A. U.; Mazza, G. Lignin in Straw of Herbaceous Crops. *Ind. Crops Prod.* **2008**, *28* (3), 237–259.
- (39) Sun, X. F.; Sun, R. C.; Fowler, P.; Baird, M. S. Extraction and Characterization of Original Lignin and Hemicelluloses from Wheat Straw. *J. Agric. Food Chem.* **2005**, *53* (4), 860–870.
- (40) Giummarella, N.; Pu, Y.; Ragauskas, A. J.; Lawoko, M. A Critical Review on the Analysis of Lignin Carbohydrate Bonds. *Green Chem.* **2019**, *21* (7), 1573–1595.
- (41) Ghaffar, S. H.; Fan, M. Structural Analysis for Lignin Characteristics in Biomass Straw. *Biomass Bioenergy* **2013**, *57*, 264–279.
- (42) Zhou, Y.; Yin, X.; Yang, H.; Su, J.; Yu, H.; Wang, Y.; Zhou, S.; Zavadlav, S. Stable Isotopic Evidence for the Widespread Presence of Oxygen-Containing Chemical Linkages between α -Cellulose and Lignin in Poaceae (Gramineae) Grass Leaves. *ACS Sustainable Chem. Eng.* **2017**, *5* (4), 3250–3260.
- (43) Lan, W.; Lu, F.; Regner, M.; Zhu, Y.; Rencoret, J.; Ralph, S. A.; Zakai, U. I.; Morreel, K.; Boerjan, W.; Ralph, J. Tricin, a Flavonoid Monomer in Monocot Lignification. *Plant Physiol.* **2015**, *167* (4), 1284–1295.
- (44) Rossberg, C.; Bremer, M.; Machill, S.; Koenig, S.; Kerns, G.; Boeriu, C.; Windeisen, E.; Fischer, S. Separation and Characterisation of Sulphur-Free Lignin from Different Agricultural Residues. *Ind. Crops Prod.* **2015**, *73* (2015), 81–89.
- (45) Nanayakkara, B.; Manley-Harris, M.; Suckling, I. D. Understanding the Degree of Condensation of Phenolic and Etherified C-9 Units of in Situ Lignins. *J. Agric. Food Chem.* **2011**, *59* (23), 12514–12519.
- (46) Xiao, B.; Sun, X. F.; Sun, R. Chemical, Structural, and Thermal Characterizations of Alkali-Soluble Lignins and Hemicelluloses, and Cellulose from Maize Stems, Rye Straw, and Rice Straw. *Polym. Degrad. Stab.* **2001**, *74*, 307–319.
- (47) Wen, J. L.; Sun, S. L.; Xue, B. L.; Sun, R. C. Structural Elucidation of Inhomogeneous Lignins from Bamboo. *Int. J. Biol. Macromol.* **2015**, *77*, 250–259.
- (48) Xu, G.; Shi, Z.; Zhao, Y.; Deng, J.; Dong, M.; Liu, C.; Murugadoss, V.; Mai, X.; Guo, Z. Structural Characterization of Lignin and Its Carbohydrate Complexes Isolated from Bamboo (*Dendrocalamus Sinicus*). *Int. J. Biol. Macromol.* **2019**, *126*, 376–384.
- (49) You, T. T.; Mao, J. Z.; Yuan, T. Q.; Wen, J. L.; Xu, F. Structural Elucidation of the Lignins from Stems and Foliage of *Arundo Donax* Linn. *J. Agric. Food Chem.* **2013**, *61* (22), 5361–5370.
- (50) del Río, J. C.; Lino, A. G.; Colodette, J. L.; Lima, C. F.; Gutiérrez, A.; Martínez, A. T.; Lu, F.; Ralph, J.; Rencoret, J. Differences in the Chemical Structure of the Lignins from Sugarcane Bagasse and Straw. *Biomass Bioenergy* **2015**, *81*, 322–338.
- (51) Elbersen, H. W.; Christian, D. G.; Bacher, W.; Alexopoulou, E.; Pignatelli, V.; van den Berg, D. Switchgrass Variety Choice in Europe. *Proc. 1st World Conf. Biomass Energy Ind.* **2000**, 3–6.
- (52) Chen, Z.; Bai, X.; A, L.; Zhang, H.; Wan, C. Insights into Structural Changes of Lignin toward Tailored Properties during Deep Eutectic Solvent Pretreatment. *ACS Sustainable Chem. Eng.* **2020**, *8* (26), 9783–9793.
- (53) Hu, Z.; Sykes, R.; Davis, M. F.; Charles Brummer, E.; Ragauskas, A. J. Chemical Profiles of Switchgrass. *Bioresour. Technol.* **2010**, *101* (9), 3253–3257.
- (54) Tao, L.; Aden, A.; Elander, R. T.; Pallapolu, V. R.; Lee, Y. Y.; Garlock, R. J.; Balan, V.; Dale, B. E.; Kim, Y.; Mosier, N. S.; Ladisch, M. R.; Falls, M.; Holtzapfel, M. T.; Sierra, R.; Shi, J.; Ebrik, M. A.; Redmond, T.; Yang, B.; Wyman, C. E.; Hames, B.; Thomas, S.; Warner, R. E. Process and Technoeconomic Analysis of Leading Pretreatment Technologies for Lignocellulosic Ethanol Production Using Switchgrass. *Bioresour. Technol.* **2011**, *102* (24), 11105–11114.
- (55) Zhou, Z.; Lei, F.; Li, P.; Jiang, J. Lignocellulosic Biomass to Biofuels and Biochemicals: A Comprehensive Review with a Focus on Ethanol Organosolv Pretreatment Technology. *Biotechnol. Bioeng.* **2018**, *115* (11), 2683–2702.
- (56) Bhatia, S. K.; Jagtap, S. S.; Bedekar, A. A.; Bhatia, R. K.; Patel, A. K.; Pant, D.; Rajesh Banu, J.; Rao, C. V.; Kim, Y. G.; Yang, Y. H. Recent Developments in Pretreatment Technologies on Lignocellulosic Biomass: Effect of Key Parameters, Technological Improvements, and Challenges. *Bioresour. Technol.* **2020**, *300*, 122724.
- (57) Baruah, J.; Nath, B. K.; Sharma, R.; Kumar, S.; Deka, R. C.; Baruah, D. C.; Kalita, E. Recent Trends in the Pretreatment of

Lignocellulosic Biomass for Value-Added Products. *Front. Energy Res.* **2018**, *6* (DEC), 1–19.

(58) Amin, F. R.; Khalid, H.; Zhang, H.; Rahman, S. u; Zhang, R.; Liu, G.; Chen, C. Pretreatment Methods of Lignocellulosic Biomass for Anaerobic Digestion. *AMB Express* **2017**, *7* (1), 72.

(59) Seidel, C. M.; Brethauer, S.; Gyenge, L.; Rudolf Von Rohr, P.; Studer, M. H. Two-Stage Steam Explosion Pretreatment of Softwood with 2-Naphthol as Carbocation Scavenger. *Biotechnol. Biofuels* **2019**, *12* (1), 1–12.

(60) Moodley, P.; Gueguim Kana, E. B. Development of a Steam or Microwave-Assisted Sequential Salt-Alkali Pretreatment for Lignocellulosic Waste: Effect on Delignification and Enzymatic Hydrolysis. *Energy Convers. Manage.* **2017**, *148*, 801–808.

(61) Jin, M.; Dale, B. E. AFEX™ Pretreatment-Based Biorefinery Technologies. In *Handbook of Biorefinery Research and Technology*; Park, J. M., Ed.; Springer Netherlands: Dordrecht, 2018; pp 1–16.

(62) Gandolfi, S.; Ottolina, G.; Consonni, R.; Riva, S.; Patel, I. Fractionation of Hemp Hurds by Organosolv Pretreatment and Its Effect on Production of Lignin and Sugars. *ChemSusChem* **2014**, *7* (7), 1991–1999.

(63) Gandolfi, S.; Ottolina, G.; Riva, S.; Fantoni, G. P.; Patel, I. Complete Chemical Analysis of Carmagnola Hemp Hurds and Structural Features of Its Components. *BioResources* **2013**, *8* (2), 2641–2656.

(64) Marques, F. P.; Silva, L. M. A.; Lomonaco, D.; Rosa, M. de F.; Leitão, R. C. Steam Explosion Pretreatment to Obtain Eco-Friendly Building Blocks from Oil Palm Mesocarp Fiber. *Ind. Crops Prod.* **2020**, *143*, 111907.

(65) Wu, D.; Wei, Z.; Zhao, Y.; Zhao, X.; Mohamed, T. A.; Zhu, L.; Wu, J.; Meng, Q.; Yao, C.; Zhao, R. Improved Lignocellulose Degradation Efficiency Based on Fenton Pretreatment during Rice Straw Composting. *Bioresour. Technol.* **2019**, *294*, 122132.

(66) Kaur, D.; Bhardwaj, N. K.; Lohchab, R. K. Impact of Modifying Conventional Chlorine Dioxide Stage to Hot Chlorine Dioxide during Rice Straw Pulp Bleaching on Pulp, Paper and Effluent Characteristics. *Cellulose* **2019**, *26* (12), 7469–7482.

(67) Kumar, A.; Biswas, B.; Saini, K.; Kumar, A.; Kumar, J.; Krishna, B. B.; Bhaskar, T. Effect of Hydrogen Peroxide on the Depolymerization of Prot Lignin. *Ind. Crops Prod.* **2020**, *150*, 112355.

(68) Sindhu, R.; Binod, P.; Pandey, A. Biological Pretreatment of Lignocellulosic Biomass - An Overview. *Bioresour. Technol.* **2016**, *199*, 76–82.

(69) Elgharabawy, A. A.; Alam, M. Z.; Moniruzzaman, M.; Goto, M. Ionic Liquid Pretreatment as Emerging Approaches for Enhanced Enzymatic Hydrolysis of Lignocellulosic Biomass. *Biochem. Eng. J.* **2016**, *109*, 252–267.

(70) Hughes, G.; Lewis, J. C. Introduction: Biocatalysis in Industry. *Chem. Rev.* **2018**, *118* (1), 1–3.

(71) Jurado, M.; Prieto, A.; Martínez-Alcalá, Á.; Martínez, Á. T.; Martínez, M. J. Laccase Detoxification of Steam-Exploded Wheat Straw for Second Generation Bioethanol. *Bioresour. Technol.* **2009**, *100* (24), 6378–6384.

(72) Rico, A.; Rencoret, J.; del Río, J. C.; Martínez, A. T.; Gutiérrez, A. Pretreatment with Laccase and a Phenolic Mediator Degrades Lignin and Enhances Saccharification of Eucalyptus Feedstock. *Biotechnol. Biofuels* **2014**, *7* (1), 6.

(73) Chakar, F. S.; Ragauskas, A. J. Review of Current and Future Softwood Kraft Lignin Process Chemistry. *Ind. Crops Prod.* **2004**, *20* (2), 131–141.

(74) Boakye-Boaten, N. A.; Kurkalova, L.; Xiu, S.; Shahbazi, A. Techno-Economic Analysis for the Biochemical Conversion of Miscanthus x Giganteus into Bioethanol. *Biomass Bioenergy* **2017**, *98*, 85–94.

(75) Venkateswar Rao, L.; Goli, J. K.; Gentela, J.; Koti, S. Bioconversion of Lignocellulosic Biomass to Xylitol: An Overview. *Bioresour. Technol.* **2016**, *213*, 299–310.

(76) Lebo, S.; Braten, S. M.; Fredheim, G. E.; Lutnaes, B. F.; Lauten, R. A.; Myrvold, B. O.; McNally, T. In *Characterization of Lignocellulosic Materials*; Hu, T. Q., Ed.; Wiley Online Library, 2009; pp 189–205.

(77) Batidzirai, B.; Valk, M.; Wicke, B.; Junginger, M.; Daioglou, V.; Euler, W.; Faaij, A. P. C. Current and Future Technical, Economic and Environmental Feasibility of Maize and Wheat Residues Supply for Biomass Energy Application: Illustrated for South Africa. *Biomass Bioenergy* **2016**, *92*, 106–129.

(78) Chen, M.; Smith, P. M. The U.S. Cellulosic Biofuels Industry: Expert Views on Commercialization Drivers and Barriers. *Biomass Bioenergy* **2017**, *102*, 52–61.

(79) Keller, R. G.; Di Marino, D.; Blindert, M.; Wessling, M. Hydrotronic Solutions Enable Homogeneous Fenton Treatment of Lignin. *Ind. Eng. Chem. Res.* **2020**, *59* (10), 4229–4238.

(80) Clarke, C. J.; Tu, W. C.; Levers, O.; Bröhl, A.; Hallett, J. P. Green and Sustainable Solvents in Chemical Processes. *Chem. Rev.* **2018**, *118* (2), 747–800.

(81) Alriols, M. G.; García, A.; Llano-Ponte, R.; Labidi, J. Combined Organosolv and Ultrafiltration Lignocellulosic Biorefinery Process. *Chem. Eng. J.* **2010**, *157* (1), 113–120.

(82) Rumpf, J.; Do, X. T.; Burger, R.; Monakhova, Y. B.; Schulze, M. Extraction of High-Purity Lignins via Catalyst-Free Organosolv Pulping from Low-Input Crops. *Biomacromolecules* **2020**, *21*, 1929.

(83) Teng, J.; Ma, H.; Wang, F.; Wang, L.; Li, X. Catalytic Fractionation of Raw Biomass to Biochemicals and Organosolv Lignin in a Methyl Isobutyl Ketone/H₂O Biphasic System. *ACS Sustainable Chem. Eng.* **2016**, *4* (4), 2020–2026.

(84) Toscan, A.; Morais, A. R. C.; Paixão, S. M.; Alves, L.; Andreus, J.; Camassola, M.; Dillon, A. J. P.; Lukasik, R. M. Effective Extraction of Lignin from Elephant Grass Using Imidazole and Its Effect on Enzymatic Saccharification to Produce Fermentable Sugars. *Ind. Eng. Chem. Res.* **2017**, *56* (17), 5138–5145.

(85) Toscan, A.; Fontana, R. C.; Andreus, J.; Camassola, M.; Lukasik, R. M.; Dillon, A. J. P. New Two-Stage Pretreatment for the Fractionation of Lignocellulosic Components Using Hydrothermal Pretreatment Followed by Imidazole Delignification: Focus on the Polysaccharide Valorization. *Bioresour. Technol.* **2019**, *285* (April), 121346.

(86) Chambon, C. L.; Fitriyanti, V.; Verdía, P.; Yang, S. M.; Hérou, S.; Titirici, M. M.; Brandt-Talbot, A.; Fennell, P. S.; Hallett, J. P. Fractionation by Sequential Antisolvent Precipitation of Grass, Softwood, and Hardwood Lignins Isolated Using Low-Cost Ionic Liquids and Water. *ACS Sustainable Chem. Eng.* **2020**, *8* (9), 3751–3761.

(87) Liu, C.; Li, Y.; Hou, Y. Behavior of Oxygen-Containing Groups in Grass Lignin during Dissolution in Basic Ionic Liquids. *Cellulose* **2019**, *26* (2), 737–749.

(88) Poletto, P.; Pereira, G. N.; Monteiro, C. R. M.; Pereira, M. A. F.; Bordignon, S. E.; de Oliveira, D. Xylooligosaccharides: Transforming the Lignocellulosic Biomasses into Valuable 5-Carbon Sugar Prebiotics. *Process Biochem.* **2020**, *91*, 352–363.

(89) Zhao, C.; Cao, Y.; Ma, Z.; Shao, Q. Optimization of Liquid Ammonia Pretreatment Conditions for Maximizing Sugar Release from Giant Reed (*Arundo Donax* L.). *Biomass Bioenergy* **2017**, *98*, 61–69.

(90) Zhao, C.; Shao, Q.; Chundawat, S. P. S. Recent Advances on Ammonia-Based Pretreatments of Lignocellulosic Biomass. *Bioresour. Technol.* **2020**, *298*, 122446.

(91) Chundawat, S. P. S.; Pal, R. K.; Zhao, C.; Campbell, T.; Teymour, F.; Videto, J.; Nielson, C.; Wiefelich, B.; Sousa, L.; Dale, B. E.; Balan, V.; Chipkar, S.; Aguado, J.; Burke, E.; Ong, R. G. Ammonia Fiber Expansion (AFEX) Pretreatment of Lignocellulosic Biomass. *J. Visualized Exp.* **2020**, *2020* (158), 1–8.

(92) Duque, A.; Manzanares, P.; Ballesteros, M. Extrusion as a Pretreatment for Lignocellulosic Biomass: Fundamentals and Applications. *Renewable Energy* **2017**, *114*, 1427–1441.

(93) Lorenci Woiciechowski, A.; Dalmas Neto, C. J.; Porto de Souza Vandenberghe, L.; de Carvalho Neto, D. P.; Novak Sydney, A. C.; Letti, L. A. J.; Karp, S. G.; Zevallos Torres, L. A.; Soccol, C. R. Lignocellulosic Biomass: Acid and Alkaline Pretreatments and Their Effects on Biomass Recalcitrance – Conventional Processing and Recent Advances. *Bioresour. Technol.* **2020**, *304*, 122848.

- (94) Kang, X.; Zhang, Y.; Li, L.; Sun, Y.; Kong, X.; Yuan, Z. Enhanced Methane Production from Anaerobic Digestion of Hybrid Pennisetum by Selectively Removing Lignin with Sodium Chlorite. *Bioresour. Technol.* **2020**, *295*, 122289.
- (95) Silverman, J. R.; Danby, A. M.; Subramaniam, B. Intensified Ozonolysis of Lignins in a Spray Reactor: Insights into Product Yields and Lignin Structure. *React. Chem. Eng.* **2019**, *4* (8), 1421–1430.
- (96) Danby, A. M.; Lundin, M. D.; Subramaniam, B. Valorization of Grass Lignins: Swift and Selective Recovery of Pendant Aromatic Groups with Ozone. *ACS Sustainable Chem. Eng.* **2018**, *6* (1), 71–76.
- (97) Zucca, P.; Rescigno, A.; Rinaldi, A. C.; Sanjust, E. Biomimetic Metalloporphines and Metalloporphyrins as Potential Tools for Delignification: Molecular Mechanisms and Application Perspectives. *J. Mol. Catal. A: Chem.* **2014**, *388–389*, 2.
- (98) Monlau, F.; Kaparaju, P.; Trably, E.; Steyer, J. P.; Carrere, H. Alkaline Pretreatment to Enhance One-Stage CH₄ and Two-Stage H₂/CH₄ production from Sunflower Stalks: Mass, Energy and Economical Balances. *Chem. Eng. J.* **2015**, *260*, 377–385.
- (99) Li, M.; Foster, C.; Kelkar, S.; Pu, Y.; Holmes, D.; Ragauskas, A.; Saffron, C. M.; Hodge, D. B. Structural Characterization of Alkaline Hydrogen Peroxide Pretreated Grasses Exhibiting Diverse Lignin Phenotypes. *Biotechnol. Biofuels* **2012**, *5*, 38.
- (100) Ibarra-Díaz, N.; Castañón-Rodríguez, J. F.; Gómez-Rodríguez, J.; Aguilar-Uscanga, M. G. Optimization of Peroxide-Alkaline Pretreatment and Enzymatic Hydrolysis of Barley Straw (*Hordeum Vulgare* L.) to Produce Fermentable Sugars Using a Box–Behnken Design. *Biomass Convers. Biorefin.* **2020**, DOI: 10.1007/s13399-020-00853-4.
- (101) Qiao, X.; Zhao, C.; Shao, Q.; Hassan, M. Structural Characterization of Corn Stover Lignin after Hydrogen Peroxide Pre-soaking Prior to Ammonia Fiber Expansion Pretreatment. *Energy Fuels* **2018**, *32* (5), 6022–6030.
- (102) Mota, T. R.; Oliveira, D. M.; Morais, G. R.; Marchiosi, R.; Buckeridge, M. S.; Ferrarese-Filho, O.; dos Santos, W. D. Hydrogen Peroxide-Acetic Acid Pretreatment Increases the Saccharification and Enzyme Adsorption on Lignocellulose. *Ind. Crops Prod.* **2019**, *140*, 111657.
- (103) Wan, X.; Tian, D.; Shen, F.; Hu, J.; Yang, G.; Zhang, Y.; Deng, S.; Zhang, J.; Zeng, Y. Fractionating Wheat Straw via Phosphoric Acid with Hydrogen Peroxide Pretreatment and Structural Elucidation of the Derived Lignin. *Energy Fuels* **2018**, *32* (4), 5218–5225.
- (104) Wang, Q.; Tian, D.; Hu, J.; Shen, F.; Yang, G.; Zhang, Y.; Deng, S.; Zhang, J.; Zeng, Y.; Hu, Y. Fates of Hemicellulose, Lignin and Cellulose in Concentrated Phosphoric Acid with Hydrogen Peroxide (PHP) Pretreatment. *RSC Adv.* **2018**, *8* (23), 12714–12723.
- (105) Li, X.; Zhang, Y. Metal Catalyst-Free Oxidative C–C Bond Cleavage of a Lignin Model Compound by H₂O₂ in Formic Acid. *ChemSusChem* **2020**, *13* (7), 1740–1745.
- (106) Barbash, V.; Trembus, I.; Sokolovska, N. Performic Pulp from Wheat Straw. *Cellul. Chem. Technol.* **2018**, *52* (7–8), 673–680.
- (107) Wu, K.; Ying, W.; Shi, Z.; Yang, H.; Zheng, Z.; Zhang, J.; Yang, J. Fenton Reaction-Oxidized Bamboo Lignin Surface and Structural Modification to Reduce Nonproductive Cellulase Binding and Improve Enzyme Digestion of Cellulose. *ACS Sustainable Chem. Eng.* **2018**, *6* (3), 3853–3861.
- (108) Sagues, W. J.; Bao, H.; Nemenyi, J. L.; Tong, Z. Lignin-First Approach to Biorefining: Utilizing Fenton's Reagent and Supercritical Ethanol for the Production of Phenolics and Sugars. *ACS Sustainable Chem. Eng.* **2018**, *6* (4), 4958–4965.
- (109) Zhang, K.; Si, M.; Liu, D.; Zhuo, S.; Liu, M.; Liu, H.; Yan, X.; Shi, Y. A Bionic System with Fenton Reaction and Bacteria as a Model for Bioprocessing Lignocellulosic Biomass. *Biotechnol. Biofuels* **2018**, *11* (1), 1–14.
- (110) Sigoillot, J.-C.; Berrin, J.-G.; Bey, M.; Lesage-Meessen, L.; Levasseur, A.; Lomascolo, A.; Record, E.; Uzan-Boukhris, E. Fungal Strategies for Lignin Degradation. *Advances in Botanical Research*; Elsevier Ltd., 2012; Vol. 61, pp 263–308.
- (111) Zabed, H. M.; Akter, S.; Yun, J.; Zhang, G.; Awad, F. N.; Qi, X.; Sahu, J. N. Recent Advances in Biological Pretreatment of Microalgae and Lignocellulosic Biomass for Biofuel Production. *Renewable Sustainable Energy Rev.* **2019**, *105*, 105–128.
- (112) Wan, C.; Li, Y. Fungal Pretreatment of Lignocellulosic Biomass. *Biotechnol. Adv.* **2012**, *30* (6), 1447–1457.
- (113) Rodríguez-Couto, S. Industrial and Environmental Applications of White-Rot Fungi. *Mycosphere* **2017**, *8* (3), 456–466.
- (114) van Erven, G.; Hilgers, R.; Waard, P. de; Gladbeek, E.-J.; van Berkel, W. J. H.; Kabel, M. A. Elucidation of In Situ Ligninolytic Mechanisms of the Selective White-Rot Fungus *Ceriporiopsis Subvermispora*. *ACS Sustainable Chem. Eng.* **2019**, *7* (19), 16757–16764.
- (115) Asgher, M.; Shahid, M.; Kamal, S.; Iqbal, H. M. N. Recent Trends and Valorization of Immobilization Strategies and Ligninolytic Enzymes by Industrial Biotechnology. *J. Mol. Catal. B: Enzym.* **2014**, *101*, 56–66.
- (116) Plácido, J.; Capareda, S. Ligninolytic Enzymes: A Biotechnological Alternative for Bioethanol Production. *Bioresour. Bioprocess.* **2015**, *2* (1), 23.
- (117) Christopher, L. P.; Yao, B.; Ji, Y. Lignin Biodegradation with Laccase-Mediator Systems. *Front. Energy Res.* **2014**, *2* (MAR), 1–13.
- (118) Falade, A. O.; Nwodo, U. U.; Iweriebor, B. C.; Green, E.; Mabinya, L. V.; Okoh, A. I. Lignin Peroxidase Functionalities and Prospective Applications. *MicrobiologyOpen* **2017**, *6*, e00394.
- (119) Nugroho Prasetyo, E.; Kudanga, T.; Østergaard, L.; Rencoret, J.; Gutiérrez, A.; del Río, J. C.; Ignacio Santos, J.; Nieto, L.; Jiménez-Barbero, J.; Martínez, A. T.; Li, J.; Gellerstedt, G.; Lepifre, S.; Silva, C.; Kim, S. Y.; Cavaco-Paulo, A.; Seljebakken Klausen, B.; Lutnaes, B. F.; Nyanhongo, G. S.; Guebitz, G. M. Polymerization of Lignosulfonates by the Laccase-HBT (1-Hydroxybenzotriazole) System Improves Dispersion. *Bioresour. Technol.* **2010**, *101* (14), 5054–5062.
- (120) Haemmerli, S. D.; Leisola, M. S. A.; Fiechter, A. No Title. *FEMS Microbiol. Lett.* **1986**, *35* (1), 33–36.
- (121) Curreli, N.; Rescigno, A.; Rinaldi, A.; Pisu, B.; Sollai, F.; Sanjust, E. Degradation of Juglone by *Pleurotus Sajor-Caju*. *Mycol. Res.* **2004**, *108* (8), 913.
- (122) Viswanath, B.; Rajesh, B.; Janardhan, A.; Kumar, A. P.; Narasimha, G. Fungal Laccases and Their Applications in Bioremediation. *Enzyme Res.* **2014**, *2014*, 1–21.
- (123) Bertrand, B.; Martínez-Morales, F.; Trejo-Hernández, M. R. Upgrading Laccase Production and Biochemical Properties: Strategies and Challenges. *Biotechnol. Prog.* **2017**, *33* (4), 1015–1034.
- (124) Zucca, P.; Cocco, G.; Sollai, F.; Sanjust, E. Fungal Laccases as Tools for Biodegradation of Industrial Dyes. *Biocatalysis* **2016**, *1* (1), 82–108.
- (125) Zucca, P.; Rescigno, A.; Olianias, A.; Maccioni, S.; Sollai, F. A.; Sanjust, E. Induction, Purification, and Characterization of a Laccase Isozyme from *Pleurotus Sajor-Caju* and the Potential in Decolorization of Textile Dyes. *J. Mol. Catal. B: Enzym.* **2011**, *68* (2), 216–222.
- (126) Baldrian, P. Fungal Laccases – Occurrence and Properties. *FEMS Microbiol. Rev.* **2006**, *30* (2), 215–242.
- (127) Manavalan, T.; Manavalan, A.; Heese, K. Characterization of Lignocellulolytic Enzymes from White-Rot Fungi. *Curr. Microbiol.* **2015**, *70* (4), 485–498.
- (128) Fillat, Ú.; Ibarra, D.; Eugenio, M.; Moreno, A.; Tomás-Pejó, E.; Martín-Sampedro, R. Laccases as a Potential Tool for the Efficient Conversion of Lignocellulosic Biomass: A Review. *Fermentation* **2017**, *3* (2), 17.
- (129) Sondhi, S.; Sharma, P.; George, N.; Chauhan, P. S.; Puri, N.; Gupta, N. An Extracellular Thermo-Alkali-Stable Laccase from *Bacillus tequilensis* SN4, with a Potential to Biobleach Softwood Pulp. *3 Biotech* **2015**, *5* (2), 175–185.
- (130) Bonugli-Santos, R. C.; dos Santos Vasconcelos, M. R.; Passarini, M. R. Z.; Vieira, G. A. L.; Lopes, V. C. P.; Mainardi, P. H.; dos Santos, J. A.; de Azevedo Duarte, L.; Otero, I. V. R.; da Silva Yoshida, A. M.; Feitosa, V. A.; Pessoa, A.; Sette, L. D. Marine-Derived Fungi: Diversity of Enzymes and Biotechnological Applications. *Front. Microbiol.* **2015**, *6*, 269.
- (131) Rodríguez-Couto, S. Industrial and Environmental Applications of White-Rot Fungi. *Mycosphere* **2017**, *8* (3), 456–466.

- (132) D'Souza-Ticlo, D.; Sharma, D.; Raghukumar, C. A Thermostable Metal-Tolerant Laccase with Bioremediation Potential from a Marine-Derived Fungus. *Mar. Biotechnol.* **2009**, *11* (6), 725–737.
- (133) Brenelli, L. B.; Persinoti, G. F.; Cairo, J. P. L. F.; Liberato, M. V.; Gonçalves, T. A.; Otero, I. V. R.; Mainardi, P. H.; Felby, C.; Sette, L. D.; Squina, F. M. Novel Redox-Active Enzymes for Ligninolytic Applications Revealed from Multiomics Analyses of *Peniophora* Sp. CBMAI 1063, a Laccase Hyper-Producer Strain. *Sci. Rep.* **2019**, *9* (1), 1–15.
- (134) Mainardi, P. H.; Feitosa, V. A.; Brenelli de Paiva, L. B.; Bonugli-Santos, R. C.; Squina, F. M.; Pessoa, A.; Sette, L. D. Laccase Production in Bioreactor Scale under Saline Condition by the Marine-Derived Basidiomycete *Peniophora* Sp. CBMAI 1063. *Fungal Biol.* **2018**, *122* (5), 302–309.
- (135) Tufvesson, P.; Lima-Ramos, J.; Haque, N. A.; Gernaey, K. V.; Woodley, J. M. Advances in the Process Development of Biocatalytic Processes. *Org. Process Res. Dev.* **2013**, *17*, 1233.
- (136) Biko, O. D. V.; Viljoen-Bloom, M.; van Zyl, W. H. Microbial Lignin Peroxidases: Applications, Production Challenges and Future Perspectives. *Enzyme Microb. Technol.* **2020**, *141* (July), 109669.
- (137) Madhavan, A.; Sindhu, R.; Binod, P.; Sukumaran, R. K.; Pandey, A. Strategies for Design of Improved Biocatalysts for Industrial Applications. *Bioresour. Technol.* **2017**, *245*, 1304–1313.
- (138) Camarero, S.; Pardo, I.; Cañas, A. I.; Molina, P.; Record, E.; Martínez, A. T.; Martínez, M. J.; Alcalde, M. Engineering Platforms for Directed Evolution of Laccase from *Pycnoporus cinnabarinus*. *Appl. Environ. Microbiol.* **2012**, *78* (5), 1370–1384.
- (139) Kwiatos, N.; Jędrzejczak-Krzepkowska, M.; Krzemińska, A.; Delavari, A.; Paneth, P.; Bielecki, S. Evolved *Fusarium oxysporum* Laccase Expressed in *Saccharomyces cerevisiae*. *Sci. Rep.* **2020**, *10* (1), 3244.
- (140) Pardo, I.; Camarero, S. *Cell. Mol. Life Sci.* **2015**, *72*, 897–910.
- (141) Fang, Z.; Li, T.; Wang, Q.; et al. A Bacterial Laccase from Marine Microbial Metagenome Exhibiting Chloride Tolerance and Dye Decolorization Ability. *Appl. Microbiol. Biotechnol.* **2011**, *89*, 1103–1110.
- (142) Fang, Z.; Zhou, P.; Chang, F.; Yin, Q.; Fang, W.; Yuan, J.; Zhang, X.; Xiao, Y. Structure-Based Rational Design to Enhance the Solubility and Thermostability of a Bacterial Laccase Lac15. *PLoS One* **2014**, *9*, e102423.
- (143) Yin, Q.; Zhou, G.; Peng, C.; Zhang, Y.; Kües, U.; Liu, J.; Xiao, Y.; Fang, Z. The First Fungal Laccase with an Alkaline pH Optimum Obtained by Directed Evolution and Its Application in Indigo Dye Decolorization. *AMB Express* **2019**, *9* (1), 151.
- (144) Lahtinen, M.; Kruus, K.; Heinonen, P.; Sipila, J. On the Reactions of Two Fungal Laccases Differing in Their Redox Potential with Lignin Model Compounds: Products and Their Rate of Formation. *J. Agric. Food Chem.* **2009**, *57* (18), 8357–8365.
- (145) Zerva, A.; Simić, S.; Topakas, E.; Nikodinovic-Runic, J. Applications of Microbial Laccases: Patent Review of the Past Decade (2009–2019). *Catalysts* **2019**, *9* (12), 1023.
- (146) Johannes, C.; Majcherczyk, A. Natural Mediators in the Oxidation of Polycyclic Aromatic Hydrocarbons by Laccase Mediator Systems. *Appl. Environ. Microbiol.* **2000**, *66* (2), 524–528.
- (147) Rencoret, J.; Pereira, A.; del Río, J. C.; Martínez, Á. T.; Gutiérrez, A. Delignification and Saccharification Enhancement of Sugarcane Byproducts by a Laccase-Based Pretreatment. *ACS Sustainable Chem. Eng.* **2017**, *5* (8), 7145–7154.
- (148) Rencoret, J.; Pereira, A.; del Río, J. C.; Martínez, A. T.; Gutiérrez, A. Laccase-Mediator Pretreatment of Wheat Straw Degrades Lignin and Improves Saccharification. *BioEnergy Res.* **2016**, *9* (3), 917–930.
- (149) Ciriminna, R.; Pagliaro, M. Industrial Oxidations with Organocatalyst TEMPO and Its Derivatives. *Org. Process Res. Dev.* **2010**, *14* (1), 245–251.
- (150) Gutiérrez, A.; Rencoret, J.; Cadena, E. M.; Rico, A.; Barth, D.; del Río, J. C.; Martínez, Á. T. Demonstration of Laccase-Based Removal of Lignin from Wood and Non-Wood Plant Feedstocks. *Bioresour. Technol.* **2012**, *119*, 114–122.
- (151) Xie, S.; Sun, Q.; Pu, Y.; Lin, F.; Sun, S.; Wang, X.; Ragauskas, A. J.; Yuan, J. S. Advanced Chemical Design for Efficient Lignin Bioconversion. *ACS Sustainable Chem. Eng.* **2017**, *5* (3), 2215–2223.
- (152) Navas, L. E.; Martínez, F. D.; Taverna, M. E.; Fetherolf, M. M.; Eltis, L. D.; Nicolau, V.; Estenoz, D.; Campos, E.; Benintende, G. B.; Berretta, M. F. A Thermostable Laccase from *Thermus* Sp. 2.9 and Its Potential for Delignification of Eucalyptus Biomass. *AMB Express* **2019**, *9* (1), 24.
- (153) Hilgers, R.; Van Erven, G.; Boerkamp, V.; Sulaeva, I.; Potthast, A.; Kabel, M. A.; Vincken, J. P. Understanding Laccase/HBT-Catalyzed Grass Delignification at the Molecular Level. *Green Chem.* **2020**, *22* (5), 1735–1746.
- (154) Longe, L. F.; Couvreur, J.; Leriche Grandchamp, M.; Garnier, G.; Allais, F.; Saito, K. Importance of Mediators for Lignin Degradation by Fungal Laccase. *ACS Sustainable Chem. Eng.* **2018**, *6* (8), 10097–10107.
- (155) Rencoret, J.; Pereira, A.; Del Río, J. C.; Martínez, Á. T.; Gutiérrez, A. Delignification and Saccharification Enhancement of Sugarcane Byproducts by a Laccase-Based Pretreatment. *ACS Sustainable Chem. Eng.* **2017**, *5* (8), 7145–7154.
- (156) Song, Q.; Deng, X.; Song, R. Q. Expression of *Pleurotus ostreatus* Laccase Gene in *Pichia pastoris* and Its Degradation of Corn Stover Lignin. *Microorganisms* **2020**, *8* (4), 601.
- (157) Zhu, D.; Liang, N.; Zhang, R.; Ahmad, F.; Zhang, W.; Yang, B.; Wu, J.; Geng, A.; Gabriel, M.; Sun, J. Insight into Depolymerization Mechanism of Bacterial Laccase for Lignin. *ACS Sustainable Chem. Eng.* **2020**, *8* (34), 12920–12933.
- (158) Financie, R.; Moniruzzaman, M.; Uemura, Y. Enhanced Enzymatic Delignification of Oil Palm Biomass with Ionic Liquid Pretreatment. *Biochem. Eng. J.* **2016**, *110*, 1–7.
- (159) Moniruzzaman, M.; Ono, T. Separation and Characterization of Cellulose Fibers from Cypress Wood Treated with Ionic Liquid Prior to Laccase Treatment. *Bioresour. Technol.* **2013**, *127*, 132–137.
- (160) Stevens, J. C.; Das, L.; Mobley, J. K.; Asare, S. O.; Lynn, B. C.; Rodgers, D. W.; Shi, J. Understanding Laccase–Ionic Liquid Interactions toward Biocatalytic Lignin Conversion in Aqueous Ionic Liquids. *ACS Sustainable Chem. Eng.* **2019**, *7* (19), 15928–15938.
- (161) Galai, S.; P. de los Ríos, A.; Hernández-Fernández, F. J.; Haj Kacem, S.; Tomas-Alonso, F. Over-Activity and Stability of Laccase Using Ionic Liquids: Screening and Application in Dye Decolorization. *RSC Adv.* **2015**, *5* (21), 16173–16189.
- (162) Al-Zuhair, S.; Abualreesh, M.; Ahmed, K.; Abdul Razak, A. Enzymatic Delignification of Biomass for Enhanced Fermentable Sugars Production. *Energy Technol.* **2015**, *3* (2), 121–127.
- (163) Rezaei, S.; Shahverdi, A. R.; Faramarzi, M. A. Isolation, One-Step Affinity Purification, and Characterization of a Polyextremotolerant Laccase from the Halophilic Bacterium *Aquasalibacillus elongatus* and Its Application in the Delignification of Sugar Beet Pulp. *Bioresour. Technol.* **2017**, *230*, 67–75.
- (164) Rezaie, R.; Rezaei, S.; Jafari, N.; Foroootanfar, H.; Khoshayand, M. R.; Faramarzi, M. A. Delignification and Detoxification of Peanut Shell Bio-Waste Using an Extremely Halophilic Laccase from an *Aquasalibacillus elongatus* Isolate. *Extremophiles* **2017**, *21* (6), 993–1004.
- (165) Asgher, M.; Wahab, A.; Bilal, M.; Iqbal, H. M. N. Delignification of Lignocellulose Biomasses by Alginate–Chitosan Immobilized Laccase Produced from *Trametes versicolor* IBL-04. *Waste Biomass Valorization* **2018**, *9* (11), 2071–2079.
- (166) Amin, R.; Khorshidi, A.; Shojaei, A. F.; Rezaei, S.; Faramarzi, M. A. Immobilization of Laccase on Modified Fe₃O₄@SiO₂@Kit-6 Magnetite Nanoparticles for Enhanced Delignification of Olive Pomace Bio-Waste. *Int. J. Biol. Macromol.* **2018**, *114*, 106–113.
- (167) Smith, E. L.; Abbott, A. P.; Ryder, K. S. Deep Eutectic Solvents (DESs) and Their Applications. *Chem. Rev.* **2014**, *114* (21), 11060–11082.
- (168) Zhang, Q.; De Oliveira Vigier, K.; Royer, S.; Jérôme, F. Deep Eutectic Solvents: Syntheses, Properties and Applications. *Chem. Soc. Rev.* **2012**, *41* (21), 7108.

- (169) Wang, Z. K.; Hong, S.; Wen, J.; Ma, C. Y.; Tang, L.; Jiang, H.; Chen, J. J.; Li, S.; Shen, X. J.; Yuan, T. Q. Lewis Acid-Facilitated Deep Eutectic Solvent (DES) Pretreatment for Producing High-Purity and Antioxidative Lignin. *ACS Sustainable Chem. Eng.* **2020**, *8* (2), 1050–1057.
- (170) Yu, W.; Wang, C.; Yi, Y.; Wang, H.; Zeng, L.; Li, M.; Yang, Y.; Tan, Z. Comparison of Deep Eutectic Solvents on Pretreatment of Raw Ramie Fibers for Cellulose Nanofibril Production. *ACS Appl. Mater. Interfaces* **2020**, *5*, 5580.
- (171) Gotor-Fernández, V.; Paul, C. E. Deep Eutectic Solvents for Redox Biocatalysis. *J. Biotechnol.* **2019**, *293*, 24–35.
- (172) Toledo, M. L.; Pereira, M. M.; Freire, M. G.; Silva, J. P. A.; Coutinho, J. A. P.; Tavares, A. P. M. Laccase Activation in Deep Eutectic Solvents. *ACS Sustainable Chem. Eng.* **2019**, *7* (13), 11806–11814.
- (173) Dai, Y.; van Spronsen, J.; Witkamp, G.-J.; Verpoorte, R.; Choi, Y. H. Natural Deep Eutectic Solvents as New Potential Media for Green Technology. *Anal. Chim. Acta* **2013**, *766*, 61–68.
- (174) Khodaverdian, S.; Dabirmanesh, B.; Heydari, A.; Dashtban-Moghadam, E.; Khajeh, K.; Ghazi, F. Activity, Stability and Structure of Laccase in Betaine Based Natural Deep Eutectic Solvents. *Int. J. Biol. Macromol.* **2018**, *107*, 2574–2579.
- (175) Ji, Q.; Yu, X.; Yagoub, A. E.-G. A.; Chen, L.; Zhou, C. Efficient Removal of Lignin from Vegetable Wastes by Ultrasonic and Microwave-Assisted Treatment with Ternary Deep Eutectic Solvent. *Ind. Crops Prod.* **2020**, *149*, 112357.
- (176) Muley, P. D.; Mobley, J. K.; Tong, X.; Novak, B.; Stevens, J.; Moldovan, D.; Shi, J.; Boldor, D. Rapid Microwave-Assisted Biomass Delignification and Lignin Depolymerization in Deep Eutectic Solvents. *Energy Convers. Manage.* **2019**, *196*, 1080–1088.
- (177) Suopajarvi, T.; Ricci, P.; Karvonen, V.; Ottolina, G.; Liimatainen, H. Acidic and Alkaline Deep Eutectic Solvents in Delignification and Nanofibrillation of Corn Stalk, Wheat Straw, and Rapeseed Stem Residues. *Ind. Crops Prod.* **2020**, *145*, 111956.
- (178) Procentese, A.; Johnson, E.; Orr, V.; Garruto Campanile, A.; Wood, J. A.; Marzocchella, A.; Rehmann, L. Deep Eutectic Solvent Pretreatment and Subsequent Saccharification of Corn cob. *Bioresour. Technol.* **2015**, *192*, 31–36.
- (179) Glenn, J. K.; Morgan, M. A.; Mayfield, M. B.; Kuwahara, M.; Gold, M. H. An Extracellular H₂O₂-Requiring Enzyme Preparation Involved in Lignin Biodegradation by the White Rot Basidiomycete *Phanerochaete Chrysosporium*. *Biochem. Biophys. Res. Commun.* **1983**, *114* (3), 1077–1083.
- (180) Wesenberg, D. White-Rot Fungi and Their Enzymes for the Treatment of Industrial Dye Effluents. *Biotechnol. Adv.* **2003**, *22* (1–2), 161–187.
- (181) Xu, C.; Arancon, R. A. D.; Labidi, J.; Luque, R. Lignin Depolymerisation Strategies: Towards Valuable Chemicals and Fuels. *Chem. Soc. Rev.* **2014**, *43* (22), 7485–7500.
- (182) Chan, J. C.; Paice, M.; Zhang, X. Enzymatic Oxidation of Lignin: Challenges and Barriers Toward Practical Applications. *ChemCatChem* **2020**, *12* (2), 401–425.
- (183) Wariishi, H.; Gold, M. H. Lignin Peroxidase Compound III Mechanism of Formation and Decomposition. *J. Biol. Chem.* **1990**, *265* (4), 2070–2077.
- (184) Pham, L. T. M.; Seo, H.; Kim, K.-J.; Kim, Y. H. In Silico-Designed Lignin Peroxidase from *Phanerochaete Chrysosporium* Shows Enhanced Acid Stability for Depolymerization of Lignin. *Biotechnol. Biofuels* **2018**, *11* (1), 325.
- (185) Yee, K. L.; Jansen, L. E.; Lajoie, C. A.; Penner, M. H.; Morse, L.; Kelly, C. J. Furfural and 5-Hydroxymethyl-Furfural Degradation Using Recombinant Manganese Peroxidase. *Enzyme Microb. Technol.* **2018**, *108*, 59–65.
- (186) Ryu, K.; Hwang, S. Y.; Kim, K. H.; Kang, J. H.; Lee, E. K. Functionality Improvement of Fungal Lignin Peroxidase by DNA Shuffling for 2,4-Dichlorophenol Degradability and H₂O₂ Stability. *J. Biotechnol.* **2008**, *133* (1), 110–115.
- (187) Garcia-Ruiz, E.; Gonzalez-Perez, D.; Ruiz-Dueñas, F. J.; Martínez, A. T.; Alcalde, M. Directed Evolution of a Temperature-, Peroxide- and Alkaline PH-Tolerant Versatile Peroxidase. *Biochem. J.* **2012**, *441* (1), 487–498.
- (188) Gonzalez-Perez, D.; Garcia-Ruiz, E.; Ruiz-Dueñas, F. J.; Martínez, A. T.; Alcalde, M. Structural Determinants of Oxidative Stabilization in an Evolved Versatile Peroxidase. *ACS Catal.* **2014**, *4* (11), 3891–3901.
- (189) Tien, M.; Kirk, T. K. Lignin-Degrading Enzyme from the Hymenomycete *Phanerochaete Chrysosporium* Burds. *Science (Washington, DC, U. S.)* **1983**, *221* (4611), 661–663.
- (190) Chan, J. C.; Paice, M.; Zhang, X. Enzymatic Oxidation of Lignin: Challenges and Barriers Toward Practical Applications. *ChemCatChem* **2020**, *12* (2), 401–425.
- (191) Ruiz-Dueñas, F. J.; Martínez, A. T. Microbial Degradation of Lignin: How a Bulky Recalcitrant Polymer Is Efficiently Recycled in Nature and How We Can Take Advantage of This. *Microb. Biotechnol.* **2009**, *2* (2), 164–177.
- (192) Goodwin, D. C.; Aust, S. D.; Grover, T. A. Evidence for Veratryl Alcohol as a Redox Mediator in Lignin Peroxidase-Catalyzed Oxidation. *Biochemistry* **1995**, *34* (15), 5060–5065.
- (193) Zhang, H.; Zhang, X.; Geng, A. Expression of a Novel Manganese Peroxidase from *Cerrena Unicolor* BBP6 in *Pichia Pastoris* and Its Application in Dye Decolorization and PAH Degradation. *Biochem. Eng. J.* **2020**, *153*, 107402.
- (194) Siddeeg, S. M.; Tahoona, M. A.; Mnif, W.; Ben Rebah, F. Iron Oxide/Chitosan Magnetic Nanocomposite Immobilized Manganese Peroxidase For Decolorization of Textile Wastewater. *Processes* **2020**, *8*, 5.
- (195) Martínez, M. J.; Böckle, B.; Camarero, S.; Guillén, F.; Martínez, A. T. MnP Isoenzymes Produced by Two *Pleurotus* Species in Liquid Culture and During Wheat-Straw Solid-State Fermentation. In *Enzymes for Pulp and Paper Processing*; Jeffries, T. W., Viikari, L., Eds.; ACS Symposium Series; American Chemical Society, 1996; Vol. 655, pp 183–196.
- (196) Masran, R.; Zanirun, Z.; Bahrin, E. K.; Ibrahim, M. F.; Lai Yee, P.; Abd-Aziz, S. Harnessing the Potential of Ligninolytic Enzymes for Lignocellulosic Biomass Pretreatment. *Appl. Microbiol. Biotechnol.* **2016**, *100* (12), 5231–5246.
- (197) Asgher, M.; Ahmad, Z.; Iqbal, H. M. N. Alkali and Enzymatic Delignification of Sugarcane Bagasse to Expose Cellulose Polymers for Saccharification and Bio-Ethanol Production. *Ind. Crops Prod.* **2013**, *44*, 488–495.
- (198) Kong, W.; Chen, H.; Lyu, S.; Ma, F.; Yu, H.; Zhang, X. Characterization of a Novel Manganese Peroxidase from White-Rot Fungus *Echinodontium taxodii* 2538, and Its Use for the Degradation of Lignin-Related Compounds. *Process Biochem.* **2016**, *51* (11), 1776–1783.
- (199) Magner, E. Immobilisation of Enzymes on Mesoporous Silicate Materials. *Chem. Soc. Rev.* **2013**, *42* (15), 6213–6222.
- (200) Bilal, M.; Asgher, M.; Iqbal, H. M. N.; Hu, H.; Zhang, X. Delignification and Fruit Juice Clarification Properties of Alginate-Chitosan-Immobilized Ligninolytic Cocktail. *LWT* **2017**, *80*, 348–354.
- (201) Salis, A.; Pisano, M.; Monduzzi, M.; Solinas, V.; Sanjust, E. Laccase from *Pleurotus Sajor-Caju* on Functionalised SBA-15 Mesoporous Silica: Immobilisation and Use for the Oxidation of Phenolic Compounds. *J. Mol. Catal. B: Enzym.* **2009**, *58* (1–4), 175–180.
- (202) Naseri, M.; Pitzalis, F.; Carucci, C.; Medda, L.; Fotouhi, L.; Magner, E.; Salis, A. Lipase and Laccase Encapsulated on Zeolite Imidazolate Framework: Enzyme Activity and Stability from Voltammetric Measurements. *ChemCatChem* **2018**, *10* (23), 5425–5433.
- (203) Chang, K.-L.; Thitikorn-Amorn, J.; Chen, S.-H.; Hsieh, J.-F.; Ratanakhanokchai, K.; Huang, P.-J.; Lin, T.-C.; Chen, S.-T. Improving the Remaining Activity of Lignocellulolytic Enzymes by Membrane Entrapment. *Bioresour. Technol.* **2011**, *102* (2), 519–523.
- (204) Muthuvelu, K. S.; Rajarathinam, R.; Selvaraj, R. N.; Rajendren, V. B. A Novel Method for Improving Laccase Activity by Immobilization onto Copper Ferrite Nanoparticles for Lignin Degradation. *Int. J. Biol. Macromol.* **2020**, *152*, 1098.

(205) Sadeghian-Abadi, S.; Rezaei, S.; Yousefi-Mokri, M.; Faramarzi, M. A. Enhanced Production, One-Step Affinity Purification, and Characterization of Laccase from Solid-State Culture of *Lentinus Tigrinus* and Delignification of Pistachio Shell by Free and Immobilized Enzyme. *J. Environ. Manage.* **2019**, *244* (March), 235–246.

(206) Kirupa Sankar, M.; Ravikumar, R.; Naresh Kumar, M.; Sivakumar, U. Development of Co-Immobilized Tri-Enzyme Biocatalytic System for One-Pot Pretreatment of Four Different Perennial Lignocellulosic Biomass and Evaluation of Their Bioethanol Production Potential. *Bioresour. Technol.* **2018**, *269* (June), 227–236.

PAPER II



Article

Adsorption of Malachite Green and Alizarin Red S Dyes Using Fe-BTC Metal Organic Framework as Adsorbent

Giulia Rossella Delpiano ¹, Davide Tocco ¹, Luca Medda ², Edmond Magner ^{3,*} and Andrea Salis ^{1,4,*}

¹ Dipartimento di Scienze Chimiche e Geologiche, Università di Cagliari, Cittadella Universitaria, S.S. 554 bivio Sestu, 09042 Monserrato (CA), Italy; delpiano@unica.it (G.R.D.); davide.tocco@unica.it (D.T.)

² Laboratorio NEST Scuola Normale Superiore di Pisa, 56127 Pisa, Italy; medda.luc@gmail.com

³ Department of Chemical Sciences, Bernal Institute, University of Limerick, Limerick V94 T9PX, Ireland

⁴ Consorzio Interuniversitario per lo Sviluppo dei Sistemi a Grande Interfase (CSGI), Unità Operativa University of Cagliari, 09042 Monserrato (CA), Italy

* Correspondence: edmond.magner@ul.ie (E.M.); asalis@unica.it (A.S.)

Abstract: Synthetic organic dyes are widely used in various industrial sectors but are also among the most harmful water pollutants. In the last decade, significant efforts have been made to develop improved materials for the removal of dyes from water, in particular, on nanostructured adsorbent materials. Metal organic frameworks (MOFs) are an attractive class of hybrid nanostructured materials with an extremely wide range of applications including adsorption. In the present work, an iron-based Fe-BTC MOF, prepared according to a rapid, aqueous-based procedure, was used as an adsorbent for the removal of alizarin red S (ARS) and malachite green (MG) dyes from water. The synthesized material was characterized in detail, while the adsorption of the dyes was monitored by UV-Vis spectroscopy. An optimal adsorption pH of 4, likely due to the establishment of favorable interactions between dyes and Fe-BTC, was found. At this pH and at a temperature of 298 K, adsorption equilibrium was reached in less than 30 min following a pseudo-second order kinetics, with k'' of 4.29×10^{-3} and $3.98 \times 10^{-2} \text{ g} \cdot \text{mg}^{-1} \text{ min}^{-1}$ for ARS and MG, respectively. The adsorption isotherm followed the Langmuir model with maximal adsorption capacities of $80 \text{ mg} \cdot \text{g}^{-1}$ (ARS) and $177 \text{ mg} \cdot \text{g}^{-1}$ (MG), and K_L of $9.30 \cdot 10^3 \text{ L} \cdot \text{mg}^{-1}$ (ARS) and $51.56 \cdot 10^3 \text{ L} \cdot \text{mg}^{-1}$ (MG).

Keywords: metal organic frameworks; wastewater remediation; adsorption; malachite green; alizarin red S



Citation: Delpiano, G.R.; Tocco, D.; Medda, L.; Magner, E.; Salis, A. Adsorption of Malachite Green and Alizarin Red S Dyes Using Fe-BTC Metal Organic Framework as Adsorbent. *Int. J. Mol. Sci.* **2021**, *22*, 788. <https://doi.org/10.3390/ijms22020788>

Received: 16 December 2020

Accepted: 10 January 2021

Published: 14 January 2021

Publisher's Note: MDPI stays neutral with regard to jurisdictional claims in published maps and institutional affiliations.



Copyright: © 2021 by the authors. Licensee MDPI, Basel, Switzerland. This article is an open access article distributed under the terms and conditions of the Creative Commons Attribution (CC BY) license (<https://creativecommons.org/licenses/by/4.0/>).

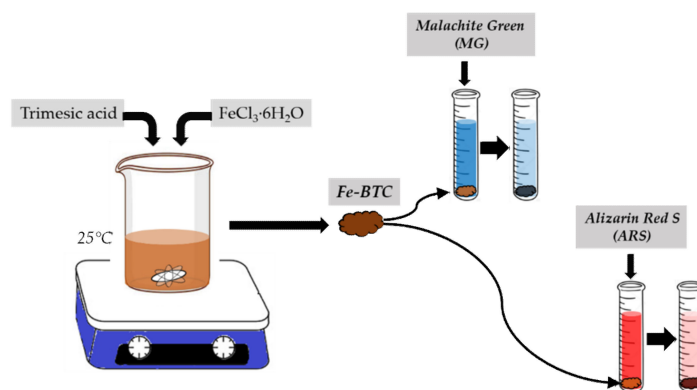
1. Introduction

Synthetic organic dyes are among the most harmful polluting agents. It is estimated that 80,000 tons of dyes are produced and consumed each year [1]. They are cheap, offer a wide range of colors, and are used for numerous applications in the paper, tanning, pharmaceutical, photographic, and cosmetic industries [2]. However, synthetic dyes are mainly earmarked for the textile industry, as they possess reactive groups which have a strong binding ability for fiber [3]. The colors of dye molecules are due to chromogenic groups which absorb visible light. Indeed, dye molecules generally have a complex aromatic structure which is often characterized by a high chemical stability. Unfortunately, dyes are highly toxic and can have carcinogenic and mutagenic effects on living organisms, even at low concentrations [4]. In addition, due to their ability to absorb light, the release of dyes into surface waters also causes unwanted effects in the aquatic ecosystem. These effects arise from a reduced level of penetration of the sun's rays in water, which alters photosynthetic cycles and reduces the oxygen supply in the water body [5]. Due to their high chemical stability, the removal of dyes from water is a challenging issue [6]. Numerous methods have been proposed to remove dyes from wastewaters, such as electrochemical degradation [7,8], membrane-based separation [9], ultrafiltration [10], extraction [11], and biological treatment [12]. While these methods have a number of advantages, they cannot be applied on a large scale due to high costs, secondary pollution, production of waste, etc [3].

Adsorption is a simple method of dye removal that has significant advantages. Indeed, it can be applied to almost any type of dye or mixtures of dyes, it does not require any special equipment or pretreatment, and it can be repeated a number of times until the adsorbent has reached its maximal adsorbing capacity. Adsorption processes are also economic as they can be carried out in mild conditions, reducing the actual costs to that of the adsorbent, which can be selected accordingly [13,14]. The main features of a good adsorbent are high surface area, high adsorption capacity, short adsorption times, and economic and environmentally-friendly production process.

Metal organic frameworks (MOFs) are organic-inorganic hybrid porous materials characterized by a cage-like structure consisting of an array of metal cations held together by organic linkers [15]. Thanks to their large surface area, tunable structural properties and thermal stability, MOFs have been studied for a range of applications, including catalysis [16], gas storage [17,18], enzyme carriers [19,20], sensing [21], and adsorption [22–24]. The adsorption capacities of MOFs toward dyes are remarkable [25]. Tian et al. prepared a water-stable cationic Fe-based metal organic framework (CPM-97-Fe) for the adsorption of both anionic and cationic dyes, with adsorption capacities ranging from 157 to 831 mg/g [26]. There are many types of MOFs and, depending on the material, they can range from low to high cost. The lowest cost materials are those whose synthesis is rapid and requires mild conditions as well as environmentally-friendly solvents and reagents. Recently, Sanchez-Sanchez et al. proposed a facile and rapid method to synthesize a Basolite F300-like Fe-BTC MOF under environmentally and economically sustainable conditions (few minutes at room temperature using water as solvent) [27]. This material, was used as a support for enzyme immobilization [28]. To the best of our knowledge, there are only a few studies about dyes' adsorption using Fe-BTC [29–33]. While adsorption properties of Fe-BTC are significant (e.g., up to 1105 mg/g of methylene blue) [34], the synthetic procedures used require high temperatures or the use of organic solvents.

The purpose of this work was to examine the adsorption properties of a Fe-BTC MOF, synthesized according to the method described by Sanchez-Sanchez et al. [27], to remove the anionic dye alizarin red S (ARS) and the cationic dye malachite green (MG) from water (Scheme 1). ARS is a synthetic anthraquinonic acid–base indicator [35,36], used in histology to stain and locate calcium deposits in tissues [37], in geology to identify carbonate minerals, and widely used in textile dyeing. MG is a toxic and carcinogenic triphenylmethane dye, and is widely used in the textile and food industries, as well as in aquaculture as an antifungal, antimicrobial, and antiparasitic agent [38–41]. The synthesized MOF was characterized by means of XRD (X-ray diffraction), N_2 -adsorption isotherms, SEM (Scanning Electro Microscopy), FTIR (Fourier-Transform Infrared Spectroscopy), TGA (Thermogravimetric Analysis), and ELS (Electrophoretic Light Scattering) techniques. The adsorption kinetics and isotherms of MG and ARS on Fe-BTC MOF were determined in water at room temperature (298 K) by means of UV-Vis spectroscopy to examine the application of Fe-BTC MOF for the removal of toxic dyes from waters.



Scheme 1. Use of Fe-BTC metal organic framework (MOF) for adsorption of alizarin red (S) and malachite green.

2. Results

2.1. Physico-Chemical Characterizations

Figure 1a shows the XRD pattern of the synthesized Fe-BTC MOF. The pattern is well resolved with peaks at $2\theta = 11^\circ, 19^\circ, 24^\circ, 28^\circ$ and 34° , in agreement with the literature reports for Fe-BTC MOF [42,43]. The surface area and pore size distribution were obtained by N_2 adsorption/desorption isotherms (Figure 1b), using the Brunauer–Emmett–Teller (BET) and Barrett–Joyner–Halenda (BJH) methods. The specific surface area was $443 \text{ m}^2/\text{g}$ and a multi-modal pore size distribution ranged from 4 to 40 nm (Figure S2). Thermogravimetric analysis (Figure 1c) showed a typical two-step decomposition pattern. The initial mass loss at $T < 100^\circ\text{C}$ is due to the removal of water from the powder. The mass loss in the range $100\text{--}325^\circ\text{C}$ can be attributed to the loss of coordination water [44]. Finally, the mass loss from 325 to 520°C is ascribed to the decomposition of the organic moiety (trimesic acid) of the MOF [45,46]. The FTIR spectrum of Fe-BTC MOF is shown in Figure 1d. The broad band from 3400 to 3600 cm^{-1} is due to the O-H stretching of adsorbed water. The bands at 1627 and 1572 cm^{-1} and at 1450 and 1372 cm^{-1} are assigned to the asymmetric and the symmetric stretching of the carboxylate groups of Fe-BTC [29,46,47], respectively. The peaks between 770 and 450 cm^{-1} are due to the bending of aromatic C-H bonds.

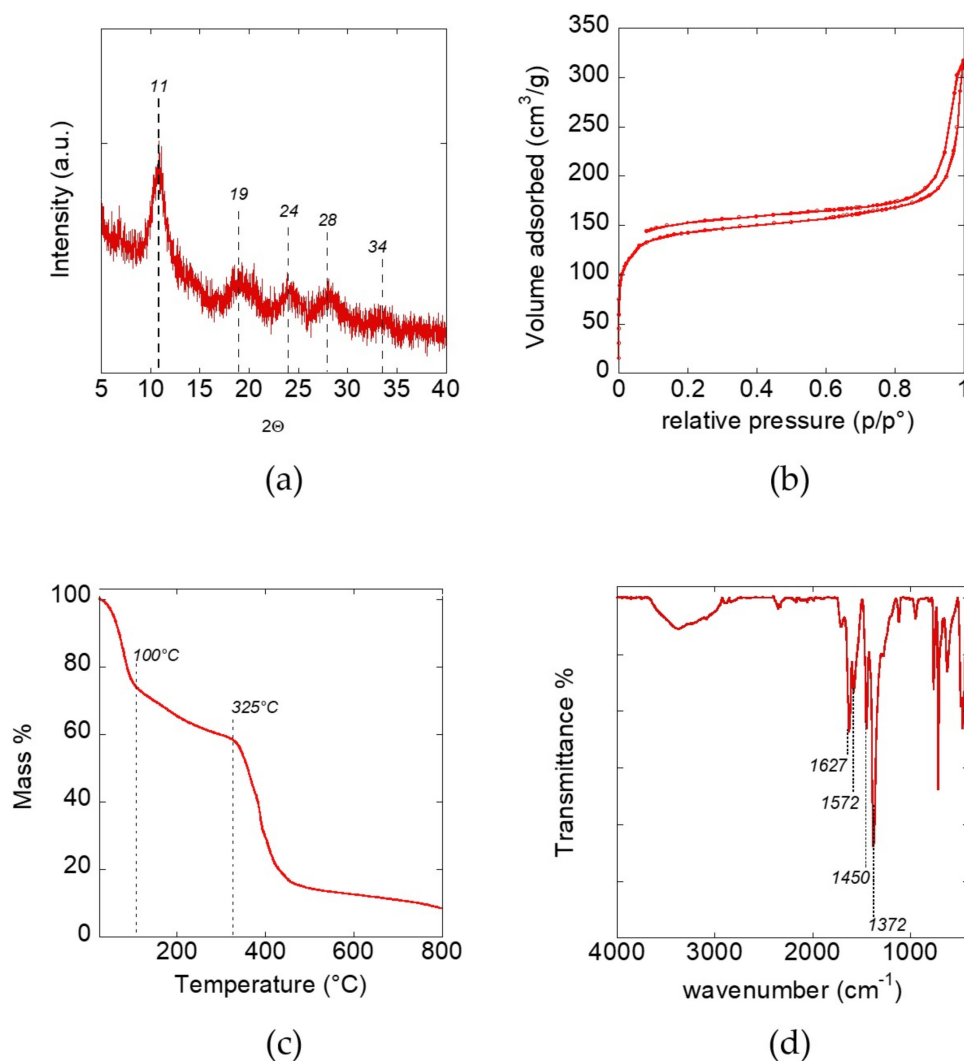
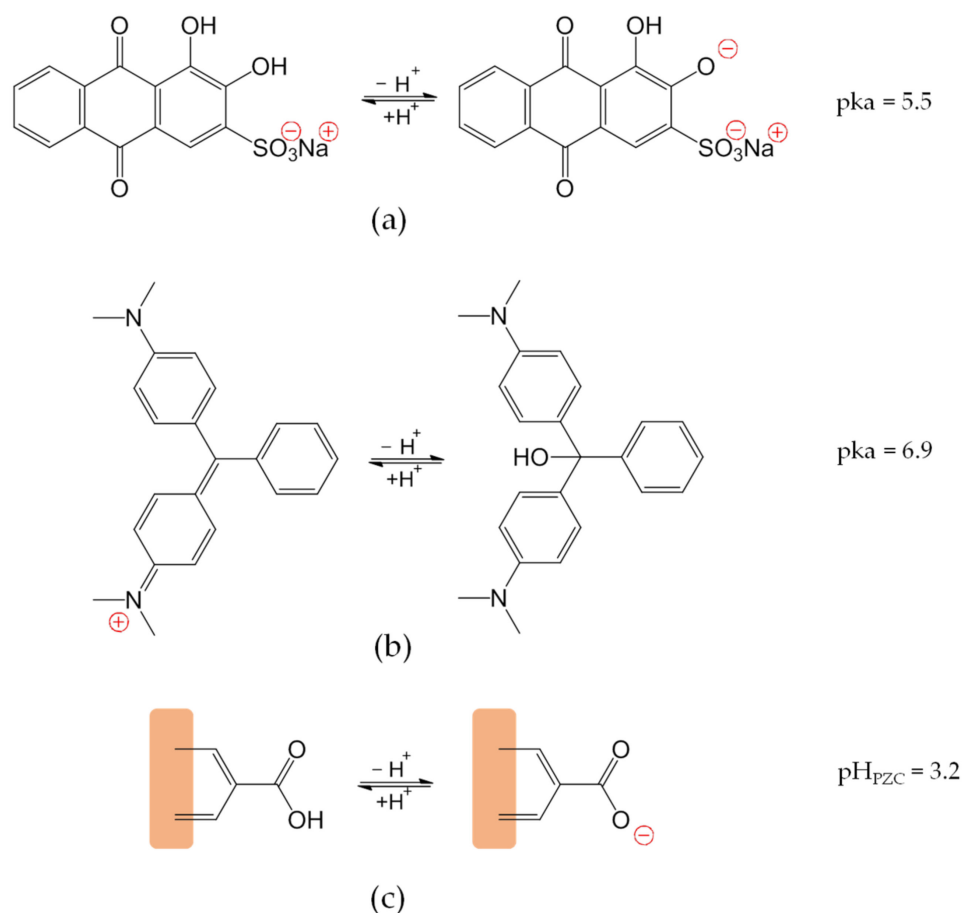


Figure 1. Characterization of Fe-BTC MOF. (a) XRD pattern; (b) N_2 physisorption isotherm; (c) Thermogravimetric analysis; (d) FT-IR spectrum.

2.2. Effect of pH on Dyes Adsorption on Fe-BTC MOF

The synthesized Fe-BTC MOF was used to adsorb alizarin red S (ARS) and malachite green (MG) from water. Some studies have shown that dye adsorption on MOFs was governed by electrostatic interactions [48]. Thus, it is expected that the pH of the adsorbing solution affects the amount of adsorbed dye as a consequence of the presence/absence of electric charges on both the dye molecules and the adsorbent surface. The pK_a of ARS and MG are 5.5 [49] and 6.9 [39], respectively. The former is due to the dissociation of one of the phenolic groups (Scheme 2) [50], and the latter to the conversion of the cation into a carbinol base through addition of OH^- (Scheme 2) [51,52].



Scheme 2. Acid–base equilibria of (a) Alizarin red S (ARS) (b) Malachite green (MG) and (c) Fe-BTC MOF.

The zeta potential of Fe-BTC suspension in water was measured over the pH range 3–7 (Figure 2a and Table S1). Fe-BTC is slightly positive at pH 3 ($\zeta = +8.3 \pm 3$ mV) and is negatively charged at pH > 4 ($\zeta = -10.3 \pm 3$ mV) with a pH_{PZC} (point of zero charge) value of about 3.2 [53], in agreement with the literature [32]. Figure 2b shows the effect of pH on the adsorbed amount at equilibrium (q_e , mg/g) of ARS and MG on Fe-BTC. The q_e values of MG are generally higher than those of ARS. Moreover, while the q_e of MG is unaffected by pH, that of ARS linearly decreases in the pH range 3–7.

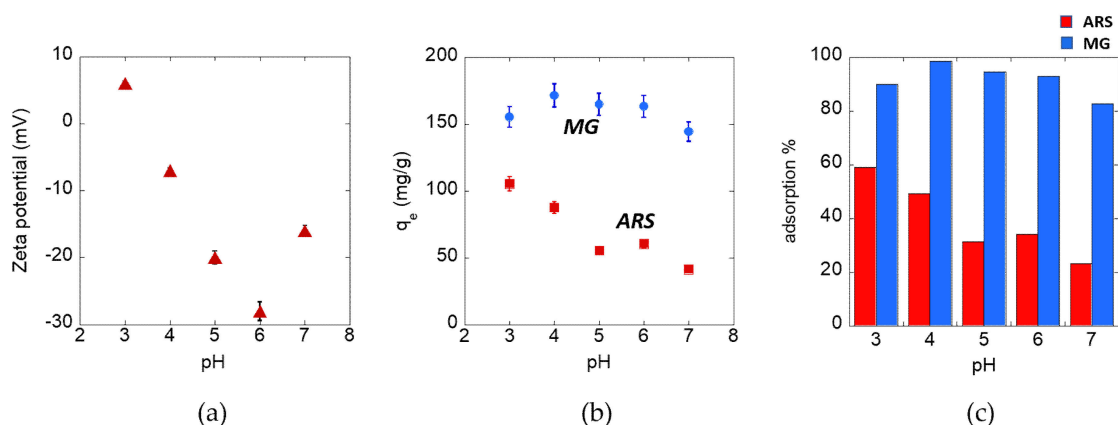


Figure 2. (a) Zeta potential of Fe-BTC as a function of pH; (b) Adsorption capacity (q_e) of Fe-BTC toward ARS and MG as a function of pH; (c) Percentage adsorption of dyes as a function of pH.

Since the pH_{PZC} (point of zero charge) of Fe-BTC is ca. 3.2 [53], anionic dyes are adsorbed to a lower extent than cationic dyes [54]. Hence, as compared with ARS, higher amounts of MG would be expected to be adsorbed. The two dyes also show different adsorption efficiency (adsorbed amount %) trends (Figure 2c and Table S1) with Fe-BTC possessing a maximum MG adsorption value of 98.5% at pH 4, while the highest value for ARS was 59.1% at pH 3 (Figure 2c). At pH 7, the adsorption capacity was still high for MG (82.9%), but quite low for ARS (23.3%). These trends can be explained by the fact that, at pH 7, MG is neutral, and thus adsorption would predominantly occur via van der Waals forces and would not be affected by electrostatic interactions. Adsorption of ARS on Fe-BTC is not favored at pH 7 as both the dye and the adsorbent are negatively charged.

2.3. Adsorption Kinetics

The adsorption kinetics of MG and ARS on Fe-BTC MOF were examined in aqueous solution (pH = 4, 298 K). The adsorption process was rapid for both dyes, reaching equilibrium values (corresponding to the plateau in Figure 3a) in 30 min for ARS and 15 min for MG. Under these conditions ($T = 298$ K, pH = 4, initial concentrations of MG and ARS of 1.5 mM), the q_e of MG on Fe-BTC MOF was 177.3 mg/g, while that of ARS reached $q_e = 80.4$ mg/g. The experimental data were fitted to three different kinetic models, namely, the pseudo-first order (Figure 3b), the pseudo-second order (Figure 3c), and the intraparticle diffusion models (Figure 3d). The kinetic parameters obtained by each model are listed in Table 1. The fitting of the experimental data using the pseudo-first order gave low correlation coefficients (Table 1), thus, demonstrating the inadequacy of this model to describe both ARS and MG adsorption on Fe-BTC. On the contrary, the pseudo-second order model resulted in a very good fitting, as demonstrated by the high correlation coefficients ($R > 0.99$) and a good residuals plot (Figure S3b). Moreover, the values of q_e calculated from pseudo-second order models (177.31 mg/g for MG and 81.09 mg/g for ARS) are very similar to the experimentally observed values (177.28 mg/g for MG and 80.39 mg/g for ARS, Figure 3a). The values of the kinetic constant (k'') confirmed that the adsorption process for MG ($k'' = 3.98 \times 10^{-2} \text{ g}\cdot\text{mg}^{-1} \text{ min}^{-1}$) was faster than that for ARS ($k'' = 4.29 \times 10^{-3} \text{ g}\cdot\text{mg}^{-1} \text{ min}^{-1}$). The fit of the model to the adsorption data demonstrate that the adsorption of the dyes on the adsorbent sites is the rate determining step [29,55]. Figure 3d shows the variation of q_t versus $t^{0.5}$ according with the intraparticle diffusion model. The slopes of the three straight lines in Figure 3d represent the kinetic constants of the different steps (1, external diffusion; 2, internal diffusion; and 3, adsorption) involved in the adsorption of ARS and MG dyes on Fe-BTC MOF. However, the fit of this model is of lower quality than that of the pseudo-second order model (Figure S3c), which gives the best description of the obtained kinetic data.

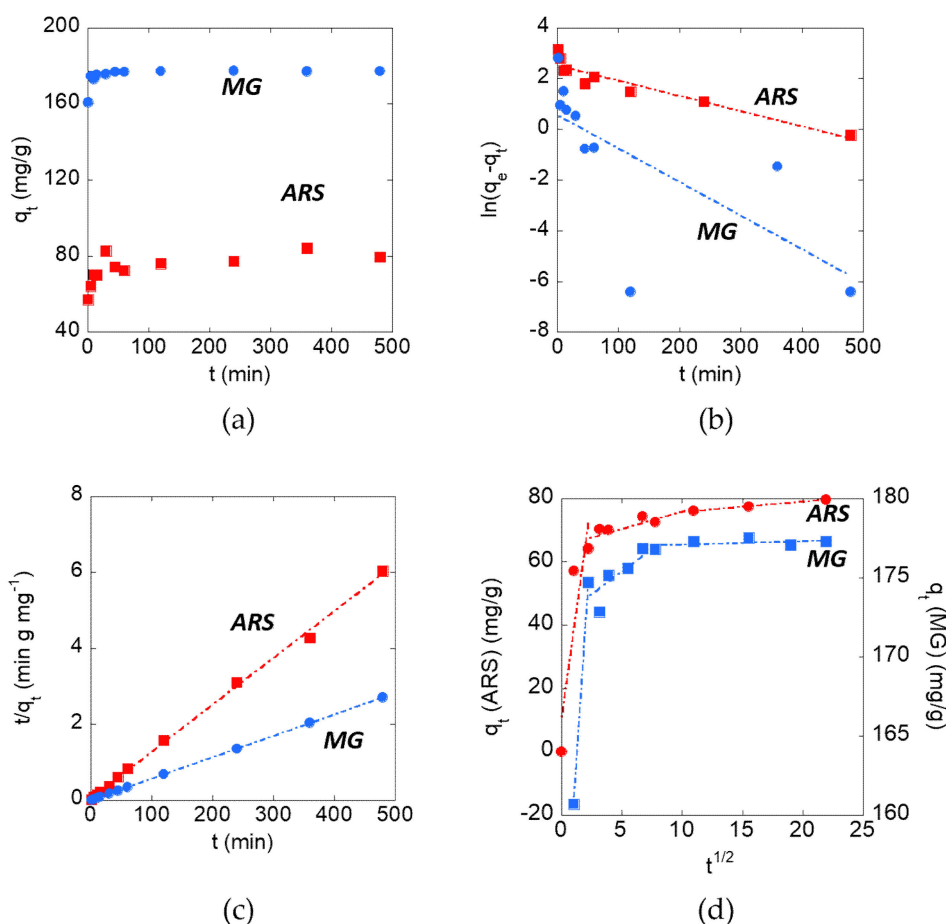


Figure 3. (a) Amount of alizarin red S and malachite green adsorbed, q_t , as a function of contact time. The data were fit using linearized kinetics models; (b) Pseudo-first order; (c) Pseudo-second order; (d) Intraparticle diffusion. The experiments were carried out in water at pH = 4 and $T = 298$ K.

Table 1. Comparison among different adsorption kinetic models for MG and ARS on Fe-BTC MOF.

	$q_{e\ exp}$ (mg g^{-1})	Pseudo-First Order			Pseudo-Second Order			Intraparticle Diffusion		
		k' (min^{-1})	$q_{e\ cal}$ (mg g^{-1})	R	k'' ($\text{g mg}^{-1} \text{min}^{-1}$)	$q_{e\ cal}$ (mg g^{-1})	R	k_i ($\text{g mg}^{-1} \text{min}^{-1/2}$)	x_i (mg g^{-1})	R
ARS	80.39	5.98×10^{-3}	12.78	0.946	4.29×10^{-3}	81.09	0.992	27.77 1.10 0.33	10.44 64.81 72.38	0.885 0.873 0.999
MG	177.28	1.3210^{-2}	1.75	0.707	3.98×10^{-2}	177.31	1	11.33 0.58 0.02	149.38 172.51 176.88	1 0.828 0.434

2.4. Adsorption Isotherms

The adsorption isotherms of ARS and MG on Fe-BTC MOF ($T = 298$ K, pH 4) are shown in Figure 4a. The MOF adsorbed MG to a greater extent than ARS, reaching the maximal adsorbed amounts ($q_{e,max}$), corresponding to the isotherm plateaus, $q_{e,max} = 177.3$ mg/g and $q_{e,max} = 80.4$ mg/g for MG and ARS, respectively. Then, experimental data were tested by applying a fitting procedure based on different linearized isotherm models, namely, Temkin (Figure 4b), Freundlich (Figure 4c), and Langmuir (Figure 4d). The constants associated with each model are reported in Table 2.

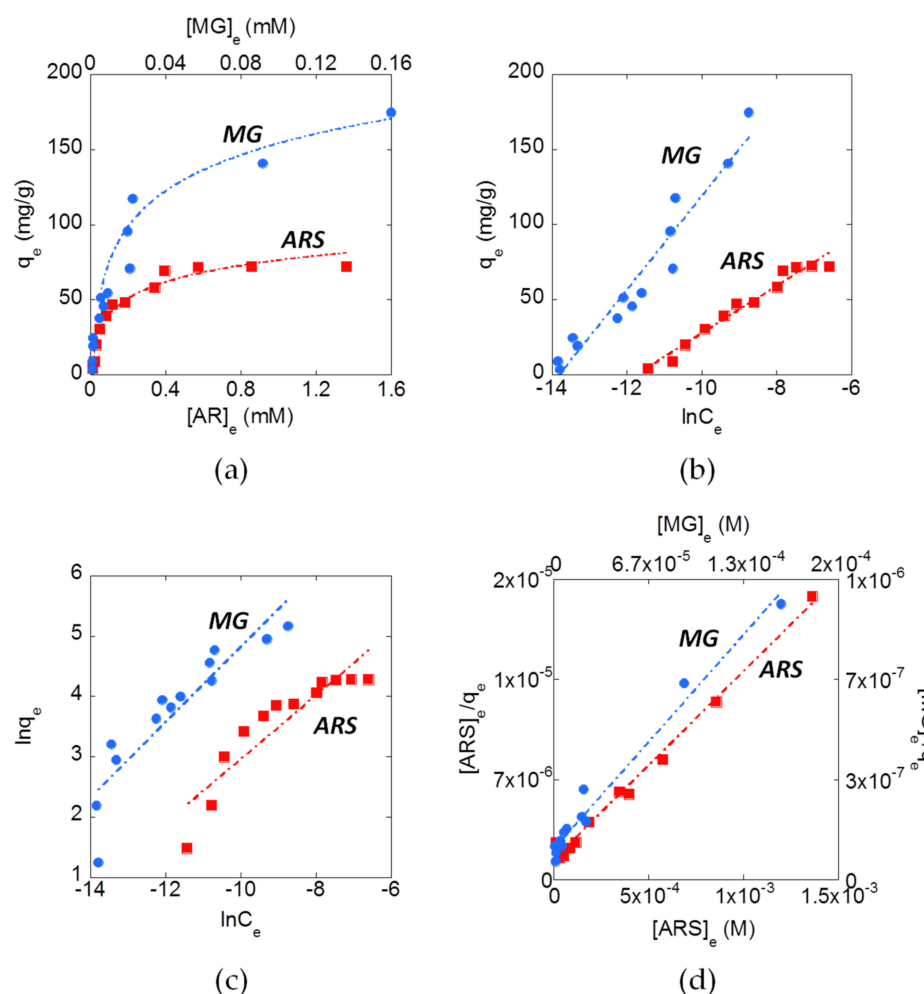


Figure 4. (a) Adsorption isotherms of MG and ARS with MOF where q_e is a function of the equilibrium concentration. Adsorption data were fitted using linearized isotherms; (b) Temkin; (c) Freundlich; (d) Langmuir. The experiments were carried out in distilled water for 24 h, at $T = 298$ K.

Table 2. Comparison among different isotherm models for ARS and MG adsorption on Fe-BTC MOF ($\text{pH} = 4$, $T = 298$ K).

	b_T	Temkin		Freundlich			Langmuir			ΔG° (KJ mol ⁻¹)
		A_T (L mg ⁻¹)	R	K_F (L mg ⁻¹)	$1/n$	R	K_L (L mg ⁻¹)	$q_{e,max}$ (mg g ⁻¹)	R	
ARS	157.59	$1.28 \cdot 10^5$	0.982	$3.85 \cdot 10^3$	0.529	0.910	$9.30 \cdot 10^3$	79.88	0.995	-54.21
MG	79.34	$9.87 \cdot 10^5$	0.967	$63.77 \cdot 10^3$	0.624	0.909	$51.56 \cdot 10^3$	187.24	0.967	-58.61

By comparing the correlation coefficients (R) obtained by applying the different linearized isotherms to the experimental data, with the resulting residual plots (Figure S4), the Langmuir model fits the experimental data better than the other two models. This indicates that a monolayer of adsorbate (dye molecules) was formed on the adsorbent surface (Fe-BTC MOF). Generally, the larger the Langmuir constant K_L , the more favorable the adsorption process [56]. This confirms that adsorption of MG ($K_L = 51.56 \cdot 10^3$ L/mg) was favored over that of ARS ($K_L = 9.30 \cdot 10^3$ L/mg) [57]. Then, the Langmuir constant, K_L , was used to calculate the thermodynamic equilibrium constant K_e^0 by means of the equation [58] as:

$$K_e^0 = \frac{K_L M M_{\text{Adsorbate}} [\text{Adsorbate}]^0}{\gamma} \quad (1)$$

where $MM_{\text{Adsorbate}}$ is the molecular mass of the adsorbate ($MM_{\text{MG}} = 364.91 \text{ g mol}^{-1}$ and $MM_{\text{ARS}} = 342.26 \text{ g mol}^{-1}$), $[\text{Adsorbate}]^\circ$ is the standard concentration of the adsorbate (1 mol L^{-1}), and γ is the activity coefficient (dimensionless) that can be considered to have a value of 1 in dilute solution. The K_e^0 values thus calculated were used to determine the standard Gibbs free energy (ΔG^0) for the adsorption process, according to the relationship:

$$\Delta G^0 = -RT \ln K_e^0 \quad (2)$$

where R is the universal gas constant ($8.314 \text{ J K}^{-1} \text{ mol}^{-1}$) and T is the absolute temperature (298.13 K). As shown in Table 2, ΔG^0 values were $-54.21 \text{ kJ mol}^{-1}$ and $-58.61 \text{ kJ mol}^{-1}$ for the adsorption of ARS and MG, respectively. This indicates that, in standard conditions, the desorption \rightleftharpoons adsorption equilibrium lies far to the right for both dyes, in agreement with experimental observations.

3. Discussion

The adsorption of malachite green on a range of MOFs has been reported [59–62]. Table 3 summarizes the data from studies relevant to the present work. Among the various types of MOFs tested, the lowest performing in terms of dye adsorption capacity were Cu-BTC [57] and Mil-53-Al-NH₂ [59]. Both the ZIF-67 prepared by Jin et al. [61] and the UiO-66 prepared by Embaby et al. [55] acted as strong adsorbents with q_e values of 2545 and 400 mg/g, respectively, with adsorption times between 30 and 60 min. The Fe-BTC synthesized by Huo et al. [32] and the mixed-ligand Cu-BDC-BTC compound prepared by Shi et al. [60] had adsorption capacities comparable to those obtained here, 205 and 185 mg/g, respectively, but the time required for the adsorption process (120 min) was four times higher than that obtained by us (30 min).

Table 3. Comparison with other systems like that studied in this article.

Adsorbent	T (°C)	Synthesis		Dye	$q_e^{(exp)}$ (mg/g)	t (min)	Kinetic k'' (g·mg ⁻¹ ·min)	Isotherm		Ref.
		t (h)	Solvent					Model	K (L·mg ⁻¹)	
Fe-BTC	25	<1	H ₂ O	Alizarin red S	80	30	4.29×10^{-3}	Langmuir	$9.30 \cdot 10^3$	This work
				Malachite green	177	30	3.98×10^{-2}	Langmuir	$51.56 \cdot 10^3$	
Fe-BTC	150	12	H ₂ O	Malachite green	205	120	$6.67 \cdot 10^{-3}$	Freundlich	6.49	[32]
UiO-66	120	1	DMF	Alizarin red S	400	36	$2.3 \cdot 10^{-4}$	Langmuir	0.06	[55]
Cu-BTC	100	10	EtOH/DMF	Methylene blue	4.68	10	42.39	Langmuir	1.89	[57]
Mil-53(Al)-NH ₂	150	24	DMF/H ₂ O	Malachite green	37.8	200	-	Langmuir	0.29	[59]
				Methylene blue	45.2	200	-	Langmuir	0.67	
Cu-BTC/BDC	120	12	EtOH	Malachite green	185	-	-	Freundlich	-	[60]
ZIF-67/PAN	25	<1	H ₂ O	Malachite green	2545	60	$2.7 \cdot 10^{-3}$	Langmuir	0.05	[61]
NH-ZIF-67	25	<1	MeOH	Malachite green	114.1	240	-	-	-	[62]

Li et al. found that the absorption capacity of MIL-53(Al) increased after functionalization with amino groups [59], an increase that can be attributed to hydrogen bond interactions [62] between the amino groups of the dye molecules and the amino groups of MIL-53(Al)-NH₂; the adsorption capacity achieved by this system is, however, rather low (45.2 mg/g in the case of methylene blue and 37.8 mg/g in the case of malachite green). Jin et al. prepared a ZIF-67 MOF integrated on a polyacrylonitrile membrane to recover the MOF from water solution at the end of the adsorption process [61]. This system had an adsorption capacity of 2545 mg/g of MG, and the time required to complete the process was 60 min. The only study reported to date on the adsorption of alizarin red S by MOFs (Table 3) was carried out by Embaby et al., who reported an adsorption capacity of 400 mg/g for ARS on zirconium-based MOF UiO-66 [55].

Most studies have confirmed that the Langmuir isotherm is the optimal model to describe the adsorption of dyes on the MOF materials described in this study, with the

pseudo-second order model representing the best kinetic model. However, in addition to fast kinetics and a high adsorbing capacity, the successful use of an adsorbent for environmental remediation should not be assessed only based on its performance, but also in terms of factors such as cost and ease of preparation. The majority of reports on the use of MOFs utilize synthetic methods that use organic solvents and/or high temperatures. For example, among the adsorbents with higher q_e , the synthesis of UiO-66 was carried out in 1 h in dimethylformamide at 120 °C [55], while Cu-BDC-BTC was prepared in ethanol by heating to 120 °C, for 12 h [60]. The Fe-BTC synthesized by Huo et al., despite being prepared in water, required long synthetic times (12 h) and high temperatures (150 °C in an autoclave) [32]. The most interesting material, both from the point of view of the high adsorbing capacity and of synthesis conditions (25 °C in H₂O), was the ZIF-67/PAN fibrous membrane proposed by Jin et al. [61]. However, one of the starting reagents of this MOF is the 2-methylimidazole, which is a carcinogenic compound [63,64]. The Fe-BTC used here is significantly easier (and lower cost) to prepare, in an environmentally-friendly manner, with synthesis in less than 1 h at room temperature, using distilled water as the solvent and the reagents, FeCl₃ and trimesic acid.

4. Material and Methods

4.1. Chemicals

Tris(hydroxymethyl)-aminomethane (TRIS, ≥99.8%) was purchased from Bio-Rad Laboratories. Iron(III) chloride (97%), sodium hydroxide, trimesic acid, and 4-[[4-(dimethylamino)phenyl](phenyl)methylidene]-*N,N*-dimethylcyclohexa-2,5-dien-1-iminium chloride (malachite green) were purchased from Sigma-Aldrich. 3,4-Dihydroxy-9,10-dioxo-2-anthracenesulfonic acid (alizarin red S) was purchased as the sodium salt from Fluka Chemie.

4.2. Synthesis and Characterization of Fe-BTC MOF

The Fe-BTC type MOF was prepared following the procedure reported by Sanchez-Sanchez et al. [27,65]. Briefly, 0.3048 g of FeCl₃ was dissolved in 10.203 mL of distilled water. Then, a solution containing 0.263 g of trimesic acid, 3.685 mL of NaOH 1.06 M, and 6.388 mL of H₂O was added dropwise under stirring. The solid was collected by filtration under vacuum, washed with distilled water, and dried in air.

X-ray diffraction (XRD) analysis was carried out using an X'PERT Pro PANalytical diffractometer using a Cu K_α radiation source. The data were collected from 5 to 40° with a 2θ step size of 0.013, for 99.19 s. The N₂ adsorption/desorption isotherms at 77 K were carried out on a ASAP 2020 (Micromeritics) instrument to obtain the surface area (Brunauer–Emmett–Teller, BET) [66] and pore size distribution (Barrett–Joyner–Halenda, BJH) [67]. The FTIR analysis was performed using a Bruker Tensor 27 spectrophotometer equipped with a diamond-ATR accessory and a DTGS detector. A number of 128 scans at a resolution of 2 cm⁻¹ were averaged in the spectral range 4000–400 cm⁻¹. Thermal analysis data were collected with a STA6000 (Perkin Elmer) thermal analyzer in the 25–850 °C range, under oxygen flow (heating rate = 10 °C/min, flow rate = 40 mL min⁻¹). The Zeta potential of Fe-BTC was measured using a Zetasizer Nano ZSP (Malvern Instruments) in backscatter configuration (θ = 173°), at a laser wavelength of λ = 633 nm, using Zetasizer software (version 7.03) to analyze the data. Zeta potential values were calculated by means of the Henry equation using water as the dispersant medium (ε_r = 78.5 and η = 0.89 cP at 25 °C) and $f(\kappa a) = 1.5$ (Smoluchowski approximation). The sample was prepared by suspending Fe-BTC (2 mg/mL) in distilled water adding HCl and NaOH to vary the pH from 3 to 7. Before the measurements the samples were sonicated for 30 min and left stirring overnight. The scattering cell temperature was fixed at 25 °C.

4.3. Adsorption Studies

A mass of 100 mg of the synthesized MOF was dispersed in 1 mL of distilled water using a vortex mixer (Figure S1a). To evaluate the optimal pH for the adsorption process, a series of Eppendorf tubes were filled with 1 mL of dye solution and 35 μL of solid dispersion

(Figure S1a) at different pH in the range 3–7. The pH was measured using a Metrohm pH-meter and adjusted adding small volumes of HCl and NaOH solutions. All the mixtures were put in a rotating mixer overnight, and then collected by centrifugation (1000 rpm for 1 min). The concentration of dye in the solutions before and after adsorption experiments was determined using a Cary 60 UV-Vis spectrophotometer (Agilent) ($\lambda = 516$ nm for ARS and 620 nm for MG). The solutions were diluted in Tris-HCl buffer (pH 7, 10 mM) to ensure a constant pH during the measurements, since the absorbance peaks of the dyes, especially in the case of ARS, are influenced by pH [68,69].

Adsorption kinetic studies were carried out analyzing samples withdrawn at different times (from 1 min to 8 h) at a fixed pH of 4 and at a constant concentration of the dyes (1.5 mM). Adsorption isotherms at $T = 298$ K were obtained at constant adsorption time (24 h) and pH (4) at varying initial dye concentrations (from 0.01 to 2 mM).

4.3.1. Adsorption Kinetic Models

The adsorption kinetics were studied by measuring the decrease in concentration of the dyes in solution at given times (q_t) through the following equation,

$$q_t = \frac{(C_i - C_t)V}{m} \quad (3)$$

where C_i and C_t are the dye concentrations at time = 0 and time = t , while V and m are the volumes of the solution and the mass of the solid, respectively.

The experimental data were fitted using the linearized equations of three different kinetic models. A pseudo-first order model as follows:

$$\ln(q_e - q_t) = \ln q_e - k' \cdot t \quad (4)$$

A pseudo-second order model [70,71] as follows:

$$\frac{t}{q_t} = \frac{1}{q_e^2 \cdot k''} + \frac{t}{q_e} \quad (5)$$

and an intraparticle diffusion model [72] as follows:

$$q_e = k_i \cdot t^{1/2} + x_i \quad (6)$$

where q_e is the amount of adsorbed dye at the equilibrium, k' , k'' and k_i are the pseudo-first order constant, pseudo-second order constant, and intraparticle diffusion constant, respectively.

4.3.2. Adsorption Isotherm Models

The adsorption isotherms were obtained by plotting the experimentally adsorbed amounts of dyes, q_e , versus the equilibrium concentration, C_e . The experimental data were fitted through three different isotherm models', i.e., Temkin (Equation (7)), Freundlich (Equation (8)), and Langmuir (Equation (9)), in their linearized forms [73]:

$$q_e = \frac{RT}{b_T} \ln A_T + \frac{RT}{b_T} \ln C_e \quad (7)$$

where q_e is the amount of adsorbed dye at the equilibrium, $q_{e,max}$ is the maximum monolayer coverage capacity, b_T is the Temkin constant, and A_T is the Temkin equilibrium binding constant.

$$\ln q_e = \ln K_F + \frac{1}{n} \ln C_e \quad (8)$$

where $1/n$ (dimensionless) and K_F are the Freundlich constants, the heterogeneity factor, and support capacity (characteristic of each adsorbate-adsorbent pair), respectively.

$$\frac{C_e}{q_e} = \frac{1}{q_m \cdot K_L} + \frac{1}{q_m} C_e \quad (9)$$

where K_L is the Langmuir constant [5,74].

5. Conclusions

An Fe-BTC MOF was synthesized following the procedure proposed by Sanchez-Sanchez et al. The structure of the material was characterized by XRD, while its pore diameter distribution (4–40 nm) and surface area (443 m²/g) were determined from N₂ adsorption/desorption isotherms. The zeta potential of aqueous dispersions of Fe-BTC was determined by ELS and a point of zero charge (pH_{pzc}) of 3.2 was obtained. Further qualitative characterizations were carried out using FTIR and TGA techniques. The data obtained were comparable with those reported in the literature. Then, the Fe-BTC was used as an adsorbent for the removal of two toxic dyes from water, alizarin red S (ARS) and malachite green (MG). The adsorption capacity was measured as a function of time and of the concentration of dye required to obtain the kinetic profiles and the adsorption isotherms of the process, respectively. The adsorption of both dyes was rapid (<30 min) as compared with other reports, which reached equilibrium generally in 60–200 min. The Langmuir model provided the best fit to the adsorption process, with maximum adsorption capacities of 80 and 177 mg/g for ARS and MG on Fe-BTC MOF, respectively. The data obtained for adsorption on to Fe-BTC MOF compare favorably with literature reports. However, what distinguishes this work is the green method used to synthesize the adsorbing material. Indeed, the synthesis of the Fe-BTC MOF was performed in an aqueous solution at room temperature in less than 1 h, unlike the generally used syntheses which require organic solvents or high temperatures and longer times. Furthermore, the adsorption rate of the dyes was higher than most of the other reported MOFs. Future work could be devoted to test the adsorption performance of other toxic dyes or even other classes of toxic substances and to verify the feasibility of continuous processes or on a larger scale. Further work is needed to find the optimal conditions for dye desorption and MOF reuse for multiple adsorption cycles.

Supplementary Materials: Supplementary materials can be found at <https://www.mdpi.com/1422-0067/22/2/788/s1>.

Author Contributions: Conceptualization, A.S. and G.R.D.; investigation, G.R.D. and D.T.; data curation, writing—original draft preparation, G.R.D., D.T., L.M., E.M., and A.S.; writing—review and editing, G.R.D., D.T., L.M., E.M., and A.S.; supervision, A.S. and E.M. All authors have read and agreed to the published version of the manuscript.

Funding: This research was funded by MIUR PON-RI (DOT1304455).

Institutional Review Board Statement: Not applicable.

Informed Consent Statement: Not applicable.

Data Availability Statement: The data presented in this study are available in this paper and supplementary file.

Acknowledgments: W. Redington and F. Otero Diez (University of Limerick) for the XRD characterization.

Conflicts of Interest: The authors declare no conflict of interest. The funders had no role in the design of the study; in the collection, analyses, or interpretation of data; in the writing of the manuscript, or in the decision to publish the results.

Abbreviations

MOF	Metal organic frameworks
MG	Malachite green
ARS	Alizarin red S
XRD	X-ray diffraction
FTIR	Fourier transform infrared spectroscopy
TGA	Thermogravimetric analysis

References

1. Hessel, C.; Allegre, C.; Maisseu, M.; Charbit, F.; Moulin, P. Guidelines and legislation for dye house effluents. *J. Environ. Manag.* **2007**, *83*, 171–180. [[CrossRef](#)] [[PubMed](#)]
2. Martínez-Huitle, C.A.; Brillas, E. Decontamination of wastewaters containing synthetic organic dyes by electrochemical methods: A general review. *Appl. Catal. B Environ.* **2009**, *87*, 105–145. [[CrossRef](#)]
3. Bilal, M.; Asgher, M. Sandal reactive dyes decolorization and cytotoxicity reduction using manganese peroxidase immobilized onto polyvinyl alcohol-alginate beads. *Chem. Cent. J.* **2015**, *9*, 47. [[CrossRef](#)] [[PubMed](#)]
4. Zhang, F.; Ma, B.; Jiang, X.; Ji, Y. Dual function magnetic hydroxyapatite nanopowder for removal of malachite green and Congo red from aqueous solution. *Powder Technol.* **2016**, *302*, 207–214. [[CrossRef](#)]
5. Mashkooor, F.; Nasar, A.; Inamuddin; Asiri, A.M. Exploring the reusability of synthetically contaminated wastewater containing crystal violet dye using tectona grandis sawdust as a very low-cost adsorbent. *Sci. Rep.* **2018**, *8*, 1–16. [[CrossRef](#)]
6. Collivignarelli, M.C.; Abbà, A.; Carnevale Miino, M.; Damiani, S. Treatments for color removal from wastewater: State of the art. *J. Environ. Manag.* **2019**, *236*, 727–745. [[CrossRef](#)]
7. Amaterz, E.; Tara, A.; Bouddouch, A.; Taoufiq, A.; Bakiz, B.; Lazar, F.; Gilliot, M.; Benhachemi, A.; Bazzi, L.; Jbara, O. Hierarchical flower-like SrHPO₄ electrodes for the photoelectrochemical degradation of Rhodamine B. *J. Appl. Electrochem.* **2020**. [[CrossRef](#)]
8. Zhang, X.; Shao, D.; Lyu, W.; Xu, H.; Yang, L.; Zhang, Y.; Wang, Z.; Liu, P.; Yan, W.; Tan, G. Design of magnetically assembled electrode (MAE) with Ti/PbO₂ and heterogeneous auxiliary electrodes (AEs): The functionality of AEs for efficient electrochemical oxidation. *Chem. Eng. J.* **2020**, *395*. [[CrossRef](#)]
9. Ge, Q.; Wang, P.; Wan, C.; Chung, T.S. Polyelectrolyte-promoted Forward Osmosis-Membrane Distillation (FO-MD) hybrid process for dye wastewater treatment. *Environ. Sci. Technol.* **2012**, *46*, 6236–6243. [[CrossRef](#)]
10. Yang, C.; Xu, W.; Nan, Y.; Wang, Y.; Hu, Y.; Gao, C.; Chen, X. Fabrication and characterization of a high performance polyimide ultrafiltration membrane for dye removal. *J. Colloid Interface Sci.* **2020**, *562*, 589–597. [[CrossRef](#)]
11. Bukman, L.; De Souza, V.R.; Fernandes, N.R.C.; Caetano, W.; Batistela, V.R.; Hioka, N. Reverse micellar extraction of dyes based on fatty acids and recoverable organic solvents. *Sep. Purif. Technol.* **2020**, *242*. [[CrossRef](#)]
12. Madhushika, H.G.; Ariyadasa, T.U.; Gunawardena, S.H.P. Biological decolourization of textile industry wastewater by a developed bacterial consortium. *Water Sci. Technol.* **2020**, *80*, 1910–1918. [[CrossRef](#)]
13. Katheresan, V.; Kannedo, J.; Lau, S.Y. Efficiency of various recent wastewater dye removal methods: A review. *J. Environ. Chem. Eng.* **2018**, *6*, 4676–4697. [[CrossRef](#)]
14. Rodríguez-Couto, S.; Osma, J.F.; Toca-Herrera, J.L. Removal of synthetic dyes by an eco-friendly strategy. *Eng. Life Sci.* **2009**, *9*, 116–123. [[CrossRef](#)]
15. Furukawa, H.; Cordova, K.E.; O’Keeffe, M.; Yaghi, O.M. The chemistry and applications of metal-organic frameworks. *Science* **2013**, *341*. [[CrossRef](#)] [[PubMed](#)]
16. Jiao, L.; Wang, Y.; Jiang, H.L.; Xu, Q. Metal–Organic Frameworks as Platforms for Catalytic Applications. *Adv. Mater.* **2018**, *30*, e1703663. [[CrossRef](#)]
17. Alqadami, A.A.; Naushad, M.; Alothman, Z.A.; Ahamad, T. Adsorptive performance of MOF nanocomposite for methylene blue and malachite green dyes: Kinetics, isotherm and mechanism. *J. Environ. Manag.* **2018**, *223*, 29–36. [[CrossRef](#)]
18. Ghanbari, T.; Abnisa, F.; Wan Daud, W.M.A. A review on production of metal organic frameworks (MOF) for CO₂ adsorption. *Sci. Total Environ.* **2020**, *707*, 135090. [[CrossRef](#)]
19. Pitzalis, F.; Carucci, C.; Naseri, M.; Fotouhi, L.; Magner, E.; Salis, A. Lipase Encapsulation onto ZIF-8: A Comparison between Biocatalysts Obtained at Low and High Zinc/2-Methylimidazole Molar Ratio in Aqueous Medium. *ChemCatChem* **2018**, *10*, 1578–1585. [[CrossRef](#)]
20. Naseri, M.; Pitzalis, F.; Carucci, C.; Medda, L.; Fotouhi, L.; Magner, E.; Salis, A. Lipase and Laccase Encapsulated on Zeolite Imidazolate Framework: Enzyme Activity and Stability from Voltammetric Measurements. *ChemCatChem* **2018**, *10*, 5425–5433. [[CrossRef](#)]
21. Lustig, W.P.; Mukherjee, S.; Rudd, N.D.; Desai, A.V.; Li, J.; Ghosh, S.K. Metal-organic frameworks: Functional luminescent and photonic materials for sensing applications. *Chem. Soc. Rev.* **2017**, *46*, 3242–3285. [[CrossRef](#)] [[PubMed](#)]
22. Li, J.; Wang, X.; Zhao, G.; Chen, C.; Chai, Z.; Alsaedi, A.; Hayat, T.; Wang, X. Metal-organic framework-based materials: Superior adsorbents for the capture of toxic and radioactive metal ions. *Chem. Soc. Rev.* **2018**, *47*, 2322–2356. [[CrossRef](#)] [[PubMed](#)]
23. Samokhvalov, A. Adsorption on Mesoporous Metal-Organic Frameworks in Solution: Aromatic and Heterocyclic Compounds. *Chem. Eur. J.* **2015**, *21*, 16726–16742. [[CrossRef](#)] [[PubMed](#)]

24. Jiang, D.; Chen, M.; Wang, H.; Zeng, G.; Huang, D.; Cheng, M.; Liu, Y.; Xue, W.; Wang, Z.W. The application of different typological and structural MOFs-based materials for the dyes adsorption. *Coord. Chem. Rev.* **2019**, *380*, 471–483. [[CrossRef](#)]
25. Lv, S.W.; Liu, J.M.; Wang, Z.H.; Ma, H.; Li, C.Y.; Zhao, N.; Wang, S. Recent advances on porous organic frameworks for the adsorptive removal of hazardous materials. *J. Environ. Sci. (China)* **2019**, *80*, 169–185. [[CrossRef](#)] [[PubMed](#)]
26. Tian, S.; Xu, S.; Liu, J.; He, C.; Xiong, Y.; Feng, P. Highly efficient removal of both cationic and anionic dyes from wastewater with a water-stable and eco-friendly Fe-MOF via host-guest encapsulation. *J. Clean. Prod.* **2019**, *239*, 117767. [[CrossRef](#)]
27. Sanchez-Sanchez, M.; De Asua, I.; Ruano, D.; Diaz, K. Direct Synthesis, Structural Features, and Enhanced Catalytic Activity of the Basolite F300-like Semiamorphous Fe-BTC Framework. *Cryst. Growth Des.* **2015**, *15*, 4498–4506. [[CrossRef](#)]
28. Gascón, V.; Carucci, C.; Jiménez, M.B.; Blanco, R.M.; Sánchez-Sánchez, M.; Magner, E. Rapid in Situ Immobilization of Enzymes in Metal–Organic Framework Supports under Mild Conditions. *ChemCatChem* **2017**, *9*, 1182–1186. [[CrossRef](#)]
29. García, E.R.; Medina, R.L.; Lozano, M.M.; Pérez, I.H.; Valero, M.J.; Maubert Franco, A.M. Adsorption of azo-dye Orange II from aqueous solutions using a metal-organic framework material: Iron- benzenetricarboxylate. *Materials (Basel)* **2014**, *7*, 8037–8057. [[CrossRef](#)]
30. Han, Q.; Wang, Z.; Chen, X.; Jiao, C.; Li, H.; Yu, R. Facile Synthesis of Fe-based MOFs (Fe-BTC) as Efficient Adsorbent for Water Purifications. *Chem. Res. Chin. Univ.* **2019**, *35*, 564–569. [[CrossRef](#)]
31. Guesh, K.; Caiuby, C.A.D.; Mayoral, Á.; Díaz-García, M.; Díaz, I.; Sanchez-Sanchez, M. Sustainable Preparation of MIL-100 (Fe) and Its Photocatalytic Behavior in the Degradation of Methyl Orange in Water. *Cryst. Growth Des.* **2017**, *17*, 1806–1813. [[CrossRef](#)]
32. Huo, S.H.; Yan, X.P. Metal-organic framework MIL-100 (Fe) for the adsorption of malachite green from aqueous solution. *J. Mater. Chem.* **2012**, *22*, 7449–7455. [[CrossRef](#)]
33. Jia, Y.; Jin, Q.; Li, Y.; Sun, Y.; Huo, J.; Zhao, X. Investigation of the adsorption behaviour of different types of dyes on MIL-100 (Fe) and their removal from natural water. *Anal. Methods* **2015**, *7*, 1463–1470. [[CrossRef](#)]
34. Tan, F.; Liu, M.; Li, K.; Wang, Y.; Wang, J.; Guo, X.; Zhang, G.; Song, C. Facile synthesis of size-controlled MIL-100 (Fe) with excellent adsorption capacity for methylene blue. *Chem. Eng. J.* **2015**, *281*, 360–367. [[CrossRef](#)]
35. Zhu, C.; Jiang, C.; Chen, S.; Mei, R.; Wang, X.; Cao, J.; Ma, L.; Zhou, B.; Wei, Q.; Ouyang, G.; et al. Ultrasound enhanced electrochemical oxidation of Alizarin Red S on boron doped diamond(BDD) anode: Effect of degradation process parameters. *Chemosphere* **2018**, *209*, 685–695. [[CrossRef](#)]
36. Hanif, S.; Shahzad, A. Removal of chromium(VI) and dye Alizarin Red S (ARS) using polymer-coated iron oxide (Fe₃O₄) magnetic nanoparticles by co-precipitation method. *J. Nanoparticle Res.* **2014**, *16*. [[CrossRef](#)]
37. Legan, L.; Retko, K.; Ropret, P. Vibrational spectroscopic study on degradation of alizarin carmine. *Microchem. J.* **2016**, *127*, 36–45. [[CrossRef](#)]
38. Srivastava, S.; Sinha, R.; Roy, D. Toxicological effects of malachite green. *Aquat. Toxicol.* **2004**, *66*, 319–329. [[CrossRef](#)]
39. Culp, S.J.; Beland, F.A. Malachite Green: A Toxicological Review. *J. Am. Coll. Toxicol.* **1996**, 219–238. [[CrossRef](#)]
40. Hashimoto, J.C.; Paschoal, J.A.R.; De Queiroz, J.F.; Reyes, F.G.R. Considerations on the use of malachite green in aquaculture and analytical aspects of determining the residues in fish: A review. *J. Aquat. Food Prod. Technol.* **2011**, *20*, 273–294. [[CrossRef](#)]
41. Sacara, A.M.; Nairi, V.; Salis, A.; Turdean, G.L.; Muresan, L.M. Silica-modified Electrodes for Electrochemical Detection of Malachite Green. *Electroanalysis* **2017**, *29*, 2602–2609. [[CrossRef](#)]
42. Pangkumhang, B.; Jutaporn, P.; Sorachoti, K.; Khamdahsag, P.; Tanboonchuy, V. Applicability of iron (III) Trimesic (Fe-BTC) to enhance lignin separation from pulp and paper wastewater. *Sains Malays.* **2019**, *48*, 199–208. [[CrossRef](#)]
43. Du, M.; Li, L.; Li, M.; Si, R. Adsorption mechanism on metal organic frameworks of Cu-BTC, Fe-BTC and ZIF-8 for CO₂ capture investigated by X-ray absorption fine structure. *RSC Adv.* **2016**, *6*, 62705–62716. [[CrossRef](#)]
44. Salazar-Aguilar, A.D.; Vega, G.; Casas, J.A.; Vega-Díaz, S.M.; Tristan, F.; Meneses-Rodríguez, D.; Belmonte, M.; Quintanilla, A. Direct hydroxylation of phenol to dihydroxybenzenes by H₂O₂ and fe-based metal-organic framework catalyst at room temperature. *Catalysts* **2020**, *10*, 172. [[CrossRef](#)]
45. Majano, G.; Ingold, O.; Yulikov, M.; Jeschke, G.; Pérez-Ramírez, J. Room-temperature synthesis of Fe-BTC from layered iron hydroxides: The influence of precursor organisation. *CrystEngComm* **2013**, *15*, 9885–9892. [[CrossRef](#)]
46. Yang, Y.; Bai, Y.; Zhao, F.; Yao, E.; Yi, J.; Xuan, C.; Chen, S. Effects of metal organic framework Fe-BTC on the thermal decomposition of ammonium perchlorate. *RSC Adv.* **2016**, *6*, 67308–67314. [[CrossRef](#)]
47. Dhakshinamoorthy, A.; Alvaro, M.; Chevreau, H.; Horcajada, P.; Devic, T.; Serre, C.; Garcia, H. Iron(iii) metal-organic frameworks as solid Lewis acids for the isomerization of α -pinene oxide. *Catal. Sci. Technol.* **2012**, *2*, 324–330. [[CrossRef](#)]
48. Hasanzadeh, M.; Simchi, A.; Shahriyari Far, H. Nanoporous composites of activated carbon-metal organic frameworks for organic dye adsorption: Synthesis, adsorption mechanism and kinetics studies. *J. Ind. Eng. Chem.* **2020**, *81*, 405–414. [[CrossRef](#)]
49. Niazi, A.; Ghalie, M.; Yazdanipour, A.; Ghasemi, J. Spectrophotometric determination of acidity constants of Alizarine Red S in water, water-Brij-35 and water-SDS micellar media solutions. *Spectrochim. Acta Part A Mol. Biomol. Spectrosc.* **2006**, *64*, 660–664. [[CrossRef](#)]
50. Chin, Y.P.; Abdul Raof, S.F.; Sinniah, S.; Lee, V.S.; Mohamad, S.; Abdul Manan, N.S. Inclusion complex of Alizarin Red S with β -cyclodextrin: Synthesis, spectral, electrochemical and computational studies. *J. Mol. Struct.* **2015**, *1083*, 236–244. [[CrossRef](#)]
51. Cheriaa, J.; Khaireddine, M.; Rouabhia, M.; Bakhrouf, A. Removal of triphenylmethane dyes by bacterial consortium. *Sci. World J.* **2012**, *2012*. [[CrossRef](#)] [[PubMed](#)]

52. Ghodbane, I.; Kherrrat, R.; Zougar, S.; Lamari, R.; Haddadji, R.; Medjram, M.S. Kinetic study and characterization of a platinum electrode/sensitive membrane for malachite green detection. *Sens. Rev.* **2018**, *38*, 335–344. [[CrossRef](#)]
53. Zhang, B.L.; Qiu, W.; Wang, P.P.; Liu, Y.L.; Zou, J.; Wang, L.; Ma, J. Mechanism study about the adsorption of Pb(II) and Cd(II) with iron-trimesic metal-organic frameworks. *Chem. Eng. J.* **2020**, *385*, 123507. [[CrossRef](#)]
54. Mon, M.; Bruno, R.; Ferrando-Soria, J.; Armentano, D.; Pardo, E. Metal-organic framework technologies for water remediation: Towards a sustainable ecosystem. *J. Mater. Chem. A* **2018**, *6*, 4912–4947. [[CrossRef](#)]
55. Embaby, M.S.; Elwany, S.D.; Setyaningsih, W.; Saber, M.R. The adsorptive properties of UiO-66 towards organic dyes: A record adsorption capacity for the anionic dye Alizarin Red S. *Chin. J. Chem. Eng.* **2018**, *26*, 731–739. [[CrossRef](#)]
56. Hasan, Z.; Choi, E.J.; Jhung, S.H. Adsorption of naproxen and clofibric acid over a metal-organic framework MIL-101 functionalized with acidic and basic groups. *Chem. Eng. J.* **2013**, *219*, 537–544. [[CrossRef](#)]
57. Lin, S.; Song, Z.; Che, G.; Ren, A.; Li, P.; Liu, C.; Zhang, J. Adsorption behavior of metal-organic frameworks for methylene blue from aqueous solution. *Microporous Mesoporous Mater.* **2014**, *193*, 27–34. [[CrossRef](#)]
58. Lima, E.C.; Hosseini-Bandegharai, A.; Moreno-Piraján, J.C.; Anastopoulos, I. A critical review of the estimation of the thermodynamic parameters on adsorption equilibria. Wrong use of equilibrium constant in the Van't Hoof equation for calculation of thermodynamic parameters of adsorption. *J. Mol. Liq.* **2019**, *273*, 425–434. [[CrossRef](#)]
59. Li, C.; Xiong, Z.; Zhang, J.; Wu, C. The Strengthening Role of the Amino Group in Metal-Organic Framework MIL-53 (Al) for Methylene Blue and Malachite Green Dye Adsorption. *J. Chem. Eng. Data* **2015**, *60*, 3414–3422. [[CrossRef](#)]
60. Shi, Z.; Li, L.; Xiao, Y.; Wang, Y.; Sun, K.; Wang, H.; Liu, L. Synthesis of mixed-ligand Cu-MOFs and their adsorption of malachite green. *RSC Adv.* **2017**, *7*, 30904–30910. [[CrossRef](#)]
61. Jin, L.; Ye, J.; Wang, Y.; Qian, X.; Dong, M. Electrospinning Synthesis of ZIF-67/PAN Fibrous Membrane with High-capacity Adsorption for Malachite Green. *Fibers Polym.* **2019**, *20*, 2070–2077. [[CrossRef](#)]
62. Li, F.; Zheng, K.; Zhang, H.; Duan, C.; Xi, H. Nanoscale Hierarchically Porous Metal-Organic Frameworks: Facile Synthesis, Mechanism Research, and Application. *ACS Sustain. Chem. Eng.* **2019**, *7*, 11080–11087. [[CrossRef](#)]
63. Wu, X.; Huang, M.; Kong, F.; Yu, S. Short communication: Study on the formation of 2-methylimidazole and 4-methylimidazole in the Maillard reaction. *J. Dairy Sci.* **2015**, *98*, 8565–8571. [[CrossRef](#)] [[PubMed](#)]
64. Schlee, C.; Markova, M.; Schrank, J.; Laplagne, F.; Schneider, R.; Lachenmeier, D.W. Determination of 2-methylimidazole, 4-methylimidazole and 2-acetyl-4-(1,2,3,4-tetrahydroxybutyl)imidazole in caramel colours and cola using LC/MS/MS. *J. Chromatogr. B Anal. Technol. Biomed. Life Sci.* **2013**, *927*, 223–226. [[CrossRef](#)] [[PubMed](#)]
65. Gascón, V.; Jiménez, M.B.; Blanco, R.M.; Sanchez-Sanchez, M. Semi-crystalline Fe-BTC MOF material as an efficient support for enzyme immobilization. *Catal. Today* **2018**, *304*, 119–126. [[CrossRef](#)]
66. Brunauer, S.; Emmett, P.H.; Teller, E. Adsorption of Gases in Multimolecular Layers. *J. Am. Chem. Soc.* **1938**, *60*, 309–319. [[CrossRef](#)]
67. Barrett, E.P.; Joyner, L.G.; Halenda, P.P. The determination of pore volume and area distributions in porous substances. Computations from nitrogen isotherm. *J. Am. Chem. Soc.* **1951**, *73*, 373–380. [[CrossRef](#)]
68. Jamal, M.M.E.; Mousaoui, A.M.; Naoufal, D.M. Effect of Operating Parameters on Electrochemical Degradation of Alizarin Red S on Pt and BDD Electrodes. *Port. Electrochim. Acta* **2014**, *32*, 233–242. [[CrossRef](#)]
69. Yu, S.; Yuan, X.; Yang, J.; Yuan, J.; Shi, J.; Wang, Y.; Chen, Y. Spectrochimica Acta Part A: Molecular and Biomolecular Spectroscopy A chemometric-assisted method for the simultaneous determination of malachite green and crystal violet in water based on absorbance–pH data generated by a homemade pH gradient apparatus. *Spectrochim. Acta Part A Mol. Biomol. Spectrosc.* **2015**, *150*, 403–408. [[CrossRef](#)]
70. Ho, Y.S.; Mckay, G. Pseudo-second order model for sorption processes. *Process Biochem.* **1999**, *34*, 451–465. [[CrossRef](#)]
71. Azizian, S. Kinetic models of sorption: A theoretical analysis. *J. Colloid Interface Sci.* **2004**, *276*, 47–52. [[CrossRef](#)] [[PubMed](#)]
72. Qiu, H.; Lv, L.; Pan, B.C.; Zhang, Q.J.; Zhang, W.M.; Zhang, Q.X. Critical review in adsorption kinetic models. *J. Zhejiang Univ. Sci. A* **2009**, *10*, 716–724. [[CrossRef](#)]
73. Lachowicz, J.I.; Delpiano, G.R.; Zanda, D.; Piludu, M.; Sanjust, E.; Monduzzi, M.; Salis, A. Adsorption of Cu²⁺ and Zn²⁺ on SBA-15 mesoporous silica functionalized with triethylenetetramine chelating agent. *J. Environ. Chem. Eng.* **2019**, *7*. [[CrossRef](#)]
74. Mall, I.D.; Srivastava, V.C.; Agarwal, N.K.; Mishra, I.M. Removal of congo red from aqueous solution by bagasse fly ash and activated carbon: Kinetic study and equilibrium isotherm analyses. *Chemosphere* **2005**, *61*, 492–501. [[CrossRef](#)]

Supporting information

Adsorption of Malachite Green and Alizarin Red S dyes using Fe-BTC metal organic framework as adsorbent

Giulia Rossella Delpiano¹, Davide Tocco¹, Luca Medda², Edmond Magner^{3*}, Andrea Salis^{1,4*}

¹ Dipartimento di Scienze Chimiche e Geologiche, Università di Cagliari, Cittadella Universitaria, S.S. 554 bivio Sestu, 09042 Monserrato (CA), Italy; delpiano@unica.it (G.R.D.); davide.tocco@unica.it (D.T.)

² Laboratorio NEST Scuola Normale Superiore di Pisa, 56127 Pisa, Italy; medda.luc@gmail.com

³ Department of Chemical Sciences, Bernal Institute, University of Limerick, Limerick V94 T9PX, Ireland

⁴ Consorzio Interuniversitario per lo Sviluppo dei Sistemi a Grande Interfase (CSGI), Unità Operativa University of Cagliari, Monserrato (CA) 09042, Italy

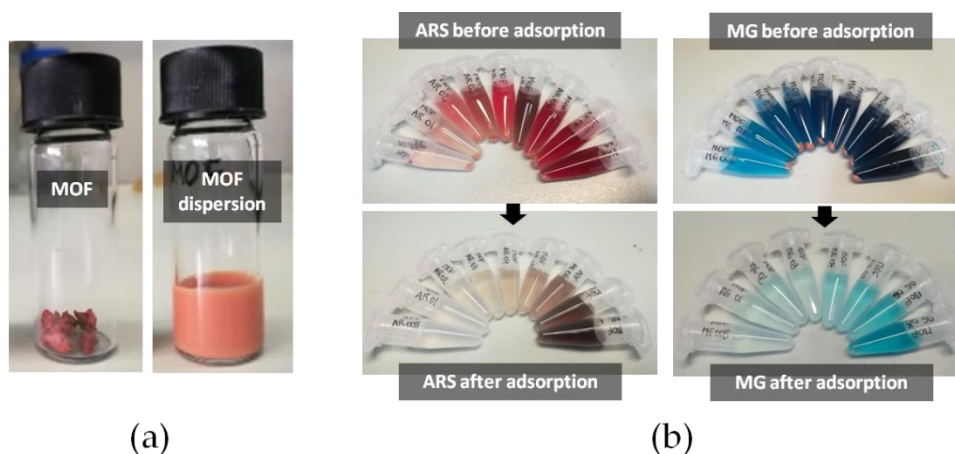


Figure S1 - Images of a) the synthesized MOF before and after dispersion in distilled water; b) Solutions of ARS and MG prior to and after (20 h) adsorption .

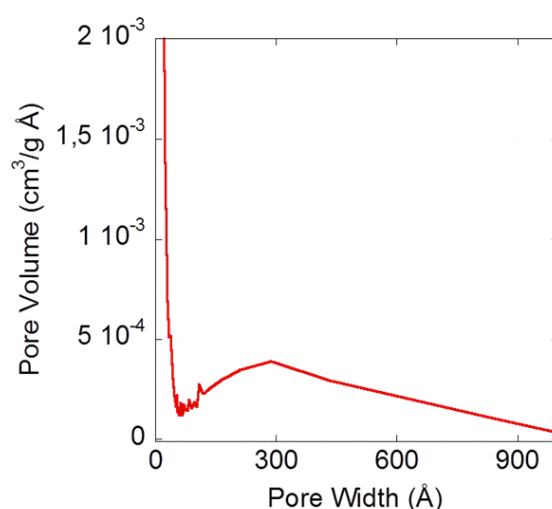


Figure S2 – Pore size distribution (BJH method).

Table S1. Zeta potential of Fe-BTC dispersed in H₂O and the percentage of dyes adsorbed at different pH values (initial concentration of dyes of 1.5 mM).

pH	Fe-BTC Zeta potential (mV)	ARS adsorption%	MG adsorption%
3	+ 6	59.1	89.3
4	- 7	49.2	98.5
5	- 20	31.3	94.7
6	- 28	34.1	93.1
7	-16	23.3	82.9

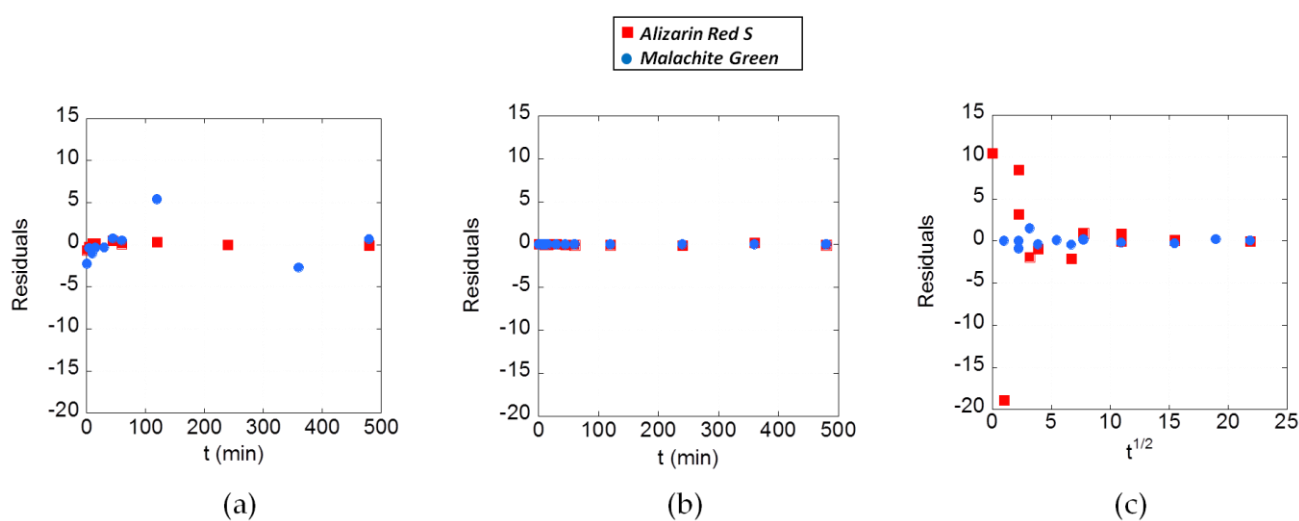


Figure S3 – Residuals graph relative to a) Pseudo-First order, b) Pseudo-Second order and c) Intraparticle diffusion kinetic models.

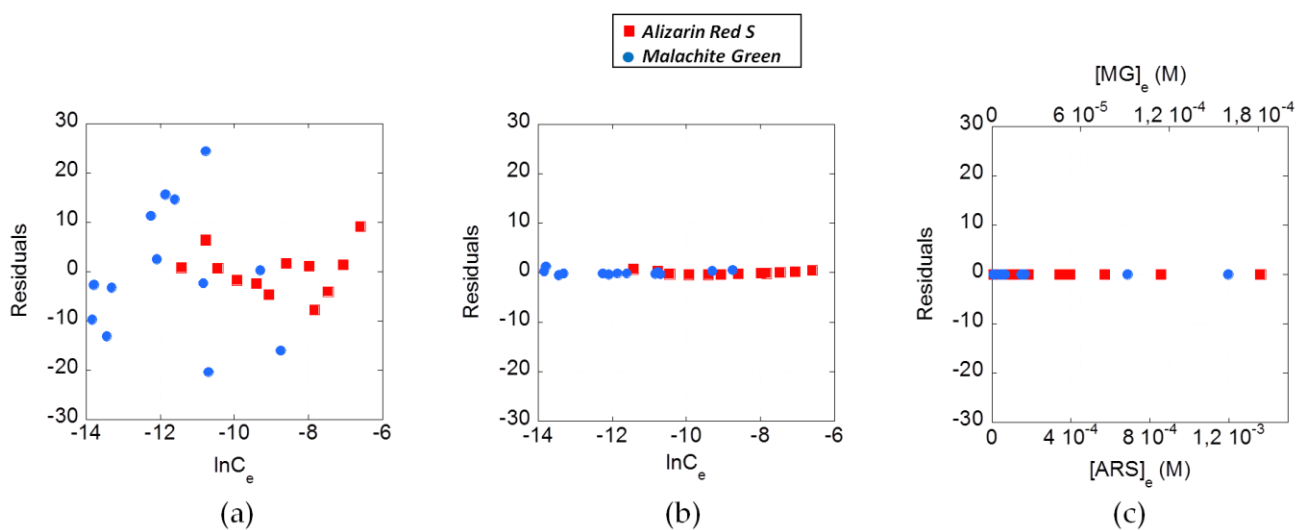


Figure S4 – Residuals graph relative to a) Temkin, b) Freundlich and c) Langmuir isotherms models.

PAPER III



Protocols

Enzyme immobilization on metal organic frameworks: Laccase from *Aspergillus* sp. is better adapted to ZIF-zni rather than Fe-BTC

Davide Tocco^{a,d,e,f}, Cristina Carucci^{a,d,e,f,*}, Debora Todde^a, Kim Shortall^b, Fernando Otero^b, Enrico Sanjust^{c,d,e,f}, Edmond Magner^{b,**}, Andrea Salis^{a,d,e,f,*}

^a Department of Chemical and Geological Sciences, University of Cagliari, and Centro NanoBiotecnologie Sardegna (CNBS), Cittadella Universitaria, SS 554 bivio Sestu, 09042, Monserrato (CA), Italy

^b Department of Chemical Sciences and Bernal Institute, University of Limerick, Limerick V94 T9PX, Ireland

^c Department of Biomedical Sciences, University of Cagliari, Cittadella Universitaria, SS 554 bivio Sestu, 09042 Monserrato (CA), Italy

^d Consorzio Interuniversitario per lo Sviluppo dei Sistemi a Grande Interfase (CSGI), via della Lastruccia 3, 50019, Sesto Fiorentino (FI), Italy

^e Unità Operativa University of Cagliari, Italy

^f Cittadella Universitaria, SS 554 bivio Sestu, 09042 Monserrato (CA), Italy

ARTICLE INFO

Keywords:

Laccase
Enzyme
Metal organic frameworks
Biocatalysis: Enzyme Immobilization

ABSTRACT

Laccase from *Aspergillus* sp. (LC) was immobilized within Fe-BTC and ZIF-zni metal organic frameworks through a one-pot synthesis carried out under mild conditions (room temperature and aqueous solution). The Fe-BTC, ZIF-zni MOFs, and the LC@Fe-BTC, LC@ZIF-zni immobilized LC samples were characterized by X-ray diffraction, scanning electron microscopy, Fourier transform infrared spectroscopy, and thermogravimetric analysis. The kinetic parameters (K_M and V_{max}) and the specific activity of the free and immobilized laccase were determined. Immobilized LCs resulted in a lower specific activity compared with that of the free LC ($7.7 \mu\text{mol min}^{-1} \text{mg}^{-1}$). However, LC@ZIF-zni was almost 10 times more active than LC@Fe-BTC ($1.32 \mu\text{mol min}^{-1} \text{mg}^{-1}$ vs $0.17 \mu\text{mol min}^{-1} \text{mg}^{-1}$) and only 5.8 times less active than free LC. The effect of enzyme loading showed that LC@Fe-BTC had an optimal loading of 45.2 mg g^{-1} , at higher enzyme loadings the specific activity decreased. In contrast, the specific activity of LC@ZIF-zni increased linearly over the loading range investigated. The storage stability of LC@Fe-BTC was low with a significant decrease in activity after 5 days, while LC@ZIF retained up to 50% of its original activity after 30 days storage. The difference in activity and stability between LC@Fe-BTC and LC@ZIF-zni is likely due to release of Fe^{3+} and the low stability of Fe-BTC MOF. Together, these results indicate that ZIF-zni is a superior support for the immobilization of laccase.

1. Introduction

Enzyme immobilization on solid supports has been widely explored [1–3]. Immobilized enzymes usually display high resistance to harsh environmental conditions and may exhibit improved thermal stability when compared to free enzymes. The enzymatic activity and stability depend on the choice of the support as well as on the method of immobilization [1,4,5]. A wide range of materials, e.g. mesoporous silica [6–8], xerogels [9], magnetic nanomaterials [10], agarose [11], liquid crystals [12], nanofibrous polymers [13] and metal organic frameworks (MOFs) have been utilized for the immobilization of

enzymes [14–17]. MOFs are composed of metal ions and organic linkers connected through coordination bonds to form a three-dimensional network [18]. They have been used for a range of applications, including storage of gases [19], catalysis [20], removal of pollutants [21], biomedicine and sensing applications [22,23], and, more recently, as enzyme supports [24–26]. In comparison with other supports, enzymes immobilized on MOFs can exhibit high catalytic activities, improved stability, and reusability [27–29]. Enzymes can be readily immobilized in situ in MOFs. Such in situ immobilization is facile, rapid and results in high enzyme loadings [30]. In this approach, enzyme molecules are entrapped in the three-dimensional network formed by

* Corresponding authors at: Department of Chemical and Geological Sciences, University of Cagliari, and Centro NanoBiotecnologie Sardegna (CNBS), Cittadella Universitaria, SS 554 bivio Sestu, 09042, Monserrato (CA), Italy.

** Corresponding author.

E-mail addresses: cristina.carucci@unica.it (C. Carucci), Edmond.Magner@ul.ie (E. Magner), asalis@unica.it (A. Salis).

<https://doi.org/10.1016/j.colsurfb.2021.112147>

Received 21 May 2021; Received in revised form 24 September 2021; Accepted 28 September 2021

Available online 1 October 2021

0927-7765/© 2021 Elsevier B.V. All rights reserved.

the metal ions and the organic linkers. While a number of reports have focused on the catalytic activity of the immobilized enzymes, the spatial distribution has not been described in detail [31,32]. For example Liang et al [33], tagged catalase (CAT) with fluorescein isothiocyanate (FITC) and used confocal laser scanning microscopy to show that the distribution and localization of the enzyme depended on the type of MOF used. A more homogeneous distribution was observed on MAF-7 and ZIF-90 in comparison to ZIF-8. Li et al [34], immobilized cytochrome c and demonstrated that the protein was embedded in the Cu-BTC framework rather than within the pores. Finally, a number of enzymes can be co-immobilized within the same support [35]. However, the synthesis of MOF usually requires long reaction times (several days for solvothermal and hydrothermal techniques and weeks for diffusion methods) and are often carried out under harsh conditions (high temperatures, use of organic solvents) [36]. Such conditions are generally not appropriate for enzymes and result in denaturation and loss of catalytic activity. Recently, Gascón et al. immobilized different enzymes, e.g. alcohol dehydrogenase (ADH), glucose oxidase (GOx), and lipase in a basolite F300-like MOF using an in situ mild synthetic method [37,38]. This method involves entrapment of the enzyme within a MOF based on Fe^{3+} and the tridentate linker trimesic acid, in a process that is rapid and facile (room temperature and close to neutral pH). The synthesis occurs under mild conditions with the material displaying micro and meso-porous structure [37]. Similarly, Kida et al. developed a method to synthesize zeolite imidazole frameworks (ZIF-8) in aqueous solution [39] while Falcaro and co-workers immobilized several enzymes within a ZIF-8 material [17]. ZIF-zni is a robust, dense, non-porous material [40,41]. ZIF-zni, one of the most stable MOF materials, is usually synthesized at very high temperatures and in organic solvents [40]. Nevertheless, it can be also prepared at room temperature, using water as the solvent [42].

Laccases (LCs, E.C. 1.10.3.2, p-diphenol: dioxygen oxidoreductase), are multicopper oxidases that catalyze the oxidation of various phenolic and non-phenolic compounds [43] via reduction of molecular oxygen to water [44]. In addition to p-diphenols (quinols), o-diphenols (catechols), alkoxyphenols and their derivatives, aromatic amines and aminophenols can also act as substrates for laccase. Due to their strong electron-rich character, nonphenolic substrates such as polymethoxybenzenes [45] can act as substrates for laccases. The radical products produced in the catalytic reaction are particularly favored when the lone electron can be efficiently delocalized in the aromatic systems, forming semiquinones, with further reaction depending on the properties of the products, pH and the concentration of oxygen. In nature, laccases (LCs) are present in plants, bacteria, insects and white rot fungi [46,47]. Due to their low substrate specificity, LCs are used for a wide range of applications, such as bleaching of denim and paper [48], removal of toxicants released during combustion processes [49], decolorisation [50], elimination of phenolics [6], and biomass delignification [51–53]. Recently Naseri et al. immobilized laccase from *Trametes versicolor* on ZIF-zni and ZIF-8, two different zeolite imidazolate frameworks, to study enzymatic activity and stability to storage and recycling [54]. Li et al. encapsulated laccase (*Ganoderma lucidum*) in ZIF-8 to form an enzymatic biofuel cell based self-powered biosensor [22]. Gascon et al. compared the immobilization of laccase (*Aspergillus oryzae*) on Fe-BTC MOF obtained through a one-pot and a post-synthesis method, and also investigated the catalytic activity and enzyme leaching [55]. Although laccases are very useful enzymes for a wide range of applications [44,56], they possess low stability in their soluble form, being easily perishable at neutral and basic pH [57]. Moreover, when immobilized on solid supports, the catalytic activity and stability of laccases is strongly affected by the amount of water present in the preparation, indeed the activity and stability rapidly decrease upon drying [58].

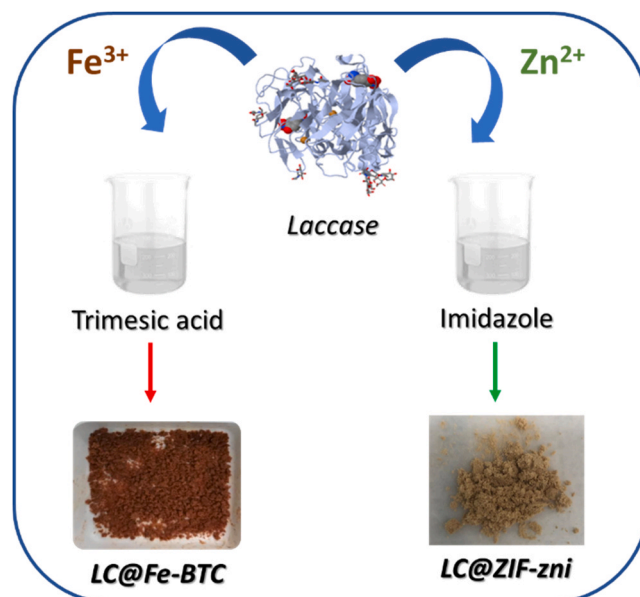
The majority of reports on the immobilization of enzymes on MOFs focus on single MOF materials, describing the immobilization of different enzymes in the MOF [38,59,60] to demonstrate the potential

use of a specific MOF support. This study compares two different MOF materials as supports for the in situ immobilization of *Aspergillus* sp. laccase. More specifically, laccase (LC) was entrapped within Fe-BTC MOF and ZIF-zni, to obtain LC@Fe-BTC and LC@ZIF-zni biocatalysts [38,54] (Scheme 1). The properties of the immobilized biocatalysts were extensively characterized, and the kinetic parameters, K_M and V_{max} compared with those of the free laccase. Specific activities for different laccase loadings were measured, together with the storage stability. This study enabled a detailed comparison of in situ enzyme immobilization on the two MOF supports, Fe-BTC and ZIF-zni.

2. Results and discussion

2.1. Characterisation of Fe-BTC, LC@Fe-BTC, ZIF-zni and LC@ZIF-zni samples

Fe-BTC and ZIF-zni and laccase modified MOFs (LC@Fe-BTC and LC@ZIF-zni) were characterised using X-ray diffraction. The XRD patterns (Fig. 1A) show sharp peaks at 11° , 19° , 24° , 28° , and 34° confirming the formation of the Fe-BTC structure [37,61,62]. Fig. 1B confirms the formation of the ZIF-zni materials, with characteristic peaks at 15° , 17° , 18° , 21° in agreement with previous literature reports [14,63]. The XRD patterns obtained for both LC@Fe-BTC and LC@ZIF-zni samples do not differ significantly from those of Fe-BTC and ZIF-zni demonstrating that laccase does not significantly alter the structure of the MOFs. Thermogravimetric analysis (TGA) demonstrated that Fe-BTC MOF had a loss of mass of 12% over the range 0–115 °C, while LC@Fe-BTC showed a much higher loss of up to 35% over the same temperature range. These losses can be attributed to different amounts of adsorbed water in the samples [55]. Fe-BTC MOF showed a loss of 14.5% over the range 115–330 °C and of 43% over the range 330–500 °C, with the latter likely due to the decomposition of the Fe-BTC structure. In contrast to Fe-BTC, the LC@Fe-BTC sample did not show a clear loss in mass at 330 °C, as confirmed by the derivative plot (dm/dT vs T , Fig. S1). Enzyme immobilization thus shifted the thermal decomposition of the MOF to higher temperatures. For LC@Fe-BTC samples, the mass loss over the temperature range 115–430 °C is likely due to the decomposition of BTC and of LC encapsulated in the support. However, the exact mass loss due to the enzyme decomposition cannot be quantified as it overlaps that of trimesic acid (Fig. 1C) [64]. Finally, the mass loss measured above 430 °C for LC@Fe-BTC is assigned



Scheme 1. Synthesis and immobilization of LC in ZIF-zni and Fe-BTC supports.

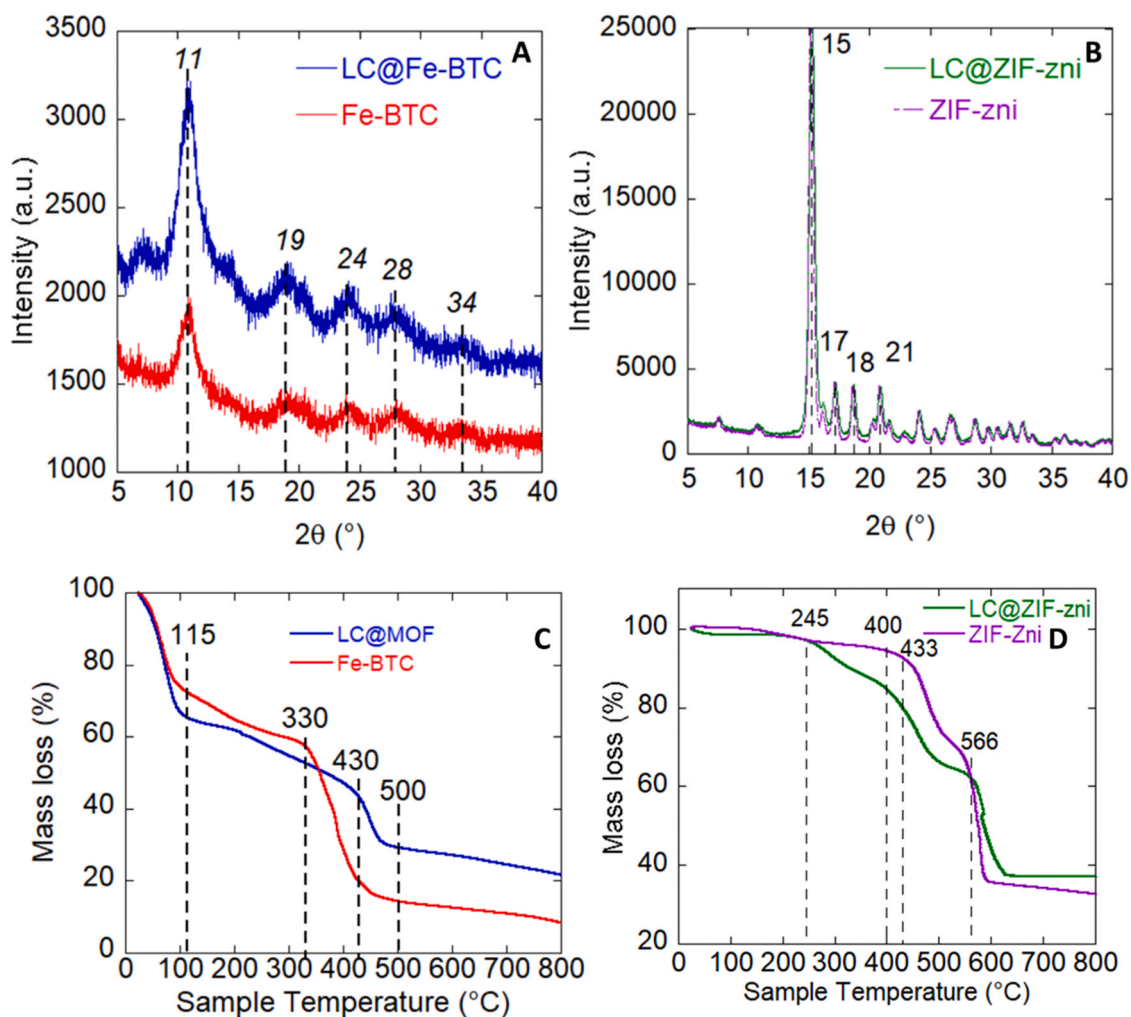


Fig. 1. XRD patterns of a) Fe-BTC and LC@Fe-BTC and b) ZIF-zni and LC@ZIF-zni. Thermogravimetric analysis (TGA) curve from 25 °C to 800 °C of c) Fe-BTC MOF and LC@Fe-BTC 45.2 mg g⁻¹ and d) ZIF-zni and LC@ZIF-zni 84 mg g⁻¹.

to the decomposition of the MOF structure [65]. Thermogravimetric analysis of ZIF-zni and LC@ZIF-zni (Fig. 1D) shows that the materials exhibited good thermal stability in air, up to 433 °C, in agreement with literature reports [66]. ZIF-zni had mass losses of 10% and 25% over the ranges, 433–566 °C and 566–700 °C. The first mass loss can be attributed to the partial loss of ZIF crystallinity which is favoured in oxidizing environments [67] while the latter can be ascribed to the complete decomposition and collapse of the ZIF-zni structure [68]. Thermogravimetric analysis of LC@ZIF-zni was comparable with ZIF-zni except for the mass loss of 13% over the temperature range, 245–400 °C. ZIF-zni displayed a loss in mass of 2.8% over this range, indicating that loss in mass of LC@ZIF-zni could be ascribed to the thermal decomposition of immobilized laccase (Table S1).

Scanning electron microscopy (SEM) images (Fig. 2 A-B) of Fe-BTC show agglomerates of irregular particles and are similar to literature reports [69]. SEM images (Fig. 2 C-D) of ZIF-zni show a more regular crystalline morphology. LC@Fe-BTC samples have a more irregular particle shape, likely due to enzyme immobilization (Fig. 2 B). Similar to immobilization in ZIFs, encapsulation of laccase in Fe-BTC led to changes in particle morphology, in which the particles lose their regular shape in favor of more disordered agglomerates, in agreement with other reports on the immobilization of enzymes such as lipase, glucose oxidase and alcohol dehydrogenase [30,38].

The FTIR spectrum of Fe-BTC (Fig. 3A) showed a band above 3300 cm⁻¹ assigned to OH stretching, indicative of the presence of

adsorbed water. The peak at 1625 cm⁻¹ can be attributed to the C=O stretching of carboxylate groups [65]. The peaks, arising from the carboxylate groups of trimesic acid, likely mask the NH-C=O amide bands of the protein. The bands at 1447 cm⁻¹ and 1375 cm⁻¹ are due to asymmetric and symmetric stretching of the O-C-O group, respectively [70]. The other two sharp peaks at 750 and 703 cm⁻¹ correspond to the bending of aromatic C-H bonds [61,71]. FTIR spectra of ZIF-zni and LC@ZIF-zni samples are shown in Figs. 3C and 3D. The bands in the range of 600–1500 cm⁻¹ are ascribed to the stretching and bending modes of the imidazole ring [72]. The presence of imidazole bands obscures the amide band expected for the enzyme.

In particular, the sharp peaks in the range 1100–1400 cm⁻¹ region are attributed to the C=N stretching [73]. The peak at 668 cm⁻¹ is due to the stretching of the Zn-N coordination bond between Zn and the imidazole ring [74]. The presence of laccase was confirmed by EDX measurements with 0.14% and 0.20% (m/m) of copper for LC@Fe-BTC and LC@ZIF-zni (Fig. S8), respectively, in agreement with the ratio of laccase loadings for both materials.

A wide range of studies have been described on the use of iron based MOFs [75], but their long term stability, especially of Fe-BTC, has not been studied in detail. Oveisi et al. reported leaching of 0.3 ppm of Fe²⁺ (0.01% of the initial amount) in the synthesis of Fe-BTC MOF [76]. Sanchez et al. reported similar negligible amounts of iron leaching (0.3 ppm) [37]. Aguilar et al. studied the hydroxylation of phenol using Fe-BTC. Fe leaching was absent or negligible at room temperature but

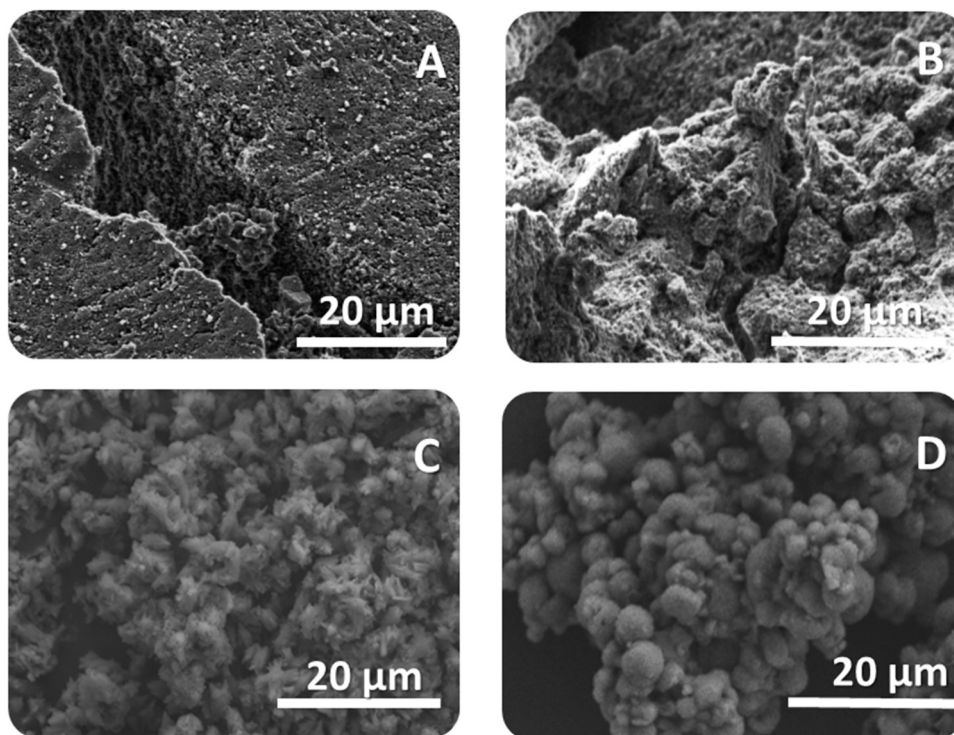


Fig. 2. SEM images of A-B) Fe-BTC and LC@Fe-BTC C-D) ZIF-zni and LC@ZIF-zni samples.

increased with temperature up to 26 ppm at 50 °C [77]. A study demonstrated how nanoparticles of MIL-100 progressively lose their crystallinity when incubated in PBS (phosphate buffer saline) solution from 6 h to 3 days due to the interaction between phosphate and iron ions [78]. Similarly to MIL-100, Fe-BTC is unstable in aqueous buffer solutions. Determination of iron release from Fe-BTC was analyzed following a SCN^- based colorimetric assay (Fig. S6). Iron release was assayed by suspending Fe-BTC in citrate, phosphate and Tris-HCl buffers (10 and 100 mM) at pH 5, 7 and 9, respectively under static and shaking conditions for 24 and 48 h (Fig. S7). Samples suspended in 10 mM buffer in shaking conditions demonstrated a higher concentration of iron release (up to 35 μM at pH 5 and 9 after 48 h) than samples stored in static conditions (up to 25 μM at pH 5 after 24 and 48 h). In 100 mM buffer solutions, samples at pH 5 showed comparable leaching levels of iron (25 μM) with no significant differences between static and shaking conditions and between 24 and 48 h of storage. Samples stored at pH 7 and 9 demonstrated an increase in iron release up to 40 μM after 48 h. The increased amounts of iron released in 100 mM buffer indicates that the buffer concentration is a factor in the stability of the material. Overall, the data demonstrate that Fe-BTC is unstable upon exposure to aqueous buffer, limiting its use as a support for enzymes. A comparable systematic study of ZIF-8 stability in PBS demonstrated that ZIF-8 is unstable and releases metal ions in the presence of specific buffer solutions [79]. In that work Falcaro et al. demonstrated that ZIF-8 particles can rapidly lose crystallinity when incubated in PBS for 1 to 24 h, leading to the formation of zinc phosphate particles with the rate of degradation depending on the size of the ZIF-8 particles. In another work, Gassensmith et al. demonstrated that ZIF-8 is more stable in some buffers and cell media [80]. The stability of ZIF-8 stability is dependent on the stability of the bond between Zn^{2+} and 2-methylimidazole linker. Both phosphate and bicarbonate can bind to Zn^{2+} competing with the linker and reducing the stability of the material. The stability of ZIF-8 was assessed by examining the surface morphology, degree of crystallinity of the material and leaching of the protein. No significant leaching of protein or changes in crystallinity were observed indicating that ZIF-8 is stable in the buffers used.

SEM and XRD were used to evaluate the structural stability of LC@Fe-BTC and LC@ZIF-zni after use (Fig. S10-S11). While the XRD pattern of LC@ZIF-zni displayed more noise and was more irregular, the main peaks (2 θ peak position: 10, 15, 18, 20) were retained indicative of a partial loss of the MOF structure. SEM images confirmed that the surface morphology was not significantly changed (Fig. S11). The XRD pattern of Fe-BTC is not well defined due to the semi-amorphous nature of the material. The XRD patterns before and after use were similar (Fig. S10) As with LC@ZIF-zni, SEM images confirmed that there were no substantial changes in the morphology of LC@Fe-BTC after use (Fig. S11).

2.2. The effect of immobilization on kinetic properties

Fig. 4 shows the kinetic data obtained for the free and immobilized laccases, while the associated kinetic parameters are listed in Table 1. The laccase from *Aspergillus sp.* used in this work showed a 45-fold loss in specific activity once immobilized within Fe-BTC (from 7.7 to 0.17 $\mu\text{mol min}^{-1} \text{mg}^{-1}$). Gascón et al [55]. reported the immobilization of a laccase from *Aspergillus oryzae* within Fe-BTC. Their results showed a 95-fold decrease in catalytic activity (from 378 to 4 $\mu\text{mol min}^{-1} \text{mg}^{-1}$) when the laccase was entrapped in Fe-BTC. With LC@ZIF-zni, a much lower decrease in activity, by a factor of 5.8, was observed (V_{max} decreased from 7.7 to 1.32 $\mu\text{mol min}^{-1} \text{mg}^{-1}$).

The decrease in V_{max} observed with both supports may be due to diffusional limitations or, alternatively to enzyme inactivation. LC@Fe-BTC showed an increase in K_M (2.7 times higher than free laccase) suggesting that the substrate had a lower affinity for the enzyme when immobilized on Fe-BTC. LC@ZIF-zni sample showed an increase in K_M (x 1.6) compared with the free enzyme. Differences in the kinetic parameters frequently arise upon immobilization of an enzyme [81]. Differences in kinetic parameters between free and immobilized enzymes can arise from a range of factors that include changes in conformation, in the structure or degree of accessibility of the enzyme's active site, in the rate of diffusion and/or in partitioning of the substrate to the active site [82]. Similar to the results described here, Patil et al., immobilized laccase

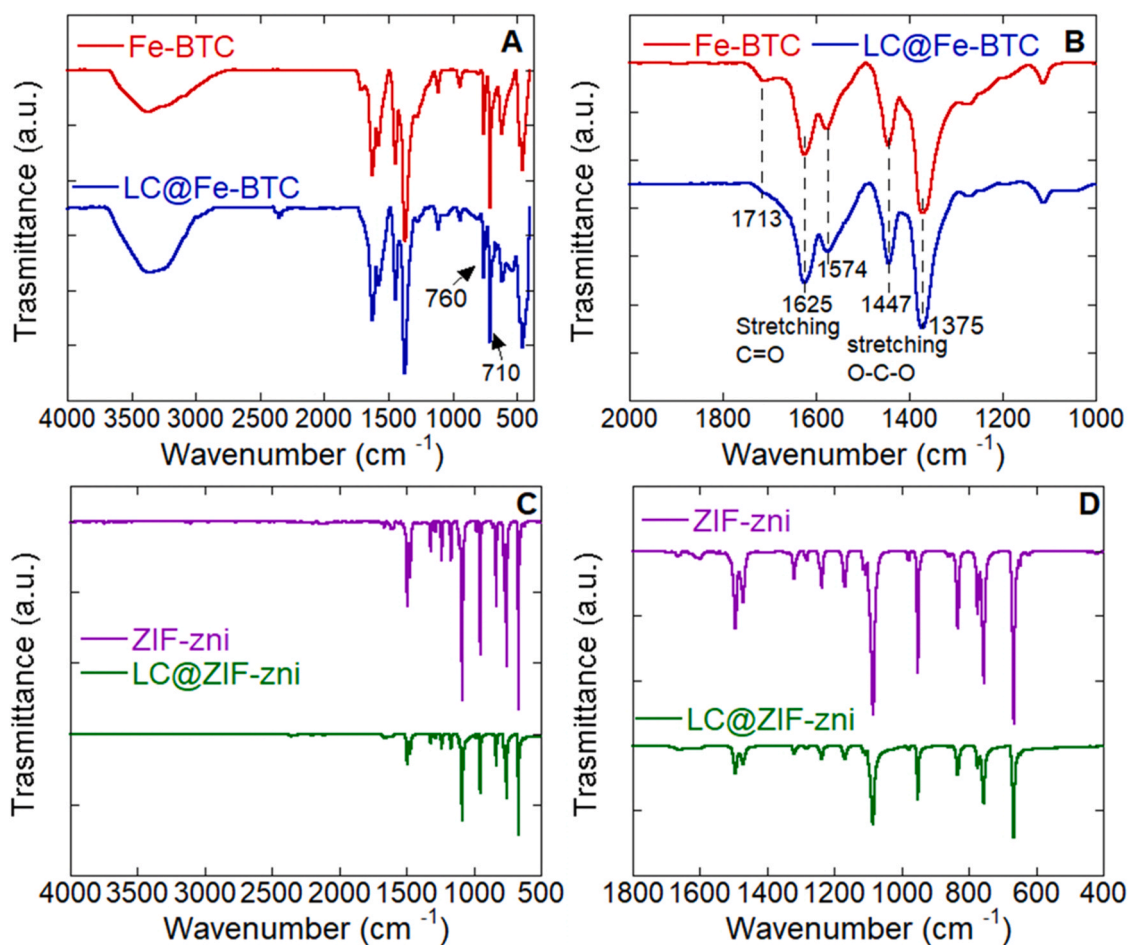


Fig. 3. FT-IR spectrum of a) Fe-BTC wavenumber range from 450 to 4000 cm^{-1} b) LC@Fe-BTC wavenumber range from 1000 to 1800 cm^{-1} and c) ZIF-zni wavenumber range from 500 to 4000 cm^{-1} d) LC@ZIF-zni wavenumber range from 400 to 1800 cm^{-1} .

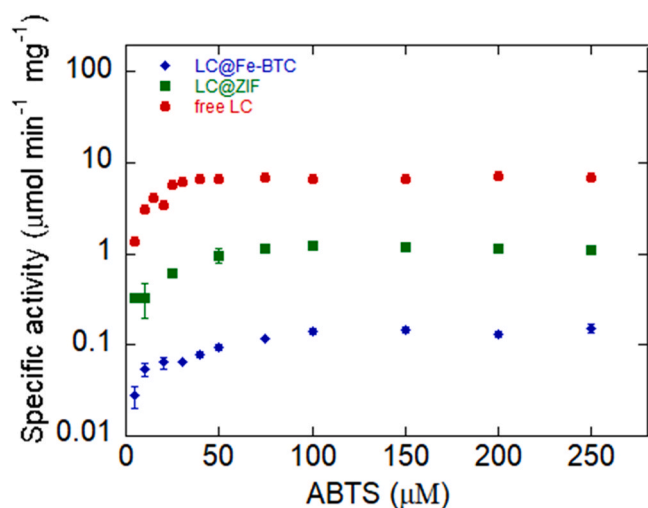


Fig. 4. Michaelis-Menten plots of the activity of free laccase, LC@Fe-BTC (9 mg mL^{-1}) and LC@ZIF-zni (9 mg mL^{-1}).

from *Trametes hirsuta* in ZIF-8 and reported a 1.5 fold increase in K_M , and a 1.2 fold decrease in V_{\max} suggesting that the ZIF materials may be suitable supports for the immobilization of laccase [83]. Some enzymes such as catalase showed a decrease in catalytic activity upon immobilization on ZIF-8 [33]. This was ascribed to the hydrophobic nature of

Table 1

Kinetic parameters obtained with free laccase, LC@MOF and LC@ZIF-zni samples.

Samples	K_M (μM)	V_{\max} ($\mu\text{mol min}^{-1} \text{mg}^{-1}$)
Free laccase	13 ± 3	7.7 ± 0.4
LC@Fe-BTC	35 ± 7	0.17 ± 0.01
LC@ZIF-zni	22 ± 6	1.32 ± 0.08

ZIF-8 that may interact with hydrophobic residues of the enzyme. In another work, lipase (*Candida antarctica B*) was immobilized on Fe-BTC with no significant loss of enzymatic activity [55]. On the other hand, when laccase (*Aspergillus oryzae*) was immobilized on the same material, the activity decreased (up to $0.2 \mu\text{mol min}^{-1} \text{mg}^{-1}$), thus suggesting that Fe-BTC was not a good host for the enzyme [55].

2.3. Effect of enzyme loading on specific activity

Different LC@Fe-BTC and LC@ZIF-zni samples with increasing protein loading were prepared using enzyme concentrations in the range $6\text{--}10 \text{ mg mL}^{-1}$ (LC@Fe-BTC) and $5\text{--}12.5 \text{ mg mL}^{-1}$ (LC@ZIF-zni) during the in situ immobilization process. LC@Fe-BTC loadings, quantified by means of the Bradford assay, varied from 29.8 mg g^{-1} to 52.7 mg g^{-1} (Fig. 5A; Table S1) while LC@ZIF-zni loadings ranged from 17.8 mg g^{-1} to 59.5 mg g^{-1} (Fig. 5C; Table S2). The immobilization efficiency (IE%), defined as the ratio (%) between the amount of immobilized protein and the total protein in solution, was 100% for all LC@Fe-BTC samples, demonstrating that all of the laccase was immobilized within Fe-BTC

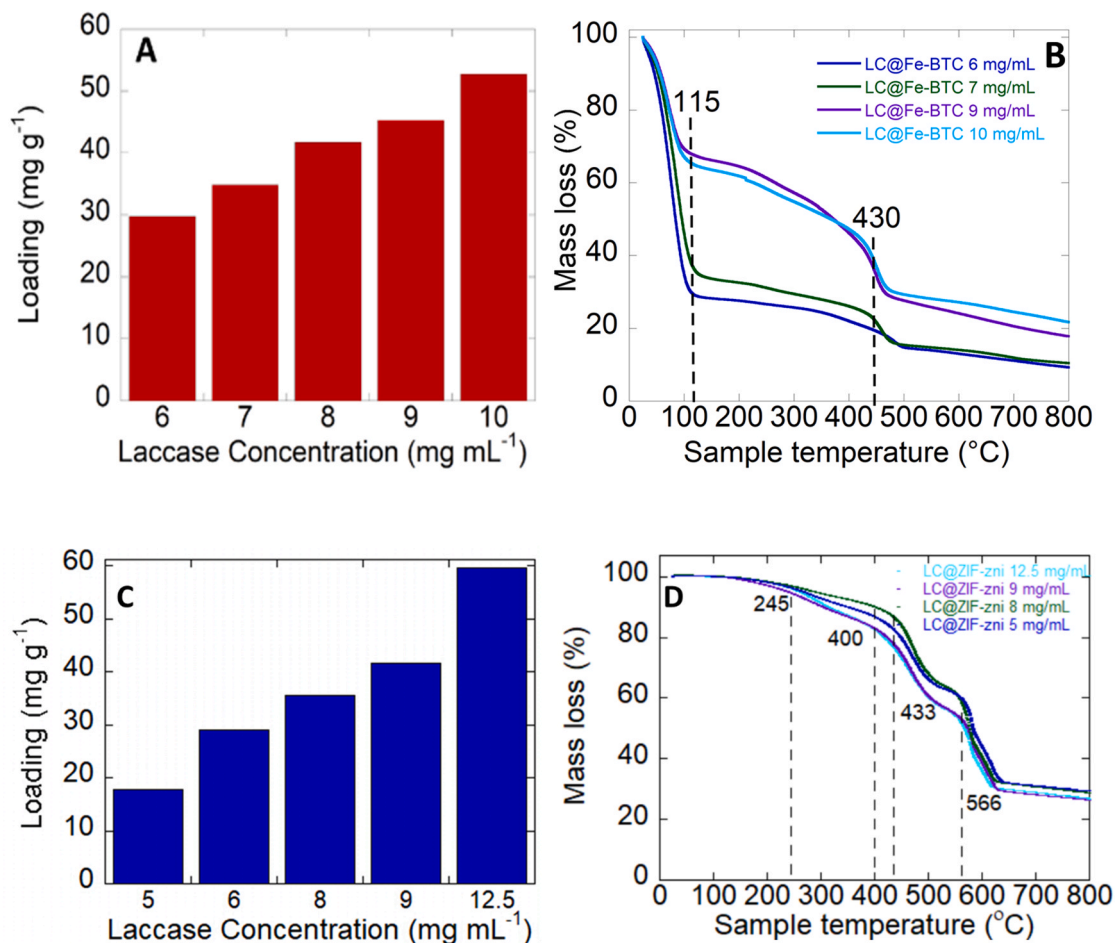


Fig. 5. a) Protein loading of Fe-BTC MOF, b) thermogravimetric analysis (TGA) of LC@Fe-BTC with different enzyme loadings c) Protein loading of ZIF-zni samples d) thermogravimetric analysis (TGA) of LC@ZIF-zni with different enzyme loadings.

material. When LC@ZIF-zni was analyzed, IE% varied between 97% and 99% for all samples showing, also in this case, a very high immobilization efficiency. For LC@Fe-BTC samples, the increase in enzyme loading shown in Fig. 5A is supported by TGA analysis (Fig. 5B). TGA analysis of LC@Fe-BTC samples (6 and 7 mg mL⁻¹) displayed a loss in mass of 70% over the range 0 and 115 °C due to the loss of water. At higher enzyme concentrations (9 and 10 mg mL⁻¹). LC@Fe-BTC samples had losses in mass of 25%, likely due to a lower water content. The % mass loss in the range 115–430 °C increased with increasing enzyme loading from 9.5% to 22%, with the exception of LC@Fe-BTC with a loading of 45.2 mg g⁻¹ that showed a mass loss of 27%. TGA curve for Fe-BTC did not show any mass losses in the range between 200 and 300 °C. On the other hand, in the same temperature range LC@Fe-BTC samples showed a low mass loss (more visible in the derivative curve, Fig. S1) that increased with increasing enzyme loading. Gascón et al. investigated the mass loss of enzymes immobilized within Fe-BTC MOF through thermogravimetric analysis coupled to mass spectrometry [55]. In that work, they attributed the mass loss over the temperature range 200–300 °C to water retained by the enzyme [55]. LC@ZIF-zni samples showed a linear increase in mass loss in the temperature range 245–400 °C except for the loading at 19.8 mg g⁻¹ that showed a mass loss of 9.5% (Table S2).

2.4. Specific activity of LC@Fe-BTC and LC@ZIF-zni

The specific activities of the samples at different enzyme loadings were examined. In the absence of diffusional limitations, the activity should increase as the loading is increased. Fig. 6 shows an initial linear

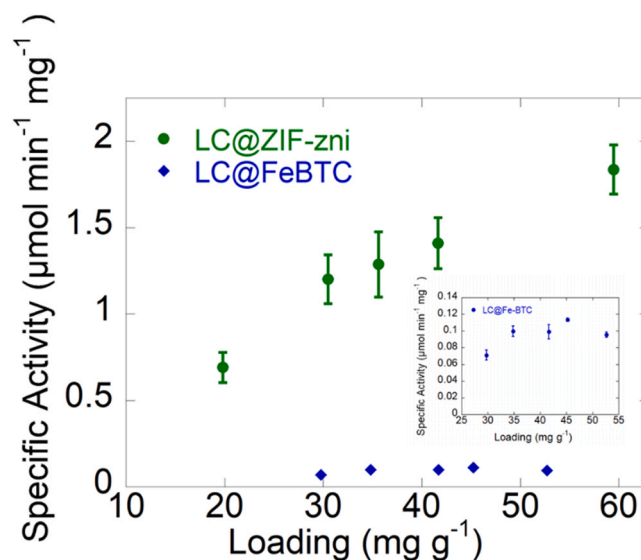


Fig. 6. Effect of loading on specific activity of LC@Fe-BTC and LC@ZIF-zni. Inset: enlargement of data for LC@Fe-BTC.

increase in activity with enzyme loading on LC@Fe-BTC up to an activity of 0.08 units to a loading of 45.2 mg g⁻¹. Above this loading the specific activity decreased, likely arising from limitations in substrate diffusion within the pores [6,84] For the loadings examined, the specific

activity is an order of magnitude higher for ZIF-zni samples than Fe-BTC biocatalysts. In contrast, with LC@ZIF-zni an increase in activity over the range investigated (Fig. 6), was observed, indicating diffusional limitations were not observed. Naseri et al [54]. obtained a high retention of activity of a laccase from *T. versicolor* in ZIF-zni demonstrating a very high adaptability of laccases for ZIF-zni support. The laccase from *Aspergillus sp.* is a glycoprotein containing about 10% sugar content [44,85]. The presence of asparagine-N-linked sugar residues on the enzyme confer polar, hydrophilic properties on the enzyme.

As studied recently by Liang et al., the enzyme polarity is likely related to high activity retention in ZIF materials [33]. Likely, ZIF-zni materials offer a more favorable environment for laccase activity in comparison with Fe-BTC supports. When Knedel et al [16]. immobilized laccase from *Corynebacterium glutamicum* in ZIF-8, no activity was observed when ABTS was used as the substrate. The lack of activity was explained on the basis that the small ZIF-8 pore windows (3.4 Å) which did not allow ABTS to enter the pores and reach the enzyme active site. Liang et al. demonstrated how, even in porous ZIFs, ca. 40% of the enzyme was on the surface rather than entrapped in the material [42].

Knedel et al. also reported how laccase immobilization in ZIF materials using 2,6-dimethoxyphenol and syringaldazine substrates enhanced stability in ethanol and N,N-dimethylformamide (DMF) [16] meaning that, upon immobilization in ZIF-8, laccase works also in the absence of water. When laccase is immobilized in chitosan the laccase water requirement decreased up to 7% in water content [86]. In our work, the relative amount of water present in the Fe-BTC and ZIF-zni samples can be seen by the differential scanning calorimetry (DSC) plot. A small endothermic (positive) peak between 100 and 200 °C can be attributed to water retained in ZIF-zni samples (Fig. S3). Over the temperature range 80–130 °C, a much bigger endothermic peak was seen for Fe-BTC samples (Fig. S4) indicative of a higher water content. As shown in Fig. 5B-D, from TGA data, LC@ZIF-zni resulted in dryer samples for all the assayed loadings in comparison with LC@Fe-BTC samples. In principle, drying of the immobilized biocatalyst should result in a significant decrease in laccase activity [6]. In fact, LC@ZIF-zni retained higher activities at various enzymatic loadings even if samples with reduced moisture content (1% vs 35% in water content for biocatalyst with 59.4 and 52.7 mg g⁻¹ of enzymatic loading for ZIF-zni and Fe-BTC respectively) than Fe-BTC were used (Fig. 5D). It is worth noticing that also at the optimal Fe-BTC loadings, LC@ZIF-zni displayed a 10-fold higher activity than LC@Fe-BTC (1.32 μmol min⁻¹ mg⁻¹ vs 0.17 μmol min⁻¹ mg⁻¹) indicative of a superior immobilization environment in ZIF-zni when compared to Fe-BTC.

2.5. Storage stability of LC@Fe-BTC and LC@ZIF-zni

Samples of LC@Fe-BTC and LC@ZIF-zni were stored at 4 °C and the residual activity was checked every 3–5 days. The storage stability of LC@Fe-BTC showed a rapid linear decrease, retaining only 16% of initial activity (0.59 ± 0.11 μmol min⁻¹ g⁻¹) after eight days, while LC@ZIF-zni retained 82% of its initial activity (8.18 ± 0.14 μmol min⁻¹ g⁻¹). On comparison of the two supports there was over 60% difference in retention of activity, confirming that ZIF-zni is a superior support. Furthermore, LC@ZIF-zni retained about 50% of its initial activity at the 30th day. The rapid decrease in LC activity may be due to enzyme denaturation in the Fe-BTC material, but the lower stability of the Fe-BTC material is likely a significant factor. Good retention of catalytic activity in ZIF materials was reported by Ulu who described the immobilization of asparaginase in ZIF-8 [87] with the immobilized enzyme retaining 40% of initial activity after four weeks, similar to the data described here. The stability of laccase (*Trametes hirsute*) immobilized on ZIF-8 was described by Patil et al [83]. with only 20% loss of activity after storage for 20 days at 30 °C. The good storage stability of laccase in ZIF-zni highlights its possible use as a support for laccase immobilization. (Fig. 7).

Reuse is an important aspect in evaluating immobilized enzymes.

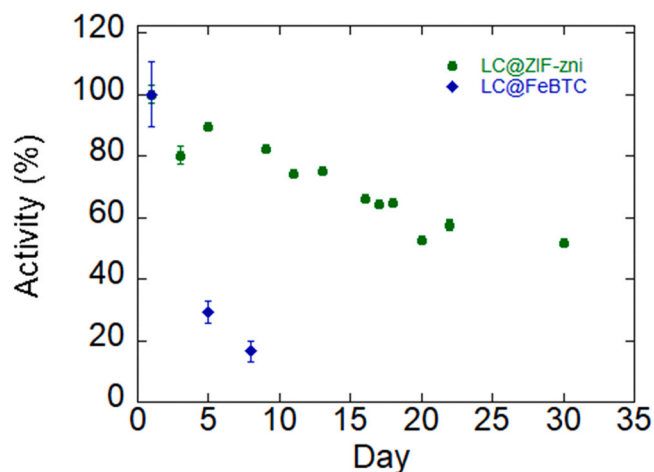


Fig. 7. Storage stability of LC@Fe-BTC and LC@ZIF-zni, activity normalized at 3.6 and 13.7 μmol min⁻¹ g⁻¹ respectively.

Samples of LC@Fe-BTC and LC@ZIF-zni were evaluated for reuse. (Fig. S9). ZIF-zni samples showed a rapid decrease after use, with a residual activity of 6.2% after three cycles. On the contrary, Fe-BTC displayed a significantly better performance retaining 18.2% activity after the 10th cycle. The rapid decrease in activity of the ZIF-zni samples is likely due to practical difficulties in recovering the samples as the crystal size of the ZIF biocatalysts dissolve when in contact with some buffers making its recover and reuse very challenging. A similar phenomenon was recently observed by Maddigan et al [88].

3. Conclusions

The comparison between two MOF materials used for the in situ immobilization of *Aspergillus sp.* laccase was described. The structures of both supports were characterized using XRD, SEM, TGA and FTIR techniques. Immobilization efficiency was 100% for all LC@Fe-BTC loadings while for ZIF samples it was slightly lower (from 97% to 99%). Surprisingly, LC@ZIF-zni showed a much higher V_{max} when compared with LC@Fe-BTC samples. The K_M value of LC@ZIF-zni is lower (21.6 μM) than that of LC@Fe-BTC (35.5 μM) suggesting more efficient substrate binding by laccase in ZIF-zni. The enzymatic activities were studied in a wide range of loadings. In the case of Fe-BTC samples, a maximal specific activity was observed at an optimal loading of 42.5 mg g⁻¹ whereas higher loadings resulted in a specific activity decrease. Differently, LC@ZIF-zni samples did not show any decrease in activity up to 59.4 mg g⁻¹ indicating that a higher amount of laccase can be immobilized without observed limitations. Lastly, the storage stability of both immobilized biocatalysts was studied indicating a much higher activity retention for LC@ZIF-zni samples (50% loss of initial activity after 30 days) than LC@Fe-BTC (84% loss of initial activity after 8 days). ZIF-zni material is a promising material for the in situ immobilization of laccase with good retention of activity while Fe-BTC materials do not possess long term stability.

Funding sources

Any funds used to support the research of the manuscript should be placed here (per journal style).

CRediT authorship contribution statement

Daide Tocco: Conceptualization, Methodology, Investigation, Data curation, Writing original draft, Writing review and editing, **Cristina Carucci:** Conceptualization, Methodology, Investigation, Data curation, Writing original draft, Writing review and editing, **Debora Todde:**

Methodology, Investigation, **Kim Shortall**: Methodology, Investigation, **Fernando Otero**: Methodology, Investigation, **Enrico Sanjust**: Writing review and editing, **Edmond Magner**: Data curation, Writing review and editing, **Andrea Salis**: Conceptualization, data curation, Writing original draft, Writing review and editing, Funding acquisition. All authors have read and agreed to the published version of the manuscript.

Declaration of Competing Interest

The authors declare that they have no known competing financial interests or personal relationships that could have appeared to influence the work reported in this paper.

Acknowledgment

DT thanks Erasmus+ and MIUR (PON RI 2014–2020, Azione I.1 "Dottorati Innovativi con Caratterizzazione industriale"- DOT1304455 2) for financing his PhD scholarship. CC gratefully acknowledges MIUR (PON-AIM Azione I.2 – DD n. 407–27.02.2018, AIM1890410 - 2). AS gratefully thanks financial support from FIR 2020, and MIUR (FFABR 2017). We wish to acknowledge the assistance of Dr. Wynette Redington (XRD characterization) and of Denise Demurtas and Simin Arshi (SEM and EDX characterization).

Author contributions

The manuscript was written through contributions of all authors. All authors have given approval to the final version of the manuscript.

Appendix A. Supporting information

Supplementary data associated with this article can be found in the online version at [doi:10.1016/j.colsurfb.2021.112147](https://doi.org/10.1016/j.colsurfb.2021.112147).

References

- [1] E. Magner, Immobilisation of enzymes on mesoporous silicate materials, *Chem. Soc. Rev.* 42 (15) (2013) 6213–6222, <https://doi.org/10.1039/c3cs35450k>.
- [2] A. Basso, S. Serban, Industrial applications of immobilized enzymes—a review, *Mol. Catal.* 479 (March) (2019), 110607, <https://doi.org/10.1016/j.mcat.2019.110607>.
- [3] F. Molina, A. Rueda, J.M. Bosque-Sendra, L. Megías, Determination of proteins in the presence of imidazole buffers, *J. Pharm. Biomed. Anal.* 14 (3) (1996) 273–280, [https://doi.org/10.1016/0731-7085\(95\)01615-5](https://doi.org/10.1016/0731-7085(95)01615-5).
- [4] U. Hanefeld, L. Gardossi, E. Magner, Understanding enzyme immobilisation, *Chem. Soc. Rev.* 38 (2) (2009) 453–468, <https://doi.org/10.1039/B711564B>.
- [5] R.A. Sheldon, S. van Pelt, Enzyme immobilisation in biocatalysis: why, what and how, *Chem. Soc. Rev.* 42 (15) (2013) 6223–6235, <https://doi.org/10.1039/c3cs60075k>.
- [6] A. Salis, M. Pisano, M. Monduzzi, V. Solinas, E. Sanjust, Laccase from pleurotus Sajor-Caju on functionalised SBA-15 mesoporous silica: immobilisation and use for the oxidation of phenolic compounds, *J. Mol. Catal. B Enzym.* 58 (1–4) (2009) 175–180, <https://doi.org/10.1016/j.molcatb.2008.12.008>.
- [7] F. Pitzalis, M. Monduzzi, A. Salis, A bienzymatic biocatalyst constituted by glucose oxidase and horseradish peroxidase immobilized on ordered mesoporous silica, *Microporous Mesoporous Mater.* 241 (2017) 145–154, <https://doi.org/10.1016/j.micromeso.2016.12.023>.
- [8] M. Piras, A. Salis, M. Piludu, D. Steri, M. Monduzzi, 3D vision of human lysozyme adsorbed onto a SBA-15 nanostructured matrix, *Chem. Commun.* 47 (26) (2011) 7338–7340, <https://doi.org/10.1039/c1cc11840d>.
- [9] J.R. Fernandez Caresani, A. Dallegrave, J.H.Z. dos Santos, Amylases immobilization by sol–gel entrapment: application for starch hydrolysis, *J. Sol-Gel Sci. Technol.* 94 (1) (2020) 229–240, <https://doi.org/10.1007/s10971-019-05136-7>.
- [10] Wastewater, T.; Siddeeq, S.M.; Tahoan, M.A.; Mnif, W. Iron Oxide/Chitosan Magnetic Nanocomposite Immobilized Manganese Peroxidase For.
- [11] P. Zucca, R. Fernandez-Lafuente, E. Sanjust, Agarose and its derivatives as supports for enzyme immobilization, *Molecules* 21 (11) (2016) 1577, <https://doi.org/10.3390/molecules21111577>.
- [12] M. Valldeperas, A. Salis, J. Barauskas, F. Tiber, T. Arnebrant, V. Razumas, M. Monduzzi, T. Nylander, Enzyme encapsulation in nanostructured self-assembled structures: toward biofunctional supramolecular assemblies, *Curr. Opin. Colloid Interface Sci.* 44 (2019) 130–142, <https://doi.org/10.1016/j.cocis.2019.09.007>.
- [13] Z. Temoçin, M. Inal, M. Gökçöz, M. Yiğitöglü, Immobilization of horseradish peroxidase on electrospun poly(Vinyl Alcohol)–polyacrylamide blend nanofiber membrane and its use in the conversion of phenol, *Polym. Bull.* 75 (5) (2018) 1843–1865, <https://doi.org/10.1007/s00289-017-2129-5>.
- [14] F. Pitzalis, C. Carucci, M. Naseri, L. Fotouhi, E. Magner, A. Salis, Lipase encapsulation onto ZIF-8: a comparison between biocatalysts obtained at low and high zinc/2-methylimidazole molar ratio in aqueous medium, *ChemCatChem* 10 (7) (2018) 1578–1585, <https://doi.org/10.1002/cctc.201701984>.
- [15] L. Zhong, Y. Feng, G. Wang, Z. Wang, M. Bilal, H. Lv, S. Jia, J. Cui, Production and use of immobilized lipases in/on nanomaterials: a review from the waste to biodiesel production, *Int. J. Biol. Macromol.* 152 (2020) 207–222, <https://doi.org/10.1016/j.ijbiomac.2020.02.258>.
- [16] T.O. Knedel, E. Ricklefs, C. Schlüsener, V.B. Urlacher, C. Janiak, Laccase encapsulation in ZIF-8 metal-organic framework shows stability enhancement and substrate selectivity, *ChemistryOpen* 8 (11) (2019) 1337–1344, <https://doi.org/10.1002/open.201900146>.
- [17] K. Liang, R. Ricco, C.M. Doherty, M.J. Styles, S. Bell, N. Kirby, S. Mudie, D. Haylock, A.J. Hill, C.J. Doonan, P. Falcaro, Biomimetic mineralization of metal-organic frameworks as protective coatings for biomacromolecules, *Nat. Commun.* 6 (2015) 4–11, <https://doi.org/10.1038/ncomms8240>.
- [18] X. Wu, M. Hou, J. Ge, Metal-organic frameworks and inorganic nanoflowers: a type of emerging inorganic crystal nanocarrier for enzyme immobilization, *Catal. Sci. Technol.* 5 (12) (2015) 5077–5085, <https://doi.org/10.1039/C5CY01181G>.
- [19] A. Gulati, R. Kakkur, DFT studies on storage and adsorption capacities of gases on MOFs, *Phys. Sci. Rev.* 3 (8) (2018), <https://doi.org/10.1515/psr-2017-0196>.
- [20] C. Van Nguyen, B.M. Matsagar, J.-Y. Yeh, W.-H. Chiang, K.C.W. Wu, MIL-53-NH₂-derived carbon-Al₂O₃ composites supported Ru catalyst for effective hydrogenation of levulinic acid to γ -valerolactone under ambient conditions, *Molecular Catalysis* 475 (1) (2019), 110478, <https://doi.org/10.1016/j.mcat.2019.110478>.
- [21] S. Shams, W. Ahmad, A.H. Memon, Y. Wei, Q. Yuan, H. Liang, Facile synthesis of laccase mimic Cu/H 3 BTC MOF for efficient dye degradation and detection of phenolic pollutants, *RSC Adv.* 9 (70) (2019) 40845–40854, <https://doi.org/10.1039/C9RA07473B>.
- [22] X. Li, D. Li, Y. Zhang, P. Lv, Q. Feng, Q. Wei, Encapsulation of enzyme by metal-organic framework for single-enzymatic biofuel cell-based self-powered biosensor, *Nano Energy* 68 (November 2019) (2020), 104308, <https://doi.org/10.1016/j.nanoen.2019.104308>.
- [23] S. Ashoka Sahadevan, N. Monni, M. Oggianu, A. Abhervé, D. Marongiu, M. Saba, A. Mura, G. Bongiovanni, V. Mameli, C. Cannas, N. Avarvari, F. Quochi, M. L. Mercuri, Heteroleptic NIR-emitting Yb III /anilate-based neutral coordination polymer nanosheets for solvent sensing, *ACS Appl. Nano Mater.* 3 (1) (2020) 94–104, <https://doi.org/10.1021/acsnan.9b01740>.
- [24] J. Mehta, N. Bhardwaj, S.K. Bhardwaj, K.H. Kim, A. Deep, Recent advances in enzyme immobilization techniques: metal-organic frameworks as novel substrates, *Coord. Chem. Rev.* 322 (2016) 30–40, <https://doi.org/10.1016/j.ccr.2016.05.007>.
- [25] F. Lyu, Y. Zhang, R.N. Zare, J. Ge, Z. Liu, One-pot synthesis of protein-embedded metal-organic frameworks with enhanced biological activities, *Nano Lett.* 14 (10) (2014) 5761–5765, <https://doi.org/10.1021/nl5026419>.
- [26] V. Lykourinou, Y. Chen, X. Wang, Sen, L. Meng, T. Hoang, L.J. Ming, R. L. Musselman, S. Ma, Immobilization of MP-11 into a mesoporous metal-organic framework, MP-11@mesoMOF: a new platform for enzymatic catalysis, *J. Am. Chem. Soc.* 133 (27) (2011) 10382–10385, <https://doi.org/10.1021/ja2038003>.
- [27] A.J. Howarth, Y. Liu, P. Li, Z. Li, T.C. Wang, J.T. Hupp, O.K. Farha, Chemical, thermal and mechanical stabilities of metal-organic frameworks, *Nat. Rev. Mater.* 1 (2016) 15018.
- [28] M. Safaei, M.M. Foroughi, N. Ebrahimpoor, S. Jahani, A. Omid, M. Khatami, A review on metal-organic frameworks: synthesis and applications, *TrAC Trends Anal. Chem.* 118 (2019) 401–425, <https://doi.org/10.1016/j.trac.2019.06.007>.
- [29] R.J. Drout, L. Robison, O.K. Farha, Catalytic applications of enzymes encapsulated in metal-organic frameworks, *Coord. Chem. Rev.* 381 (2019) 151–160, <https://doi.org/10.1016/j.ccr.2018.11.009>.
- [30] C. Carucci, L. Bruen, V. Gascón, F. Paradisi, E. Magner, Significant enhancement of structural stability of the hyperphalophilic ADH from haloferax volcanii via entrapment on metal organic framework support, *Langmuir* 34 (28) (2018) 8274–8280, <https://doi.org/10.1021/acs.langmuir.8b01037>.
- [31] M.B. Majewski, A.J. Howarth, P. Li, M.R. Wasielewski, J.T. Hupp, O.K. Farha, Enzyme encapsulation in metal-organic frameworks for applications in catalysis, *CrystEngComm* 19 (29) (2017) 4082–4091, <https://doi.org/10.1039/c7ce00022g>.
- [32] H. Xia, N. Li, X. Zhong, Y. Jiang, Metal-organic frameworks: a potential platform for enzyme immobilization and related applications, *Front. Bioeng. Biotechnol.* 8 (June) (2020) 1–16, <https://doi.org/10.3389/fbioe.2020.00695>.
- [33] W. Liang, H. Xu, F. Carraro, N.K. Maddigan, Q. Li, S.G. Bell, D.M. Huang, A. Tarzia, M.B. Solomon, H. Amenitsch, L. Vaccari, C.J. Sumbly, P. Falcaro, C.J. Doonan, Enhanced activity of enzymes encapsulated in hydrophilic metal-organic frameworks, *J. Am. Chem. Soc.* 141 (2019) 2348–2355, <https://doi.org/10.1021/jacs.8b10302>.
- [34] Z. Li, H. Xia, S. Li, J. Pang, W. Zhu, Y. Jiang, In situ hybridization of enzymes and their metal-organic framework analogues with enhanced activity and stability by biomimetic mineralisation, *Nanoscale* 9 (40) (2017) 15298–15302, <https://doi.org/10.1039/c7nr06315f>.
- [35] M. Zhao, Y. Li, X. Ma, M. Xia, Y. Zhang, Adsorption of cholesterol oxidase and entrapment of horseradish peroxidase in metal-organic frameworks for the colorimetric biosensing of cholesterol, *Talanta* 200 (December 2018) (2019) 293–299, <https://doi.org/10.1016/j.talanta.2019.03.060>.
- [36] Y.-R. Lee, J. Kim, W.-S. Ahn, Synthesis of metal-organic frameworks: a mini review, *Korean J. Chem. Eng.* 30 (9) (2013) 1667–1680, <https://doi.org/10.1007/s11814-013-0140-6>.

- [37] M. Sanchez-Sanchez, I. de Asua, D. Ruano, K. Diaz, Direct synthesis, structural features, and enhanced catalytic activity of the basolite F300-like semiamorphous Fe-BTC framework, *Cryst. Growth Des.* 15 (9) (2015) 4498–4506, <https://doi.org/10.1021/acs.cgd.5b00755>.
- [38] V. Gascón, C. Carucci, M.B. Jiménez, R.M. Blanco, M. Sánchez-Sánchez, E. Magner, Rapid in situ immobilization of enzymes in metal-organic framework supports under mild conditions, *ChemCatChem* 9 (7) (2017) 1182–1186, <https://doi.org/10.1002/cctc.201601342>.
- [39] K. Kida, M. Okita, K. Fujita, S. Tanaka, Y. Miyake, Formation of high crystalline ZIF-8 in an aqueous solution, *CrystEngComm* 15 (9) (2013) 1794–1801, <https://doi.org/10.1039/c2ce26847g>.
- [40] Tan, J.C.; Bennett, T.D.; Cheetham, A.K. Chemical structure, network topology, and porosity effects on the mechanical properties of zeolitic imidazolate frameworks. *Proc. Natl. Acad. Sci. U. S. A.* 2010, 107 (22), 9938–9943. <https://doi.org/10.1073/pnas.1003205107>.
- [41] Serhan, M.; Sprowls, M.; Jackemeyer, D.; Long, M.; Perez, I.D.; Maret, W.; Tao, N.; Forzani, E. Total Iron Measurement in Human Serum with a Smartphone. *AIChE Annu. Meet. Conf. Proc.* 2019, 2019–November. <https://doi.org/10.1039/x0xx00000x>.
- [42] W. Liang, R. Ricco, N.K. Maddigan, R.P. Dickinson, H. Xu, Q. Li, C.J. Sumbly, S. G. Bell, P. Falcaro, C.J. Doonan, Control of structure topology and spatial distribution of biomacromolecules in protein@ZIF-8 biocomposites, *Chem. Mater.* 30 (3) (2018) 1069–1077, <https://doi.org/10.1021/acs.chemmater.7b04977>.
- [43] P. Zucca, G. Cocco, F. Sollai, E. Sanjust, Fungal laccases as tools for biodegradation of industrial dyes, *Biocatalysis* 1 (1) (2016) 82–108, <https://doi.org/10.1515/boca-2015-0007>.
- [44] S. Riva, Laccases: blue enzymes for green chemistry, *Trends Biotechnol.* 24 (5) (2006) 219–226, <https://doi.org/10.1016/j.tibtech.2006.03.006>.
- [45] P.J. Kersten, B. Kalyanaraman, K.E. Hammel, B. Reinhammar, T.K. Kirk, Comparison of lignin peroxidase, horseradish peroxidase and laccase in the oxidation of methoxybenzenes, *Biochem. J.* 268 (2) (1990) 475–480, <https://doi.org/10.1042/bj2680475>.
- [46] B. Bertrand, F. Martínez-Morales, M.R. Trejo-Hernández, Upgrading laccase production and biochemical properties: strategies and challenges, *Biotechnol. Prog.* 33 (4) (2017) 1015–1034, <https://doi.org/10.1002/btpr.2482>.
- [47] D. Tocco, C. Carucci, M. Monduzzi, A. Salis, E. Sanjust, Recent developments in the delignification and exploitation of grass lignocellulosic biomass, *ACS Sustain. Chem. Eng.* 9 (6) (2021) 2412–2432, <https://doi.org/10.1021/acscuschemeng.0c07266>.
- [48] J.O. Unuofin, Treasure from dross: application of agroindustrial wastes-derived thermo-halotolerant laccases in the simultaneous biocouring of denim fabric and decolorization of dye bath effluents, *Ind. Crops Prod.* 147 (February) (2020), 112251, <https://doi.org/10.1016/j.indcrop.2020.112251>.
- [49] E.N. Prasetyo, S. Semlitsch, G.S. Nyanhongo, Y. Lemmouchi, G.M. Guebitz, Laccase oxidation and removal of toxicants released during combustion processes, *Chemosphere* 144 (2016) 652–660, <https://doi.org/10.1016/j.chemosphere.2015.07.082>.
- [50] P. Zucca, E. Sanjust, Inorganic materials as supports for covalent enzyme immobilization: methods and mechanisms, *Molecules* 19 (9) (2014) 14139–14194, <https://doi.org/10.3390/molecules190914139>.
- [51] D.W.S. Wong, Structure and action mechanism of ligninolytic enzymes, *Appl. Biochem. Biotechnol.* 157 (2) (2009) 174–209, <https://doi.org/10.1007/s12010-008-8279-z>.
- [52] A. Rico, J. Rencoret, J.C. del Río, A.T. Martínez, A. Gutiérrez, Pretreatment with laccase and a phenolic mediator degrades lignin and enhances saccharification of eucalyptus feedstock, *Biotechnol. Biofuels* 7 (1) (2014) 6, <https://doi.org/10.1186/1754-6834-7-6>.
- [53] M. Asgher, A. Wahab, M. Bilal, H.M.N. Iqbal, Delignification of lignocellulose biomass by alginate–chitosan immobilized laccase produced from *Trametes versicolor* IBL-04, *Waste Biomass Valorization* 9 (11) (2018) 2071–2079, <https://doi.org/10.1007/s12649-017-9991-0>.
- [54] M. Naseri, F. Pitzalis, C. Carucci, L. Medda, L. Fotouhi, E. Magner, A. Salis, Lipase and laccase encapsulated on zeolite imidazolate framework: enzyme activity and stability from voltammetric measurements, *ChemCatChem* 10 (23) (2018) 5425–5433, <https://doi.org/10.1002/cctc.201801293>.
- [55] V. Gascón, M.B. Jiménez, R.M. Blanco, M. Sanchez-Sanchez, Semi-crystalline Fe-BTC MOF material as an efficient support for enzyme immobilization, *Catal. Today* 304 (October 2017) (2018) 119–126, <https://doi.org/10.1016/j.cattod.2017.10.022>.
- [56] M. Marzorati, B. Danieli, D. Haltrich, S. Riva, Selective laccase-mediated oxidation of sugars derivatives, *Green Chem* 7 (5) (2005) 310–315, <https://doi.org/10.1039/b416668j>.
- [57] P. Baldrian, Fungal laccases – occurrence and properties, *FEMS Microbiol. Rev.* 30 (2) (2006) 215–242, <https://doi.org/10.1111/j.1574-4976.2005.00010.x>.
- [58] L. Gianfreda, F. Xu, J.M. Bollag, Laccases: a useful group of oxidoreductive enzymes, *Bioremediat. J.* 3 (1) (1999) 1–26, <https://doi.org/10.1080/10889869991219163>.
- [59] T.H. Wei, S.H. Wu, Y. Da Huang, W.S. Lo, B.P. Williams, S.Y. Chen, H.C. Yang, Y. S. Hsu, Z.Y. Lin, X.H. Chen, P.E. Kuo, L.Y. Chou, C.K. Tsung, F.K. Shieh, Rapid mechanochemical encapsulation of biocatalysts into robust metal–organic frameworks, *Nat. Commun.* 10 (1) (2019) 1–8, <https://doi.org/10.1038/s41467-019-12966-0>.
- [60] X. Liu, W. Qi, Y. Wang, R. Su, Z. He, A facile strategy for enzyme immobilization with highly stable hierarchically porous metal-organic frameworks, *Nanoscale* 9 (44) (2017) 17561–17570, <https://doi.org/10.1039/c7nr06019j>.
- [61] G. Autie-Castro, M.A. Autie, E. Rodríguez-Castellón, C. Aguirre, E. Reguera, Cu-BTC and Fe-BTC Metal-organic frameworks: role of the materials structural features on their performance for volatile hydrocarbons separation, *Colloids Surfaces A Physicochem. Eng. Asp.* 481 (2015) 351–357, <https://doi.org/10.1016/j.colsurfa.2015.05.044>.
- [62] Y.K. Seo, J.W. Yoon, J.S. Lee, U.H. Lee, Y.K. Hwang, C.H. Jun, P. Horcajada, C. Serre, J.S. Chang, Large scale fluoride-free synthesis of hierarchically porous Iron(III) trimesate MIL-100(Fe) with a zeolite MTN topology, *Microporous Mesoporous Mater.* 157 (2012) 137–145, <https://doi.org/10.1016/j.micromeso.2012.02.027>.
- [63] T. Hikov, C.A. Schröder, J. Cravillon, M. Wiebecke, K. Huber, In situ static and dynamic light scattering and scanning electron microscopy study on the crystallization of the dense zinc imidazolate framework ZIF-Zn, *Phys. Chem. Chem. Phys.* 14 (2) (2012) 511–521, <https://doi.org/10.1039/c1cp22855b>.
- [64] S. Huang, K.-L. Yang, X.-F. Liu, H. Pan, H. Zhang, S. Yang, MIL-100(Fe)-catalyzed efficient conversion of hexoses to lactic acid, *RSC Adv.* 7 (10) (2017) 5621–5627, <https://doi.org/10.1039/C6RA26469G>.
- [65] Y. Yang, Y. Bai, F. Zhao, E. Yao, J. Yi, C. Xuan, S. Chen, Effects of metal organic framework Fe-BTC on the thermal decomposition of ammonium perchlorate, *RSC Adv.* 6 (71) (2016) 67308–67314, <https://doi.org/10.1039/C6RA12634K>.
- [66] J. Cravillon, R. Nayuk, S. Springer, A. Feldhoff, K. Huber, M. Wiebecke, Controlling zeolitic imidazolate framework nano- and microcrystal formation: insight into crystal growth by time-resolved in situ static light scattering, *Chem. Mater.* 23 (8) (2011) 2130–2141, <https://doi.org/10.1021/cm103571y>.
- [67] J.B. James, Y.S. Lin, Kinetics of ZIF-8 thermal decomposition in inert, oxidizing, and reducing environments, *J. Phys. Chem. C* 120 (26) (2016) 14015–14026, <https://doi.org/10.1021/acs.jpcc.6b01208>.
- [68] Park, K.S.; Ni, Z.; Côté, A.P.; Choi, J.Y.; Huang, R.; Uribe-Romo, F.J.; Chae, H.K.; O’Keeffe, M.; Yaghi, O.M. Exceptional chemical and thermal stability of zeolitic imidazolate frameworks. *Proc. Natl. Acad. Sci. U. S. A.* 2006, 103 (27), 10186–10191. <https://doi.org/10.1073/pnas.0602439103>.
- [69] G. Majano, O. Ingold, M. Yulikov, G. Jeschke, J. Pérez-Ramírez, Room-temperature synthesis of Fe–BTC from layered iron hydroxides: the influence of precursor organisation, *CrystEngComm* 15 (46) (2013) 9885, <https://doi.org/10.1039/c3ce41366g>.
- [70] H. Lv, H. Zhao, T. Cao, L. Qian, Y. Wang, G. Zhao, Efficient degradation of high concentration Azo-dye wastewater by heterogeneous fenton process with iron-based metal-organic framework, *J. Mol. Catal. A Chem.* 400 (May 2015) (2015) 81–89, <https://doi.org/10.1016/j.molcata.2015.02.007>.
- [71] B. Pangkumhang, P. Jutaporn, K. Sorachoti, P. Khamdagsag, V. Tanboonchuy, Applicability of Iron (III) trimesic (Fe-BTC) to enhance lignin separation from pulp and paper wastewater, *Sains Malaysiana* 48 (1) (2019) 199–208, <https://doi.org/10.17576/jsm-2019-4801-23>.
- [72] S. Rafiei, S. Tangestaninejad, P. Horcajada, M. Moghadam, V. Mirkhani, I. Mohammadpoor-Baltork, R. Kardanpour, F. Zadehahmadi, Efficient biodiesel production using a lipase@ZIF-67 nanobioreactor, *Chem. Eng. J.* 334 (October 2017) (2018) 1233–1241, <https://doi.org/10.1016/j.cej.2017.10.094>.
- [73] J. Liu, J. He, L. Wang, R. Li, P. Chen, X. Rao, L. Deng, L. Rong, J. Lei, NiO-PTA supported on ZIF-8 as a highly effective catalyst for hydrocracking of jatropha oil, *Sci. Rep.* 6 (1) (2016) 23667, <https://doi.org/10.1038/srep23667>.
- [74] N. Nasihat Sheno, S. Farhadi, A. Maleki, M. Hamidi, A novel approach for the synthesis of phospholipid bilayer-coated zeolitic imidazolate frameworks: preparation and characterization as a PH-responsive drug delivery system, *New J. Chem.* 43 (4) (2019) 1956–1963, <https://doi.org/10.1039/C8NJ04715D>.
- [75] Q. Xia, H. Wang, B. Huang, X. Yuan, J. Zhang, J. Zhang, L. Jiang, T. Xiong, G. Zeng, State-of-the-art advances and challenges of iron-based metal organic frameworks from attractive features, synthesis to multifunctional applications, *Small* 15 (2) (2019) 1–25, <https://doi.org/10.1002/sml.201803088>.
- [76] A.R. Oveisi, A. Khorramabadi-Zad, S. Daliran, Iron-based metal-organic framework, Fe(BTC): an effective dual-functional catalyst for oxidative cyclization of bisnaphthols and tandem synthesis of quinazolin-4(3H)-ones, *RSC Adv.* 6 (2) (2016) 1136–1142, <https://doi.org/10.1039/c5ra19013d>.
- [77] A.D. Salazar-Aguilar, G. Vega, J.A. Casas, S.M. Vega-Díaz, F. Tristan, D. Meneses-Rodríguez, M. Belmonte, A. Quintanilla, Direct hydroxylation of phenol to dihydroxybenzenes by H₂O₂ and Fe-based metal-organic framework catalyst at room temperature, *Catalysts* 10 (2) (2020) 1–14, <https://doi.org/10.3390/catal10020172>.
- [78] X. Li, L. Lachmanski, S. Safi, S. Sene, C. Serre, J.M. Grenèche, J. Zhang, R. Gref, New insights into the degradation mechanism of metal-organic frameworks drug carriers, *Sci. Rep.* 7 (1) (2017) 1–11, <https://doi.org/10.1038/s41598-017-13323-1>.
- [79] M.D.J. Velásquez-Hernández, R. Ricco, F. Carraro, F.T. Limpoco, M. Linares-Moreau, E. Leitner, H. Wilsche, J. Rattenberger, H. Schröttner, P. Frühwirth, E. M. Stadler, G. Gescheidt, H. Amenitsch, C.J. Doonan, P. Falcaro, Degradation of ZIF-8 in phosphate buffered saline media, *CrystEngComm* 21 (31) (2019) 4538–4544, <https://doi.org/10.1039/c9ce00757a>.
- [80] M.A. Luzuriaga, C.E. Benjamin, M.W. Gaertner, H. Lee, F.C. Herbert, S. Mallick, J. J. Gassensmith, ZIF-8 degrades in cell media, serum, and some—but not all—common laboratory buffers, *Supramol. Chem.* 31 (8) (2019) 485–490, <https://doi.org/10.1080/10610278.2019.1616089>.
- [81] Y. Du, J. Gao, L. Zhou, L. Ma, Y. He, X. Zheng, Z. Huang, Y. Jiang, MOF-based nanotubes to hollow nanospheres through protein-induced soft-templating pathways, *Adv. Sci.* 6 (6) (2019) 6–11, <https://doi.org/10.1002/adv.201801684>.
- [82] M. Gökgöz, H. Altinok, Immobilization of laccase on polyacrylamide and polyacrylamide κ carragennan-based semi-Interpenetrating polymer networks,

- Artif. Cells Blood Substitutes Biotechnol. 40 (5) (2012) 326–330, <https://doi.org/10.3109/10731199.2012.658469>.
- [83] P.D. Patil, G.D. Yadav, Rapid in situ encapsulation of laccase into metal-organic framework support (ZIF-8) under biocompatible conditions, *ChemistrySelect* 3 (17) (2018) 4669–4675, <https://doi.org/10.1002/slct.201702852>.
- [84] A. Salis, I. Svensson, M. Monduzzi, V. Solinas, P. Adlercreutz, The atypical lipase B from *Candida Antarctica* is better adapted for organic media than the typical lipase from *Thermomyces Lanuginosa*, *Biochim. Biophys. Acta - Proteins Proteomics* 1646 (1–2) (2003) 145–151, [https://doi.org/10.1016/S1570-9639\(02\)00556-3](https://doi.org/10.1016/S1570-9639(02)00556-3).
- [85] P. Giardina, V. Faraco, C. Pezzella, A. Piscitelli, S. Vanhulle, G. Sanna, Laccases: a never-ending story, *Cell. Mol. Life Sci.* 67 (3) (2010) 369–385, <https://doi.org/10.1007/s00018-009-0169-1>.
- [86] Y.Y. Wan, R. Lu, L. Xiao, Y.M. Du, T. Miyakoshi, C.L. Chen, C.J. Knill, J.F. Kennedy, Effects of organic solvents on the activity of free and immobilised laccase from *Rhus vernicifera*, *Int. J. Biol. Macromol.* 47 (4) (2010) 488–495, <https://doi.org/10.1016/j.ijbiomac.2010.07.003>.
- [87] A. Ulu, Metal-organic frameworks (MOFs): a novel support platform for ASNase immobilization, *J. Mater. Sci.* 55 (14) (2020) 6130–6144, <https://doi.org/10.1007/s10853-020-04452-6>.
- [88] N.K. Maddigan, O.M. Linder-Patton, P. Falcaro, C.J. Sumbly, S.G. Bell, C.J. Doonan, Influence of the synthesis and storage conditions on the activity of candida antarctica lipase B ZIF-8 biocomposites, *ACS Appl. Mater. Interfaces* (2021), [acsami.1c04785](https://doi.org/10.1021/acsami.1c04785), <https://doi.org/10.1021/acsami.1c04785>.

Supporting information

Enzyme Immobilization on Metal Organic Frameworks: Laccase from *Aspergillus* sp is better adapted to ZIF-zni rather than Fe-BTC.

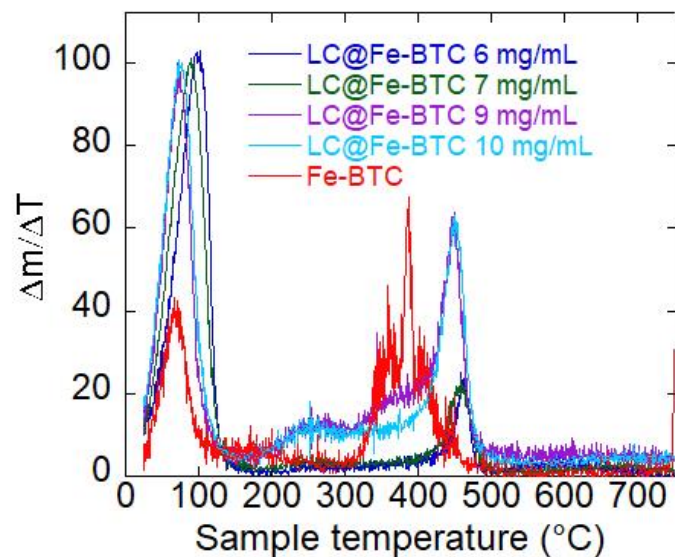


Figure S1. Derivative dm/dT vs T of Fe-BTC MOF samples

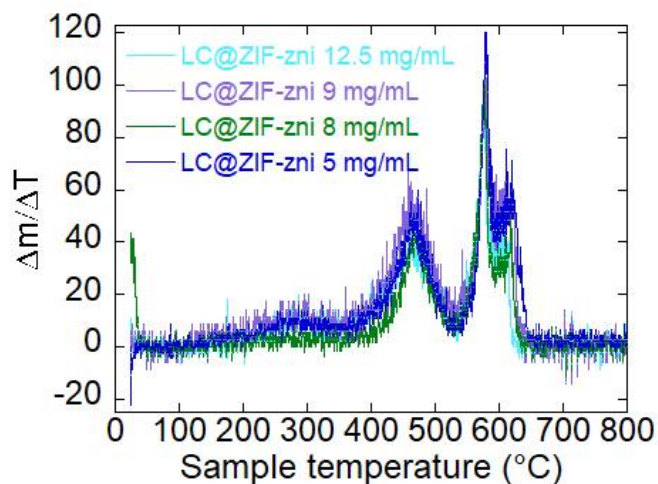


Figure S2. Derivative dm/dT vs T of ZIF-zni samples

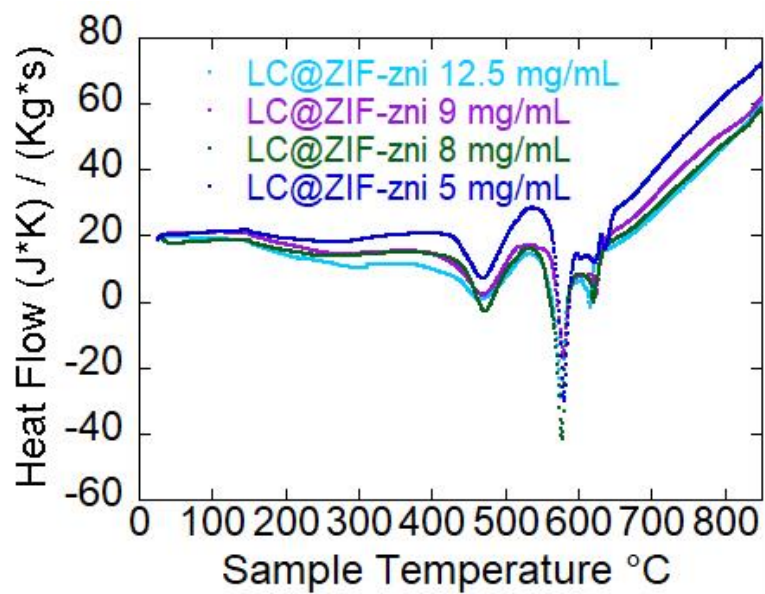


Figure S3. Heat flow vs T of ZIF-zni samples

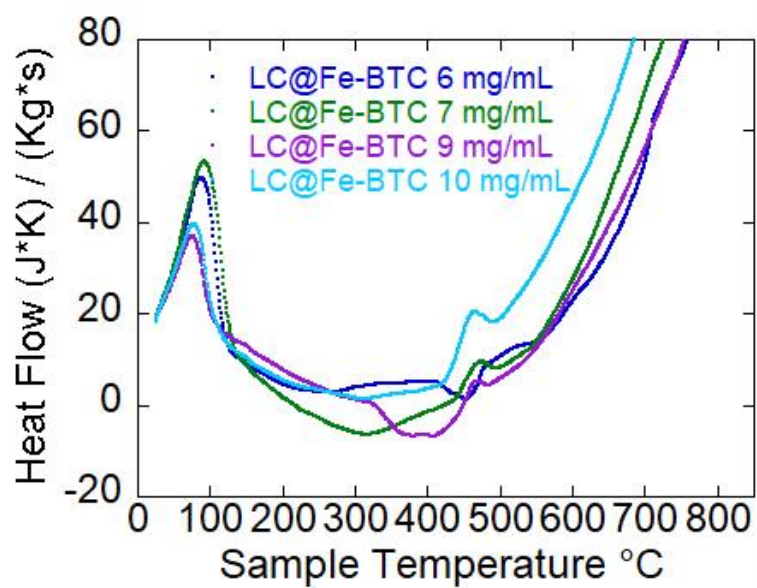


Figure S4. Heat flow vs T of FeBTC samples

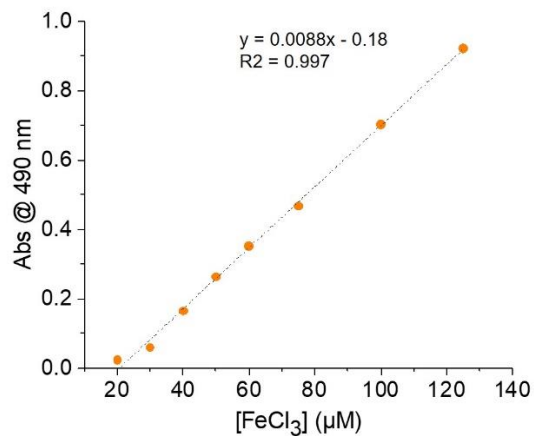


Figure S5. Standard curve of Fe^{3+} concentration by complexing with SCN^- . Standard deviation error bars are hidden by the symbols.

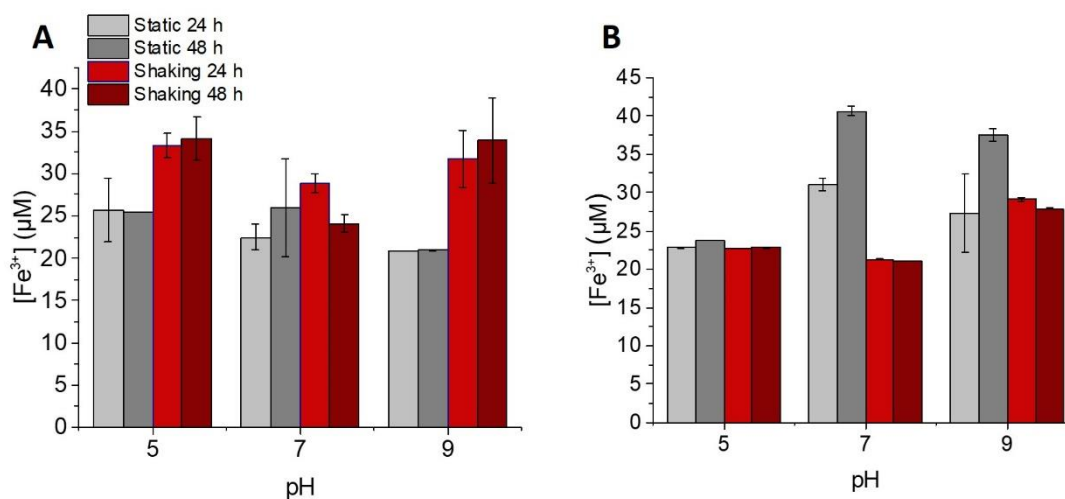


Figure S6. Detection of iron in solution following Fe-BTC MOF storage in aqueous buffer a) 10 mM buffer, b) 100 mM buffer.

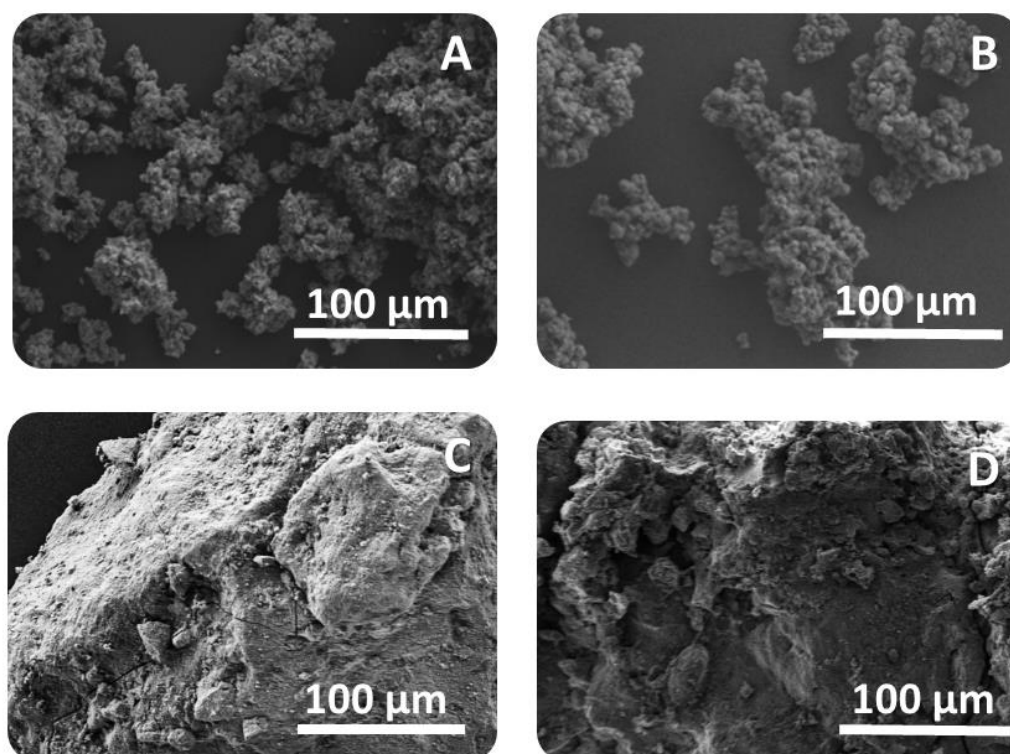


Figure S7. SEM images of A-B) ZIF-zni and LC@ZIF-zni samples C-D) Fe-BTC and LC@Fe-BTC

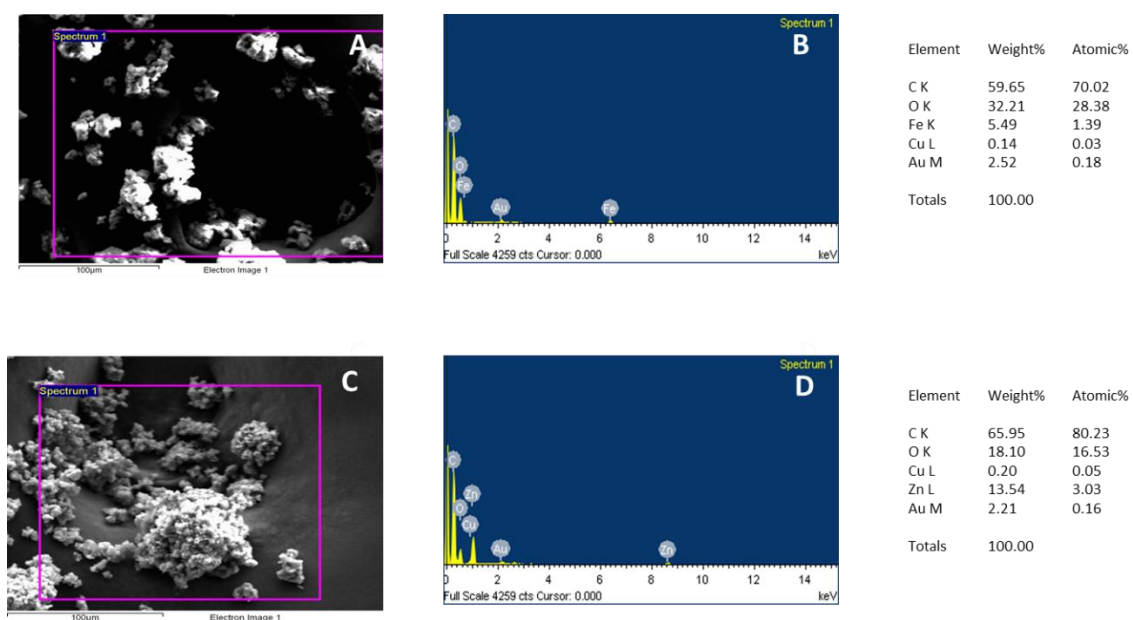


Figure S8 SEM analysis of LC@Fe-BTC A) with respective EDX B). SEM analysis of LC@ZIF-zni C) with respective EDX D)

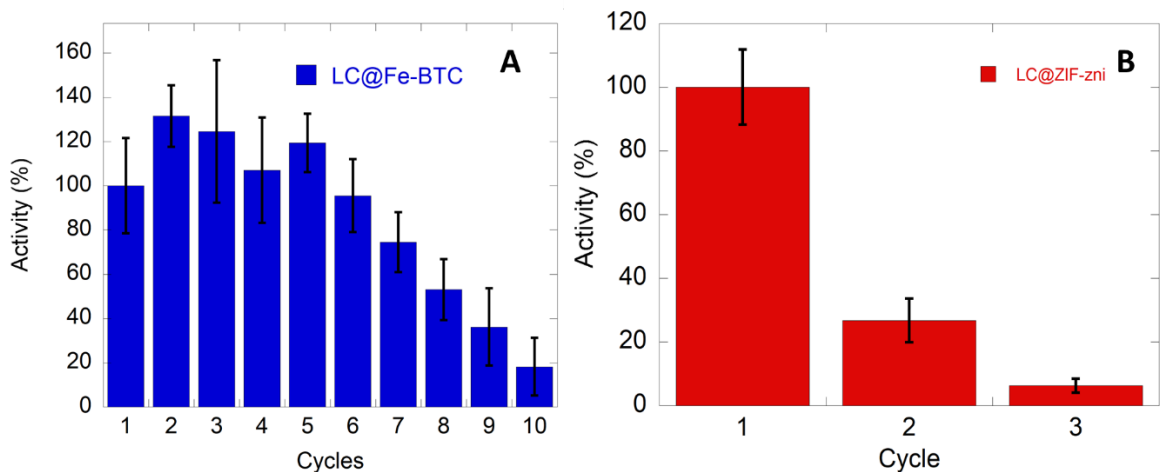


Figure S9 Reuse measurements of LC@Fe-BTC A) and LC@ZIF-zni B). Enzymatic Activity was normalized at $1.9 \pm 0.6 \mu\text{mol min}^{-1}$ and $5.4 \pm 0.7 \mu\text{mol min}^{-1}$ respectively.

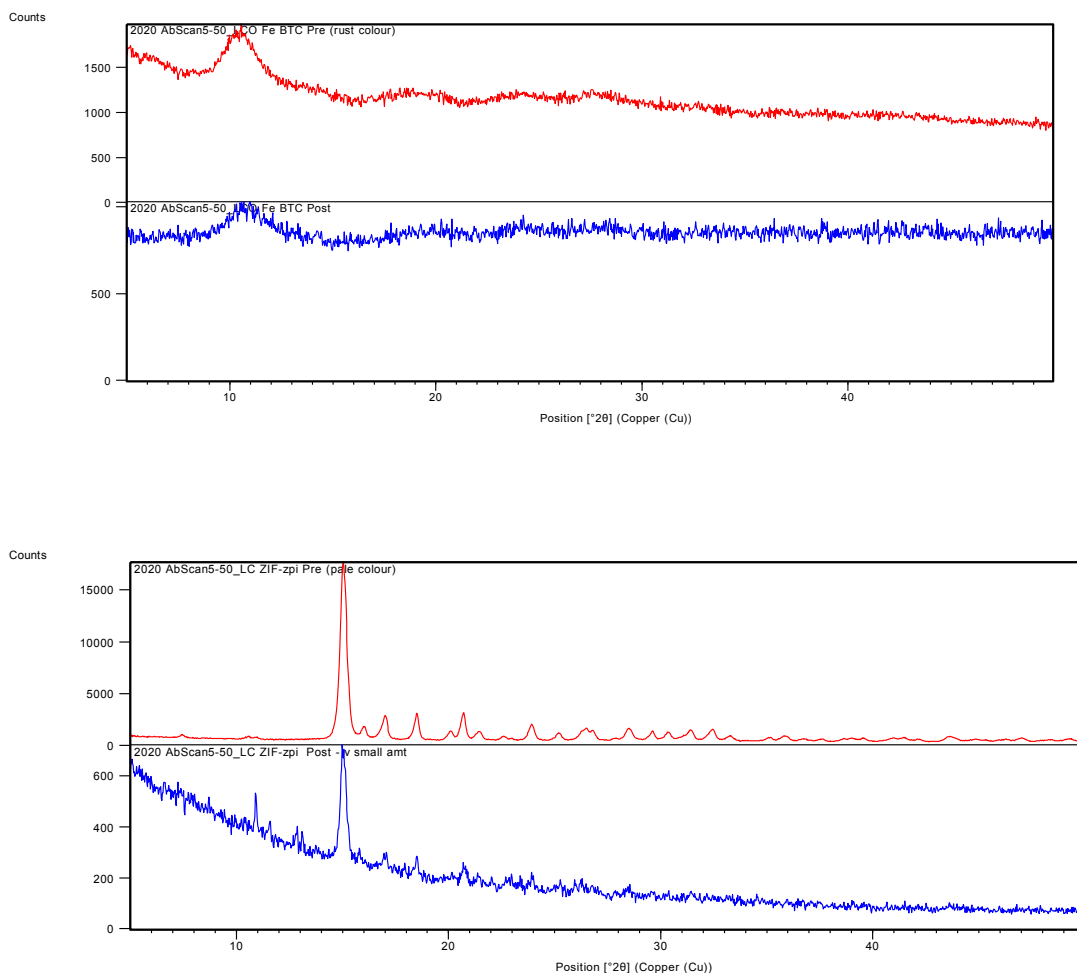


Figure S10 XRD measurements of LC@Fe-BTC A) and LC@ZIF-zni before and after use

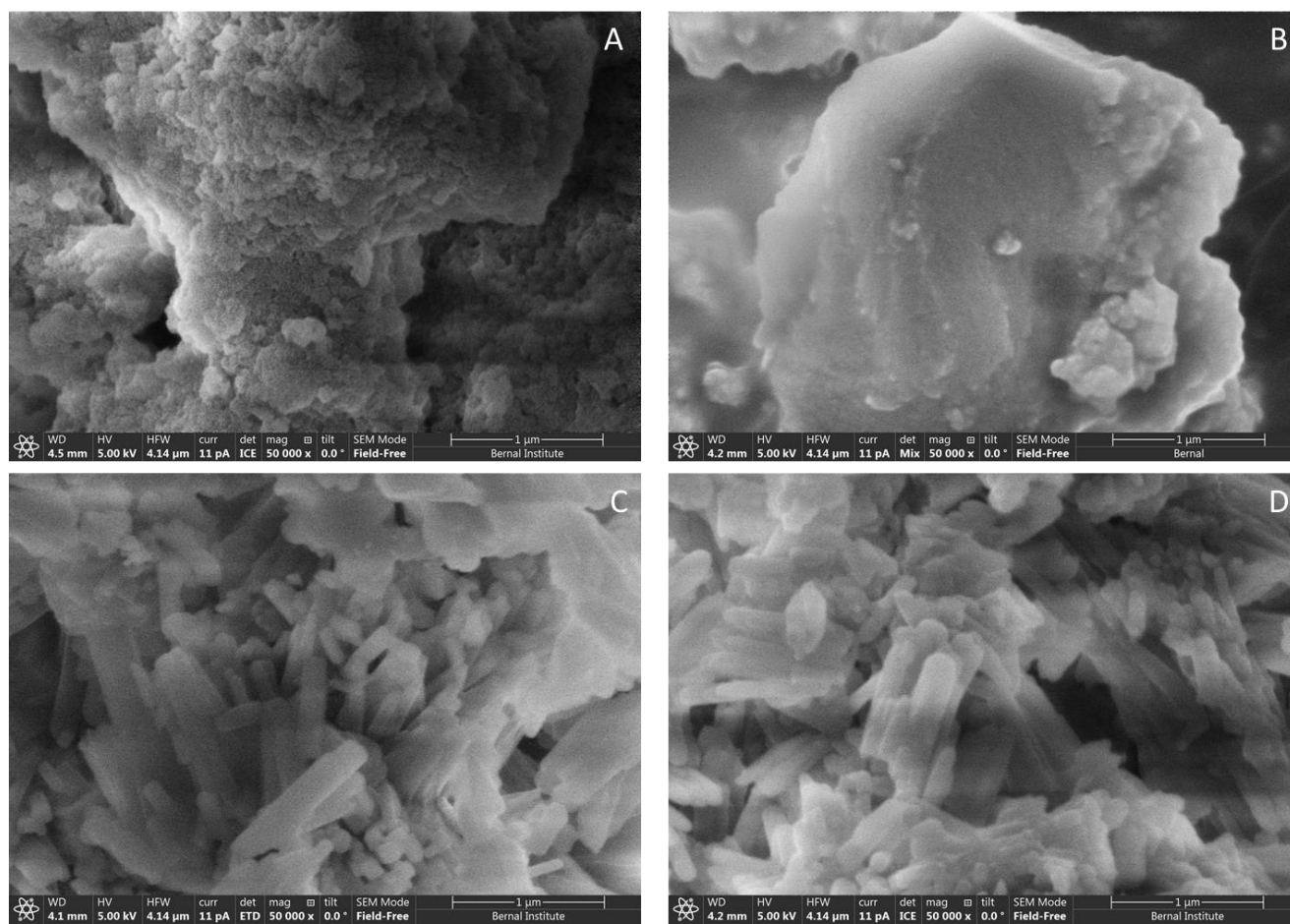


Figure S11 SEM images of LC@Fe-BTC respectively before and after use A-B) and LC@ZIF-zni respectively before and after use C-D)

Table S1. Mass loss (%) of Fe-BTC MOF and LC@Fe-BTC samples

Samples	Mass loss (%) T < 115 °C	Mass loss (%) 115 °C < T < 430 °C	Mass loss (%) T > 430 °C	Loading (mg g ⁻¹)	IE (%)
LC@Fe-BTC (6 mg/mL)	70.5	9.5	5.5	29.8	100
LC@Fe-BTC (7 mg/mL)	63	13	9	34.8	100
LC@Fe-BTC (8 mg/mL)	-	-	-	41.7	100
LC@Fe-BTC (9 mg/mL)	32	27	13.5	45.2	100
LC@Fe-BTC (10 mg/mL)	35	22	14	52.7	100

	Mass loss (%) T < 115 °C	Mass loss (%) 115°C < T < 430 °C	Mass loss (%) 330 °C < T < 500°C		
Fe-BTC MOF	28	14.5	43	-	-

Table S2 Mass loss (%) of ZIF and LC@ZIF samples

Samples	Mass loss (%) 245 °C < T < 400 °C	Mass loss (%) 400°C < T < 433 °C	Mass loss (%) 433°C < T < 566°C	Loading (mg g⁻¹)	IE (%)
LC@ZIF-zni (5 mg/mL)	9.5	3.8	23.9	19.8	97.3
LC@ZIF-zni (6 mg/mL)	6.5	3	29.9	30.5	98.6
LC@ZIF-zni (8 mg/mL)	-	-	-	35.6	97.2
LC@ZIF-zni (9 mg/mL)	11.6	4.7	26.1	41.6	97.3
LC@ZIF-zni (12.5 mg/mL)	13.5	5.3	26.8	59.4	97.2
ZIF-zni	2.8	1.9	33.6	-	-

Experimental Section

Chemicals

Laccase from *Aspergillus* sp (activity of ≥ 1000 LAMU g^{-1}); 2,2'-azinobis-(3-ethylbenzothiazoline-6-sulfonate) diammonium salt ($\geq 98\%$); ferric chloride, $\text{FeCl}_3 \cdot 6\text{H}_2\text{O}$ ($> 97\%$); zinc nitrate hexahydrate (98%), imidazole ($\geq 99\%$), sodium hydroxide, NaOH; trimesic acid, H_3BTC (95%); sodium phosphate, monobasic NaH_2PO_4 (99%); sodium phosphate dibasic, Na_2HPO_4 (99%); Bradford reagent; HCl (37%); acetic acid (99%); sodium acetate (anhydrous) ($\geq 99.0\%$); were purchased from Sigma-Aldrich (Milan Italy). Sodium thiocyanate; citric acid; trisodium citrate; potassium phosphate monobasic; potassium phosphate dibasic; were all purchased from Sigma Aldrich (Ireland). All reagents were used as received without further purification. Milli-Q water ($18.2 \text{ M}\Omega \text{ cm}$) was used to prepare all aqueous solutions.

Quantification of iron by Uv-vis analysis

A standard curve of Fe^{3+} was constructed using concentrations of FeCl_3 from 20-125 μM . 500 μL of 1 M NaSCN was added to an equal amount of each iron chloride standard and left to incubate for 15 min at room temperature for the appearance of a red color. The absorbance was then analyzed at 490 nm.

Synthesis of Fe-BTC MOF

Fe-BTC MOF was synthesized according to a published procedure by Sanchez-Sanchez et al.[28] Briefly, the synthesis involves the preparation of two different solutions. Solution 1 contains the organic linker and was obtained by dissolving 0.263 g of trimesic acid (H_3BTC) in 3.685 mL of NaOH 1.06 M, once H_3BTC was totally solubilized 6.388 mL of deionized water were added. Solution 2 contains the metal source and was prepared by dissolving 0.508 g of $\text{FeCl}_3 \cdot 6\text{H}_2\text{O}$ in 10 g of H_2O . Solution 2 was then added dropwise to the solution 1 under magnetic stirring. The resulted reddish-brown suspension was maintained under stirring at 25 °C for 10 minutes. The obtained solid (Fe-BTC MOF) was collected by filtration, washed several times with Milli-Q water and dried at room temperature.

Synthesis of LC@Fe-BTC biocatalysts

LC@Fe-BTC was synthesized according to a published procedure by Gascon et al.¹ Briefly, three solutions were prepared. Solution 1 was obtained by dissolving 0.263 g of trimesic acid (H_3BTC) in 3.685 mL of NaOH 1.06 M (pH 8). Solution 2 was prepared by mixing an appropriate aliquot of LC with Milli Q water to obtain a standard solution of LC (6-7-8-9-10 mg mL^{-1}). Solution 3 was

prepared by dissolving 0.508 g of $\text{FeCl}_3 \cdot 6\text{H}_2\text{O}$ in 10 g of H_2O (pH 1.8). To maintain the enzyme around neutral pH, 6.388 mL of solution 2 was added to solution 1, while checking the pH of the mixture. Solution 3 was then added dropwise to the resulting mixture under magnetic stirring. The obtained reddish-brown suspension was maintained under stirring at 25 °C for 10 minutes. The obtained solid (LC@Fe-BTC) was recovered by filtration, washed several times with Milli-Q water and dried at room temperature.

Preparation of ZIF-zni and LC@ZIF-zni biocatalysts

LC@ZIF-zni was synthesized according to a published procedure by Naseri et al.² Briefly, a volume of 2 mL of an enzymatic solution in acetate buffer (0.1 M, pH 5) was added to 10 mL of an imidazole (0.851g) solution in Milli-Q water, and 1 mL of a $\text{Zn}(\text{NO}_3)_2$ solution (3.1 M). The obtained mixture was stirred at room temperature for 45 min, and then a solid was collected by filtration and washed three times with Milli-Q water. Finally, the obtained sample was filtered dried at room temperature for 2-3 minutes and stored at 4°C. The pure ZIF-zni synthesis was carried out in the same way except for the fact that no enzyme was added.

Characterization of Fe-BTC, ZIF-zni, LC@Fe-BTC and LC@ZIF-zni samples

Thermogravimetric analysis (TGA) was carried out by means of a TGA 4000 Perkin Elmer in a temperature range from 25 °C to 800°C and a ramp rate of 10 °C min^{-1} , under an oxygen flow (flow rate = 40 mL min^{-1}). Scanning electron microscopy (SEM) analysis was performed by using a HITACHI SU-70 at 5 kV. Samples were covered with gold by sputter coating for 40 s and then analyzed by SEM. Attenuated total reflectance Fourier transform infrared (ATR-FTIR) spectra were recorded with a single reflection platinum ATR accessory from Perkin Elmer 100 FTIR over the wavelength range, 4000 to 600 cm^{-1} . N_2 adsorption/desorption isotherms were recorded at 77 K using an ASAP 2020 (Micromeritics). Samples were firstly degassed under vacuum for 12 h at 25 °C. The Brunauer–Emmett–Teller (BET)³ and the Barret–Joyner–Halenda (BJH)⁴ methods were used to calculate the specific surface area, the pore volume, and the pore size distribution. A X'PERT Pro PANalytical diffractometer was used for X-ray diffraction (XRD) experiments with $\text{Cu K}\alpha$ radiation. The data were collected with a 2θ step size of 0.013 from 5 to 40° and an accumulation time of 99.19 s. An Agilent Cary 60 UV-Vis spectrophotometer equipped with probe was used for enzymatic activity tests.

Determination of immobilization efficiency and enzyme loading

Protein loading and encapsulation efficiency of the immobilised biocatalysts, LC@Fe-BTC, were obtained by means of Bradford assay.⁵ Briefly, the protein content was determined using the

Bradford reagent (Bio-Rad) and BSA (bovine serum albumin) as the protein standard (20 mg/L). The calibration curve was built by preparing a set of BSA solutions in acetate buffer pH 5 100 mM at different concentrations (0.5-15 mg/L) from dilution of the standard solution. Then, a 0.5 mL aliquot of each solutions were mixed to 0.5 mL of Bradford reagent in a glass cuvette. After exactly 10 min the absorbance of the solutions was measured at the wavelength of 595 nm.

The protein concentration in the supernatant was evaluated by measuring the absorbance ($\lambda = 595$ nm) of a mixture containing 0.5 mL of supernatant and 0.5 mL of Bradford reagent after 10 min of incubation. It is worth noticing that imidazole strongly interfere with Bradford reagent at concentration higher than 200 mM.⁶ However, the supernatant of raw ZIF was analyzed and the corresponding Bradford assay did not show any interference suggesting that the imidazole quantity in the supernatant post ZIF synthesis is negligible. The amount of immobilized protein is calculated from the difference between the amount used for immobilization and the amount that is in the supernatant. The enzymatic loading ($L_{LC@ZIF} = mg_{LAC} / g_{LC@ZIF-1}$) was determined by the equation:

$$\text{Protein loading} = \frac{([P]_f - [P]_i)V}{m}$$

Where, $[P]_f$ and $[P]_i$ are the final and initial protein concentrations ($mg\ mL^{-1}$), respectively; V is the volume of the enzyme solution (mL) and m is the mass of biocatalyst (g).

Encapsulation efficiency (EE%) is the percent ratio between the amount of immobilised protein and the amount of protein in the immobilizing solution:

$$IE\% = (1 - [P]_f / [P]_i) \cdot 100\%$$

where $[P]_i$ and $[P]_f$ are the initial and the final protein concentrations in the immobilizing solution.²

Determination of LC@Fe-BTC and ZIF-zni activity

Before each measurement LC@Fe-BTC were dried in a desiccator for 20 mins (25 °C). The catalytic activities of LC@Fe-BTC were quantified by Agilent Cary 60 UV-Vis spectrophotometry, at $\lambda = 420$ nm (25 °C). The activity measurement of LC@Fe-BTC was carried out adding 10 mg of LC@Fe-BTC in 4.8 mL of acetate buffer pH 5 100 mM. The reaction started by adding to the mixture a volume of 0.25 mL ABTS 250 μ M in a cell kept under stirring and at $T = 25^\circ\text{C}$. Blank was measured by mixing 4.8 mL of acetate buffer pH 5 100 mM. Test activity of Fe-BTC material was carried out as control experiment to evaluate possible interferences between material and enzymatic activity. No activity was detected for LC-free Fe-BTC MOF and LC-free ZIF-zni. All activity measurements were carried out at least in triplicate. Specific activity (U/mg) was calculated through the following formula:

$$\text{Specific activity} = \frac{\text{slope} \cdot V_{\text{cuvette}} \cdot 1000 \cdot \text{dilution factor}}{V_{\text{enzyme}} \cdot \epsilon_{\text{ABTS}^+} \cdot c(\text{enzyme})} = \left[\frac{\mu\text{mol}}{\text{mg} \cdot \text{min}} \right] = \left[\frac{\text{U}}{\text{mg}} \right]$$

One unit (U) of laccase activity is defined as the amount of enzyme required to convert 1.0 μmol of ABTS to ABTS^+ per minute at 25 °C.

Reuse of LC@Fe-BTC and LC@ZIF-Zni MOFs

A 10 mg sample of immobilized enzyme was suspended in 4.8 mL of 50 mM phosphate buffer (pH 6). The reaction was initiated by addition of a 0.25 mL aliquots of ABTS (250 μM in 50 mM phosphate buffer (pH 6) in a measuring cell for UV-Vis probe kept under stirring at 25°C. The reaction mixture was centrifuged at 3500 rpm, washed with buffer and ABTS again added to begin the next cycle.

Storage stability in buffers

The Fe-BTC MOFs stability was analyzed at pH 5 (citrate buffer), 7 (potassium phosphate buffer) and 9 (Tris-HCl) under different exposure conditions 1) static incubation at RT for 24 and 48 h and 2) agitated incubation at 250 rpm, RT, for 24 and 48 h. Storage stability solutions were prepared by making a 10 mg/mL MOF-buffer in either 10 or 100 mM buffer. For determination of the Fe^{3+} content leached during storage, a 1 mL sample of MOF suspension was centrifuged for 2 min, 10,000 rpm. The supernatant was then removed and analyzed by complexing with NaSCN with detection at 490 nm.

REFERENCES

- (1) Gascón, V.; Carucci, C.; Jiménez, M. B.; Blanco, R. M.; Sánchez-Sánchez, M.; Magner, E. Rapid In Situ Immobilization of Enzymes in Metal-Organic Framework Supports under Mild Conditions. *ChemCatChem* **2017**, *9* (7), 1182–1186. <https://doi.org/10.1002/cctc.201601342>.
- (2) Naseri, M.; Pitzalis, F.; Carucci, C.; Medda, L.; Fotouhi, L.; Magner, E.; Salis, A. Lipase and Laccase Encapsulated on Zeolite Imidazolate Framework: Enzyme Activity and Stability from Voltammetric Measurements. *ChemCatChem* **2018**, *10* (23), 5425–5433. <https://doi.org/10.1002/cctc.201801293>.
- (3) Brunauer, S.; Emmett, P. H.; Teller, E. Adsorption of Gases in Multimolecular Layers. *J. Am. Chem. Soc.* **1938**, *60* (2), 309–319. <https://doi.org/10.1021/ja01269a023>.
- (4) Barrett, E. P.; Joyner, L. G.; Halenda, P. P. The Determination of Pore Volume and Area Distributions in Porous Substances. I. Computations from Nitrogen Isotherms. *J. Am. Chem. Soc.* **1951**, *73* (1), 373–380. <https://doi.org/10.1021/ja01145a126>.
- (5) Bradford, M. M. A Rapid and Sensitive Method for the Quantitation of Microgram Quantities of Protein Utilizing the Principle of Protein-Dye Binding. *Anal. Biochem.* **1976**, *72* (1), 248–254. [https://doi.org/10.1016/0003-2697\(76\)90527-3](https://doi.org/10.1016/0003-2697(76)90527-3).
- (6) Molina, F.; Rueda, A.; Bosque-Sendra, J. M.; Megías, L. Determination of Proteins in the Presence of Imidazole Buffers. *J. Pharm. Biomed. Anal.* **1996**, *14* (3), 273–280.

[https://doi.org/10.1016/0731-7085\(95\)01615-5](https://doi.org/10.1016/0731-7085(95)01615-5).

PAPER IV

Immobilization of *Aspergillus sp.* laccase on hierarchical pure-silica MFI zeolite with embedded macropores

Davide Tocco ^{[a], [b], [c]}, Dorothea Wisser ^[a], Marcus Fischer ^[a], Wilhelm Schwieger ^[a], Andrea Salis ^{[b],[c]},
Martin Hartmann ^[a]

[a] Erlangen Center for Interface Research and Catalysis (ECRC), FAU Erlangen-Nürnberg, Egerlandstr. 3, 91058 Erlangen, Germany.

[b] Department of Chemical and Geological Sciences, University of Cagliari, Cittadella Universitaria, SS 554 bivio Sestu, 09042, Monserrato (CA) (Italy).

[c] Consorzio Interuniversitario per lo Sviluppo dei Sistemi a Grande Interfase (CSGI), via della Lastruccia 3, 50019, Sesto Fiorentino (FI), Italy.

Abstract: Laccase from *Aspergillus sp.* (LC) was immobilized on functionalized pure-silica hierarchical (microporous-macroporous) MFI zeolite (ZMFI). The obtained immobilized biocatalyst (LC@ZMFI) was characterized by X-ray diffraction (XRD), scanning electron microscopy (SEM), Fourier transform infrared spectroscopy (ATR-FTIR), N₂ adsorption/desorption isotherms, solid-state NMR spectroscopy and thermogravimetric analysis (TGA). The optimal pH, kinetic parameters (K_M and V_{max}), specific activity, as well as both storage and operational stability of LC@ZMFI were determined. The LC@ZMFI K_M and V_{max} values amount to 10.3 μM and 0.74 μmol · mg⁻¹ · min⁻¹, respectively. The dependence of specific activity on the pH for free and immobilized LC was investigated in the pH range of 2 to 7. The highest specific activity was obtained at pH = 3 for both free LC and LC@ZMFI. LC@ZMFI retained up to 50% and 30% of its original activity after storage of 21 and 30 days, respectively. Immobilization of laccase on hierarchical pure-silica MFI zeolite allows to carry out the reaction under acidic pH values without affecting the support structure.

Introduction

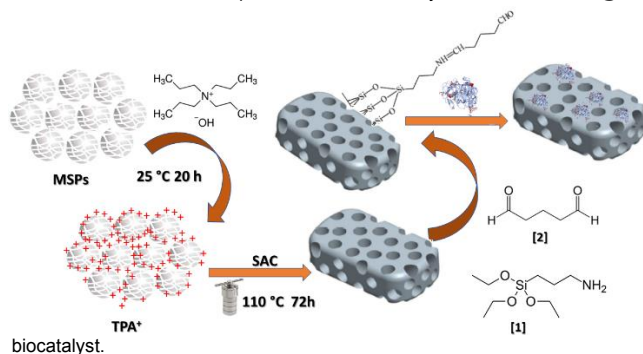
The demand of enzymes involved in industrial processes, such as food processing,^[1] leather treatment,^[2] textile,^[3] wastewater treatment,^[4] pharmaceutical chemistry,^[5] biofuels production,^[6,7] bioremediation,^[8] is continuously growing. The current global enzyme market is valued at \$5.5 billion and by 2023 it is predicted to reach \$7.0 billion.^[9] Laccases (E.C. 1.10.3.2, p-diphenol: dioxygen oxidoreductase) are active toward a wide range of substrates. To date, laccases (LCs) have been investigated for several applications, such as bleaching of denim and paper,^[10] removal of toxicants released during combustion processes,^[11] decolorization,^[12] removal of phenols from wastewaters,^[13] and biomass delignification.^[14] LCs typically comprise three domains and contain four copper ions arranged in mononuclear and trinuclear clusters.^[15] Substrate oxidation at the mononuclear site generates electrons that are transferred to the trinuclear site where O₂ is reduced to water.^[16] Although enzymes present several advantages compared with synthetic catalysts, their use in native form for industrial processes is often hampered by harsh reaction conditions (such as extreme pH values and temperatures), which could result in loss of catalytic activity.^[16] Immobilization on solid supports is considered an attractive technology for making enzymes suitable for biotechnological

applications.^[17] Indeed, immobilized enzymes usually display higher resistance to harsh environmental conditions, allow reusability and may result in improved thermal stability if compared to free enzymes.^[18] The enzymatic activity and stability depend on the choice of the support as well as the type (e.g. physical or covalent) of enzyme immobilization.^[17,19–21] Nowadays, a wide range of supports, e.g. mesoporous silica,^[13,17,22,23] xerogels,^[24] magnetic nanomaterials,^[25] agarose,^[26] nanofibrous polymers^[27] and metal organic frameworks^[28–32] have been explored as enzyme carriers. Among the several materials reported in the literature, due to their high surface area,^[33] and their well-defined pore systems, zeolites could in principle be suitable carriers for enzyme immobilization.^[34] However, most zeolites are microporous materials (pore size < 2 nm) and, thus, not suitable for enzyme immobilization. In the last 15 years, a new class of materials called hierarchically-ordered zeolites, constituted by a hierarchical pore system (bimodular or multimodular) has received increasing attention. Although the utilization of zeolites as enzyme carriers is limited by their narrow micropores, the synthesis of zeolitic systems with intracrystalline meso- or macropores can overcome this issue allowing to use zeolites as hosts for enzymes or other biomacromolecules.^[35–39] From the synthetic point of view, the introduction of macropores in zeolites is often hampered by several limitations such as the low wettability of the hard templates with zeolite precursors, poor thermal stability of the template under zeolite synthesis conditions, difficulties in controlling the thickness of the zeolitic walls, and the template removal after hydrothermal synthesis. Nevertheless, most of these drawbacks could be avoided using mesoporous silica particles (MSPs) as templates for macropores formation.^[35,40] Recently, a three step procedure to obtain a zeolite type MFI (the MFI topology consisting of intersecting straight and sinusoidal channels^[41]) with embedded macropores (with a diameter in the range 250 - 500 nm) has been reported by Machoke *et al.*^[35]

In this work, laccase from *Aspergillus sp.* was immobilized on a hierarchical micro/macroporous MFI zeolite to obtain LC@ZMFI biocatalyst with an immobilization efficiency of 79.4 %. The immobilization of the laccase was carried out post-synthetically as depicted in Scheme 1. The immobilized biocatalyst was characterized employing XRD, SEM, TGA FTIR, N₂

adsorption/desorption isotherms, solid-state Magic Angle Spinning (MAS) NMR spectroscopy and electron spin resonance (ESR) spectroscopy. The free LC, and LC@ZMFI biocatalysts were also characterized in terms of specific activity, kinetics (K_M and V_{max}) and (both storage and operational) stability. A V_{max} of $64.7 \mu\text{mol} \cdot \text{mg}^{-1} \cdot \text{min}^{-1}$ and $0.74 \mu\text{mol} \cdot \text{mg}^{-1} \cdot \text{min}^{-1}$ and a K_M of $11.2 \mu\text{M}$ and $10.3 \mu\text{M}$ were obtained at pH 3 for both free LC and LC@ZMFI, respectively. LC@ZMFI retained up to 50% and 30% of its original activity after storage of 21 and 30 days, respectively.

Scheme 1. Schematic representation of the synthesis of the LC@ZMFI



2. Results and Discussion

2.1 Samples characterization

The XRD patterns (Figure 1a) exhibit sharp reflections at $2\theta = 8^\circ$, 9° , 14° , 15° , 16° , 24° and 24.5° characteristic for zeolite MFI.^[35,42] The LC@ZMFI sample reveals a XRD pattern similar to the ZMFI parent material demonstrating that laccase immobilization did not affect the zeolite structure. The N_2 adsorption/desorption isotherms of ZMFI and LC@ZMFI samples are shown in Figure 1b. Both samples display a type I isotherm, which is characteristic for microporous materials.^[43] The ZMFI sample has a specific surface area (S_{BET}) of $534 \text{ m}^2 \text{ g}^{-1}$ that decreases to $297 \text{ m}^2 \text{ g}^{-1}$ for LC@ZMFI (Table 1). Similarly, the pore volume decreases from 0.27 (ZMFI) to $0.13 \text{ cm}^3 \text{ g}^{-1}$ (LC@ZMFI) suggesting the successful post-synthesis immobilization of the laccase on pure silica MFI zeolite.

Samples	^a S_{BET} ($\text{m}^2 \text{ g}^{-1}$)	^b V_p ($\text{cm}^3 \text{ g}^{-1}$)	IE (%)	L (mg g^{-1})
ZMFI	534	0.27	//	//
LC@ZMFI	297	0.13	79.4	9.72

^a Surface area (S_{BET}) obtained from N_2 adsorption/desorption isotherms;

^b Pore volume (V_p)

Thermogravimetric analysis (Figure 1c) confirm the high stability of MFI zeolite in the temperature range between 100°C and 500°C , where a negligible mass loss of 2% was observed. Similarly, no appreciable mass loss at $T > 500^\circ\text{C}$ is observed (data not shown). LC@ZMFI shows a mass loss of 4.3% and 4.5% in the ranges $100^\circ\text{C} - 220^\circ\text{C}$ and $220^\circ\text{C} - 445^\circ\text{C}$, respectively. At these

temperatures, the observed mass loss is likely due to the decomposition of organic molecules and of the immobilized enzyme. Although two clear distinct mass loss steps in those temperature ranges are observed, it is difficult to discriminate which one is ascribable to enzyme mass loss with absolute certainty. Finally, above 445°C , no mass loss for both ZMFI and LC@ZMFI samples is observed. Protein loading (L) of LC@ZMFI sample, quantified by means of the Bradford assay, is 9.72 mg g^{-1} (Table 1) while the immobilization efficiency (IE%, defined as the amount of immobilized protein relative to the total protein amount in the solution) is 79.4%.

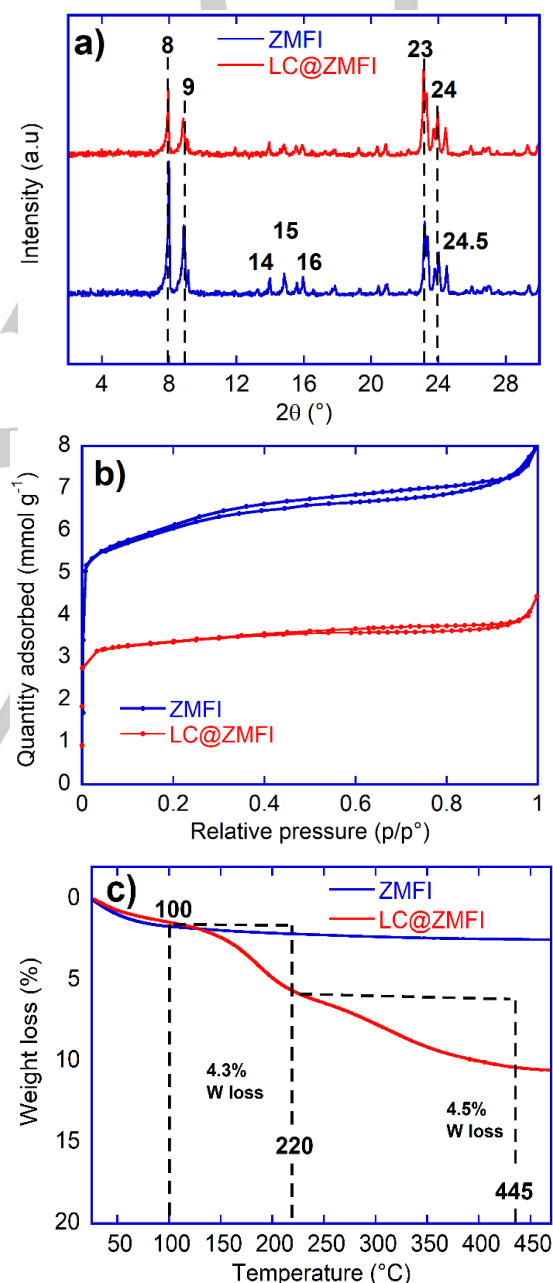


Figure 1. a) XRD patterns b) N_2 adsorption/desorption isotherms and c) thermogravimetric analysis (TGA) of ZMFI and LC@ZMFI in air.

The modification of zeolite MFI (ZMFI) was also monitored employing FT-IR and solid-state NMR spectroscopy. The FT-IR spectrum of the ZMFI (Figure 2) shows a broad band at about 1060 cm^{-1} due to Si-O-Si asymmetric stretching, a band at 960 cm^{-1} due to Si-OH stretching and one at 795 cm^{-1} due to Si-O-Si symmetric stretching. After surface modification with 3-aminopropyl-triethoxysilane (APTES), the band at 960 cm^{-1} disappears and a new band appears at 690 cm^{-1} that is ascribed to N-H bending vibrations. Additional evidence for the zeolite modification are the stretching vibration of C-H bonds at 2870 cm^{-1} , 2900 cm^{-1} and bending vibration of H-C-H bond at 1380 cm^{-1} appear confirming the reaction of free silanols with APTES.^[44-46] As a result of laccase immobilization, a band at 1647 cm^{-1} (C=N bonds), due to the reaction between the -ZMFI-CHO and laccase appears.

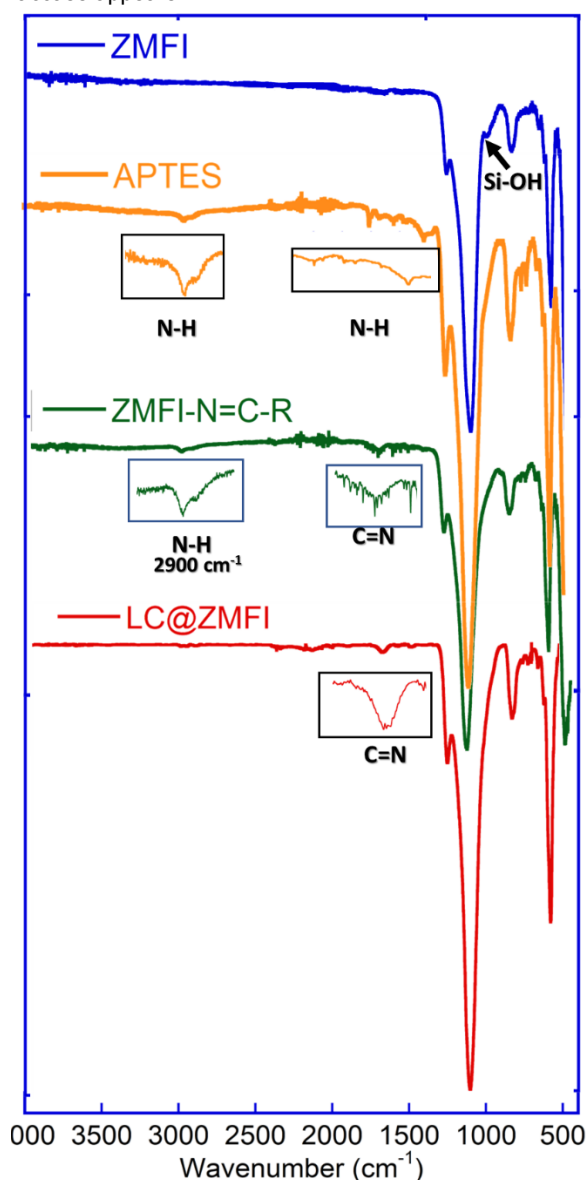


Figure 2. ATR-FT-IR spectrum of parent ZMFI zeolite, the with APTES modified sample and the LC@ZMFI biocatalyst.

^{13}C Cross Polarization (CP) solid-state NMR spectra clearly show the grafting of APTES onto the zeolite, by appearance of resonances at 10, 21, 42 and 58 ppm, characteristic for C_1 - C_3 and the amine carbon atom of APTES (Figure 3 a).^[47] After modification with glutaraldehyde, additional resonances appear at around 30 ppm, indicative for additional aliphatic groups, and at 62 ppm, assigned to the C=N functionality, but possibly overlapping with unreacted C-NH₂ amine groups from APTES. At 200 ppm, a particularly characteristic resonance for the aldehyde functionality appears. Note that we have not carried out ^{13}C CP MAS NMR on the laccase functionalized ZMFI, as the expected multitude of carbon signals of the enzyme would prohibit further detailed structural analysis. The degree of functionalization was evaluated quantitatively by ^{29}Si direct excitation, high power decoupling (HPDEC) MAS NMR spectra (Figure 3 b). T² and T³ sites corresponding to the surface-grafted species at approx. -50 and -68 ppm are visible, as well as a small amount of hydroxylated silicon sites (Q³) and non-hydroxylated Si(0Al) sites of the ZMFI framework.^[35] Integration of all resonances yields a degree of functionalization of ca. 6%. Note that this is overall a high degree of functionalization, as most silicon sites are buried inside the zeolite and are not accessible for APTES.

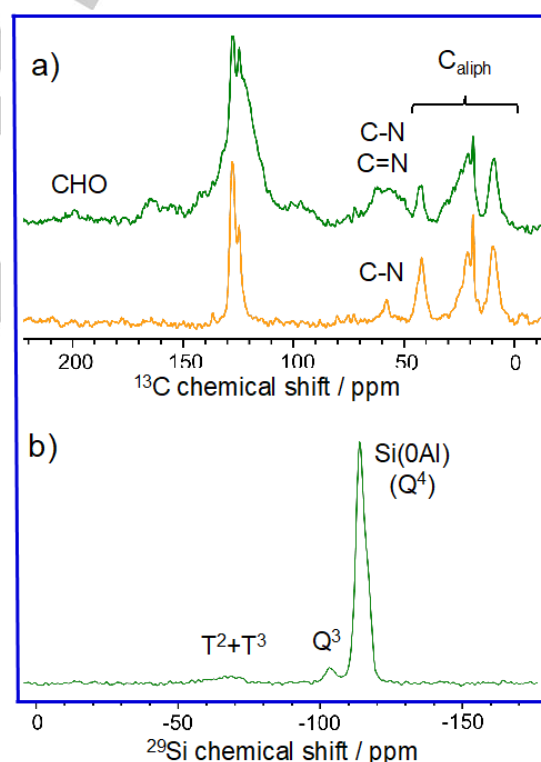


Figure 3: a) ^{13}C CP MAS NMR spectra of ZMFI-NH₂ (yellow) and ZMFI-N=C-R (green). Line broadening: 100 Hz. Signals between 110-130 ppm correspond to toluene from synthesis. b) ^{29}Si HPDEC MAS NMR spectrum of ZMFI-N=C-R. Line broadening: 50 Hz.

The successful immobilization of LC is furthermore confirmed by ESR spectroscopy (Figure 4), showing that the solid biocatalyst contains LC with no major effect on the close environment of the ESR-active Cu centers of the enzyme.

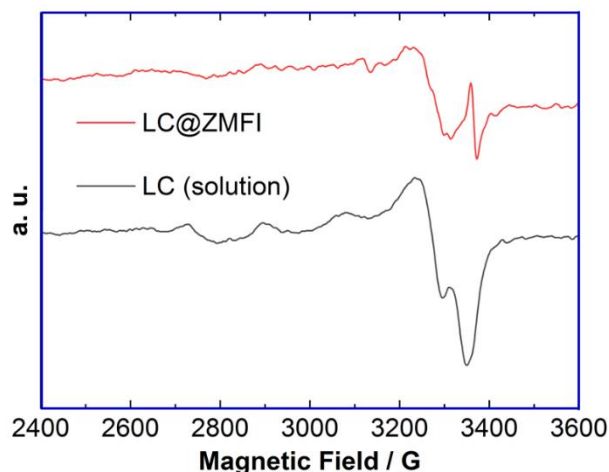


Figure 4. ESR spectra of laccase in solution as supplied and immobilized on ZMFI recorded at 100 K.

Scanning electron microscopy (SEM) images (Figure 5) of ZMFI show particles with the characteristic MFI morphology possessing additional macropores.^[48] After laccase immobilization the obtained LC@ZMFI sample retains its morphology in comparison to the parent ZMFI material (Figure 3b).

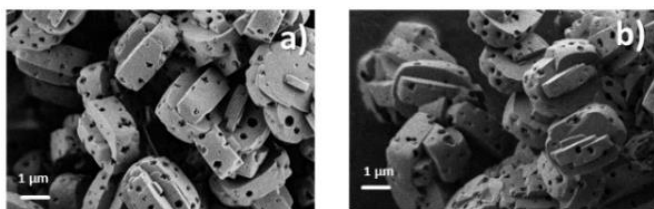


Figure 5. SEM images of a) ZMFI b) LC@ZMFI

2.2 Determination of the optimal pH for free LC and LC@ZMFI

The effect of pH on laccase activity was investigated in the pH range of 2 to 7 using 2,2'-azinobis-(3-ethylbenzothiazoline-6-sulfonate) diammonium salt (ABTS) as substrate. The different pH values were obtained by using different buffers, e.g. 100 mM citrate buffer (pH 2 - 4), 100 mM acetate buffer (pH range 5-6) and 100 mM phosphate buffer (pH 7). Both free LC and LC@ZMFI have a similar activity trend, i.e. exhibiting a maximum of catalytic activity at pH = 3 (Figure 7). The activity of LC@ZMFI decreased to almost 50 % at pH 5 and to 90% at pH 7 in comparison with the activity at pH 3. This trend is in agreement with what reported by Milleret *et al.* for *Aspergillus sp.* laccase immobilized by covalent bonding on nanozeolites.^[49] According to these results, the kinetic parameters K_M and V_{max} were determined at pH 3. This is in agreement with e.g. Wang *et al.*^[32,50,51]

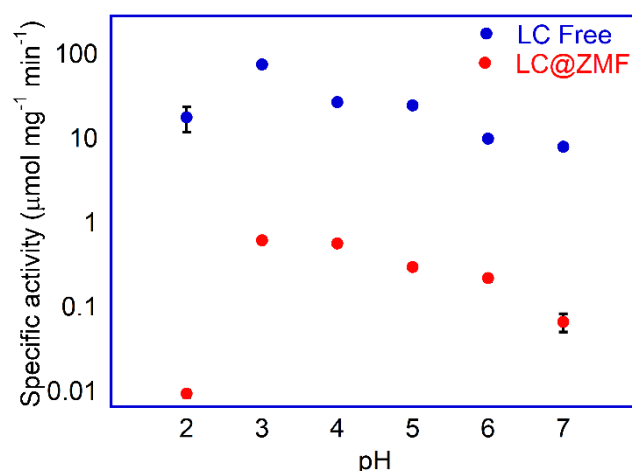


Figure 7. Specific activity as a function of pH for free laccase and @ZMFI

2.2 Determination of laccase kinetics.

The kinetics of the free and immobilized *Aspergillus sp.* laccase was studied in 0.1 M citrate buffer at pH=3 using 2,2'-azinobis-(3-ethylbenzothiazoline-6-sulfonate) diammonium salt (ABTS) as substrate (Figure 5). The Michaelis-Menten constant K_M slightly decreases upon immobilization, being 11.2 and 10.3 μM for free LC and LC@ZMFI, respectively (Table 2), suggesting that the immobilization results in a slight increase of enzyme-substrate affinity.

Table 2. Kinetic parameters of ZMFI and LC@ZMFI

Samples	K_M (μM)	V_{max} ($\mu\text{mol} \cdot \text{mg}^{-1} \text{min}^{-1}$)
Free LC	11.2	64.7
LC@ZMFI	10.3	0.74

The V_{max} instead, is strongly affected by immobilization, decreasing from 64.7 (free LC) to 0.74 $\mu\text{mol} \cdot \text{mg}^{-1} \text{min}^{-1}$ (LC@ZMFI). Such activity decrease has been previously observed for laccases immobilized on other supports.^[32] For example, the V_{max} of *Aspergillus sp.* laccase immobilized on Fe-BTC and ZIF-zni metal organic frameworks was 1.32 $\mu\text{mol} \text{min}^{-1} \text{mg}^{-1}$ and 0.17 $\mu\text{mol} \text{min}^{-1} \text{mg}^{-1}$ for LC@ZIF-zni and LC@Fe-BTC, respectively.^[52] However, a strict comparison of kinetic parameters with the present work cannot be done because the assays were carried out at different pH values. Indeed, Fe-BTC MOF is unstable under acidic conditions, so that LC@Fe-BTC was assayed at pH 5 although the optimal pH for *Aspergillus sp.* laccase is 3. Ameri *et al.* reported the immobilization by physical adsorption of laccase from *Trametes versicolor* onto two hierarchical zeolites called HR-Y and HR-Z. They obtained a V_{max} of 1.11 and 1.02 $\mu\text{mol} \text{min}^{-1}$ and a K_M of 0.26 and 0.31 mM for HR-Y and HR-Z, respectively.^[53] These results demonstrate that the kinetic parameters are affected by the nature of the support and the type (physical, covalent, entrapment, etc.) of immobilization. However, an accurate comparison of our results with those

reported in literature is difficult because the specific conditions of the activity assays (e.g. pH) are often different.

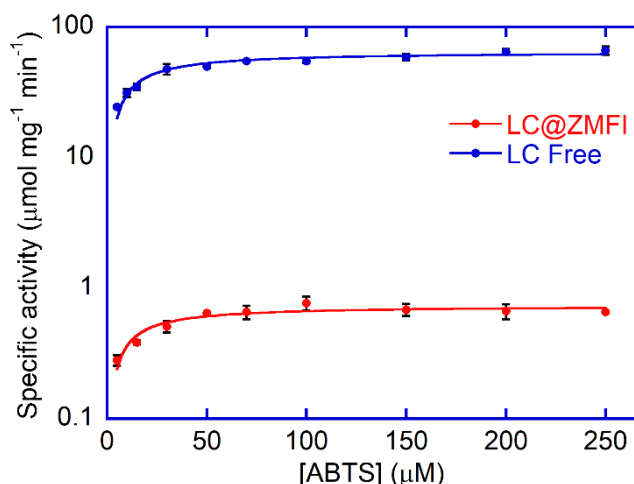


Figure 8. Michaelis-Menten plot of a) Free laccase and b) LC@ZMFI

2.4 Storage stability and reuse of LC@ZMFI

Immobilized enzymes are generally subject to a partial or even full inactivation after long storage times.^[54] The LC@ZMFI was stored at 4 °C and the residual activity was checked for 30 days. The storage stability of LC@ZMFI retained 52% of its initial activity at the 21st day and about 20% of its initial activity at the 30th day (Figure 7a). Similarly, Zheng *et al.* reported a laccase from *Trametes pubescens* immobilized on chitosan beads showed an activity retention of about 50% after 30 days.^[55] A better retention of activity (70% of initial activity after four weeks) in *Aspergillus sp.* laccase immobilized on magnetic silica nanoparticles was reported by Hu *et al.* after 30 days.^[53]

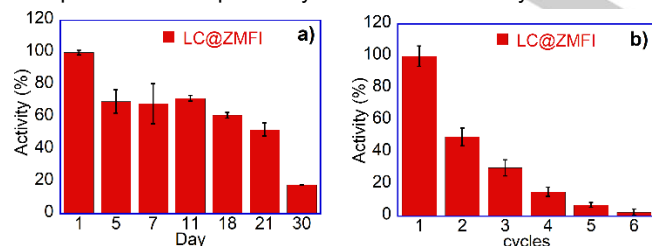


Figure 7. a) Storage stability of LC@ZMFI, activity normalized at 1.12 $\mu\text{mol min}^{-1} \text{mg}^{-1}$. b) Reuse of LC@ZMFI, activity normalized at 0.9 $\mu\text{mol min}^{-1} \text{mg}^{-1}$.

Biocatalyst reuse plays a crucial role for reducing the overall costs in industrial applications.^[52] Data in Figure 7b show the reuse studies of LC@ZMFI. LC@ZMFI retained 50.5% of its initial activity after the 1st reuse. Thereafter, it retained 30% and 15% of the initial activity at the 2nd and 3rd cycle respectively, which further decreases in the next cycles.

Conclusion

Aspergillus sp. laccase was immobilized onto a hierarchical (microporous-macroporous) MFI zeolite. The structure of MFI zeolite, characterized through XRD, SEM, TGA, and FTIR, was

not affected by LC immobilization. The values of immobilization efficiency and loading were 79.4% and 9.72 mg g^{-1} , respectively. pH strongly affected the activity of both the free LC and LC@ZMFI resulting in a maximum of specific activity at pH 3. The K_M of LC@ZMFI was a bit smaller than that of the free laccase, assayed at pH 3, suggesting a slight increase in enzyme-substrate affinity. V_{max} , instead, was much lower for LC@ZMFI compared with free laccase as a result of a partial inactivation likely due to the immobilization process. The immobilized biocatalyst retained around 70 % of its activity for 11 days, and 50 % after 21 days. It is well known that the enzymatic activity is highly influenced by pH. LCs generally display their optimum activity in the pH range of 3.0–5.5.^[56,57] Therefore, the choice of a stable material able to work at the enzymatic optimal pH is crucial. Although the use of MOFs as the enzymatic carriers is widely described in the literature, recent studies have shown that MOFs are not stable at low pH,^{[58][32]} where LCs exhibit maximum activity. The use of the pure silica hierarchical zeolite allows to carry out the reaction under the optimal pH of laccase avoiding the dissolution of the support.

Previous works reported the enzymatic immobilization on different zeolites.^[52,59] However, those systems are often affected by mass transfer limitations. To date only few works regard enzymes immobilized on hierarchical zeolites have been reported in literature.^[7,15] Further investigation in terms of mass transfer and enzymatic activity at different temperatures will be carried out using this support.

Experimental Section

Chemicals

Laccase from *Aspergillus sp.* (activity of $\geq 1000 \text{ LAMU g}^{-1}$); 2,2'-azinobis-(3-ethylbenzothiazoline-6-sulfonate) diammonium salt ($\geq 98\%$) (ABTS); sodium hydroxide, NaOH; sodium phosphate, monobasic NaH_2PO_4 (99%); sodium phosphate dibasic, Na_2HPO_4 (99%); Bradford reagent; HCl (37%); acetic acid (99%); sodium acetate (anhydrous) ($\geq 99.0\%$); citric acid ($\geq 99.5\%$); (3-Aminopropyl) triethoxysilane (APTES) (99.0%); glutaraldehyde (50% solution in water); cetyltrimethylammonium bromide (CTAB) (98 %); ethanol (96% technical grade) were purchased from Sigma-Aldrich (Germany). TPAOH solution (40 wt% technical grade, from Clariant (Germany). Tetraethyl orthosilicate (TEOS, 98 %) from Alfa Aesar. All reagents were used as received without further purification. Deionized water was used to prepare all aqueous solutions.

Synthesis of MFI-Type zeolite

The synthesis MFI-Type zeolite was carried out following the procedure reported by Machoke *et al.*^[13] Briefly, in each crucible 250 mg of mesoporous silica particles (MSPs) and 340 mg of TPAOH solution (40 wt% technical grade) were mixed and dried at RT (20 °C) for 20h. First, the MSPs have been weighted and then TPAOH has been added dropwise. Afterwards, the mix of reaction was gently mixed with a spatula and transferred into a Teflon-lined stainless-steel autoclave (45 mL) filled with 24 mL of

deionized water. Thereafter, the autoclave was closed and kept in an oven at 383 K for 72h. The white powder was recovered by filtration, washed with deionized water, and dried overnight at 348 K. Finally, the TPA⁺ was removed at 823 K for 4 h under air flow.

Immobilisation of laccase on zeolite Type MFI

The immobilization of LC on ZMFI occurred via post-synthetic treatment according to Salis *et al.*^[60] Briefly, 125 mg of zeolite type MFI (ZMFI) was added to 3.75 mL of dry toluene, then 125 μ L of 3-aminopropyltrimethoxysilane (APTS) was added to the suspension. The mixture was heated under reflux for 15 h. The zeolite-APTS was collected by filtration, washed with acetone, and dried overnight at room temperature under vacuum. Glutaraldehyde-activated (ZMFI-NH=CH) was prepared by soaking 125 mg ZMFI-NH₂ in a mixture of 100 μ L 50% aqueous glutaraldehyde and 2.75 mL 0.1M phosphate buffer solution (pH = 7.5) for 1 h. The carrier was washed twice with 5 mL of the same buffer for 30 min under stirring, centrifuged and the washing liquors removed. The wet solid was immediately used for laccase immobilisation. Finally, the LC immobilization was carried out mixing a in sodium phosphate buffer (100 mM and pH 8.0) with the modified zeolite. the result suspension was stirred for 2 h. The obtained solid (LC@ZMFI) was recovered by centrifugation at 4000 rpm for 4 min, washed 3 times with deionised water and dried at room temperature.

Characterization of ZMFI and LC@ZMFI samples

Thermogravimetric analysis (TGA) was carried out by means of a TA instruments TGA 2950 in a temperature range from 25 °C to 700 °C and a heating ramp of 5 °C min⁻¹, under synthetic air flow (flow rate = 40 mL min⁻¹). Scanning electron microscopy (SEM) analysis was performed by using a Carl-Zeiss Gemini Ultra 55 microscope with an acceleration voltage of 1 kV. Attenuated total reflectance Fourier transform infrared (ATR-FTIR) spectra were recorded using a Jasco FT/IR 4100 equipped with a PIKE GladiATR accessory with a single reflection diamond prism over the wavelength range, 4000 to 500 cm⁻¹. N₂ adsorption/desorption isotherms were recorded at 77 K using an ASAP 2010 (Micromeritics). Samples were firstly degassed under vacuum for 24 h at 80 °C. The Brunauer–Emmett–Teller (BET)^[61] and the Barret–Joyner–Halenda (BJH)^[62] methods were used to calculate the specific surface area, the pore volume, and the pore size distribution. A Panalytical X'Pert PRO diffractometer with an X'Celerator line detector was used for X-ray diffraction (XRD) experiments with Cu K α radiation. The data were collected with a 2 θ step size of 0.013 ° from 2 ° to 80 ° and an accumulation time of 10.16 s. A Jasco V-650 UV-Vis spectrophotometer was used for enzymatic activity tests.

Solid-state NMR spectra were recorded on a 500 MHz (11.7 T) wide-bore Agilent DD2 spectrometer in a 3.2 mm zirconia rotor. ²⁹Si HPDEC spectra were acquired at 10 kHz MAS rate, by applying a $\pi/2$ pulse of 3.5 μ s, followed by 86 kHz spinal-64 ¹H decoupling. 1200 scans were recorded with a recycle delay of 150 s. ¹³C CP MAS NMR spectra were acquired at 15 kHz MAS rate.

¹H 2.5 μ s pulse on ¹H was followed by a linear ramp from 41 to 54 kHz, while keeping the ¹³C RF at 53 kHz. 86 kHz spinal-64 ¹H decoupling were applied during acquisition. 25000-33000 scans were averaged with a recycle delay of 2.5 s.

EPR spectra were measured at 100 K on a Bruker EMXmicro at a MW frequency of 9.44 GHz. 5 scans were accumulated at a MW power of 2.02 mW with an attenuation of 20 dB. Modulation amplitude was set to 9 G at a modulation frequency of 100 kHz.

Determination of encapsulation efficiency

Protein loading and Immobilisation efficiency of the immobilised biocatalysts, LC@ZMFI, were obtained by means of the Bradford assay.^[29,63] Briefly, the protein content was determined using the Bradford reagent (Bio-Rad) and BSA (bovine serum albumin) as the protein standard (20 mg L⁻¹). The calibration curve was built by preparing a set of BSA solutions in acetate buffer pH 5 100 mM at different concentrations (0.5-20 mg L⁻¹) from dilution of the standard solution. Then, a 0.5 mL aliquot of each solution was mixed to 0.5 mL of Bradford reagent in a glass cuvette. After exactly 10 min the absorbance of the solutions was measured at the wavelength of 595 nm.

The protein concentration in the supernatant was evaluated by measuring the absorbance (λ = 595 nm) of a mixture containing 0.5 mL of supernatant and 0.5 mL of Bradford reagent after 10 min of incubation. The amount of immobilised protein is calculated from the difference between the amount used for immobilisation and the amount that is in the supernatant. The immobilisation efficiency (IE%) is the percent ratio between the amount of immobilised protein and the amount of protein in the immobilising solution:

$$IE\% = (1 - [P]_f / [P]_0) \cdot 100\%$$

where [P]₀ and [P]_f are the initial and the final protein concentrations in the immobilising solution.^[29,63]

Determination of biocatalytic activity

The catalytic activities of LC@ZMFI were quantified by Jasco 650 UV-Vis spectrophotometry, at λ = 420 nm (25 °C). The activity measurement of LC@ZMFI was carried out adding 5 mg of LC@ZMFI in 2.845 mL of 100 mM citrate buffer at pH 3. The reaction started by adding to the mixture a volume of 0.150 mL ABTS 5 mM in a cuvette kept under stirring and at T = 25 °C. The blank was measured by mixing 2.845 mL of citrate buffer pH 3 100 mM with 5 mg of LC@ZMFI. The activity test of the ZMFI material was carried out as control experiment to evaluate possible interferences between the material and the enzymatic activity. No activity was detected for LC-free ZMFI. All activity measurements were carried out at least in triplicate. Specific activity (U mg⁻¹) was calculated through the following formula:

$$\text{Specific activity} = \frac{\text{slope} \cdot \text{Vcuvette} \cdot 1000 \cdot \text{dilution factor}}{\text{Venzyme} \cdot \epsilon \text{ABTS} \cdot c(\text{enzyme})} = \left[\frac{\mu\text{mol}}{\text{mg} \cdot \text{min}} \right] = \left[\frac{\text{U}}{\text{mg}} \right]$$

FULL PAPER

One unit (U) of laccase activity is defined as the amount of enzyme required to convert 1.0 μmol of 2,2'-azinobis-(3-ethylbenzothiazoline-6-sulfonate) diammonium salt (ABTS) to ABTS⁺ per minute at 25 °C.

Acknowledgements

DT thanks Deutsche Akademische Austauschdienst (DAAD) and MIUR (PON RI 2014-2020, Azione I.1 "Dottorati Innovativi con Caratterizzazione industriale"- DOT1304455 2) for financing his PhD scholarship and his research period abroad at FAU Erlangen-Nürnberg. AS thanks Financial support from Fondazione di Sardegna (FdS, F72F20000230007), and Regione Autonoma della Sardegna L.R. 7 RASSR79857.

Conflict of interest

The authors declare no conflict of interest.

Keywords: • Laccase • Enzyme activity • zeolite • enzyme immobilisation

- [1] C. Ottone, O. Romero, C. Aburto, A. Illanes, L. Wilson, *Compr. Rev. Food Sci. Food Saf.* **2020**, *19*, 595–621.
- [2] S. R. Couto, M. A. Sanroman, D. Hofer, G. M. Gübitz, *Eng. Life Sci.* **2004**, *4*, 233–238.
- [3] A. Zerva, S. Simić, E. Topakas, J. Nikodinovic-Runic, *Catalysts* **2019**, *9*, 1023.
- [4] A. Amari, F. M. Alzahrani, N. S. Alsaiani, K. M. Katubi, F. Ben Rebah, M. A. Tahoona, *Processes* **2021**, *9*, 774.
- [5] G. Li, J. Wang, M. T. Reetz, *Bioorg. Med. Chem.* **2018**, *26*, 1241–1251.
- [6] A. Salis, M. Monduzzi, V. Solinas, in *Ind. Enzym.*, Springer Netherlands, Dordrecht, **2007**, pp. 317–339.
- [7] D. Tocco, C. Carucci, M. Monduzzi, A. Salis, E. Sanjust, *ACS Sustain. Chem. Eng.* **2021**, *9*, 2412–2432.
- [8] F. Pitzalis, M. Monduzzi, A. Salis, *Microporous Mesoporous Mater.* **2017**, *241*, 145–154.
- [9] A. Tarafdar, R. Sirohi, V. K. Gaur, S. Kumar, P. Sharma, S. Varjani, H. O. Pandey, R. Sindhu, A. Madhavan, R. Rajasekharan, et al., *Bioresour. Technol.* **2021**, *326*, 124771.
- [10] J. O. Unuofin, *Ind. Crops Prod.* **2020**, *147*, 112251.
- [11] E. N. Prasetyo, S. Semlitsch, G. S. Nyanhongo, Y. Lemmouchi, G. M. Guebitz, *Chemosphere* **2016**, *144*, 652–660.
- [12] P. Zucca, E. Sanjust, *Molecules* **2014**, *19*, 14139–14194.
- [13] A. Salis, M. Pisano, M. Monduzzi, V. Solinas, E. Sanjust, *J. Mol. Catal. B Enzym.* **2009**, *58*, 175–180.
- [14] D. W. S. Wong, *Appl. Biochem. Biotechnol.* **2009**, *157*, 174–209.
- [15] S. Riva, *Trends Biotechnol.* **2006**, *24*, 219–226.
- [16] R. A. Sheldon, *ACS Sustain. Chem. Eng.* **2018**, *6*, 32–48.
- [17] E. Magner, *Chem. Soc. Rev.* **2013**, *42*, 6213.
- [18] M. Hartmann, X. Kostrov, *Chem. Soc. Rev.* **2013**, *42*, 6277.
- [19] U. showed how the CLEA(s) can be used as stable and recyclable biocatalysts. By precipitating with salt (i.e. ammonium sulphate) and an organic linker (i.e. glutaraldehyde) the enzyme molecule condensate and they can be aggregated together creating the CLEAs, L. Gardossi, E. Magner, *Chem. Soc. Rev.* **2009**, *38*, 453–468.
- [20] R. A. Sheldon, S. van Pelt, *Chem. Soc. Rev.* **2013**, *42*, 6223–6235.
- [21] M. Valldeperas, A. Salis, J. Barauskas, F. Tiberg, T. Arnebrant, V. Razumas, M. Monduzzi, T. Nylander, *Curr. Opin. Colloid Interface Sci.* **2019**, *44*, 130–142.
- [22] U. Hanefeld, L. Cao, E. Magner, *Chem. Soc. Rev.* **2013**, *42*, 6211.
- [23] Z. Zhou, M. Hartmann, *Chem. Soc. Rev.* **2013**, *42*, 3894.
- [24] J. R. Fernandez Caresani, A. Dallegre, J. H. Z. dos Santos, *J. Sol-Gel Sci. Technol.* **2020**, *94*, 229–240.
- [25] T. Wastewater, S. M. Siddeeg, M. A. Tahoona, W. Mnif, n.d.
- [26] P. Zucca, R. Fernandez-Lafuente, E. Sanjust, *Molecules* **2016**, *21*, 1577.
- [27] Z. Temoçin, M. İnal, M. Gökğöz, M. Yiğitoğlu, *Polym. Bull.* **2018**, *75*, 1843–1865.
- [28] L. Zhong, Y. Feng, G. Wang, Z. Wang, M. Bilal, H. Lv, S. Jia, J. Cui, *Int. J. Biol. Macromol.* **2020**, *152*, 207–222.
- [29] F. Pitzalis, C. Carucci, M. Naseri, L. Fotouhi, E. Magner, A. Salis, *ChemCatChem* **2018**, *10*, 1578–1585.
- [30] C. Carucci, L. Bruen, V. Gascón, F. Paradisi, E. Magner, *Langmuir* **2018**, *34*, 8274–8280.
- [31] M. Naseri, F. Pitzalis, C. Carucci, L. Medda, L. Fotouhi, E. Magner, A. Salis, *ChemCatChem* **2018**, *10*, 5425.
- [32] D. Tocco, C. Carucci, D. Todde, K. Shortall, F. Otero, E. Sanjust, E. Magner, A. Salis, *Colloids Surfaces B Biointerfaces* **2021**, *208*, 112147.
- [33] M. Hartmann, W. Schwieger, M. Thommes, *Adv. Mater. Interfaces* **2021**, *8*, 2100057.
- [34] A. Corma, V. Fornes, F. Rey, *Adv. Mater.* **2002**, *14*, 71–74.
- [35] A. G. Machoke, A. M. Beltrán, A. Inayat, B. Winter, T. Weissenberger, N. Kruse, R. Güttel, E. Spiecker, W. Schwieger, *Adv. Mater.* **2015**, *27*, 1066–1070.
- [36] T. Weissenberger, A. G. F. Machoke, B. Reiprich, W. Schwieger, *Adv. Mater. Interfaces* **2021**, *8*, 2001653.
- [37] M. Hartmann, M. Thommes, W. Schwieger, *Adv. Mater. Interfaces* **2021**, *8*, 2001841.
- [38] V. R. R. Marthala, L. Urmoneit, Z. Zhou, A. G. F. Machoke, M. Schmiele, T. Unruh, W. Schwieger, M. Hartmann, *Dalt. Trans.* **2017**, *46*, 4165–4169.
- [39] S. Mitchell, J. Pérez-Ramírez, *Catal. Today* **2011**, *168*, 28–37.
- [40] T. Weissenberger, B. Reiprich, A. G. F. Machoke, K. Klühspies, J. Bauer, R. Dotzel, J. L. Casci, W. Schwieger, *Catal. Sci. Technol.* **2019**, *9*, 3259–3269.
- [41] T. L. Maesen, M. Schenk, T. J. Vlugt, B. Smit, *J. Catal.* **2001**, *203*, 281–291.
- [42] M. Okamoto, Y. Osafune, *Microporous Mesoporous Mater.* **2011**, *143*, 413–418.
- [43] M. Thommes, K. Kaneko, A. V. Neimark, J. P. Olivier, F. Rodriguez-Reinoso, J. Rouquerol, K. S. W. Sing, *Pure Appl. Chem.* **2015**, *87*, 1051–1069.
- [44] M. Weigler, M. Brodrecht, H. Breitzke, F. Dietrich, M. Sattig, G. Buntkowsky, M. Vogel, *Zeitschrift für Phys. Chemie* **2018**, *232*, 1041–1058.
- [45] A. Salis, M. Pisano, M. Monduzzi, V. Solinas, E. Sanjust, *J. Mol. Catal. B Enzym.* **2009**, *58*, 175.
- [46] P. J. Larkin, in *Infrared Raman Spectrosc.* (Ed.: P.J.B.T.-I. and R.S. (Second E. Larkin), Elsevier, **2018**, pp. 1–5.
- [47] R. Boyd, G. Smith, in *Polym. Dyn. Relax.*, Cambridge University Press, Cambridge, **2001**, pp. 44–56.
- [48] A. H. Miller, A. de Vasconcellos, A. J. Fielding, J. G. Nery, *Appl. Catal. A Gen.* **2021**, *626*, 118361.
- [49] Z. Wang, D. Ren, S. Jiang, H. Yu, Y. Cheng, S. Zhang, X. Zhang, W. Chen, *BMC Biotechnol.* **2021**, *21*, 47.
- [50] H. R. Wehaidy, M. A. Abdel-Naby, H. M. El-Hennawi, H. F. Youssef, *Biocatal. Agric. Biotechnol.* **2019**, *19*, 101135.
- [51] A. P. M. Tavares, C. G. Silva, G. Dražić, A. M. T. Silva, J. M. Loureiro, J. L. Faria, *J. Colloid Interface Sci.* **2015**, *454*, 52–60.
- [52] A. Ameri, T. Taghizadeh, A. Talebian-Kiakalaieh, H. Foroortanfar, S. Mojtavavi, H. Jahandar, S. Tarighi, M. A. Faramarzi, *J. Taiwan Inst. Chem. Eng.* **2021**, *120*, 300–312.
- [53] M. Fernández-Fernández, M. Á. Sanromán, D. Moldes,

- Biotechnol. Adv.* **2013**, *31*, 1808–25.
- [54] F. Zheng, B.-K. Cui, X.-J. Wu, G. Meng, H.-X. Liu, J. Si, *Int. Biodeterior. Biodegradation* **2016**, *110*, 69–78.
- [55] J. Hu, B. Yuan, Y. Zhang, M. Guo, *RSC Adv.* **2015**, *5*, 99439–99447.
- [56] M. D. J. Velásquez-Hernández, R. Ricco, F. Carraro, F. T. Limpoco, M. Linares-Moreau, E. Leitner, H. Wiltche, J. Rattenberger, H. Schröttner, P. Frühwirt, et al., *CrystEngComm* **2019**, *21*, 4538–4544.
- [57] D. Bůžek, S. Adamec, K. Lang, J. Demel, *Inorg. Chem. Front.* **2021**, *8*, 720–734.
- [58] T. Hashem, E. P. Valadez Sanchez, E. Bogdanova, A. Ugodchikova, A. Mohamed, M. Schwotzer, M. H. Alkordi, C. Wöll, *Membranes (Basel)*. **2021**, *11*, 1–12.
- [59] V. Smeets, W. Baaziz, O. Ersen, E. M. Gaigneaux, C. Boissière, C. Sanchez, D. P. Debecker, *Chem. Sci.* **2020**, *11*, 954–961.
- [60] S. Brunauer, P. H. Emmett, E. Teller, *J. Am. Chem. Soc.* **1938**, *60*, 309–319.
- [61] E. P. Barrett, L. G. Joyner, P. P. Halenda, *J. Am. Chem. Soc.* **1951**, *73*, 373–380.
- [62] M. M. Bradford, *Anal. Biochem.* **1976**, *72*, 248–254.
- [63] H. Li, F. Chen, *Saudi J. Biol. Sci.* **2017**, *24*, 797–802.

FULL PAPER

FULL

FULL PAPER

Page ■ – Page ■

WILEY-VCH

PAPER V

A study about the conformational changes and location of BSA upon immobilization on zeolitic imidazolate frameworks (ZIF-8 and ZIF-zni)

Davide Tocco,^[a] David Chelazzi,^[b] Andrea casini,^[b] Rosangela Mastrangelo,^[b] Andrea Salis^[a] and Piero Baglioni^[b]

[a] Mr. Davide Tocco, Prof. Andrea Salis
Dipartimento di Scienze Chimiche e Geologiche
Università degli Studi di Cagliari & CSGI (Consorzio per lo Sviluppo dei Sistemi a Grande Interfase)
s.s. 554 bivio Sestu, Monserrato (CA), I-09042, Italy

[b] Dr. David Chelazzi, Prof. P. Baglioni
Dipartimento di Chimica "Ugo Schiff"
Università degli Studi di Firenze & CSGI (Consorzio per lo Sviluppo dei Sistemi a Grande Interfase)
via della Lastruccia 3, Sesto Fiorentino (FI), I-50019, Italy
E-mail: baglioni@csqi.unifi.it email andrea

Supporting information for this article is given via a link at the end of the document.

Abstract: The enzymatic immobilization within Metal-Organic Frameworks has gained great attention in these last years. Nevertheless, the enzymatic location and its change in conformation after immobilization within MOFs are still poorly investigated. Commercial enzymes often show a very low grade of purity, and their enzymatic structure is still unknown, these aspects make tricky the investigation of their location conformation. In this regards a pure protein and well known was used as a model protein. Bovine serum albumin (BSA) was immobilized within two different zeolitic imidazolate frameworks (ZIF-zni and ZIF-8) through a one-pot synthesis carried out under mild conditions (room temperature and aqueous solution). The ZIF-zni, ZIF-8 and the BSA@ZIF-zni, BSA@ZIF-8 samples were characterized by X-ray diffraction, scanning electron microscopy, confocal laser scanning microscopy, thermogravimetric analysis, micro-FTIR and confocal Raman spectroscopy to characterize the MOF structures and evaluate the protein location in the materials. Moreover, the secondary structure and conformation changes of BSA due to its immobilization on both ZIF-zni and ZIF-8 were studied. Results showed that BSA seems to concentrate in domains of 5-40 μm , which form an extended network across the MOF. Additional information on changes in the BSA structure upon immobilization was extracted by the deconvolution of the amide I band in the reflectance spectra. Data showed that the crystalline content of BSA increases significantly when the protein is immobilized on the MOFs in BSA@ZIF-zni resulting in increased up to ~ 25% (β -sheets + α -helices), and a drastic reduction of β -turns.

Introduction

Metal-Organic Frameworks (MOFs) are porous coordination polymers constituted by a metal node and an organic ligand linked through coordination bonds.^[1] The first MOFs' publication dates back to 1989, but the term MOF was first used by Yaghi in 1995.^[2] Since then, the interest in these materials is steadily increased and numerous MOFs have been synthesized.^{[3][4] [5,6]} Due to their properties, such as high porosity (up to 90% free volume) and surface area (extending beyond 6000 $\text{m}^2 \text{g}^{-1}$),^[7] MOFs have been explored for several applications, like removal of water

pollutants,^[8] gas adsorption,^[9] catalysis,^[10] sensing, drug delivery,^[11] etc.^[8,12] Recently, MOFs have shown great potential as enzyme immobilization supports.^[13] The main advantages of immobilized versus free enzymes involve their higher stability to environmental changes (pH, temperature, etc.), the possibility to be easily separated from the reaction mixture and reused, and also their possible use in continuous processes.^[14,15] Compared to the other immobilization methods, enzyme immobilization on MOFs, obtained through either chemical (covalent attachment and cross linking) or physical methods (entrapment and adsorption),^[16] is especially advantageous as it allows the rapid and facile preparation of heterogeneous biocatalysts under mild conditions (in aqueous solution, moderate pH, atmospheric pressure and at room temperature) using low cost and commercially available starting materials.^[13,15,17-20] [15] Recent research on enzyme immobilization on MOFs has focused on zeolitic imidazolate frameworks (ZIFs), which are crystalline solids consisting of inorganic metal ions (e.g. Zn^{2+} , Co^{2+}) and organic imidazolate ligands with topologies based on those of tetrahedral zeolites.^[21] Lyu et al. (2014) firstly immobilized an enzyme (cytochrome c) in situ on a ZIF obtaining a 10-fold higher activity for the immobilized cytochrome c respect to the free enzyme.^[22] Since then, different approaches were used to find the best immobilization method to retain high enzymatic activity and stability.^[16] Among them, the encapsulation method has proved to be faster and cheaper than other methodologies, leading to suitable biocatalysts for industrial processes,^[23] with both high catalytic activity and thermal stability.^[24] For instance, Falcaro et al. encapsulated urease in ZIF-8 finding an increase of thermal stability compared to the free enzyme.^[25] In the context of biodiesel production, Rafiei et al. reported the synthesis of a heterogeneous biocatalyst by encapsulating *Candida rugosa* lipase into ZIF-67,^[26] while Adnan et al. encapsulated the lipase from *Rhizomucor miehei* within X-Shaped ZIF-8.^[27] Knedel et al. investigated the stability and selectivity at various temperatures and different organic solvents (ethanol and DMF) of the Cgl1 laccase from *Corynebacterium glutamicum* encapsulated in ZIF-8.^[28] Enzymatic co-immobilization in MOFs was demonstrated by

RESEARCH ARTICLE

Wu et al., who synthesized a multiple enzyme-embedded ZIF-8, utilized as a colorimetric sensor for glucose detection.^[29]

Despite these advances, two crucial open issues involve i. the location of the enzyme encapsulated within the MOF,^[15,30–32] and ii. the quantification of enzyme structure distortion due to its interaction with MOF support. The former has been so far mainly addressed by labelling enzymes with a marker such as the fluorescein isothiocyanate (FITC, able to react with the amino groups of most proteins yielding the fluorescein thiocarbamoyl)^[33] allowing for enzyme detection by confocal laser scanning microscopy (CLSM).^[34] Other techniques have also been reported,^[35] including the analysis of the enzyme@MOF morphology pre- and post-calcination by scanning electron microscopy (SEM).^[36] The latter aimed to address these two open and challenging topics, we investigated here for the first time the location of the model protein bovine serum albumin (BSA) during its immobilization on two zeolitic imidazolate frameworks: ZIF-zni and ZIF-8 (zinc metal ions connected through imidazole-based organic linker molecules). To this purpose, the samples were characterized using an extensive analytical setup able to achieve complementary tasks. XRD (X-ray Diffraction) was used to analyze the crystalline phases of the materials. SEM and CLSM analysis were employed to evaluate the morphological properties of the material. Chemical composition was determined through thermogravimetric analysis (TGA), whilst the spectroscopic characterization of BSA, ZIF-zni, ZIF-8, BSA@ZIF-zni and BSA@ZIF-8 was performed by attenuated total reflection Fourier transform infrared (ATR-FTIR), micro-FTIR and confocal Raman spectroscopy. In particular, micro-FTIR 2D imaging using a Focal Plane Array (FPA) detector was used to investigate the secondary structure and conformation changes of bovine serum albumin (BSA) due to its immobilization on both ZIF-zni (BSA@ZIF) and ZIF-8 (BSA@ZIF-8).

Results and Discussion

ZIF-zni and BSA modified MOFs (BSA@ZIF-zni) were characterized through X-ray diffraction (XRD). The XRD patterns (Fig.1A) confirm the formation of the ZIF-zni material, with characteristic peaks at 15°, 17°, 18°, 21°. Fig. 1B confirms the formation of the ZIF-8 material, with characteristic peaks at 7.4°, 10.5°, 12.8°, 14.8°, 16.6°, 18.2°. The XRD patterns obtained for BSA@ZIF-zni and BSA@ZIF-8 samples do not differ significantly from those of pure materials demonstrating that BSA does not meaningfully alter the structure of the MOFs. The ZIF-Zni and ZIF-8 textural properties like surface area and pore volume were characterized through nitrogen adsorption-desorption isotherms. Zni network topology is the densest of all known ZIF structures and is essentially nonporous.^[38,39] Results regarding ZIF-Zni show a non-porous material agreeing with what was reported in the literature.^[40] The network topology of ZIF-8 (SOD topology) is less dense compared with that of Zni. Data results confirm the isotherm typical type-I behavior for microporous materials for ZIF-8 (Table 1 SI). ZIF-8 had an S_{DR} of 1760 m² g⁻¹ that decreased by 7% in the presence of BSA (BSA@ZIF-8). Similarly, pore volume V_p decreased from 0.625 cm³ g⁻¹ (ZIF-8) to 0.582 cm³ g⁻¹ for BSA@ZIF-8. The encapsulation efficiencies (EE) of BSA into the MOFs were quantified through the Bradford assay (see ESI file). EE values for both BSA@ZIF-zni and BSA@ZIF-8 were 98% and 82%, respectively.

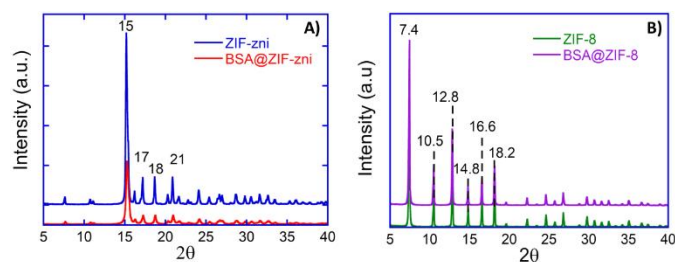
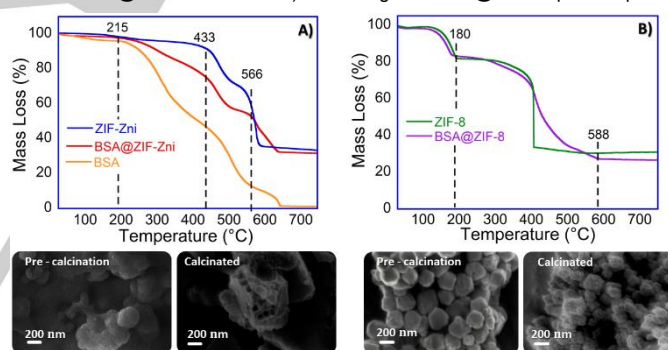


Figure 1. XRD patterns of A) ZIF-zni and BSA@ZIF-zni; B) ZIF-8 and BSA@ZIF-8

ZIF-zni and BSA@ZIF-zni were characterized by thermogravimetric analysis (Fig.2A). Both ZIF-zni and BSA@ZIF-zni samples show a low mass loss (~2.7%) over the range between 25°C - 215 °C due to humidity loss. ZIF-zni exhibited good thermal stability in air, up to 433 °C, in agreement with literature reports.^[13] ZIF-zni had mass losses of 37.7 % and 26 % over the ranges, 433 – 566 °C and 566 – 800 °C. The first mass loss can be attributed to the partial loss of ZIF crystallinity which is favored in oxidizing environments while the latter can be ascribed to the complete decomposition and collapse of the ZIF-zni structure. Thermogravimetric analysis of BSA@ZIF-zni was comparable with ZIF-zni except for the mass loss of 13.5 % over the temperature range, 215 – 344 °C assigned to the encapsulated protein molecules. (Table 1).

Figure 2. A) Thermogravimetric analysis (TGA) curve from 25 °C to 800 °C of ZIF-zni, BSA@ZIF-zni and BSA B) SEM images of BSA@ZIF-zni pre and post



calcination at 380 °C

Scanning electron microscopy (SEM) images (Figure 3) of ZIF-zni show a regular morphology with a rod shape similar to that of ZIF-7 reported in literature.^[41] The BSA immobilized into the support led to a change of particles morphology turn the material from rod shape to spherical one, in agreement with other works regarding immobilized enzymes as lipase and laccase on the same support.^[13,42] SEM characterization was carried out on ZIF-8 and BSA@ZIF-8. The results clearly show the expected rhombic dodecahedron geometry typical of ZIF-8 in *sod* phase. The same morphology was obtained for BSA@ZIF-8. These agree with other works reported in the literature. For example, Ricco et al. immobilized BSA on ZIF-8 obtaining the same material morphology.^[43] Liang et al. immobilized in situ different kinds of enzymes into ZIF-8. They demonstrated that the crystal morphology of Enzyme@ZIF-8 depends on the biomacromolecules. Indeed, typical rhombic ZIF-8 dodecahedron crystal morphology was observed in the case of ribonuclease A, lipase, urease, and lysozyme immobilization. Instead, the

RESEARCH ARTICLE

immobilization of ovalbumin, horseradish peroxidase, and trypsin resulted in leaves, flowers, and stars morphology respectively.^[44] Moreover, to investigate the location of the protein, SEM images were acquired after the material calcination at 360 °C for 2 hours (the temperature was chosen based on the thermal gravimetric analysis, Fig...). Due to the calcination the BSA@ZIF-zni

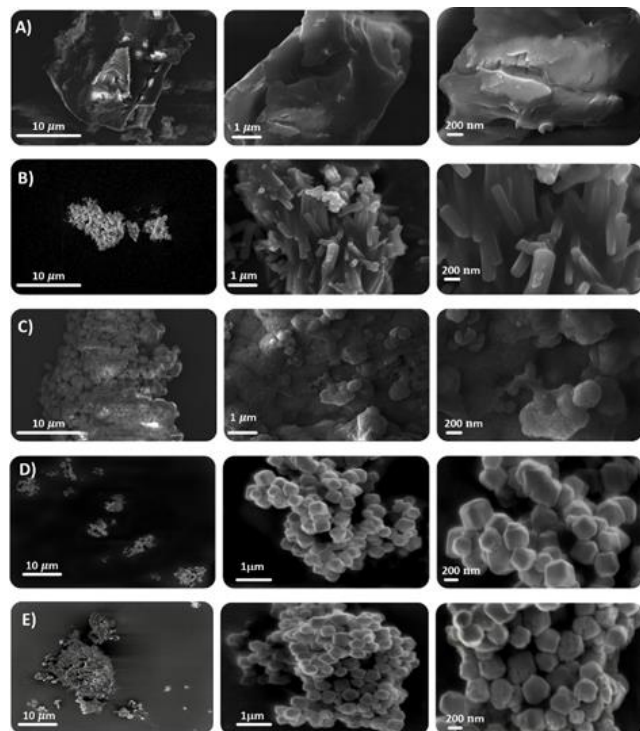


Figure 3. SEM images of A) BSA, B) ZIF-zni C) BSA@ZIF-zni D) BSA@ZIF-8 and E) ZIF-8

Confocal microscope images of FITC-BSA@ZIF-zni and FITC-BSA@ZIF-8 samples (Fig. 4) show a homogeneous distribution of BSA molecules within the MOFs. This result suggests that BSA could be both encapsulated within ZIFs structure and on the external surface of the material, in agreement with previous works of tagged enzymes by FITC immobilized on MOFs.^[24] The BSA immobilization post synthesis on ZIF-zni was carried out and the resulting material was analyzed by Confocal microscope. Data reported in Figure 4B show a more homogeneous protein distribution compared with encapsulation method.

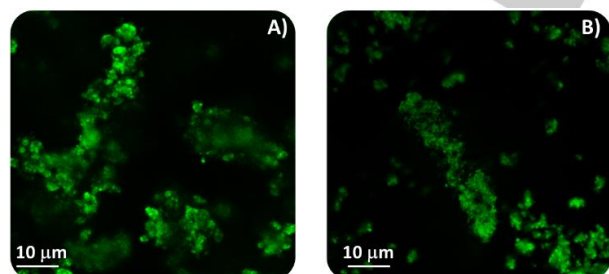


Figure 4. Confocal laser A) BSA-FITC@ZIF-zni and B) BSA-FITC@ZIF-8 samples.

Raman spectra of ZIF-zni, BSA@ZIF-zni, ZIF-8 and BSA@ZIF-8 samples are shown in Figure 5.^[45-47] The Raman spectrum of ZIF-8 showed intense bands at 176 cm⁻¹, 685 cm⁻¹, 1146 cm⁻¹, and 1458 cm⁻¹ ascribable to Zn-N stretching, imidazole ring

morphology turns from spherical to pitted rods with holes (Figure 2B).

puckering, C5-N stretching and methyl bending, respectively. The ZIF-zni spectrum showed a shift of ν Zn-N toward lower cm⁻¹ compared to ZIF-8. The Raman spectra obtained for BSA@ZIF-zni and BSA@ZIF-8 samples do not differ from those of pure materials demonstrating that BSA does not alter the structure of the MOFs.

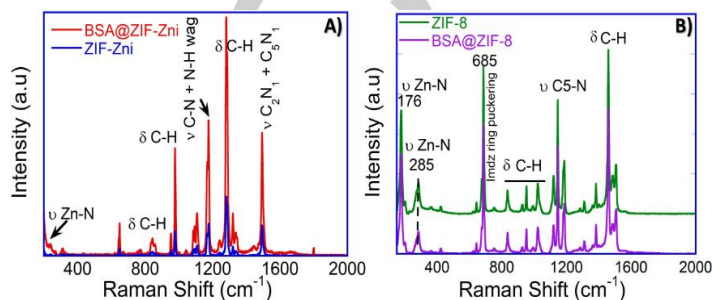


Figure 5. Raman spectrum of A) ZIF-zni, BSA@ZIF-zni and B) ZIF-8, BSA@ZIF-8. Wavenumber range from 150 to 2000 cm⁻¹.

FTIR 2D Imaging provided further information on the location of protein in the BSA@ZIF sample. Mapping the absorbance intensity (peak area) of the 3450-3200 cm⁻¹ and 1565-1525 cm⁻¹ regions, which correspond respectively to the central portion of amide A and to the amide II band of BSA, showed that the protein is found all over the MOF in BSA@ZIF (Figure S1 and LOCATION S2). In addition, details of the imaging maps at higher magnification highlighted that the protein seems to concentrate in domains of 5-40 μm, which form an extended network across the MOF surface, while such domains are not observed in the pure BSA sample (Figure S3). Imaging of amide A and amide II was preferred to amide I in order to avoid interferences from absorptions of ZIF in the 1720-1600 cm⁻¹ region, ascribed to overtone and combination bands of imidazole.^[48] Distribution was observed for concentration of the protein in micro-domains still observable in BSA@ZIF-8, even though not as evident as in BSA@ZIF-zni (Figure S4). Simply looking at the IR reflectance spectra, it is also possible to observe that the amide II band in BSA@ZIF has a clear redshift of ca. 25 cm⁻¹ compared to pure BSA (Figure S5). A similar red shift seems to occur also to amide I, even though its determination is less clear owing to modifications of the band in BSA@ZIF and its overlap with ZIF absorptions in the same region. Amide I derives mainly from C=O and C-N stretching vibrations, while amide II from N-H bending with some C-N and C-C stretching contribution; a redshift indicates bond elongation of these functional groups, which points to the formation of interactions between the protein and the MOF structure.

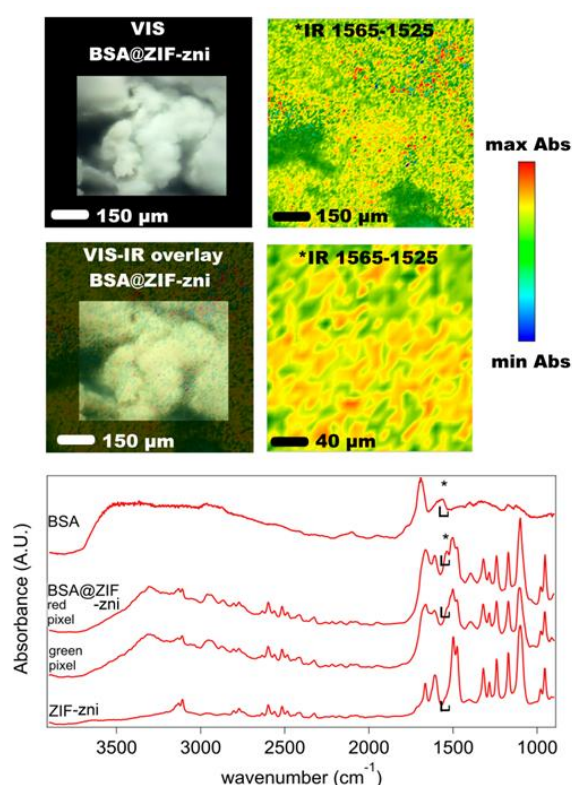


Figure 6. LOCATION MAPS. (Top panel, upper row) Visible (VIS) and FTIR 2D Imaging maps of the BSA@ZIF sample.

The IR maps were obtained imaging the absorbance intensity (peak area) of the amide II band of BSA in the 1565-1525 cm^{-1} region. (Top panel, lower row) Overlay of the VIS and IR maps, and detail of the IR map highlighting the micrometric domains where the amide II band is more intense (red pixels). (Lower panel) Reflectance spectra of ZIF, BSA and BSA@ZIF samples. The BSA and ZIF spectra were obtained on the pure BSA and ZIF samples, respectively, and are showed as references. The spectra of BSA@ZIF relate each to one pixel ($5.5 \times 5.5 \mu\text{m}^2$) of the IR maps of the top panel; two spectra are showed representative of, respectively, red and green pixels in the maps. The “**” and brackets highlight the amide II band and the spectral region that was imaged in the maps.

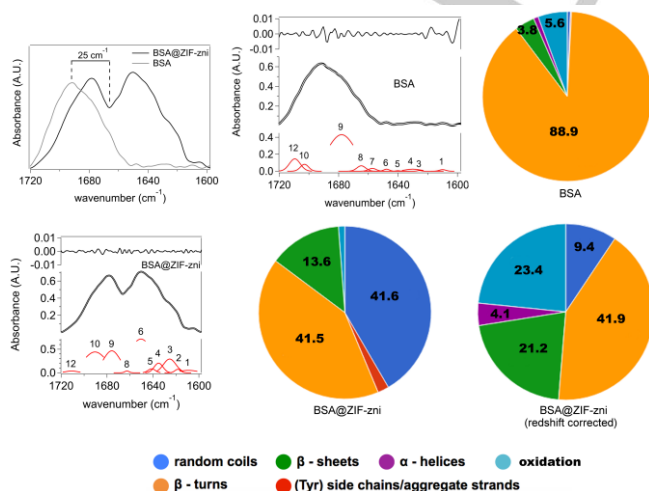


Figure 7. DECONVOLUTION REFL. (Top left) FTIR Reflectance spectra of BSA and BSA@ZIF (after subtraction of a representative ZIF spectrum) in the

1720-1600 cm^{-1} region (amide I). The 25 cm^{-1} redshift in the BSA@ZIF spectrum was evaluated comparing the regions of amide I and II (see also Figure S5) with those of BSA. (Top center, bottom left) Spectral deconvolution of the BSA and BSA@ZIF amide I bands. The bands' components are numbered as in Section 2.9, without taking into account the redshift for BSA@ZIF; the y-axis reports the absorbance of the components (red bands), the experimental spectrum (thick black line), the fitting curve (thin white line inside the experimental curve), and the fitting residuals (black line on top of the spectra). (Top right, bottom right and center) The average secondary structure for BSA and BSA@ZIF is reported in the pie charts, grouping the main structure types (relative error is ca. 0.05). For BSA@ZIF, the structure composition was also recalculated taking into account the 25 cm^{-1} redshift of the amide I components, considering the original component 12 as a baseline band.

Additional information on changes in the BSA structure upon immobilization was extracted by the deconvolution of the amide I band in the reflectance spectra. Figure 7 shows a comparison between the amide I band of BSA and that of BSA@ZIF after subtraction of the ZIF absorptions. Besides the aforementioned redshift, the band of the immobilized protein has a completely different shape with two maxima, a clear hint that structural modification has occurred. Before interaction with the MOF, amide I deconvolution indicates that BSA has a strong content in β -turns (~89%), with limited contribution from β -sheets (~4%). This is in contrast with studies in the literature where BSA structure, obtained from circular dichroism and calculations on the mean residual ellipticity, was found to be strongly based on α -helices (67%) with contributions from β -turns and extended chains (10% and 23% respectively).^[49] However, Lu et al. found, using ATR FTIR and spectral deconvolution, a significantly lower α -helices content and larger contributions from β -turns and random coils,^[50] considering also that contact pressure in ATR experiments can cause orientation of protein domains and an overestimation of crystalline phases,^[51,52] these findings are in less sharp contrast with the results reported here. Indeed, we found much closer values to Lu et al. when we analysed BSA in ATR, rather than reflectance mode (Figure S7). Another possible explanation is that, in principle, a partially derivative shape of the amide I band in the reflectance spectra might result in some overestimation of β -turns over α -helices, even though in our case amide I band distortion in the reflectance spectra of BSA did not seem to occur to a large extent (see Figure S1 and Figure S2). Most importantly to the purposes of this study, the crystalline content of BSA increases significantly when the protein is immobilized on the MOF in BSA@ZIF-zni (Figure 7). This is true even before correcting the wavenumbers of the amide I components to the 25 cm^{-1} redshift, and becomes more evident after correction, with a crystalline content increase up to ~25% (β -sheets + α -helices), and a drastic reduction of β -turns. Some increase in random coils occurred too, which accounts also for the formation of extended chains. Finally, the increase of oxidation bands can be ascribed to treatment with zinc nitrate (an oxidant) during the protein immobilization steps. A significant increase in the crystalline content of BSA@ZIF-zni and BSA@ZIF-8 was observed also when the samples were analyzed with ATR (Figure S7 and Figure S8), which overall corroborates our conclusion that BSA structure is ordered through immobilization on the MOF.] In the case of BSA@ZIF-8, the amide I band in the ATR spectra shows a marked redshift (ca. 50 cm^{-1}) from the protein's band before immobilization, i.e. even larger than in the Reflectance spectra of the same sample. A marked red shift of amide I,

indicating protein-MOF interactions, and protein structuration, was also observed on BSA@ZIF-8 (see Figure 8 and Figure S6). Interestingly, a more pronounced ordering of the protein by the MOF is observed than in BSA@ZIF-zni. In addition, oxidation bands were in this case almost absent.

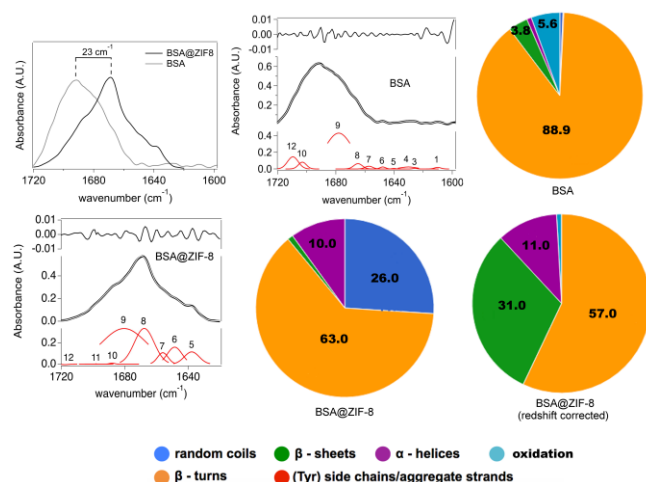


Figure 8. DECONVOLUTION REFL ZIF8. (Top left) FTIR Reflectance spectra of BSA and BSA@ZIF-8 (after subtraction of a representative ZIF-8 spectrum) in the 1720-1600 cm^{-1} region (amide I). The 23 cm^{-1} redshift in the BSA@ZIF-8 amide I is also evident before subtraction of the ZIF-8 absorptions (see Figure ZIF8 REDSHIFT). (Top center, bottom left) Spectral deconvolution of the BSA and BSA@ZIF-8 amide I bands. The bands' components are numbered as in Section 2.9, without taking into account the redshift for BSA@ZIF8; the y-axis reports the absorbance of the components (red bands), the experimental spectrum (thick black line), the fitting curve (thin white line inside the experimental curve), and the fitting residuals (black line on top of the spectra). (Top right, bottom right and center) The average secondary structure for BSA and BSA@ZIF-8 is reported in the pie charts, grouping the main structure types (relative error is ca. 0.05). For BSA@ZIF-8, the structure composition was also recalculated taking into account the 23 cm^{-1} redshift of the amide I components, considering the original component 12 as a baseline band.

Conclusion.

Among the enzyme immobilization methods reported in the literature, due to its rapid and mild condition immobilization procedure enzymatic encapsulation received immense attention in these last years. Although the location of the enzyme (within/onto) in the material has already been investigated through confocal laser scanning microscope (CLSM) and TGA coupled with SEM, these techniques do not precisely determine enzyme location. Moreover, the quantification of enzyme structure distortion due to its interaction with MOF support is poorly investigated. Here, it has been investigated for the first time the location of the model protein bovine serum albumin (BSA) during its in-situ immobilization within two different zeolitic imidazolate frameworks (ZIF-8 and ZIF-zni). Data showed that the crystalline content of BSA increases significantly when the protein is immobilized on the MOFs in BSA@ZIF-zni resulting in increased up to ~25% (β -sheets + α -helices), and a drastic reduction of β -turns. A marked red shift of amide I, indicating protein-MOF interactions, and protein structuration, was also observed on BSA@ZIF-8

Acknowledgements:

DT thanks MIUR (PON RI 2014-2020, Azione I.1 "Dottorati Innovativi con Caratterizzazione industriale"- DOT1304455 2) for financing his PhD scholarship. The authors are grateful to Dr Rita Gelli (University of Florence, Italy) for the Raman spectra acquisition.

Keywords: Zeolitic imidazolate Frameworks ZIFs • BSA • Immobilisation • boh • boh

- [1] S. R. Batten, N. R. Champness, X.-M. Chen, J. Garcia-Martinez, S. Kitagawa, L. Öhrström, M. O'Keeffe, M. Paik Suh, J. Reedijk, *Pure Appl. Chem.* **2013**, *85*, 1715–1724.
- [2] O. M. Yaghi, H. Li, *J. Am. Chem. Soc.* **1995**, *117*, 10401–10402.
- [3] B. F. Hoskins, R. Robson, *J. Am. Chem. Soc.* **1989**, *111*, 5962–5964.
- [4] A. R. Millward, O. M. Yaghi, *J. Am. Chem. Soc.* **2005**, *127*, 17998–17999.
- [5] Y. Yang, X. Arqué, T. Patiño, V. Guillermin, P.-R. Bliersch, J. Pérez-Carvajal, I. Imaz, D. MasPOCH, S. Sánchez, *J. Am. Chem. Soc.* **2020**, *142*, 20962–20967.
- [6] M. Sanchez-Sanchez, I. de Asua, D. Ruano, K. Diaz, *Cryst. Growth Des.* **2015**, *15*, 4498–4506.
- [7] H. Furukawa, N. Ko, Y. B. Go, N. Aratani, S. B. Choi, E. Choi, A. Ö. Yazaydin, R. Q. Snurr, M. O'Keeffe, J. Kim, et al., *Science (80-)*. **2010**, *329*, 424–428.
- [8] G. R. Delpiano, D. Tocco, L. Medda, E. Magner, A. Salis, *Int. J. Mol. Sci.* **2021**, *22*, 788.
- [9] G. Autie-Castro, M. A. Autie, E. Rodríguez-Castellón, C. Aguirre, E. Reguera, *Colloids Surfaces A Physicochem. Eng. Asp.* **2015**, *481*, 351–357.
- [10] K. Hemmer, M. Cokoja, R. A. Fischer, *ChemCatChem* **2021**, *13*, 1683–1691.
- [11] M.-X. Wu, Y.-W. Yang, *Adv. Mater.* **2017**, *29*, 1606134.
- [12] D. Tocco, C. Carucci, M. Monduzzi, A. Salis, E. Sanjust, *ACS Sustain. Chem. Eng.* **2021**, *9*, 2412–2432.
- [13] D. Tocco, C. Carucci, D. Todde, K. Shortall, F. Otero, E. Sanjust, E. Magner, A. Salis, *Colloids Surfaces B Biointerfaces* **2021**, *208*, 112147.
- [14] V. Gascón, M. B. Jiménez, R. M. Blanco, M. Sanchez-Sanchez, *Catal. Today* **2018**, *304*, 119–126.
- [15] V. Gascón, C. Carucci, M. B. Jiménez, R. M. Blanco, M.

- Sánchez-Sánchez, E. Magner, *ChemCatChem* **2017**, *9*, 1182–1186.
- [16] J. Boudrant, J. M. Woodley, R. Fernandez-Lafuente, *Process Biochem.* **2020**, *90*, 66–80.
- [17] P. D. Patil, G. D. Yadav, *ChemistrySelect* **2018**, *3*, 4669–4675.
- [18] R. J. Drout, L. Robison, O. K. Farha, *Coord. Chem. Rev.* **2019**, *381*, 151–160.
- [19] M. Naseri, F. Pitzalis, C. Carucci, L. Medda, L. Fotouhi, E. Magner, A. Salis, *ChemCatChem* **2018**, *10*, 5425–5433.
- [20] F. Pitzalis, C. Carucci, M. Naseri, L. Fotouhi, E. Magner, A. Salis, *ChemCatChem* **2018**, *10*, 1578–1585.
- [21] F. J. Uribe-romo, C. B. Knobler, M. O. Keeffe, O. M. Yaghi, *Acc. Chem. Res.* **2010**, *43*, 58–67.
- [22] F. Lyu, Y. Zhang, R. N. Zare, J. Ge, Z. Liu, *Nano Lett.* **2014**, *14*, 5761–5765.
- [23] R. Singh, M. Musameh, Y. Gao, B. Ozcelik, X. Mulet, C. M. Doherty, *J. Mater. Chem. C* **2021**, *9*, 7677–7688.
- [24] S. S. Nadar, V. K. Rathod, *Enzyme Microb. Technol.* **2018**, *108*, 11–20.
- [25] K. Liang, C. J. Coghlan, S. G. Bell, C. Doonan, P. Falcaro, *Chem. Commun.* **2016**, *52*, 473–476.
- [26] S. Rafiei, S. Tangestaninejad, P. Horcajada, M. Moghadam, V. Mirkhani, I. Mohammadpoor-Baltork, R. Kardanpour, F. Zadehahmadi, *Chem. Eng. J.* **2018**, *334*, 1233–1241.
- [27] M. Adnan, K. Li, L. Xu, Y. Yan, *Catalysts* **2018**, *8*, 96.
- [28] T. O. Knedel, E. Ricklefs, C. Schlüsener, V. B. Urlacher, C. Janiak, *ChemistryOpen* **2019**, *8*, 1337–1344.
- [29] X. Wu, J. Ge, C. Yang, M. Hou, Z. Liu, *Chem. Commun.* **2015**, *51*, 13408–13411.
- [30] W.-H. Chen, M. Vázquez-González, A. Zoabi, R. Abu-Reziq, I. Willner, *Nat. Catal.* **2018**, *1*, 689–695.
- [31] T. H. Wei, S. H. Wu, Y. Da Huang, W. S. Lo, B. P. Williams, S. Y. Chen, H. C. Yang, Y. S. Hsu, Z. Y. Lin, X. H. Chen, et al., *Nat. Commun.* **2019**, *10*, 1–8.
- [32] X. Li, D. Li, Y. Zhang, P. Lv, Q. Feng, Q. Wei, *Nano Energy* **2020**, *68*, 104308.
- [33] C. Wang, K. Liao, *ACS Appl. Mater. Interfaces* **2021**, *13*, 56752–56776.
- [34] M. Salgaonkar, S. S. Nadar, V. K. Rathod, *Int. J. Biol. Macromol.* **2018**, *113*, 464–475.
- [35] S. S. Nadar, L. Vaidya, V. K. Rathod, *Int. J. Biol. Macromol.* **2020**, *149*, 861–876.
- [36] M. Salgaonkar, S. S. Nadar, V. K. Rathod, *Int. J. Biol. Macromol.* **2018**, *113*, 464–475.
- [37] C. Zhou, M. Stepniewska, J. M. Sørensen, L. Scarpa, G. Magnacca, V. Boffa, T. D. Bennett, Y. Yue, *Microporous Mesoporous Mater.* **2018**, *265*, 57–62.
- [38] J.-C. Tan, B. Civaleri, A. Erba, E. Albanese, *CrystEngComm* **2015**, *17*, 375–382.
- [39] D. W. Lewis, A. R. Ruiz-Salvador, A. Gómez, L. M. Rodríguez-Albelo, F. X. Coudert, B. Slater, A. K. Cheetham, C. Mellot-Draznieks, *CrystEngComm* **2009**, *11*, 2272–2276.
- [40] J. C. Tan, T. D. Bennett, A. K. Cheetham, *Proc. Natl. Acad. Sci.* **2010**, *107*, 9938–9943.
- [41] Y.-S. Li, H. Bux, A. Feldhoff, G.-L. Li, W.-S. Yang, J. Caro, *Adv. Mater.* **2010**, *22*, 3322–3326.
- [42] M. Naseri, F. Pitzalis, C. Carucci, L. Medda, L. Fotouhi, E. Magner, A. Salis, *ChemCatChem* **2018**, *10*, 5425.
- [43] R. Ricco, P. Wied, B. Nidetzky, H. Amenitsch, P. Falcaro, *Chem. Commun.* **2020**, *56*, 5775–5778.
- [44] K. Liang, R. Ricco, C. M. Doherty, M. J. Styles, S. Bell, N. Kirby, S. Mudie, D. Haylock, A. J. Hill, C. J. Doonan, et al., *Nat. Commun.* **2015**, *6*, 4–11.
- [45] D. A. Carter, J. E. Pemberton, *J. Raman Spectrosc.* **1997**, *28*, 939–946.
- [46] G. Kumari, K. Jayaramulu, T. K. Maji, C. Narayana, *J. Phys. Chem. A* **2013**, *117*, 11006–11012.
- [47] L. M. Markham, L. C. Mayne, B. S. Hudson, M. Z. Zgierski, *J. Phys. Chem.* **1993**, *97*, 10319–10325.
- [48] K. I. Hadjiivanov, D. A. Panayotov, M. Y. Mihaylov, E. Z. Ivanova, K. K. Chakarova, S. M. Andonova, N. L. Drenchev, *Chem. Rev.* **2021**, *121*, 1286–1424.
- [49] R. C. Feldhoff, T. Peters, *Biochemistry* **1975**, *14*, 4508–4514.
- [50] R. Lu, W.-W. Li, A. Katzir, Y. Raichlin, H.-Q. Yu, B. Mizaikoff, *Analyst* **2015**, *140*, 765–770.

RESEARCH ARTICLE

- [51] Z. He, Z. Liu, X. Zhou, H. Huang, *Proteins Struct. Funct. Bioinforma.* **2018**, *86*, 621–628.
- [52] D. Badillo-Sanchez, D. Chelazzi, R. Giorgi, A. Cincinelli, P. Baglioni, *Sci. Rep.* **2019**, *9*, 17239.

WILEY-VCH

WILEY-VCH

Experimental Section

Reagents

Bovine Serum Albumin lyophilized powder, zinc nitrate hexahydrate (98%), imidazole ($\geq 99\%$), 2-Methylimidazole (99%), sodium hydroxide; Bradford reagent; Fluorescein isothiocyanate ($\geq 97.5\%$ HPLC) were purchased from Sigma-Aldrich (Milan Italy). All reagents were used as received without further purification. Milli-Q water (18.2 M Ω cm) was used to prepare all aqueous solutions.

Preparation of ZIF-zni and LC@ZIF-zni biocatalysts

BSA@ZIF-zni was synthesized according to a published procedure by Naseri et al.^[1] Briefly, a volume of 2 mL of an enzymatic solution (12.5 mg mL⁻¹) in distilled water was added to 10 mL of an imidazole (0.851g) solution in Milli-Q water, and 1 mL of a Zn(NO₃)₂ solution (3.1 M). The obtained mixture was stirred at room temperature for 45 min, and then a solid was collected by filtration and washed three times with Milli-Q water. Finally, the obtained sample was filtered dried at room temperature for 2-3 minutes and stored at 4°C. The pure ZIF-zni synthesis was carried out in the same way except for the fact that no protein was added.

Preparation of ZIF-8 and BSA@ZIF-zni biocatalysts

BSA@ZIF-8 was synthesized according to a published procedure by Wu et al.^[2] Briefly, a volume of 1 mL of BSA solution (25 mg mL⁻¹) in distilled water was added to 40 mL of a 2-methylimidazole (1.25 M), and 4 mL of a Zn(NO₃)₂ solution (0.31 M). The obtained mixture was stirred at room temperature for 45 min, and then a solid was collected by filtration and washed three times with Milli-Q water. Finally, the obtained sample was filtered dried at room temperature for 2-3 minutes and stored at 4°C. The pure ZIF-8 synthesis was carried out in the same way except for the fact that no protein was added.

Determination of encapsulation efficiency

Protein loading and encapsulation efficiency of the immobilised biocatalysts, BSA@MOF, were obtained by mean of Bradford assay.^[3] Briefly, the protein content was determined using the Bradford reagent (Bio-Rad) and BSA (bovine serum albumin) as the protein standard (20 mg/L). The calibration curve was built by preparing a set of BSA solutions in acetate buffer pH 5 100 mM at different concentrations (0.5-15 mg/L) from dilution of the standard solution. Then, a 0.5 mL aliquot of each solutions were mixed to 0.5 mL of Bradford reagent in a glass cuvette. After exactly 10 min the absorbance of the solutions was measured at the wavelength of 595 nm.

The protein concentration in the supernatant was evaluated by measuring the absorbance ($\lambda = 595$ nm) of a mixture containing 0.5 mL of supernatant and 0.5 mL of Bradford reagent after 10 min of incubation. The amount of immobilised protein is calculated from the difference between the amount used for immobilisation and the amount that is in the supernatant. Encapsulation efficiency (EE%) is the percent ratio between the amount of immobilised protein and the amount of protein in the immobilizing solution:

$$EE\% = (1 - [P]_f / [P]_0) \cdot 100\%$$

where $[P]_0$ and $[P]_f$ are the initial and the final protein concentrations in the immobilising solution.

Protein labelling by FITC

20 mg of BSA were dissolved in 10 mL of sodium carbonate buffer 0.1M pH 9. Afterwards the solution was stored for 6 hours at 4°C. Later, 50 μ L of FITC solution (1 mg/mL in DMSO) were added dropwise (aliquote of 5 μ L). The reaction was carried out at 4°C for 6 hours. The FITC excess was removed by dialysis against phosphate buffer 0.01M pH 7.4 (48h of dialysis changing the buffer every 24h).^[4]

XRD characterisation

A X'PERT Pro PANalytical diffractometer was used for X-ray diffraction (XRD) experiments with Cu K α radiation. The data were collected with a 2θ step size of 0.026 from 5 to 50° and an accumulation time of 20 s.

Scanning electron microscopy (SEM)

Analysis was performed by using. Samples were covered with by sputter coating for s and then analysed by SEM

FTIR analysis

BSA, MOFs (ZIF-zni, ZIF8), and BSA@MOFs (ZIF-zni, ZIF8) powders were analyzed (without any pre-treatment) with a Cary 670 FTIR spectrophotometer coupled to a Cary 620 FTIR microscope (Agilent Technologies), using a 15x Cassegrain objective. Measurements were carried out in reflectance mode over the powders, while background spectra were collected on a gold-plated surface. The experimental conditions were: spectral range of 3900–900 cm^{-1} , 512 scans for each acquisition, spectral resolution of 2 cm^{-1} , open windows. A 128 × 128 pixels Focal Plane Array (FPA) detector was used for the 2D μ -FTIR Imaging; the pixel size is 5.5 μm x 5.5 μm^2 , and each pixel provides an independent spectrum from the sample's surface. Each analysis delivers the spectra of a 700 × 700 μm^2 “tile” with 16384 independent spectra.

ATR-FTIR was carried out with the same IR microscope, using a single-element MCT detector and a Ge crystal slide inserted in the 15x Cassegrain objective. The experimental conditions were spectral range of 3900–450 cm^{-1} , 512 scans for each acquisition, spectral resolution of 2 cm^{-1} , open windows. The deconvolution of the powders' spectra was carried out using the multipeak fitting package of the Igor Pro software, version 7 (WaveMetrics, Inc), following a procedure reported elsewhere.^[5]The deconvoluted bands of amide I were assigned to the different protein secondary structures reported in the literature, ^[6,7] : 1) (Tyr) side chains/aggregated strands, 1605–1615 cm^{-1} ; 2) aggregate β -strand/intermolecular β -sheets (weak), 1616–1621 cm^{-1} ; 3) intermolecular β -sheets (strong), 1622–1627 cm^{-1} ; 4) intramolecular β -sheets (strong), 1628–1637 cm^{-1} ; 5) random coils/extended chains, 1638–1646 cm^{-1} ; 6) random coils, 1647–1655 cm^{-1} ; 7) α -helices, 1656–1662 cm^{-1} ; 8) β -turns, 1663–1670 cm^{-1} ; 9) β -turns, 1671–1685 cm^{-1} ; 10) β -turns, 1686–1696 cm^{-1} ; 11) intermolecular β -sheets (weak), 1697–1703 cm^{-1} ; 12) oxidation bands, 1704–1720 cm^{-1} .

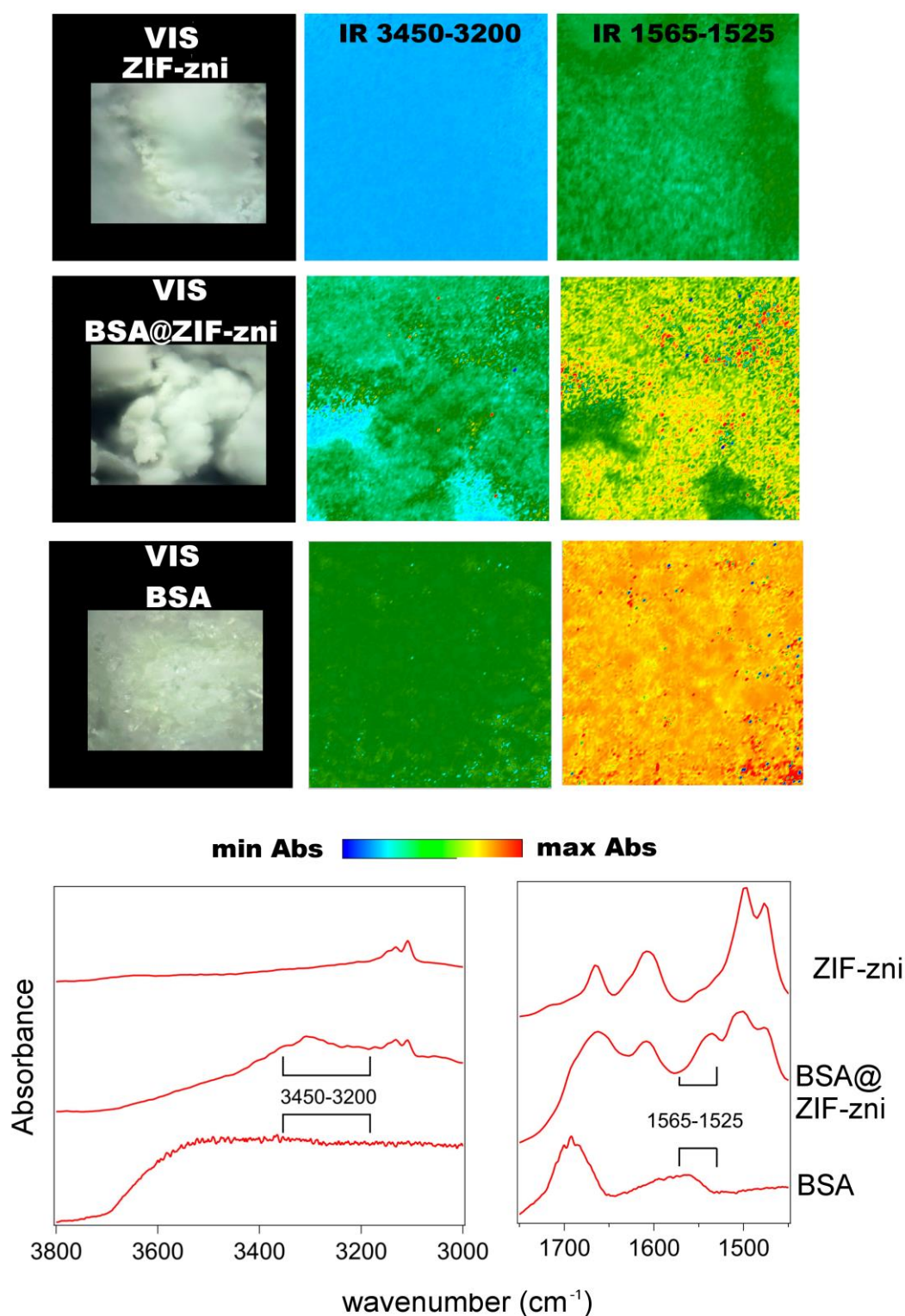


Figure S1. LOCATION S1. (Top panel) Visible (VIS) and FTIR 2D Imaging maps of the BSA, ZIF and BSA@ZIF samples. The IR maps ($700 \times 700 \mu\text{m}^2$ each) were obtained imaging the absorbance intensity (peak area) of the samples' spectra in the $3450\text{-}3200$ and $1565\text{-}1525 \text{ cm}^{-1}$ regions, which in BSA correspond to the amide A and amide II bands, respectively. (Bottom panel) Reflectance spectra of BSA, ZIF and BSA@ZIF samples. The spectra relate each to one pixel ($5.5 \times 5.5 \mu\text{m}^2$) of the IR maps of the top panel; for BSA@ZIF, the spectrum is representative of pixels with high absorbance in the maps (green pixels for the $3450\text{-}3200$ region, and red pixels for the $1565\text{-}1525 \text{ cm}^{-1}$ region).

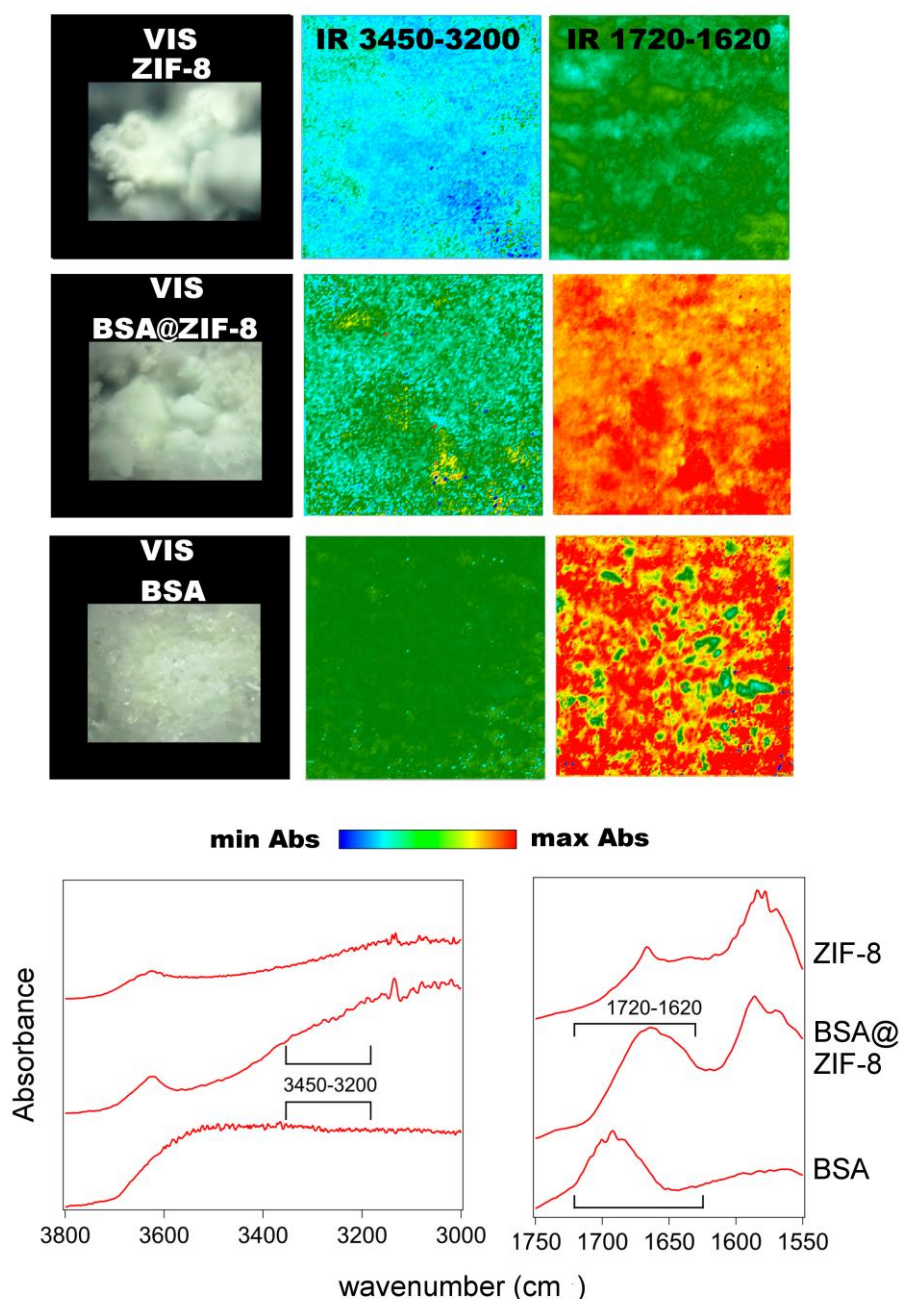


Figure S2 LOCATION MAPS ZIF8. (Top panel) Visible (VIS) and FTIR 2D Imaging maps of the BSA, ZIF-8 and BSA@ZIF-8 samples. The IR maps ($700 \times 700 \mu\text{m}^2$ each) were obtained imaging the absorbance intensity (peak area) of the samples' spectra in the $3450\text{-}3200$ and $1720\text{-}1620 \text{ cm}^{-1}$ regions, which in BSA correspond to the amide A and amide I bands, respectively. (Bottom panel) Reflectance spectra of BSA, ZIF-8 and BSA@ZIF-8 samples. The spectra relate each to one pixel ($5.5 \times 5.5 \mu\text{m}^2$) of the IR maps of the top panel; for BSA@ZIF-8, the spectrum is representative of pixels with high absorbance in the maps (green pixels for the $3450\text{-}3200$ region, and red pixels for the $1720\text{-}1620 \text{ cm}^{-1}$ region).

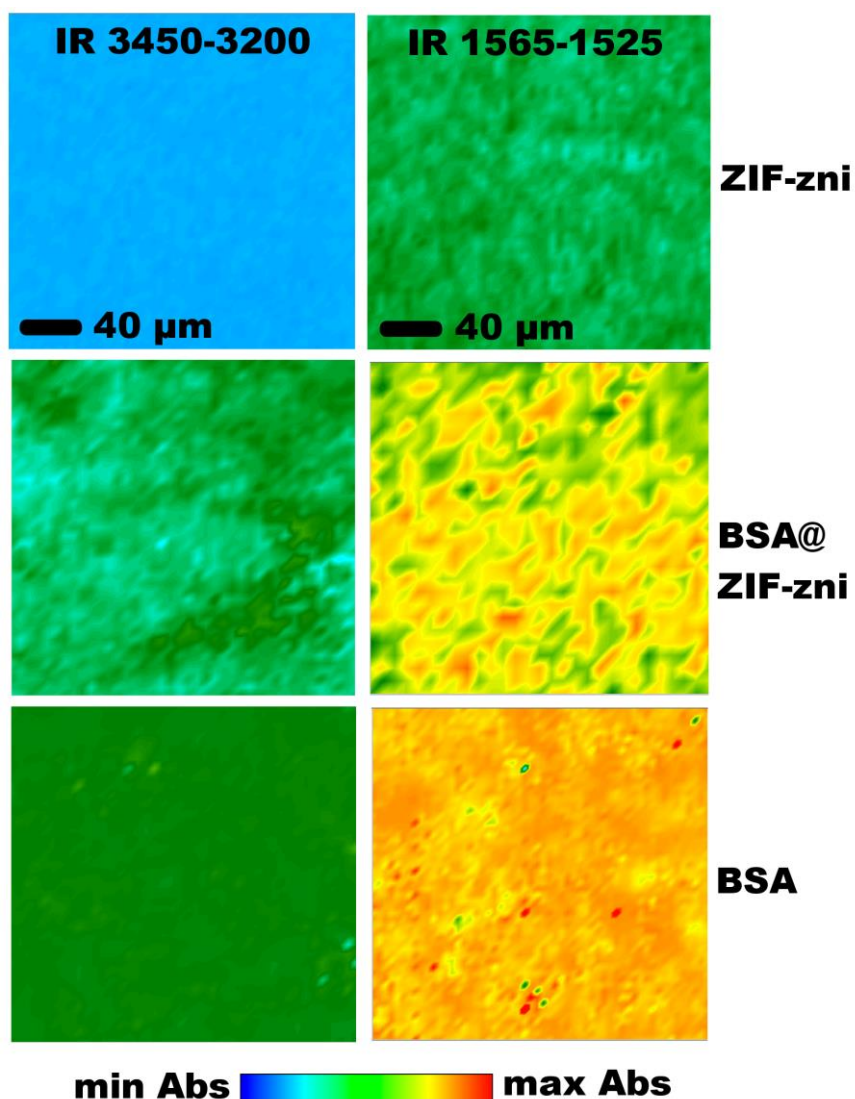


Figure S3 DECONVOLUTION ATR DETAIL. Details at higher magnification of the FTIR 2D Imaging maps of the BSA, ZIF-zni and BSA@ZIF-zni samples. The IR maps were obtained imaging the absorbance intensity (peak area) of the samples' spectra in the 3450-3200 and 1565-1525 cm^{-1} regions, which in BSA correspond to the amide A and amide II bands, respectively. The detail highlights the presence of concentrated protein domains of 5-40 μm in the BSA@ZIF-zni sample.

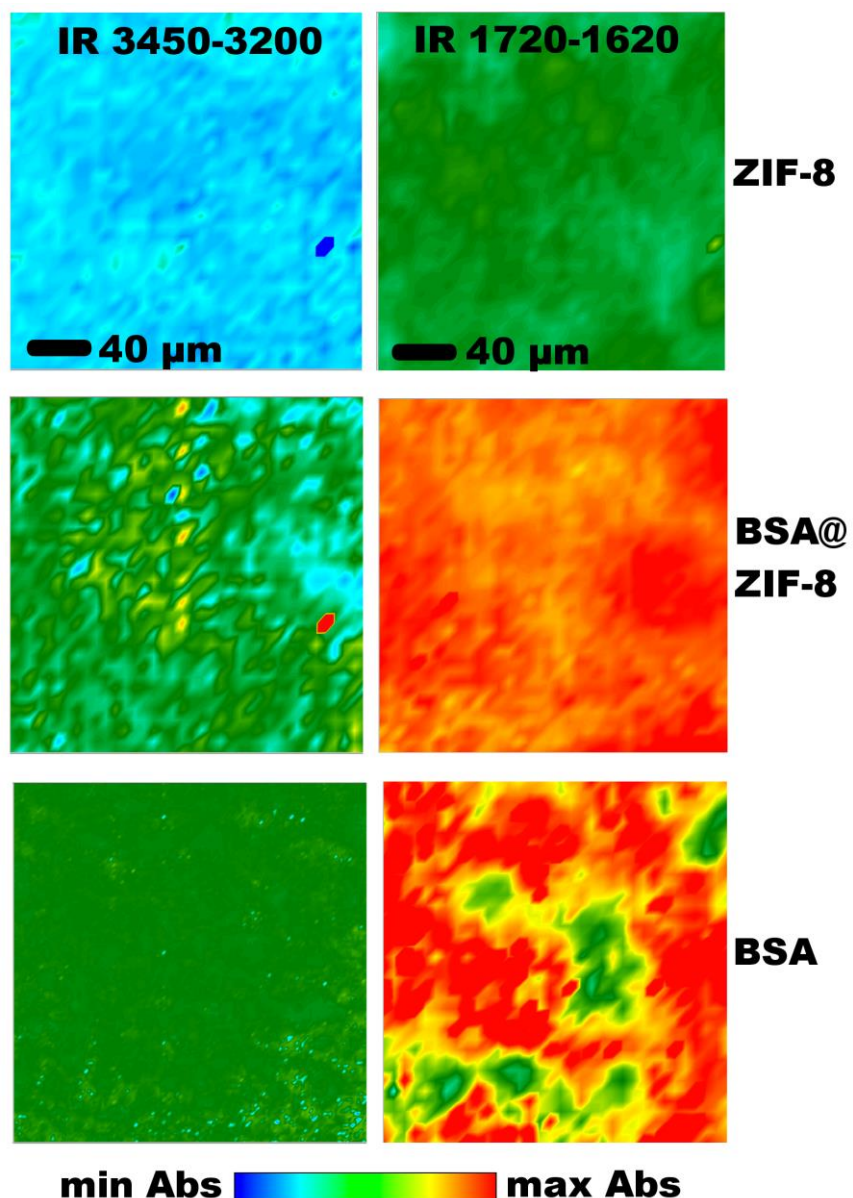
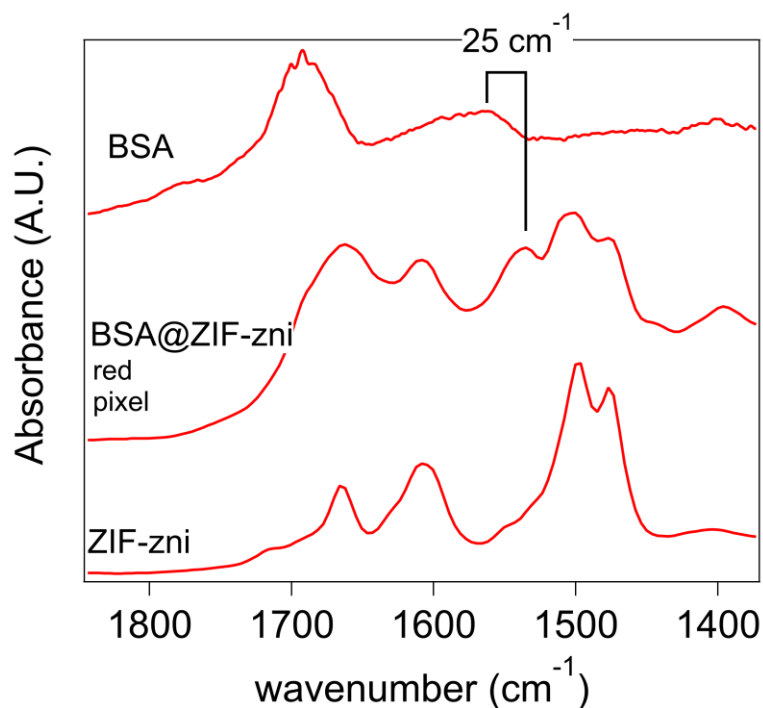


Figure S4 LOCATION SI. Details at higher magnification of the FTIR 2D Imaging maps of the BSA, ZIF-8 and BSA@ZIF-8 samples. The IR maps were obtained imaging the absorbance intensity (peak area) of the samples' spectra in the 3450-3200 and 1720-1620 cm^{-1} regions, which in BSA correspond to the amide A and amide II bands, respectively.



LOCATION SI DETAIL ZIF8 AMIDE II REDSHIFT. Detail of the FTIR reflectance spectra of ZIF, BSA and BSA@ZIF-zni samples. Each spectrum relates to one pixel ($5.5 \times 5.5 \mu\text{m}^2$) of the FTIR 2D Imaging maps showed in Figure LOCATION MAPS and Figure LOCATION SI. In particular, the BSA@ZIF-zni spectrum is representative of regions of the sample where the presence of BSA was more intense. The detail highlights the 25 cm^{-1} redshift of the BSA@ZIF-zni Amide II band as compared to the spectrum of the protein before immobilization on the MOF.

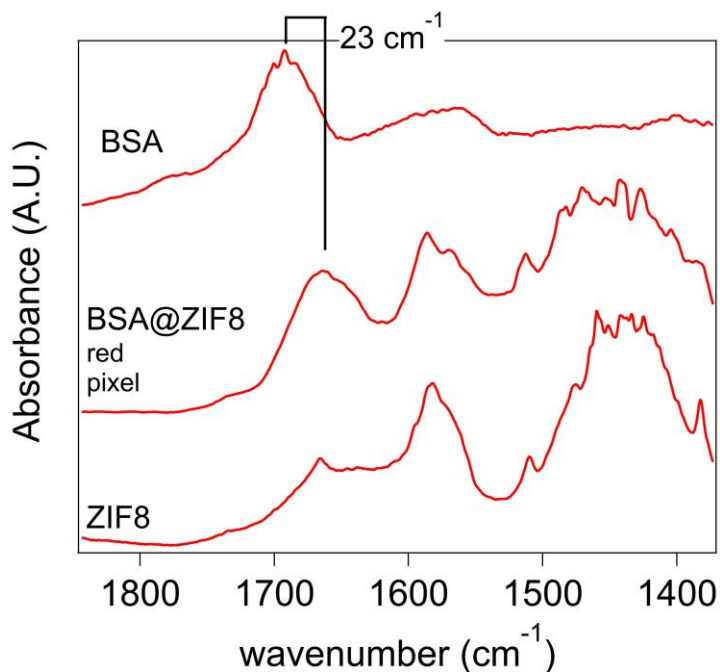


Figure S6. AMIDE II REDSHIFT. Detail of the FTIR reflectance spectra of ZIF8, BSA and BSA@ZIF8 samples. Each spectrum relates to one pixel ($5.5 \times 5.5 \mu\text{m}^2$) of the FTIR 2D Imaging maps showed in Figure LOCATION MAPS ZIF8 and Figure LOCATION SI ZIF8. In particular, the BSA@ZIF8 spectrum is representative of regions of the sample where the presence of BSA was more intense. The detail highlights the

23 cm^{-1} redshift of the BSA@ZIF8 Amide I band as compared to the spectrum of the protein before immobilization on the MOF.

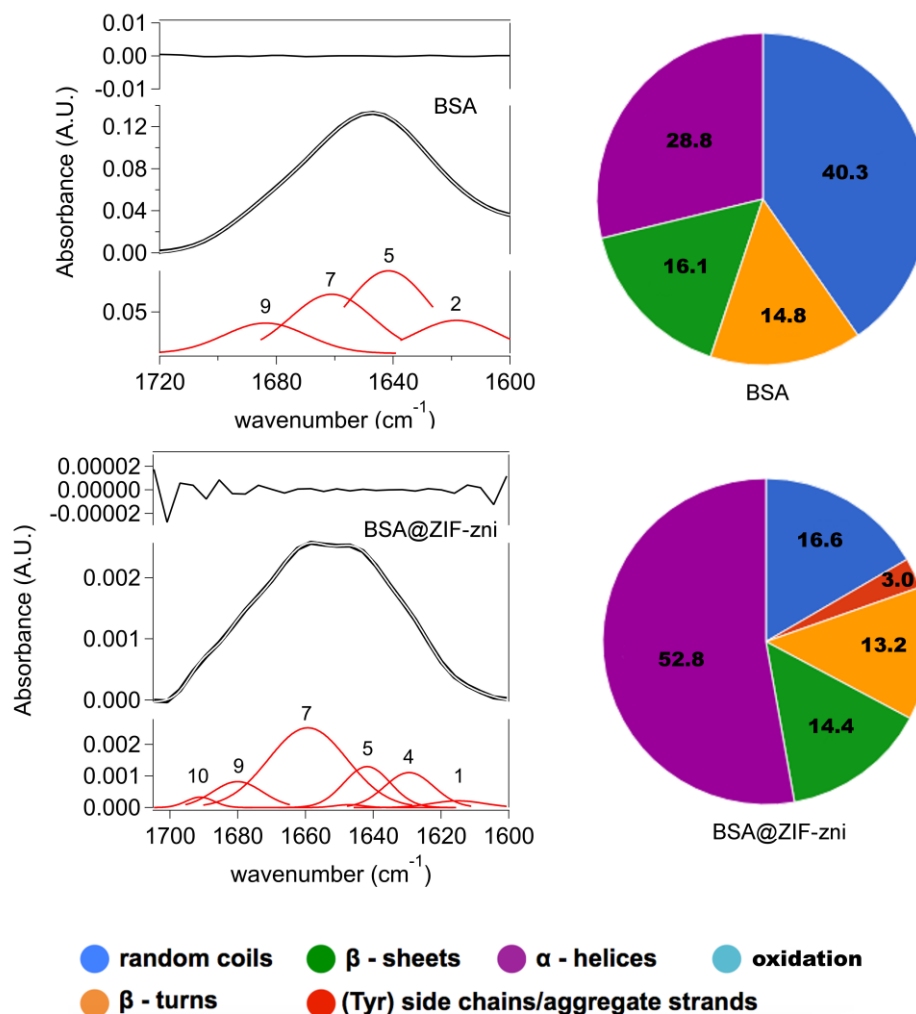


Figure S7 DECONVOLUTION ATR. (Top left, bottom left) Spectral deconvolution of the FTIR ATR Amide I band of BSA and BSA@ZIF-zni (after subtraction of a representative ZIF-zni spectrum). The bands' components are numbered as in Section 2.9; the y-axis reports the absorbance of the components (red bands), the experimental spectrum (thick black line), the fitting curve (thin white line inside the experimental curve), and the fitting residuals (black line on top of the spectra). (Top right, bottom right) The average secondary structure for BSA and BSA@ZIF-zni is reported in the pie charts, grouping the main structure types (relative error is ca. 0.05).

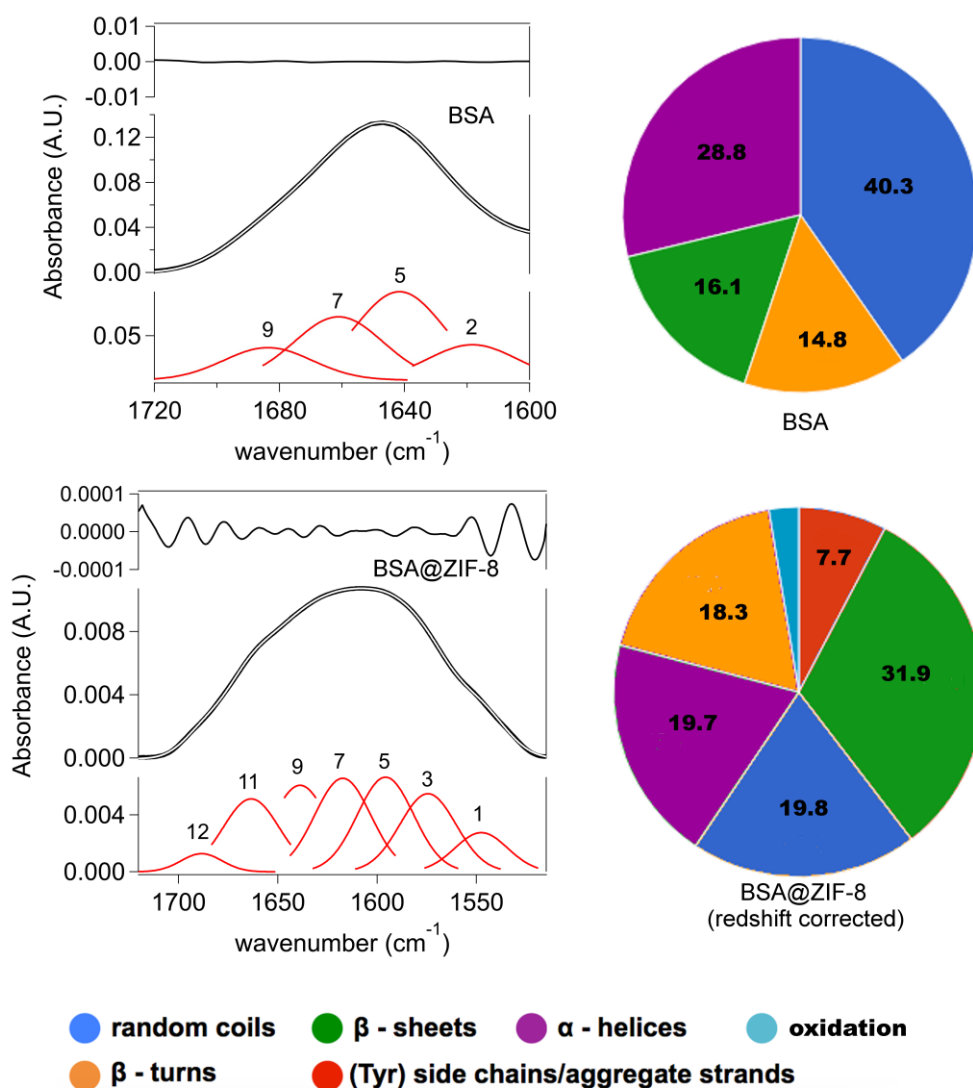


Figure S8 DECONVOLUTION ATR ZIF8. (Top left, bottom left) Spectral deconvolution of the FTIR ATR Amide I band of BSA and BSA@ZIF-8 (after subtraction of a representative ZIF-8 spectrum). The bands' components are numbered as in SI, and considering a redshift of ca. 50 cm⁻¹ from the amide I of BSA (before immobilization on the MOF); the y-axis reports the absorbance of the components (red bands), the experimental spectrum (thick black line), the fitting curve (thin white line inside the experimental curve), and the fitting residuals (black line on top of the spectra). (Top right, bottom right) The average secondary structure for BSA and BSA@ZIF-8 is reported in the pie charts, grouping the main structure types (relative error is ca. 0.05), and considering a redshift of ca. 50 cm⁻¹ from the amide I of BSA (before immobilization on the MOF).

Thermogravimetric analysis

Thermogravimetric analysis (TGA) was carried out by means of a TGA 4000 Perkin Elmer in a temperature range from 25 °C to 850 °C and a ramp rate of 10 °C min⁻¹, under an oxygen flow (flow rate = 40 mL min⁻¹).

N₂ adsorption/desorption measurements

N₂ adsorption/desorption isotherms were recorded at 77 K using an ASAP 2020 (Micromeritics). Samples were firstly degassed under vacuum for 12 h at 25 °C. The Brunauer–Emmett–Teller (BET)^[8] and the Barret–Joyner–Halenda (BJH)^[9] methods were used to calculate the specific surface area, the pore volume, and the pore size distribution.

Table 1. Physico-chemical parameters of ZIF-8 and BSA@ZIF-8

samples	^a S _{D,R} (m ² g ⁻¹)	^b V _p (cm ³ g ⁻¹)	^c Size distribution (nm)	^d ζ potential (mV)
ZIF-zni	8	0.003	15.6	n.d
BSA@ZIF-zni	n.d	n.d	n.d	n.d
ZIF-8	1760	0.625	0.458	5.30
BSA@ZIF-8	1640	0.582	n.d	n.d

^a Surface area (S_{Dubinin} and Radushkevich) obtained by N₂ adsorption/desorption isotherms; ^b Pore volume (V_p)

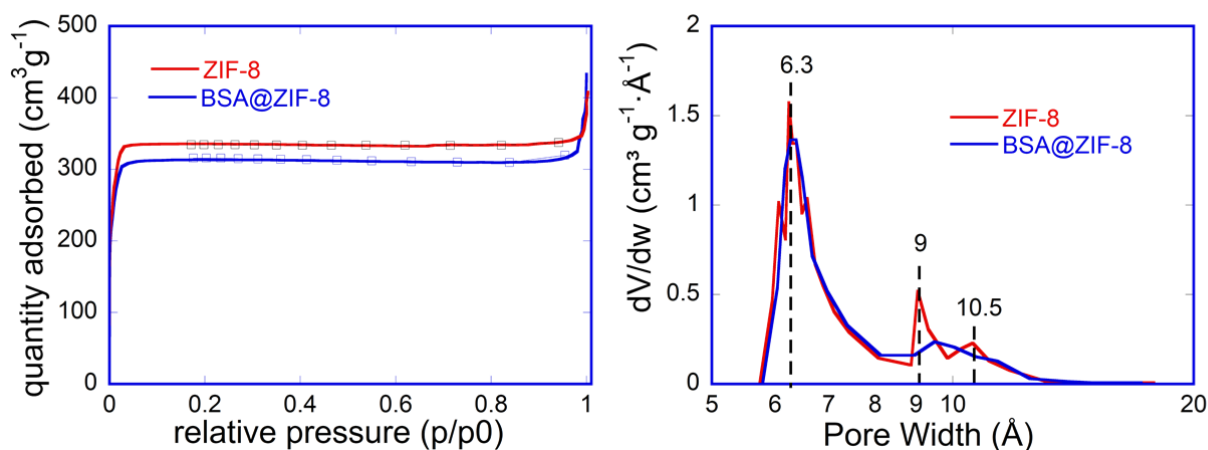


Figure S9: N₂ adsorption/desorption isotherms and pore width plot of ZIF-8 and BSA@ZIF-8.

References:

- [1] M. Naseri, F. Pitzalis, C. Carucci, L. Medda, L. Fotouhi, E. Magner, A. Salis, *ChemCatChem* **2018**, *10*, 5425–5433.
- [2] X. Wu, J. Ge, C. Yang, M. Hou, Z. Liu, *Chem. Commun.* **2015**, *51*, 13408–13411.
- [3] M. M. Bradford, *Anal. Biochem.* **1976**, *72*, 248–254.
- [4] G. Hungerford, J. Benesch, J. F. Mano, R. L. Reis, *Photochem. Photobiol. Sci.* **2007**, *6*, 152–158.
- [5] D. Badillo-Sanchez, D. Chelazzi, R. Giorgi, A. Cincinelli, P. Baglioni, *Polym. Degrad. Stab.* **2018**, *157*, 53–62.
- [6] J. KONG, S. YU, *Acta Biochim. Biophys. Sin. (Shanghai)*. **2007**, *39*, 549–559.
- [7] X. Hu, D. Kaplan, P. Cebe, *Macromolecules* **2006**, *39*, 6161–6170.
- [8] S. Brunauer, P. H. Emmett, E. Teller, *J. Am. Chem. Soc.* **1938**, *60*, 309–319.
- [9] E. P. Barrett, L. G. Joyner, P. P. Halenda, *J. Am. Chem. Soc.* **1951**, *73*, 373–380.